The University Of Sheffield.

Laser Cladding for use in Extreme Tribological Interfaces

By:

Peter Christoforou

A thesis submitted in partial fulfilment of the requirements for the degree of

Doctor of Philosophy

The University of Sheffield

Faculty of Engineering

Department of Mechanical Engineering

July 2020

“Dedicated to Emma and James”

“The important thing in science is not so much to obtain new facts

as to discover new ways of thinking about them”.

Sir William Lawrence Bragg

SUMMARY

Coatings are common in engineering applications for protecting the surface of components, either from exposure to environmental conditions or from contact with other components. Laser cladding is a coating technique which allows for thicker coatings of various alloys that enable high load bearing interfaces to operate at a wider range of loads or for longer, for example by increasing durability. This is of great benefit to the railways industry as well as other heavy industries, such as the steel industry. Laser clad coatings have been used extensively in other industries such as oil and gas for increasing the durability of drilling components; in mining and earth moving equipment, for increasing the durability of the components that come in contact with hard soil and rocks. Both are extreme interfaces.

In this study, new interfaces and extreme conditions for new industries are investigated, by highlighting the laser clad coating advantages, when used under extreme conditions. The extreme test conditions have not been investigated in published literature, especially with the use of laser clad coatings.

This project evaluated the performance of laser cladding coatings on railway components such as the wheel and rail. Other interfaces found in machinery in the steel industry were considered, specifically in the rolling of steel. A variety of interfaces were evaluated by modelling and testing, such as rolling-sliding, high pressure water jet erosion and impact. Three clad materials were identified as suitable for the chosen interfaces, martensitic stainless steel (MSS), Stellite 6 (Co-Cr) and a two-layer clad of Inconel 625 with Technolase. The clad parameters were fixed, resulting in constant material grades, allowing the coatings used in different interfaces to be comparable.

The materials choice was based on published research on similar interfaces. Tests were performed on existing test rigs for rolling-sliding and bending tests. The impact test was performed on a rig modified specifically for this study, while a bespoke rig was built for the erosion test. Metallographic techniques were used for all materials, to prepare the samples for characterisation using optical and electron microscopy, as well as nanoindentation and microhardness. Pre- and post-test material analysis was performed.

The use of computer modelling was considered mainly for the generation of test parameters, while the results from testing were compared to existing data. Key findings highlight that the use of the selected clad materials under the chosen extreme interfaces can have a positive effect on the durability of the coating, mainly by increasing the wear resistance properties of the coating. Furthermore, the two-layer clad coating showed promising results in stopping crack propagation to the substrate. The test results can be used in predictive tools by researchers in academia, as well as in industry, as a way of introducing laser cladding applications to interfaces of engineering products. Furthermore, the performance of the chosen materials indicates that this study may be used as the basis for selecting similar clad coatings for pilot trials or large scale testing.

ACKNOWLEDGMENTS

This research project was funded by the Mechanical Engineering Department at the University of Sheffield and partially funded by the ESPRC, through project no. EP/M023044/1. The author received the “Gordon Franklin PhD Scholarship”, which was set up by Miss Julia Boler in memory of Gordon Franklin. The author would like to thank the University and the sponsors for the opportunity and financial support. The author would like to thank and express his deepest gratitude to supervisors Professor Roger Lewis, Professor David Fletcher and Dr Stephen Lewis for their invaluable support and guidance.

The author would like to acknowledge further support received from staff and students; Dr Adam Beagles, Dr Christophe Pinna, Dr Ping Lu, Kate Tomlinson, Shaun Earl, Robert Dowding, David Butcher, Luke Callaghan, Richard Kay, Jamie Booth, Christopher Todd, Ian Hammond, Neil Hind, Dawn Bussey and Tes Monaghan. Contribution in kind for materials and processes was given by Ken Brooks (Sheffield Forgemasters International Ltd.), Chris Childs and Dr Gareth Evans (Sarclad Ltd.), Mark Sampson (Laser Cladding Technologies Ltd.) and the Quaker Chemical Corporation. Finally, the author would like to thank the industrial partners; Primetals Technology Ltd., the Rail Safety and Standards Board (RSSB) and British Steel for the continuing support and guidance.

NOMENCLATURE

$C(d_p)$	Particle diameter function (mm)	Pz	Peak height of primary profile (µm)
D	Radius (m)	Pq	Root-Mean-Square primary profile (µm)
d	Laser beam diameter (mm)	Ra	Average roughness of profile (µm)
tc	Collision distance (mm)	Rz	Peak height of roughness profile (µm)
E*	Reduced Elastic Modulus or Reduced Young's Modulus (GPa)	Rq	Root-Mean-Square roughness of profile (µm)
E1, E2	Elastic (Young's) Modulus (GPa)	R'	Reduced radius (m)
E_t	Exposure time of laser beam (s)	r	Radius of laser beam (mm)
F'	Laser beam fluence (J m^{-2})	rpm	Revolutions per minute
f(a)	Impact angle function (radians)	t	Time (s)
f_r	Laser scanning speed (mm s^{-1})	Tγ/A	Tee-gamma over alpha (N mm^{-2})
g	Gravitational acceleration (m s^{-2})	V	Worn volume (m^3)
h	Height of falling object (m)	v	Velocity (m s^{-1})
K	Wear coefficient	v_i	Fluid velocity at impact (m s^{-1})
L	Sliding distance (m)	v_p	Particle impact velocity (m s^{-1})
m	Mass (kg)	v_s	Speed of sound in fluid (m s^{-1})
$\dot{m}$	Mass flow rate of particles (kg s^{-1})	W	Watt (Nm s^{-1})
n	Velocity exponent	W'	Applied load (N)
P	Force (N)	Wa	Average waviness profile (µm)
p	Contact pressure on impact (Pa)	Wq	Root-Mean-Square waviness profile (µm)
P'	Laser power (W)	Wz	Peak height of waviness profile (µm)
Pavg	Average contact pressure (GPa, MPa)	α	Contact area radius (m)
P_c	Contact pressure (Pa)	ν1, ν2	Poisson's ratio (unitless ratio)
p_m	Flow pressure (equiv. to hardness)	ρ	Fluid density (kg m^{-3})
Po	Peak contact pressure (GPa, MPa)	σ	Contract Stress (MPa)
Pa	Average primary profile(µm)	π	Ratio of a circle's circumference to its diameter (3.1415…)

CONTENTS

1 INTRODUCTION

For the evaluation of the laser cladding method on various extreme interfaces, a wide approach on its applications has been implemented for this research. The focus is on five interfaces, with varying degrees of depth for each interface, resulting in an all rounded exploration of laser cladding under these conditions, as opposed to focusing on a single interface. This approach presents a collection of results available to academia and industry as a comparison between the various interfaces, but also as a reference to their individual performance, which can contribute to existing or new research. Along with the extensive literature review that is included here, this text can be used as a first point of reference for anyone researching laser cladding and its applications beyond corrosive surface protection.

The first two interfaces are related to railway rolling/sliding wear and impact at switches and crossings. The other three interfaces are inspired from steel industry components, however, the results from this study can be applicable to all industries with similar contact and wear conditions. Erosion from high pressure water, texture evolution on rolling/sliding contacts and coatings on rotating shafts. These interfaces can also be found on the railways, for example erosion from rainwater or jet washing equipment, texture on wheels and rails from grinding and protective coatings on carriage axles. Vice versa the rolling railways interfaces with rolling-sliding and impact wear mechanisms investigated in this research can be found in the steel industry, for example work rolls experience rolling-sliding wear as well as impact from first contact with incoming slab.

Specific case studies from each interface were chosen in order to determine laboratory test conditions. In railways there is a need to replace worn rail track quickly and at lower cost than the current practise. Replacing rails is costly for the operating companies and public due to the safety aspects surrounding the replacement of tracks, where various contractors are usually involved, making it an expensive process. A key area on the rail network is the switches and crossings, where the impacting force from the wheel can cause severe damage. Other areas on a rail network where severe wear is found is in tight curves, where often wear damage is caused by flange contact. Generally, critical areas in rail tracks are lubricated and modern locomotives have absolute control in traction of the driving wheels, so spinning and sliding from braking is eliminated. Spinning and sliding occurs at various levels thus causing wear, on occasions extreme wear. This could be attributed to friction modifiers, either deposited on the tracks by nature or introduced on purpose as part of rail maintenance. Different maintenance regimes are proposed with laser cladding coatings over standard rail. With an advanced material to prolong life and increase time between reprofiling or with similar material to enable in-situ repair, eliminating the need for replacing large sections of railway track. The benefits of a harder wearing material can be economical, reducing the total life-cycle cost but also safety can be increased by increasing the safety margin.

For the steel industry the aim was to increase the durability of components and the erosion of “deflector” plates in descaling equipment was selected. Typically hardened steel is used in descaling equipment as a wearing plate from erosion. Hardened steel can be ten times more expensive than standard steel used for fabricating the remaining equipment and a comparison between the standard

and hardened steel durability as well as the proposed laser clad material was essential to evaluate the performance of laser cladding and possible benefits for the steel industry. Furthermore, a specific case for a forged steel pinion which has been chrome plated to extend its operating life was considered for comparison with the laser clad. The aim is to extend the life of the pinion even further because of the thicker clad layer and the ability to grind and rebuild the material multiple times. Finally, the texturing of work rolls in skin-pass for cold and tandem mills was selected for further investigation. Similarly to the pinion, sometimes chrome plating is applied to these types of rolls in order to increase the surface hardness. Laser cladding can be a suitable alternative due to the thicker coating possible and evaluating the texture retaining properties of laser clad materials would be advantageous for this research.

Reviewing of extreme interface contacts to identify the contact conditions, and to define the test parameters, was carried out. In addition, a literature review for laser cladding was essential to identify gaps in research and to build an overall picture for laser cladding capabilities. Some of the papers reviewed were graded in order to map areas of research and prioritise relevant papers, these are referenced at the end of chapter 3, as [P1-P196]. The reviewed papers come from a variety of laser cladding topics such as alloying, residual stress measurement, cladding process and post-process techniques, and more. These have been listed first in the References to distinguish them from references used for other topics such as the various interfaces, modelling and testing.

1.1 Aim of the project

The aim of the PhD project was to compare the performance of unclad material versus laser clad material, on various interfaces and under extreme conditions, not found to be investigated previously in published research. Due to the various interfaces, the clad material parameters were fixed, allowing comparison between different interfaces, without investigating for optimal laser clad materials or processes for the chosen interfaces. The materials investigated were Technolase®, Inconel 625, Stellite 6 (Co-Cr) and Martensitic Stainless Steel, when applied as a laser clad coating from powder form. Tests were conducted for high load bearing interfaces and were evaluated in terms of wear, rolling contact fatigue, plastic damage, hardness profiling and roughness evolution. The interfaces were rolling/sliding, impact, micro-bending and erosion from high pressure water. The choice of Stellite 6 and MSS clad material was inherited from trials on previous projects at the University of Sheffield [1], while the combination of Technolase® with an intermediate layer of Inconel 625 was chosen for applications where crack propagation is of concern and an intermediate layer is used to arrest cracks from propagating into the parent material.

This project aims to answer these questions:

- Are laser clad coatings suitable for high load bearing applications?
- Is the performance for the selected applications improved, in terms of increasing the durability of the surface, as opposed to non-coated or coated with established methods?

1.2 Objectives of the project

Analysis and direct comparison of data generated from laboratory testing between clad and unclad materials, which have undergone the same testing procedure was planned. In order to define the conditions for testing, information on these interfaces for railway and steel industry applications was obtained through initial literature review and basic modelling work.

The subject matter in engineering projects, especially materials related subjects can have various degrees of scale. Macro, micro, or nano level of analysis could be applicable and implementing research that covers all levels can be challenging. The interest in this research was on microscopic damage initiation, its progression, and its impact on the substrate and interface, therefore the specimen analysis was not extended to nano scale.

It was important for the objectives of this project to explore the relevant materials from large scale in-situ, small scale in the laboratory and micro scale for metallurgical characterisation and obtaining material properties. The analysis discussion is at micro level, while the conclusions on the overall performance are finally discussed at macro level. The macro scale level is of practical use to engineers who apply laser cladding coatings onto their products. In railways for example, the geometry of a crossing nose and the application of coatings in millimetres or the wear estimation in grams over tonnage of traffic. With these scales in mind, the objectives were defined as follows:

1. Characterisation of the chosen materials for use in modelling. This was achieved by determination of the physical properties of the clad layer, dilution zone, HAZ and substrate material.
2. Definition of individual tests for the interfaces with the use of modelling for calculating the relevant information such as forces and contact pressures.
3. Hardness evolution of the clad materials to understand in-service work hardening properties. Hardness measurements were obtained before and after testing.
4. Wear resistance characterisation and comparison between clad and unclad materials for four interfaces. Mass and volume loss were obtained from four individual tests which can be used in modelling tools, for example commercial tools used in the railway industry for choosing rail grades for use in specific parts of the rail network. Other modelling tools can aid in material choice for applications where erosion damage is dominant or where maintaining surface texture is critical.
5. Characterisation of strain accumulation and stiffness of the two-layer clad material. This was achieved under bending tests and with the use of digital image correlation techniques.
6. Determination for the suitability of the chosen case studies for use in industrial trials, as the next step from this study.

The laboratory tests defined by the objectives are listed in Table 1-1 with a critique on the novelty for each test.

Table 1-1 Summary of test platforms, key conditions and novelty

Test *Rig Name*	**Typical Conditions**	**Test Conditions**	**Interface**	**Novelty**
Twin Disc *SUROS (Sheffield University ROlling Sliding)*	900-1500 MPa contact pressure	1500 MPa contact pressure, 400 rpm, 1%, 10% & 20% slip, dry	Wheel-rail rolling/sliding	10% and 20% slip and hardness mapping for premium rail materials
	1000-1300 MPa contact pressure, 1% slip from the elongation of the rolled product	1000 MPa contact pressure, 400 rpm, 1% slip and dry – lubricated discs for rolling aluminium strip at 20 rpm	Textured work roll	Similar to laser dispersing tests [2] – Cladding was never tested for EDT technology
Impact *Composites drop test rig*	75 kN-310 kN impact force, 1 GPa contact stress, values from literature (simulations)	24 kN impact force, 1 GPa contact stress	Impact at switched and crossings	Many papers on modelling impact at S&C, but not impact test data. Current data driven by tensile tests.
Water Pressure Jet *HiPEr (High Pressure Erosion)*	1 MPa Impact Pressure at 200mm standoff	1 MPa Impact Pressure (estimated) at 30 mm standoff and 20-25 mm^2 contact area	Erosion (fluid)	Particle erosion on cladding [3] – Novel for fluid erosion on cladding.
Micro-bending *Tinius Olsen UTM and Camscan SEM*	*Comparison study, not replicating field condition*	Up to 22 kN force on three point bend, 12 mm wide (5 mm thick) specimen with curved side (macro-UTM)	Bending test to obtain stiffness comparison and braking point / crack initiation	Obtaining stiffness comparison of the two coatings (electroplating and cladding). Observation of crack initiation resistance of the two coatings. Micro and macro test comparison.
	Comparison study, not replicating field condition	Up to 4.8 kN load on 8 mm wide (5 mm thick) specimen with curved side (micro-SEM)		

1.3 Thesis outline

The thesis is divided into different sections for the investigation of the interfaces (overview, laser cladding theory and literature review), modelling, testing (procedure and results) and discussion followed by conclusions. Each chapter includes a discussion on the relevant interface and the tests performed for each interface as well as test apparatus information are contained in the same chapter as the relevant interface.

A flowchart is presented in Figure 1-1, showing the structure of the thesis.

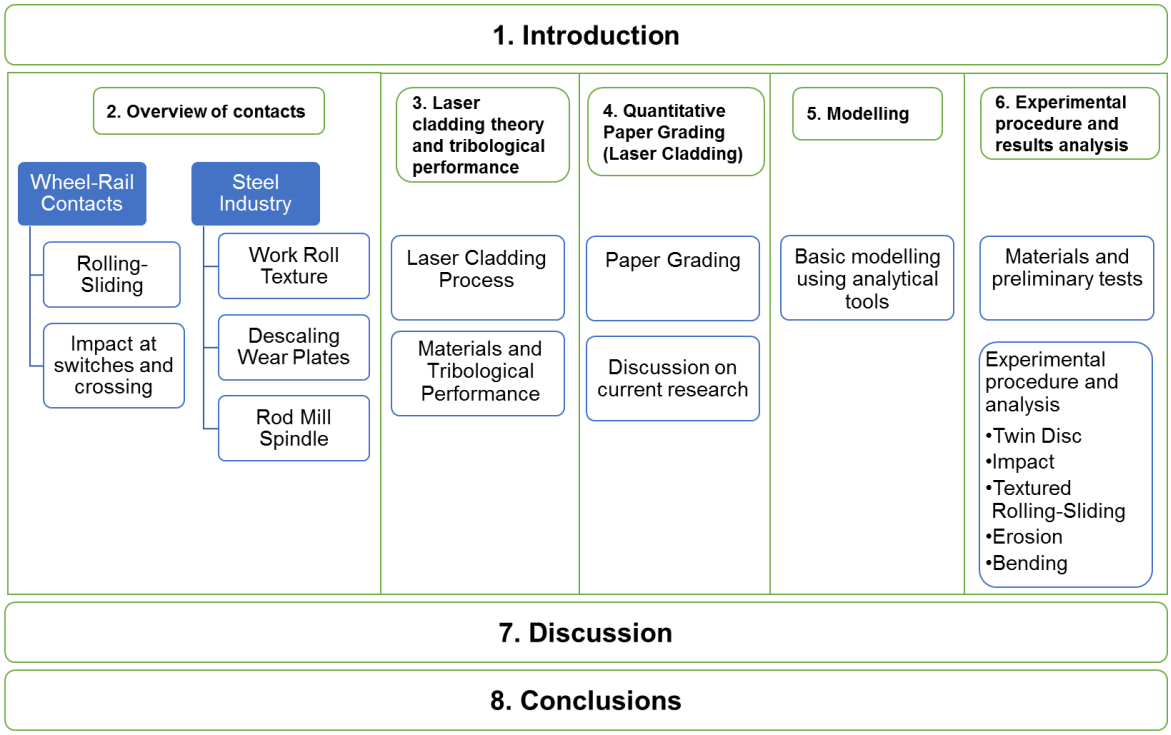

Figure 1-1 Thesis structure flowchart

This page was intentionally left blank

2 OVERVIEW OF CONTACTS

2.1 Introduction and purpose

The contact interface generally determines the most suitable surface treatment technology or coating to be used for a given application. The purpose of coatings is to protect components from environmental or other influences in the operating environment which could cause damage and possibly imminent failure of a component. For example, contact with lubricants, water, corrosive substances, gases, air, extreme temperature, impact, contact with other solid surfaces and so on. These call for protective layers in critical areas. In addition, coatings on surfaces may have other functions, such as controlling the friction coefficient when in contact with other surfaces. An example is surface coatings on bearings, whether traditional ball bearings (Carbon, Stainless or Chrome Steel) or modern dry bearings made of composites (fibres reinforced resins or ceramics). PTFE (Polytetrafluoroethylene), Thin Dense Chrome, Carbon, Ceramics (typically Aluminium Nitride/Oxide), and Zinc Phosphate/Chromate are some of the coating materials used on bearing components. With friction control as the main driver, wear reduction between the contacting surfaces of the bearing ball/roller and the bearing races is achieved, enabling longer life of components. There are of course cases where the opposite is required, such as high frictional forces in order to provide grip, generation of heat, grinding or even a cutting action, resulting in fast wear of one or both materials. Cutting tools made of tough steel normally have a surface coating of Tungsten Carbide (WC), applied as a liquid product on the sharp edges of cutting tools. The WC thin coating enhances the strength of the cutting tool and wears the target material significantly. As a result, the wear rate of the cutting tool is reduced as opposed to cutting without the WC coating.

In applications where the contacting pressures and resulting contact stresses are very high, protective coatings are prone to damage. Some coatings may break apart, delaminate or wear rapidly. Laser cladding enables bespoke alloying of coatings with good mechanical bond to the main components, resulting in coatings that can not only protect from environmental and other influencing factors but also from high forces that may induce stresses at the coating or beneath the coating. Some existing research and applications of this technology in industry have proven the ability to design extremely hard and durable coatings with laser cladding and highlighted the potential for developing coatings for new applications. Thicker coatings are key for load bearing applications as some stresses and micro-cracks exist well below the surface, where thinner coatings may not be effective.

Load bearing applications can be found in the heavy industry and an area of interest is the rolling mills industry, specifically for rolling steel and aluminium for plate, strip, foil and long products such as rails. There are plenty of “extreme” tribological interfaces in a rolling mill plant. The term extreme is used generally when there is high loading (sliding or impact) or high temperature. In addition, when referring to corrosive or contaminated surfaces, for example from oil, grease and debris. Furthermore,

high velocity erosion and wear from impact/sliding mechanisms. These tribological interfaces are mostly metal-to-metal surface contact.

Another metal-to-metal interface which can be considered “extreme” is the wheel-rail contact. A well-established and researched interface, it could benefit from further development. The reason for continuing research in railways is the demand for faster trains and for more reliable services with a continuously increasing number of passengers using trains each year. The rail industry is expected to provide trains that are safe, reliable, financially viable and comfortable to travel in.

It is paramount to avoid derailments or smaller accidents. A major problem for the railway industry is the delays in the running schedule of trains. This can be financially catastrophic for railway companies, either for train/station operators or infrastructure management, for example Network Rail in the UK. Under Schedules 4 and 8 of the UK government franchise scheme for railways, every time a service is disrupted as a result of rail failure or planned/unplanned maintenance, automatic payments are made by Network Rail to train operator companies (franchisees). This cost was £700 million in 2018-19, an increase of £200 million from the previous year [4]. Some of the technical reasons behind delays are attribute to maintenance issues and failure of equipment. Other factors can be environmental such as leaves or snow on the track, falling cargo such as liquids/sand/stone and other debris from open top freight trains, sand or dust in the environment which can vary in different parts of the world, extreme heat or heavy rain. The railways in the UK compensate for some of these factors with the use of friction modifiers, which in turn, along with the variety of train sizes and wheels running on the same network, complicates the job of designing or improving the wheel-rail contact. It is important for railway companies to lengthen the gap between maintenance and train/track downtime and this can be achieved by increasing reliability of the equipment and processes.

The quality of rails and wheel material has been improved tremendously since the beginning of commercial railways and the same goes for other components of the carriage that affect performance such as driving and suspension systems. The current railway system has been in use for nearly 200 years, for example the Liverpool and Manchester railway built in 1830 was the first public railway with steam locomotives. Despite the amount of technological progress through research and development, railway accidents continue to happen to this day. Some accidents are due to human error, such as not abiding to speed limits or stopping on time. More critical types of accidents are collisions with other trains due to signalling errors and derailments, caused by mechanical failure on the bogie assembly such as the suspension, axle, brakes and wheels. Apart from the train vehicles, the railroad components could be the cause of accidents, such as the ballast, sleepers, rail fasteners and rails. Rails can fail in many ways, from fracture of the rail to loss of the railhead profile due to extreme wear. Another factor that amplifies the need for maintenance and subsequent rising in cost each year, is that the rail network in the UK is getting busier every year, with a reported increased of 12.2% of passenger km since 2016 [4].

Despite the numerous accidents, fatalities and year on year increase of rail accidents in Europe, trains are still considered as one of the safest modes of transport, at least in Europe and other

developed regions [5]. The following figures are some published statistics on rail accident fatalities; Figure 2-1 is a comparison with other modes of transport, while Figure 2-2 and Figure 2-3 are historical fatal accidents in the EU and UK respectively.

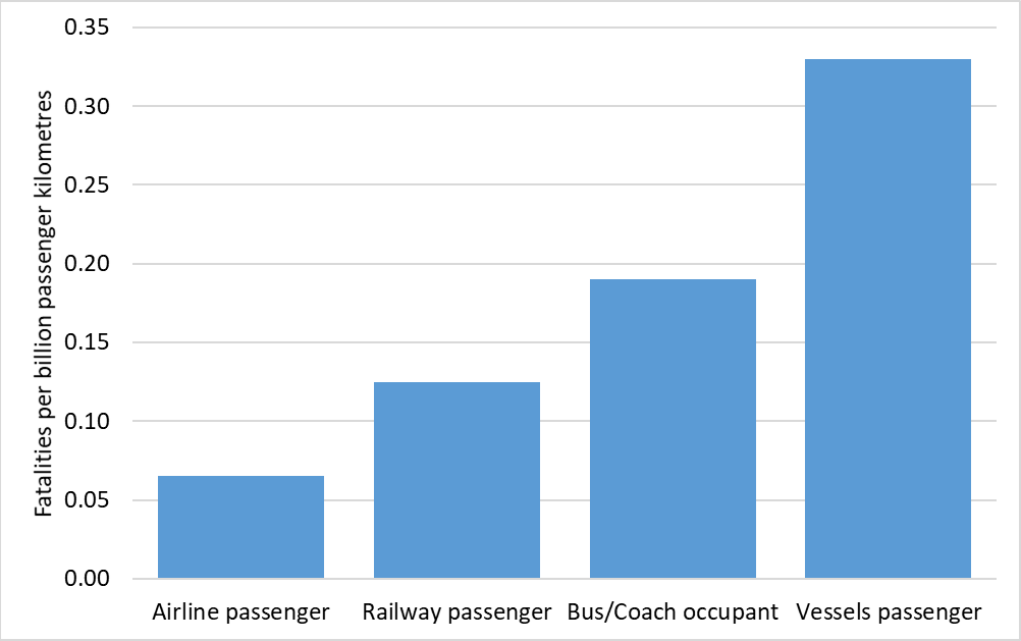

Figure 2-1 Fatalities for different modes of transport in EU-28 countries 2010-2014 (adapted from [5])

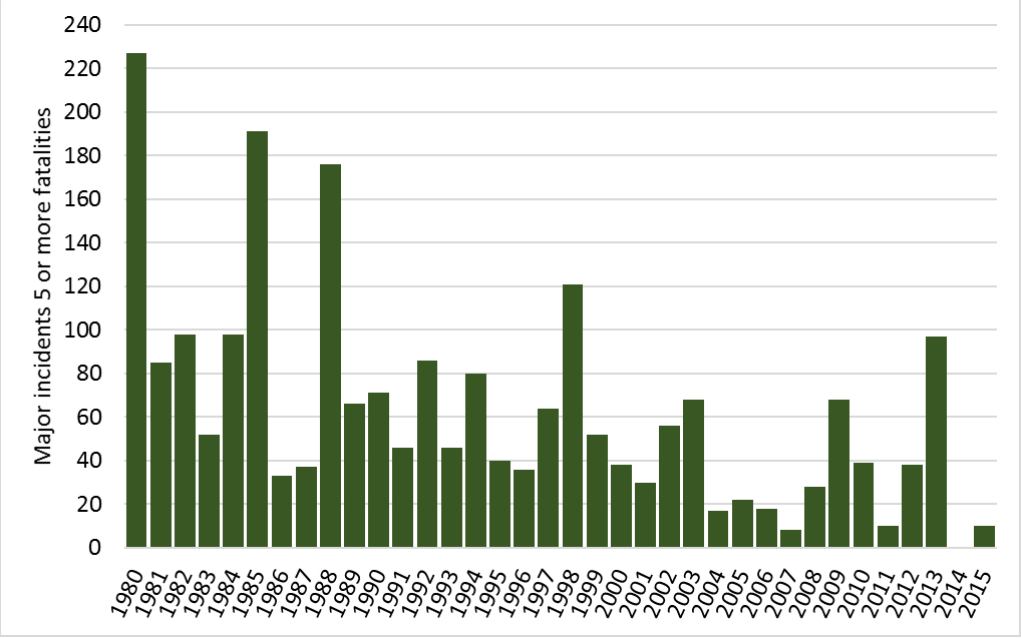

Figure 2-2 Railway accidents in EU-28 countries (adapted from [5])

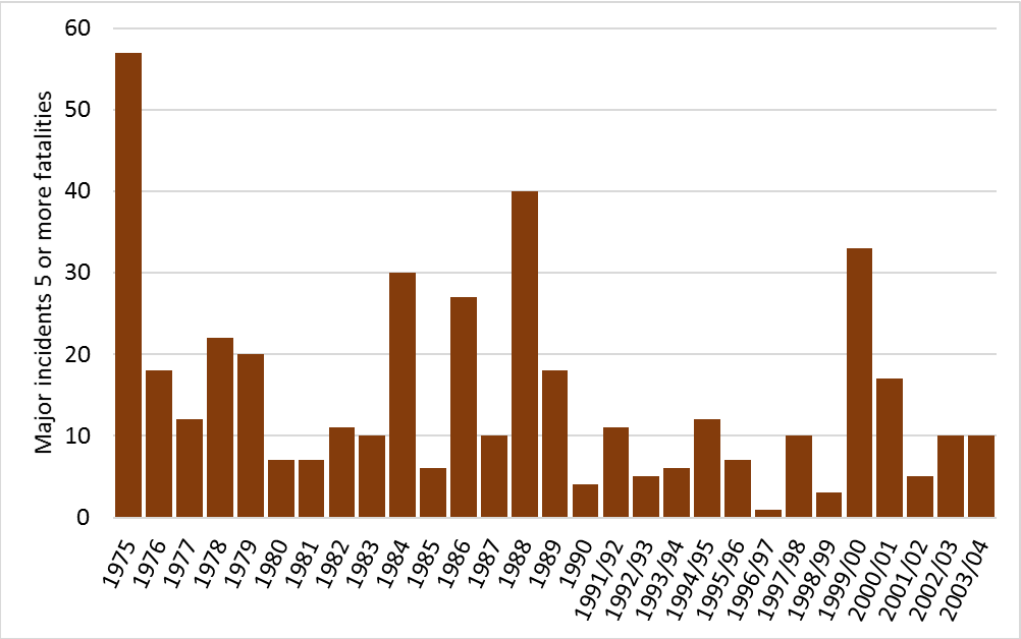

Figure 2-3 Railway accidents in the UK (adapted from [6])

Failures in railways prompted operating companies and the engineering community to investigate the failure mechanisms which has led to the creation of different engineering disciplines, theories and methodologies. These contribute to the safe design and manufacture of engineering components through theory development and proving by mechanical testing on fatigue, plasticity and fracture mechanics. This work is famously attributed to August Wöhler who was the first to systematically test railway axles and characterise the fatigue behaviour of metals in 1860. However, the concept of fatigue dates back to 1829 when Wilhelm Albert reported on failure of mining equipment, such as hoist cables from repeated loading and the first railway investigation was in 1842 by William J. M. Rankine on the Versailles railway accident [7, 8].

The interfaces investigated here will be assessed in the laboratory in terms of their tribological and mechanical performance. Scale-down wheel/rail interface tests in a twin-disc machine at 1, 10 and 20% slip, drop test rig for crossing nose impact, high pressure water jet for erosion testing, twin-disc for roughness evolution testing, and macro and micro bending tests for the roll mill pinion. The test objective is to compare the current material with laser clad material for each interface. Further analysis of the samples will consist of chemical analysis, micro-hardness testing, nano-indentation for nano-hardness and obtaining elastic modulus, surface scanning for measuring roughness and wear volume, as well as assessing wear loss with precision weighing scales. Microstructure images and chemical analysis of the samples will enable identification of the layers in the clad samples and their transformation/grain size changes before and after testing.

Two contacts are of interest for the wheel-rail interface, rolling/sliding present on standard tracks and crossings. The latter is concerned with the wheel impact effect on the rail crossing nose, due to the dynamic forces generated by various trains, which operate at different speeds.

Rolling Mill interfaces are reviewed, specifically work rolls that incorporate texture on their rolling face as part of the rolling process. Further discussion is focused on plate material used for the manufactured of descaling equipment in a typical steel rolling mill plant. Known as a descaler, hot slabs and ingots are being descaled prior to rolling, with the use of powerful water jets. The last interface from rolling mills components is a case of a pinion and the need for improving its surface, in order to increase durability.

Wear mechanisms are governed by the dissipation of energy from the contact between bodies, where the majority of the energy causes the wear, but may also be dissipated in other forms such as noise and heat. Other forms of energy loss such as heat and noise are not discussed here.

2.2 Wheel-rail contact

The wear mechanisms for the wheel-rail interface are adhesive, abrasive as well as rolling contact fatigue during normal rolling of the wheel over the rail at various speeds. The wear will differ significantly depending on the load and speed, as well as when braking, which may cause significant sliding or during acceleration, which may cause significant spinning. The main reason for sliding or spinning is when the on-board computer system fails to provide controlled braking or controlled acceleration. These events are published in various reports [9, 10] and as it is discussed in later sections, their cumulative damage is significant since the wheel or rail profile is altered. Spinning is significant to localised rail damage, although it does not occur often, the outcome is severe to extreme damage of the rail. Severe damage from spinning often cannot be rectified with grinding, but with a costly rail section replacement. In addition to these, the switches and crossings impact contact is discussed as it must be included when evaluating wheel wear [11].

The wheel-rail contact is a non-conforming contact which exhibits mostly compressive stresses caused by very high pressure, due to the small contact area and high loads, especially in freight trains. Often it is studied as a static contact in order to simplify any given case, however, it is a dynamic interface where the contact point and contact area vary depending on the location the wheel is on a track, the contact point varies because of the conicity of the wheel or there may be multiple contact points, for example there could be a contact point on the railhead and a contact point on the flange and/or railhead gauge corner at the same time. In order to analyse the wheel-rail contact, it is common to simplify the problem to a Hertzian contact which enables an instant solution to predict forces, pressure, contact area and so on and therefore further solutions for wear and damage predictions.

Analytical solutions have been developed for more complicated cases and are widely used in academia and industry. For example Magel & Kalousek have developed such models (validated with NUCARS predictions) and they have proven a significant 25% reduction of flange wear on the new design in comparison with the old design [12]. Magel & Kalousek have also develop a systems

approach to wheel-rail interface management and research, which has been adapted by Lewis and Olofsson in the format shown in Figure 2-4 [13]. The rail often can be corrugated or there may be other dynamic loads from the train that affect the contact relationship through any given time and in addition there is a varying contact and load relationship at switches and crossings due to the increasing or sudden (impact) loading the wheel-rail experiences. The wheel and rail profiles change continuously and have an inter-dependent behaviour throughout their operating lives which adds to

the complexity of modelling and analysing for the purpose of predicting wear or operating life. The wheel often has out-of-roundness defects such as wheel flats, a deviation from circularity or concentrated defects caused by non-severe rolling contact fatigue in the form of spalling or shelling defects [13].

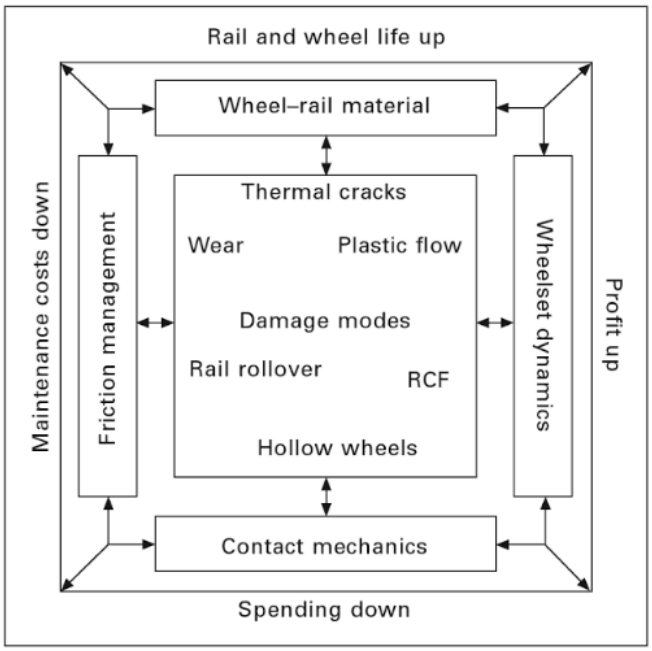

Figure 2-4 Systems approach to wheel-rail interface management and research [13]

Railways are frequently inspected and there are numerous defects that play a decisive factor in repair or replacements of rails. Such defects are shelling, head checks, spalling, squats, tache ovale, plastic flow and tongue lipping, bolt hole crack, longitudinal vertical crack, traverse crack, buckling and corrugation. Defects relevant to rolling/sliding are discussed. Figure 2-5 indicates the various features that make up a typical rail and wheel. The contact between the “conical tread” of the wheel and the “crown” of the rail is the interface that supports the vertical forces, mainly from the mass of the train and carriages. The conical geometry of the tread allows the bogie mechanism to rotate accordingly so that it follows the rail path when a curve is introduced on the track. This is because the contact patch is shifting laterally and the effective circumference of the wheel tread, under the contact patch, varies from side to side. The variation from either side of the track is due to the mirrored geometries of the conical treads. This means that two wheels on the same axles will spin at slightly different speeds when not on a straight track, thus compensating for the track curvature. For various reasons, the lateral forces can be exceeded and often this results in contact with the “corner gauge” and

"flange", which are there to prevent derailment with occasional contact, as opposed to a continuous contact with the rail.

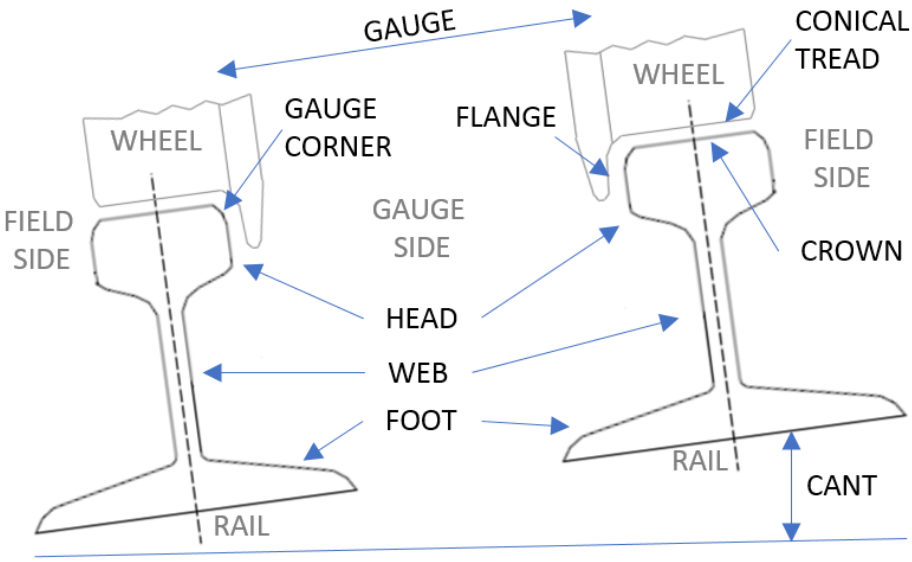

Figure 2-5 Features of wheel and rail

Lubrication and friction modifier regimes require a good balance to work efficiently together without cancelling each other. Lubrication is added in particular areas of rail track, such as curves, to reduce the friction between the wheel flange and the gauge corner of rail, where the wear is more significant than other areas of the wheel and rail. This is due to the larger diameter of the flange which means as the wheel face is rolling on the rail, the flange is definitely sliding. In addition, the outwards movements due to the centrifugal force and the cant geometry of the rail, it means that the flange is receiving some of the lateral forces on curves, while it is not intended to do so, the reality is that under certain circumstances the wheel flange-gauge corner rail contact is seeing such forces. In other circumstances friction modifiers in different forms, such as sand, are added to the rails to increase friction, for example to avoid sliding during acceleration or braking or to improve rolling during wet or icy conditions.

It is near impossible to define and characterise the wheel-rail contact parameters such as contact pressure, contact area, force magnitude and direction with precision and accuracy for all scenarios. This is due to the countless combinations or rail and wheel geometry, track morphology, speed, vehicle weight and so on. Assumptions are derived and a limited number of cases is used by experts, for example typical or extreme cases that are critical for maintenance or safety. Cases are formed by a combination of the following examples:

- Rolling on a straight track
- Rolling on a tightly curved track
- High cant rolling (superelevation)
- Track incline or decline
- Presence of third bodies (water, leaves, sand, friction modifiers, debris)

- Sliding when stopping or accelerating
- Impact over insulated bolted joints, crossing blade (on switches) and crossing nose
- Rolling over corrugated track (in vertical and horizontal planes)
- Rolling stock coupling type and possible cause of sliding
- Variable wheel types and dimensions, variable axles and bearing types
- Variable mass, centre of gravity and other influencing factors on the dynamic behaviour of the train

When considering these scenarios, it is good practise to keep parameters constant in order to make conclusions comparable. For example, the rail gauge size, wheel size, mass of the train and speed.

2.2.1 Rolling-sliding

Multiple damage mechanisms are associated with rolling/sliding contacts. These can be triggered by operating loads or by the environment, ranging from mild oxidative to severe wear. Sometimes the environmental impact may contribute to the acceleration of ongoing damage mechanisms, such as water or lubricants trapped in cracks and leaves on rails turning into third body elements. Furthermore, extreme temperature changes affect the interface and third bodies in many ways.

The variable loading conditions that the rolling-sliding contact experiences result to some degree to a very large number of different wear cases, which would make it impossible to investigate all possible scenarios of damage. In general, the main wear mechanisms in rolling-sliding are abrasive, adhesive and rolling contact fatigue, with rolling contact fatigue being a milder form of wear compared to adhesive and with abrasive causing a more rapid damage.

Abrasive wear is caused by contact between two solid bodies, where the first body's surface consists of hard particles while the second body consists of equal or softer particles, which contact can cause a rapid and severe wear with the removal of particles from the surface of the softer body and or from the surface of both bodies. There are several mechanisms acting that cause abrasive wear rather than a single mechanism, such as micro-cutting, micro-fracture, fatigue by repeated ploughing and pull-out of individual grains. Two modes of abrasive wear can be found from literature, two-body and three-body abrasive wear [14].

The wheel-rail contact in most cases falls under the three-body wear mode, which is a concept not always considered by the industry. The third body concept was introduced in the early 1980's [15] and three-body abrasive wear entails third bodies, other than the rail and wheel bodies in contact, which are described as "artificial", in opposed to "natural" third bodies where "natural" bodies are particles stemming from the wheels and rails formed during rolling. Third bodies can be "climatic" such as dead leaves, frost, water etc., "operational" such as ballast stones, sandbox sand, rail lubrication oil etc., and lastly "transported products", although most freight trains have their cargo sealed, some contaminants are exposed or passenger related debris can become third body. Descartes et al. [16] found that the rheology of the third body controls the wheel-rail contact

conditions by absorbing contaminants and by influencing friction as it responds to normal and tangential stresses.

The different combinations of phases in steels can provide them with abrasive resistance properties. Hadfield steel is very resistant to abrasion due to the high content of manganese (10-14% Mn, 1.0-1.4% C as specified in ASTM128) allowing for a virtually pure austenitic steel with a trace of martensite to form, making it suitable for situations where rocks as well as grits impact the surface (harder particles) (Stachowiak [14] citing Honeycombe [17]). The formation of carbides in steel can increase the wear resistance by four times compared to carbide free steel, up to a peak of 30% volume of carbide, as higher volume of carbide can cause brittleness and wear resistance reduction. Alloying with chromium and molybdenum can generate extremely hard carbides, for example hardness of about 1,300 HV can be achieved when alloying chromium carbides and about 1,500 HV when alloying with molybdenum carbides [14]. Laser clad materials being researched for their abrasive resistance properties are Stellites and Stainless steels which have a high content of cobalt and chromium. Stellite 21 is high performing alloy when used with the laser cladding process and it is the only one of the Stellite alloys that contains both chromium and molybdenum.

Adhesive wear can be characterised by the adhesion or transfer of material between two bodies and having high wear rates with a large unstable friction coefficient. It is not an easy task to identify and study adhesion in most systems as natural contaminants such as organic matter, oxygen, water and oil are always present providing a surface layer which can suppress adhesion between solids. The study of solids under vacuum is very beneficial as the tribological behaviour changes due to the lack of surface contaminants, especially metallic surfaces which exhibit the most dramatic changes. High roughness and hardness of the contacting bodies reduces adhesion wear and when there is strong adhesion, transfer of the weaker metal to the stronger occurs. This is attributed to electron transfer between contacting surfaces when in close proximity and the ability to exchange electrons in this way depends in the metal's crystal structure type [14].

Rolling Contact Fatigue (RCF) is a widely studied damage mechanism which affects both the wheel and the rail. RCF mainly causes surface damage by a repeated rolling contact, where very high local stresses are repeated many times from rolling-sliding and wear particles are generated by fatigue-propagating cracks formed by the deformation of the asperities of the opposing surfaces making contact. An important characteristic of the RCF is the micro-slip and creeping movement [14].

The surfaces of two bodies in contact "flow" through the contact zone and may have slightly different tangential velocities and also slightly different angular velocities. If the velocities are unequal, the rolling motion is accompanied by sliding, while if the angular velocities are unequal, then it is accompanied by spin. The presence of a tangential force provides a motion called tractive rolling while the absence of this force describes a motion called free rolling. Some contacting points (in the contact zone) may slip while others may stick and this is expected to take place in tractive rolling, as depicted in Figure 2-6. Creep is the slip that is made apparent by the difference between the tangential strains in the two bodies in the stick region [18]. Another definition for creep is that it is the fractional difference in the rolling speeds of two surfaces, which express the relationship between the

ratio of the frictional T and normal N forces. Figure 2-6 shows this relationship, where creep increases when tractive force increases, up to a limit governed by the coefficient of friction in the interface and Beagley found the limiting coefficient of friction to be independent of the load [19]. Reynolds first recognised that the contact region would be divided into stick and micro-slip zones and supported his argument by creep measurements using rubber cylinder rolling on a metal plane and vice versa [18].

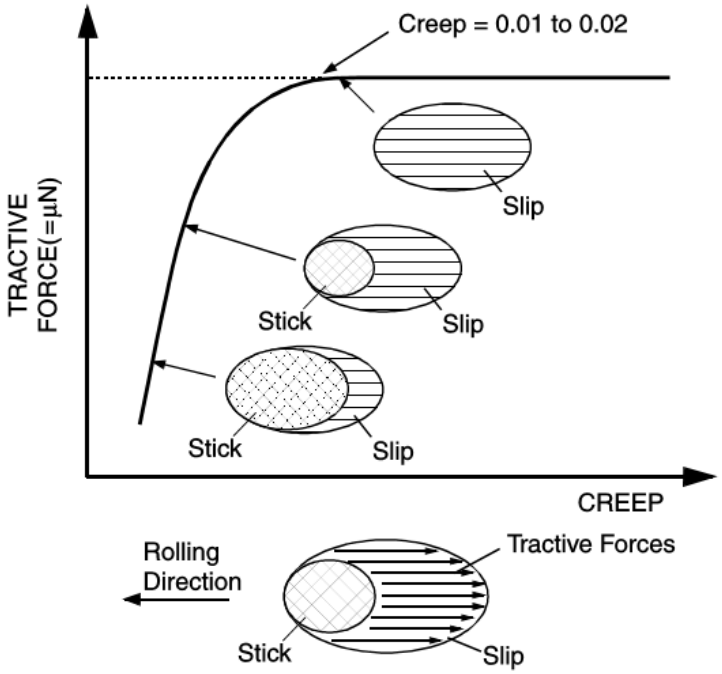

Figure 2-6 Relationship between traction and creep in the wheel-rail contact [13]

Lewis et al. explain how twin disc testing identified two wear regimes initially, mild and severe wear, while in later work, a third regime beyond severe was identified, catastrophic wear. Wheel tread wear falls within the mild regime, whereas flange wear falls in the severe or catastrophic regime [20, 21].

RCF could be described by damage such as squats, shelling and head checks where head checks are often found in curves and switches where there is higher tangential force/slip and decreased wheel-rail contact area due to interaction with flange contact [22, 23]. Severe RCF may lead to rail breaks, an example of which is shown in Figure 2-7.

Figure 2-7 Break from RCF on the railhead [24]

Head Checks are surface initiated defects (shallow cracks) on the gauge corner of the high rail in curves, see Figure 2-9. They typically occur at an angle of 30-60 degrees to the longitudinal axis of the rail. High loads and friction in the contact causes plastic strain accumulation, also known as ratchetting, resulting in head checks. It is common practise to remove head checks by grinding and re-profiling of the railhead. If not controlled, the ductility of the surface material could be exhausted, resulting in larger cracks that can cause a rail break [13]. Head checks and gauge corner crack (GCC, see Figure 2-8) differ in that the term head check is attribute mostly to cracks located on the crown (see Figure 2-5) of the rail rather than the corner.

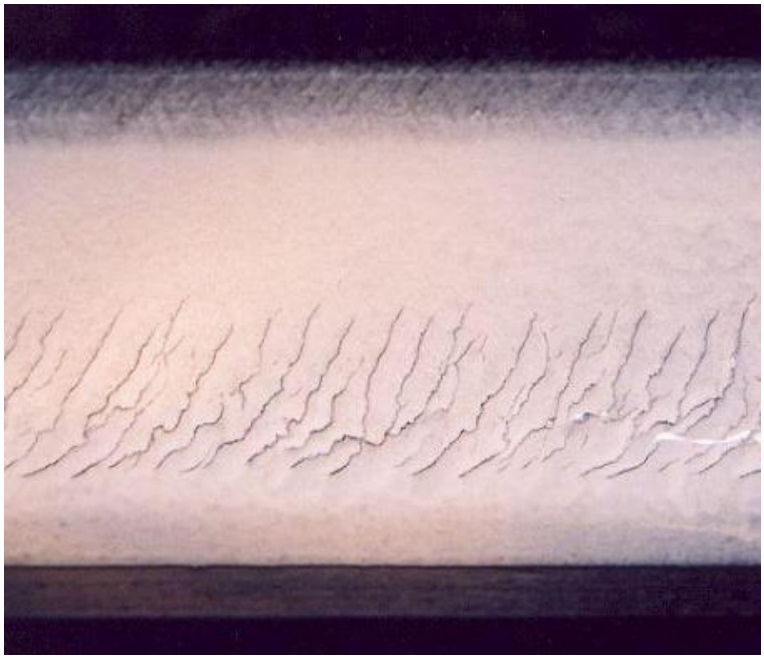

Figure 2-8 Gauge Corner Cracking from high-speed passenger rail [9]

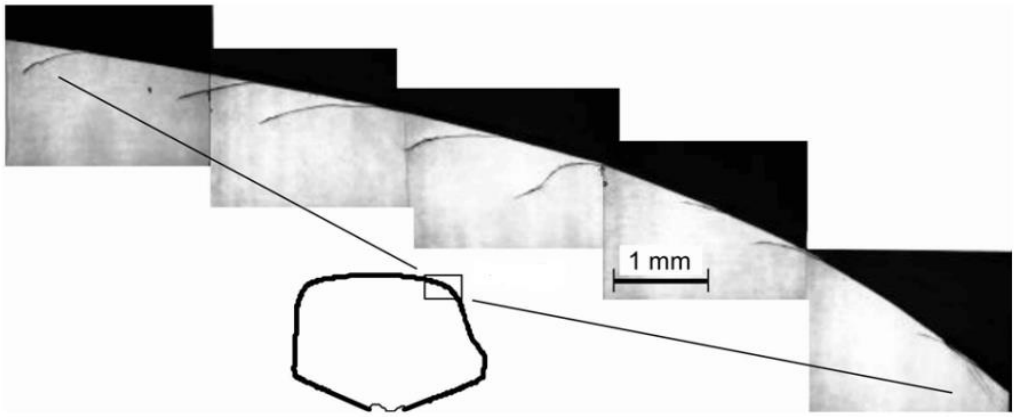

Figure 2-9 Micrographs of head check cracks [25]

Shelling occurs when surface and/or subsurface cracks linked up with other cracks, resulting in pieces of the rail surface chipping away, see Figure 2-10. Excessive stress loads at the gauge corner could cause material to yield along a slip line, resulting in shelling from gauge corner collapse, see Figure 2-11.

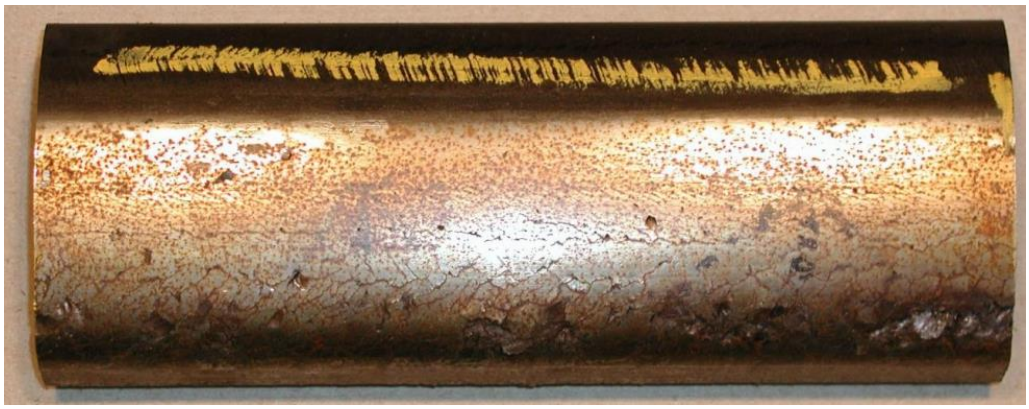

Figure 2-10 Shelling of rail [9]

Figure 2-11 Shelling from gauge corner collapse [9]

Spalling is very similar in appearance to shelling and it is caused by a different damage mechanism. Extreme wheel sliding and spinning conditions generate additional localised heat in the contact patch, resulting in temperatures exceeding the transition temperature of the material, for example 723 ^{o}C for pearlitic steel. The heat effect has a very short duration and afterwards the material cools rapidly, thus forming a white-phase martensite, which is brittle and cracks with subsequent loading. Impact in the martensitic zone must take place in order for spalling of the surface material to occur. Spalling is common on the wheel due to sliding, since the portion of the wheel affected by heat is a lot smaller than the rail, due to the longer length of the rail. The opposite effect takes place when the wheel is spinning and the heat is affecting a short portion of the rail, in this case a thin layer of martensite is left of the rail surface (Figure 2-12), similar to a squat and subsequent loading will initiate and propagate cracks from this defect.

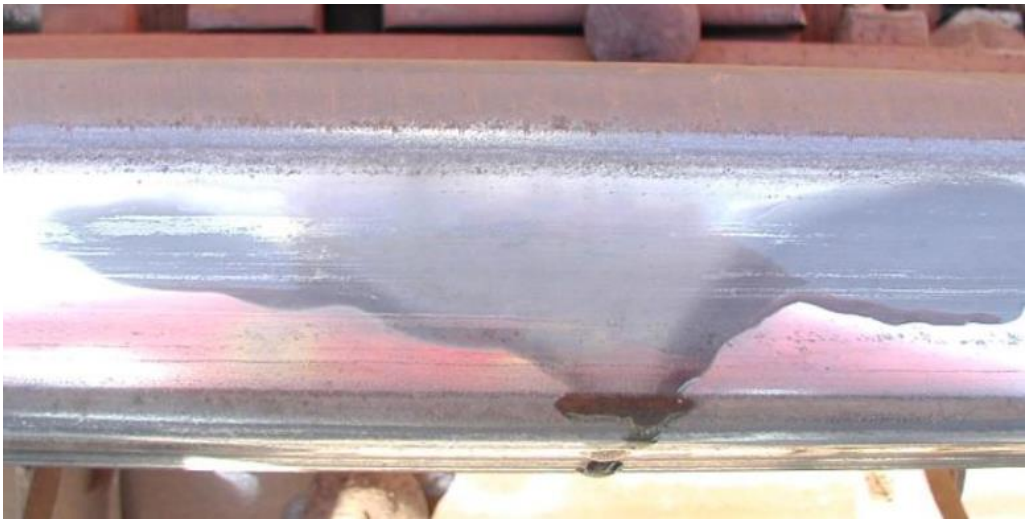

Figure 2-12 Thin streaks of martensite on the rail surface [9]

Squats are a shallow surface depression in the centre surface of the rail head, with an appearance of a dark sport. Figure 2-13 shows subsurface cracks converging near the surface, thus forming a squat.

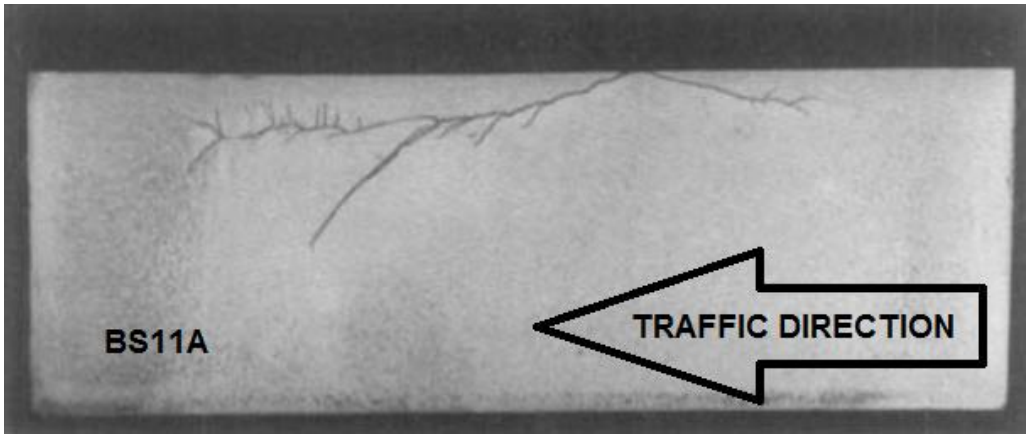

Figure 2-13 Squat RCF at the running surface [26]

Tache Ovale is the term used for fatigue rail failure initiated from the sub-surface of the rail due to large, brittle inclusions such as Ca, Al, Si and O. Material imperfections and inclusions may lead to further damage, although in recent years this problem is minimised significantly with improvements in manufacturing (minimal inclusions and low levels of hydrogen) as well as improvement in quality control and routine inspection of wheels and rail in service [13, 24, 27]. An example of a break caused by a tache ovale is shown in Figure 2-14.

Figure 2-14 Break from "tache ovale", with grainy, granular material between the shiny face of the fatigue crack and the rail surface [24]

2.2.1.1 Testing and mapping of RCF

The wear of rails and wheels has been studied extensively over the years with field measurements, specially built test tracks, laboratory full-scale tracks and scaled down versions such as twin disc testing, which has led to a greater understanding of wear mechanisms and transitions [28]. Twin disc testing in the UK originated sometime after 1935 when a new building was officially opened (known today as Hartley House) at LMS research laboratories in Derby. The twin disc machine, known as a wear testing machine at the time, was successfully completed in the end after a number of trials to overcome difficulties with scaled down versions of the wheel rail components [29]. Due to the smaller mass and radius on the scaled down version, the pieces become very hot quickly, with uneven wear, providing erratic and inconsistent results. Twin disc testing is typically characterised by three wear regimes, where the initial heating of the pieces causes initial oxidation and further wear is cause by momentarily high temperature. The three wear regimes are shown in Figure 2-15. Twin disc testing must be carefully designed to account for the effects of scaling down, temperature distribution and debris management, to avoid the effect of debris generated from wear from becoming a third body during the test.

A way to understand the wear mechanisms and improve wear prediction is with the use of wear maps, such as wear rate over Tγ/A, wear rate over percentage slip, traction coefficient over percentage slip, depth of plastic deformation over percentage slip. Adding a third parameter to a graph can provide

more information on the behaviour of wear, for example adding a material temperature to the wear rate - Tγ/A or combining wear coefficient, contact pressure and sliding speed on the same graph [21].

The expression Tγ/A (N mm^{-2}) has been adopted by researchers as a way of understanding and interpreting creep forces, by dividing the creep or traction force by the affected area. The frictional force is derived by the vertical force and friction coefficient in a given case and this is multiplied by the slip in the rolling contact to define the creep force of the flowing material. The Tγ term is expressed over a contact area in order to make it scalable and allow to correlate laboratory testing with real Tγ values. Bolton and Clayton [30] have first demonstrated the linear relation between the wear rate and Tγ, where the wear rate is expressed as weight loss per nominal contact area per unit distance rolled.

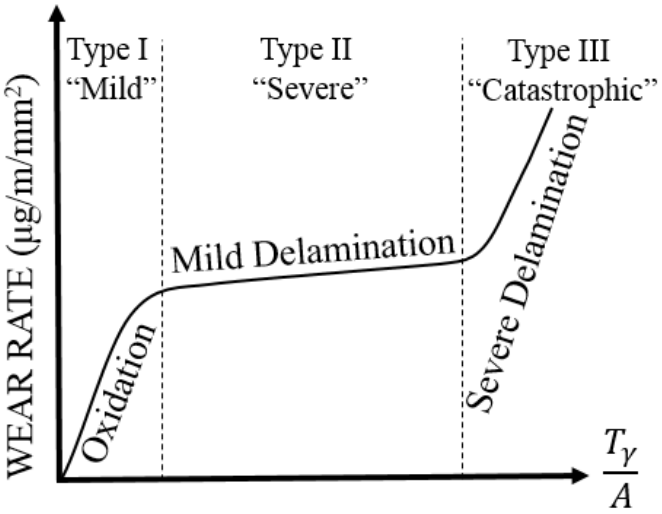

Figure 2-15 Schematic diagram of wear regimes (adapted from Lewis et al. [21])

A study in the elevated temperatures during twin-disc testing indicated a good correlation between analytical and measured temperatures [31]. Elevated temperatures may lead to a transition from severe to catastrophic. The temperatures at which the strength of the steel tested (rail UIC600 900A and R8T wheel) is around 200-250 °C. This coincides with the transition to the catastrophic regime, see Figure 2-16.

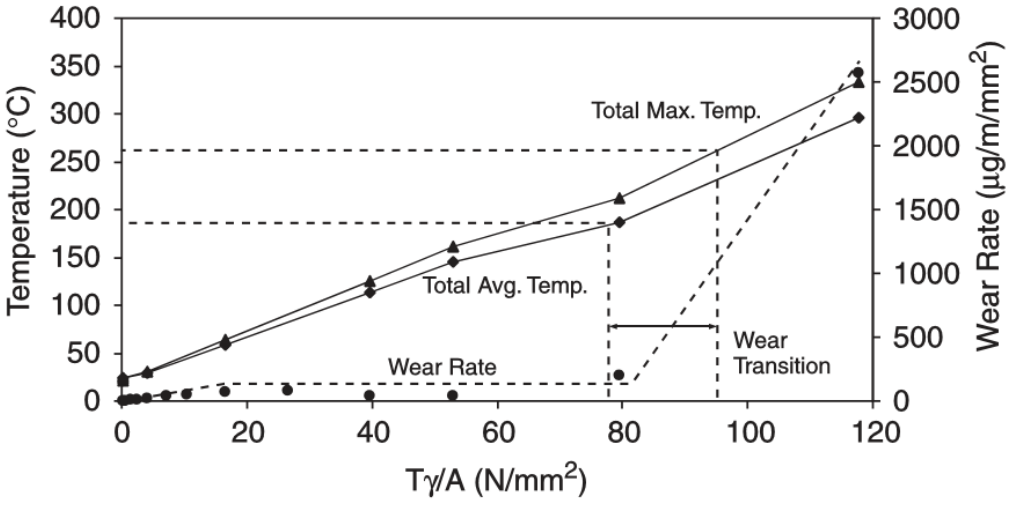

Figure 2-16 Twin-disc contact temperatures and wear coefficients [31]

Rolling contact fatigue (RCF) affects both the rail and the wheel and in particular the wheel damage is estimated to be mostly attributed to RCF than wheel flats or other causes. Wheel damage due to RCF is costly when considering reprofiling costs to achieve the initial profile, but also costly in further development of RCF as the equivalent conicity is increased with each reprofiling action, thus influencing the riding characteristics [11]. A commonly recognised practice for controlling RCF cracking on rails is to provide artificial grinding of the rails with such frequency as to remove any cracks at the same rate as they are forming, when natural wear is not sufficient to remove the cracks [24]. The concept of “magic wear rate” was suggested, where the amount of metal to be removed in order to control RCF depends on the rates of crack initiation and propagation, as well as impacting conditions such as material properties, machining approach, rail curvature and operating conditions. If the “magic wear rate” is achieved on any particular railway, then any RCF cracks that are in initial stages of development with be removed [32].

So far the use of wear coefficients has been in mapping and predicting wear and RCF. Modelling based on material properties in relation to contact conditions is required to improve the design tools [21]. This will eliminate the process of deriving wear coefficients from twin disc testing which is laborious and costly when it comes to exploring different scenarios with various loading conditions. The wear chart in Figure 2-17 from Jendel [33] characterises the typical wear coefficient map of steels, for example wear maps for bearing steels. The map in Figure 2-17 was derived from laboratory experiments where wheel and rail materials was used and the contact pressure, sliding velocity and hardness were changed. It is difficult to achieve very high contact pressures with the laboratory equipment, such as typical twin disc machines, and the high pressure wear coefficients in Figure 2-17 have been estimated based on interpolation from other regimes and past experiences. The term “H” on the map is hardness of the worn material.

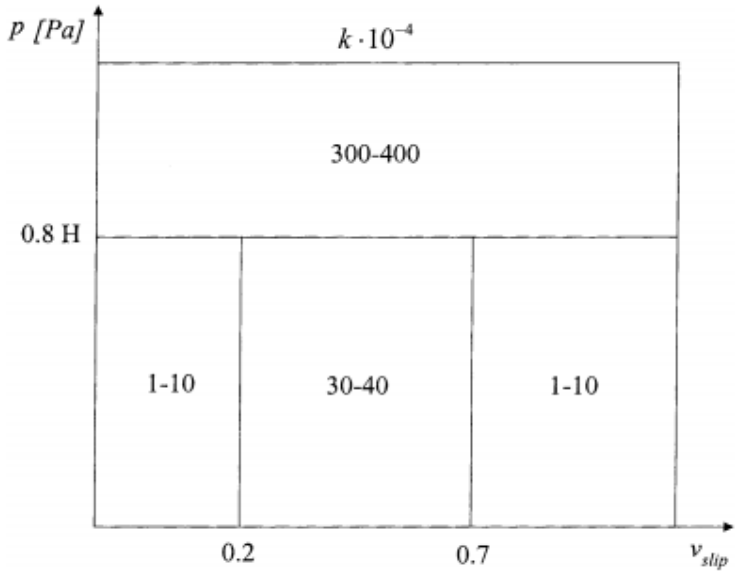

Figure 2-17 Wear coefficient against slip velocity based on laboratory measurements with wheel and rail steels [33]

The fundamental behaviour that leads to RCF is the increase of the surface shear stress due to tractive forces. Plastic deformation is accumulating beneath the surface of the contact when rolling/sliding cyclic loading is applied. A shakedown map and load carrying capacity of contact is shown in Figure 2-18. The limits of material behaviour in terms of non-dimensional contact pressure, p_0/k as a function coefficient μ (=T/N), where p_0 is the normal contact pressure, k is the shear yield strength, T is the tractive force and N is the normal load. For values of p_0/k in the "Plastic Shakedown" region the damage is irreversible and in the "Incremental Growth (Ratcheting)" region the strain is accumulated until the ductility of the material is exceeded and it is lost as wear debris or surface cracks are initiated.

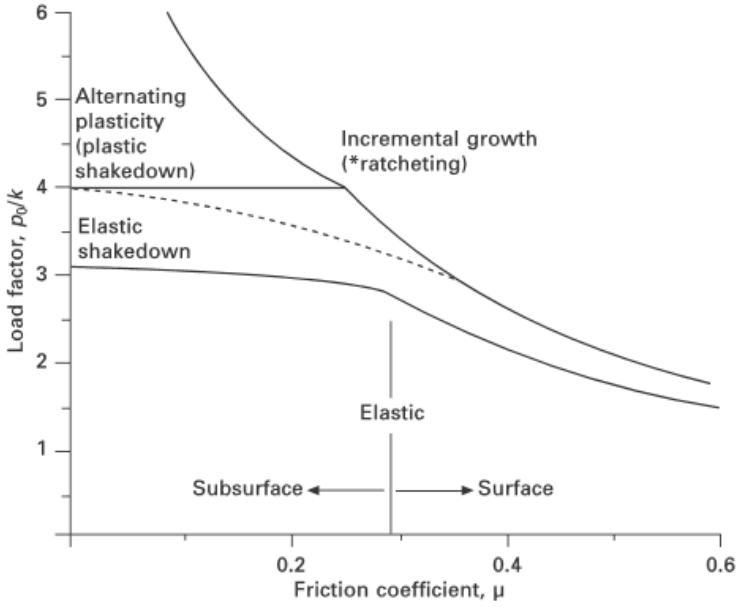

Figure 2-18 Shakedown map of friction and load-carrying capacity of contact [13, 26]

Wheel flats can affect wheel life dramatically, spalling is one of the resultant damage mechanisms. Depending on the size of the flat or spall, the wheel may be repaired by grinding in order to re-profile, thus reducing the life of the wheel (see Table 10-1 for wheel profile wear limits). Where the flat or spall is significantly large, the wheel damaged is beyond repair and the wheel is put out of service. An example of wheel flat is shown in Figure 2-19. Wheel flats are caused by insufficient adhesion in the contact, leading to extreme sliding contact. The main two reasons for having extreme sliding contact is either by a "lock up" under braking or spinning under traction, while momentarily the train is not moving and all the energy of the spinning wheel is transferred onto the contact, introducing further heat and wear. Sliding from braking will mainly cause flats on the wheel, while a spinning wheel will mainly cause flats on the rail, although in any case both the wheel and rail experience damage to some extent.

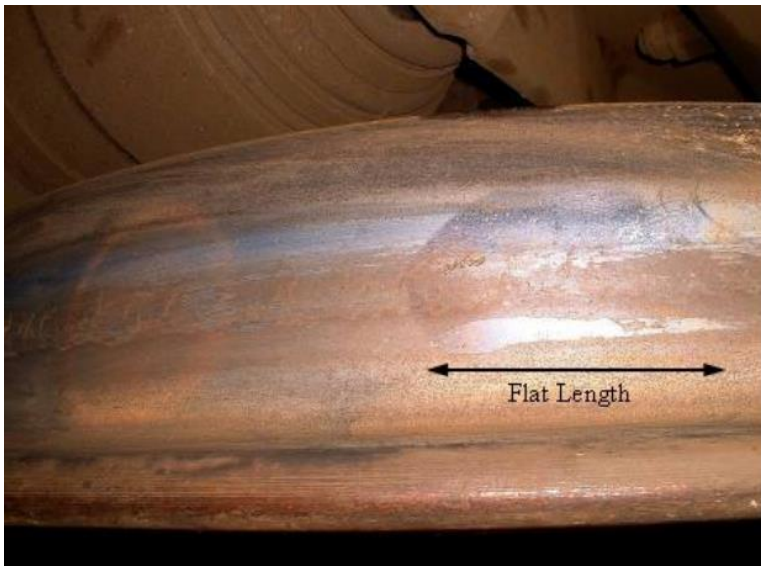

Figure 2-19 Isolated wheel flat [10]

The use of laser cladding could potentially play an important role in the manufacture or repair of rail wheels, where more durable wheel surface coatings can provide resistance to wheel flats. Such an approach must carefully consider the effect on the rail material and avoid further damage of the rail in order to prolong the life of the wheel. Similarly, for the rail, laser cladding could prove beneficial in repair of small sections, coating of switches and crossings and in particular to fill in profiles, as opposed to grinding, in areas where the grinding technique has removed more material than required. The effect of a more durable, possibly harder rail on the wheel must be considered, as well as the interaction with third bodies and friction modifiers. For evaluating the performance of laser clad rail and wheel, extensive laboratory testing and a large collection of wear data, such as wear coefficients, is required to establish accurate and coherent conclusions.

Perhaps the use of laser cladding would be of benefit in particular to the rail gauge/wheel flange contact, in areas such as the high rail in curves. Although flange wear has been a problem and in need of a solution for decades now [19], very little wear test data is available from recent research and it is clearly an area that needs to be addresses in future research, as the loading conditions, speeds and curve geometry of future rail transportation will give rise to the severity of the wheel-rail contact conditions at the wheel flange and rail gauge [21].

Rail steel comes in many grades which have been developed over the years by the industry, aiming at achieving certain properties on the head of the rail where the contact with the wheel is taking place. Rail steel grades are normally categorised by the head hardness where in most cases the grade naming designation contains the minimum hardness value Brinell. Premium rails are made with a target to increase wear resistance and RCF resistance. However, there is a trade-off between these two properties as they are competing with each other depending on the operating conditions, they may occur concurrently, with one or the other determining the life of the rail. Wear and fatigue crack initiation have a common underlying mechanism in strain accumulation by the ratchetting process, i.e. incremental accumulation of strain in each wheel pass that takes the material beyond the shakedown limit and ratchetting threshold [34]. Wear can also occur via oxidation, adhesion or

abrasion depending on the wheel-rail interface conditions, material properties and third body layers present. Material cannot accumulate strain indefinitely, and a limit of 'ductility exhaustion' will occur. At this point accumulated strain leads to generation of wear debris if ductility exhaustion is at the surface, or the formation of crack like flaws (at the surface or internally). The same mechanism leads to both wear and crack initiation. If the stress regime promotes a high crack growth rate in the material following crack initiation this means that cracks will grow faster than the material wears away at the rail surface. This will lead to large and potentially dangerous rolling contact fatigue cracks growing into the rail. Where long crack growth rate is low relative to the surface wear rate any surface cracks would be expected to stabilise at the size they are able to reach through the ratchetting mechanism alone. Hence, at low Tγ/A values wear will be low and the most likely failure mechanism is RCF crack initiation and growth which if unchecked, could lead to cracks turning down into the rail and causing complete fracture of the rail. As the Tγ/A value increases, the wear rate in the system rises which removes material from the surface of the rail, thus removing any RCF cracks that may have initiated. At high Tγ/A failure will be by wear which has less catastrophic consequences. This is encapsulated in the Whole Life Rail Model [35] that looks at wear and RCF interactions for standard grade rail. A Tγ damage curve is utilised and developed based on field data and twin disc laboratory measurements. Hiensch and Steenbergen recently extended this type of approach to map this behaviour for other rail grades. Their work is limited in its application though as the same wear rate was assumed for all materials, which further emphasises the point made earlier about a lack of data for premium rail materials [36].

Some data is available to improve this situation. Studies to characterise the wear and RCF behaviour of various grades of rail steels have been made by Stock and Pippan [37, 38]. The results indicated a reduction in wear, plastic deformation and the formation and growth of head checks (RCF) with increasing hardness and strength of five pearlitic rail steels, which were tested in a laboratory full-scale rig and also compared to track data. With regards to bainitic rail, tests indicated a lower wear resistance than the high hardness pearlitic rails, however, the potential of improved RCF resistance was highlighted [38].

Past studies investigated the wear and RCF performance of rail materials for limited contact conditions, such as contact pressure (900-1,500 MPa) or low slip ratio (creep) of around 0-6% [19, 39]. Bolton and Clayton tested at higher slip ratios, but with lower contact pressure of 1,300 MPa [20]. Under such conditions the mechanical energy that dissipates in the wheel-rail contact patch is not representative of the overall mix of loads that exist in the field. Heavy haul trains and multiple size wheels made of different steel grades affect the contact patch as do the environmental conditions, track geometry, friction modifiers as well as the driving behaviour of train drivers potentially leading to increasing slip between the wheel and rail. Such increase in slip takes place at certain sections of the track, at tight curves or in braking and accelerating sections, and repetitive occurrence can be damaging for both the rail and wheel. As part of this study the contact pressure was maintained constant, but the slip ratios were tested at 1% as well as 10% and 20%. This caused an increase in the Tγ/A value and allowed direct comparison to damaging conditions that occur in the field.

2.2.2 Switches and crossings impact wear

Switches and crossings (S&C) enable trains to follow a particular direction by switching to neighbouring rails, whether this is at speed on mainline routes or at slow pace when near a station in order to approach the allocated platform. Switches are the movable components, made of multiple parts, where a switch blade is the main rail that comes in contact with the wheel. Switch blades slide between two positions to allow trains to either continue on the same track or switch to a neighbouring track. Due to this configuration, rails from either track are converging to a point, forming a sharp rail tip between them. This is called the crossing nose (see Figure 2-20). The crossing nose enables the wheels to run over small gaps and join the new track.

Switches and crossings can be damaged by the passing wheel, resulting in wear. This is evident in Figure 2-20 and Figure 2-21, where the crossing nose is corrugated and material plastic flow is clearly visible towards the end of the crossing nose railhead. However, the wheel also wears from the rolling, sliding and impact action. The prediction of profile wear in research is done through simulations and the damage of switches and crossings due to impact has been researched greatly, as the damage is considered significant [11]. Failure modes for S&C are spalling, lipping, soft spots on the running surface, shelling, head checks, squats, transverse cracking and excess wear [40].

Network Rail initiated a number of R&D projects in 2017 to address issues with S&C in their network infrastructure, that result in significant annual costs in terms of maintenance. In addition, maintenance put in place for resolving S&C issues creates major safety risks to workers and the train operations. In order to ensure the safe operation of railways, more frequent maintenance and/or replacement of S&C is required, which is a risk to maintenance engineers and impacts the scheduling of trains; therefore it impacts the economic performance of train operating companies, thus increasing the cost of travelling by rail. It is estimated that there are over 300,000 S&C units within the networks of 27 EU countries, with an estimated maintenance cost for one S&C unit equivalent to that of 0.3 km of plain track [40]. Network Rail is tackling issues with materials used in S&C, by exploring alternatives or coatings to enhance the performance of switches by increasing the components life. In addition, optimisation of the switch profile and geometry could minimise wear/damage whilst reducing the risk of derailment. Slide plate friction management could also improve with new plate materials and coatings. Other actions planned by Network Rail are remote condition monitoring, actuation, locking, detection and inspection [41].

Figure 2-20 Crossing nose with fixed guiding (wing) rails at either side (Sheffield Train Station 2019)

Figure 2-21 Wheel running over a crossing nose (Network Rail educational video) [42]

Wear conditions for S&C can be assessed in many ways, by modelling or physical testing at small scale. Impact wear/deformation on S&C is far more damaging than rolling/sliding wear and the data collection from the field poses a risk to operations and passengers. Large scale impact testing can be extremely expensive due to the large dynamic forces involved. A scaled down test on impact rigs would be the first step to evaluate various materials and to establish the requirement for full scale laboratory testing. Careful consideration should be given when scaling down and replicating the real conditions of impact. The impacting specimens must behave and interact in the same way as in the field. Example are the wheel rebound, sliding action over the crossing nose, as well as the dynamic interaction of the wheel mass and bogie suspension.

Small scale test results such as strain accumulation for specific loads could be used in modelling tools to predict wear or in Finite Element Analysis tools to predict deformation. Thorough verification of such tests with modelling means that the resultant material and coating improvements could be applied directly in the field, eliminating the need for full scale testing.

Typical steel materials used in S&C are standard rail R260, its heat treated version of R350HT and Manganese (Hadfield) steel. R260 and R350HT materials are used in crossing nose fabrications, while the Manganese steel is used mainly as crossing nose castings, since it is not a weldable material. Cast Hadfield Manganese steel is classed as a premium crossing nose material and it is preferable over other materials. This is due to its unique feature of rapid work hardening from yield strength (379 MPa) to ultimate tensile strength (965 MPa) with hardness values of 200 BHN to 600 BHN on the surface after work hardening, thus increasing its surface hardness in service. This makes it suitable for high impact and wear resistance applications. The hardening mechanism of Manganese steel is mainly attributed to deformation twinning between Mn-C couples in austenitic steels [43]

Johansson et al. [44] have simulated the impact of freight traffic on switches made of R260 material using dynamic simulations in Abaqus. The simulation estimated the wheel-rail contact patches and the irreversible plastic deformations and work hardening of the material from cyclic loading. The results were used in wear simulation tools such as FASTSIM [45] and Archard's wear model to predict wear. The input parameters in Abaqus were obtained from GENSYS [46], which was used to simulate the vehicle motion, contact positions, patches and magnitudes of normal and tangential forces with a mass-spring-damper system. The geometry was a UIC-60-760-1:15 rail (curve radius 760 m with turnout angle 1:15) with a Y25 bogie of 25-30 tonnes, with mean train speed of 65 km h^{-1}. The resultant simulated vertical forces wear in the range of 130-170 kN for 25 tonnes axle load and 170-190 kN for 30 tonnes axle load. Daves et al. [47] simulated a dynamic FEA of a crossing nose made of manganese steel and a composite wheel (W720) of a 16 tonne axle load travelling at 160 km h^{-1}. The results produced vertical reaction forces in the region of 310 kN. In an earlier publication the authors compared various numerical approaches of the same conditions, but at 75 km h^{-1}, and found the contact pressure was in the region of 1 GPa while the Hertzian calculation was estimated to be at 1.3 GPa [48]. Kassa and Nielsen confirmed their numerical estimation of reaction forces by fitting strain gauges on the wheel web of a 25tonnes axle load test train [49]. They found that vertical forces increase with speed and on the diverging route of a crossing nose. Two models were used, GENSYS and DIFF3D [50], where the latter was found to be more accurate in capturing the high-frequency content of impact loads, with eigenfrequencies of up to 300 Hz. Measured vertical forces were in the region of 200 kN at 60 km h^{-1} and 260 kN at 80 km h^{-1} at the crossing nose, while much lower vertical forces were measured when the wheel run over the switch blade, around 75 kN at 60 km h^{-1} and 85 kN at 80 km h^{-1}. Wei et al. [51] have used accelerometers on the wheelset to measure the degradation of crossings and evaluate it by identifying various types of degradation. Modelling results from Skrypnyk et al. [52] showed that after 41,400 cycles and with a simulated traffic load of 0.8 MGT, the pearlitic R350HT rail material experienced half of the ratchetting strain compared to the austenitic Mn13 rail. This highlights the extended deformation that Manganese steel can withstand and which is reflected in modelling which is based on experimental data.

Beyond introducing new materials for S&C, the use of coatings such as laser clad coatings is an important technological advantage for the railway industry, only recently being tested in the field [53]. Cladding both parts of the interface, the S&C and the wheel, provides an opportunity to design for particular contact requirements with control over friction, wear and overall strength of the components. As a starting point, laser cladding on only one of the interfaces should take place in order to understand the behaviour of the substrate and coatings, prior to testing laser cladding on both interfaces at the same time.

2.3 Steel industry equipment contacts

2.3.1 Cold mill work roll texture

In the rolling mill process for flat products, the work rolls are the components directly in contact with the rolled product, unlike the back-up rolls; so they have an influence on the surface with regards to the final texture as well as the near surface mechanical properties of the final product. Their construction and surface finish is important. The surface finish affects further processing of the sheets, plates or long products. This is of utmost importance in some cold rolling processes, especially in temper rolling. In hot rolling the work rolls generally have a ground finish, designed to “grab” the incoming product with the appropriate contact friction without marking the surface, while in other cold processes, especially in aluminium foil mills, the texture is such that it entraps the rolling oil in order to generate hydrodynamic rolling. The tribo-system in cold rolling is complex due to the wear debris and heat generated during rolling, which requires an emulsion to be circulated for washing off the debris and for cooling of the rolls, therefore a mixed-lubrication regime dominates and for this reason the roughness of the work rolls is paramount [54].

Cold mills may use dull finish rolls in the first and final stand to improve rolling performance and to prevent sticking of strip in succeeding annealing processes, while temper mills use textured work rolls in order to improve the product drawability and paintability [55].

There are four principal methods of texturing work rolls: Shot Blasting Texturing (SBT); Electrical Discharge Texturing (EDT); Laser Beam Texturing (LBT); and Electron Beam Texturing (EBT). A wide range of surfaces can be created from textured rolls and three surface types can be characterised by the geometry and configuration features. Stochastic surfaces have a statistical distribution of geometrically different configuration features; deterministic surfaces have a predefined layout of geometrically identical, but separate configuration features; and semi-deterministic surfaces have a predefined layout of geometrically identical and unseparated configuration features. Stochastic surface structures can be made with SBT and EDT, deterministic surface structures can be made with LBT, while EBT is capable of producing all types of surfaces mentioned. The texturing method is the decisive factor for transferring the work roll texture to the surface of the rolled product and the wear characteristics of the work roll are influenced by the thermal treatment during the textured process [56].

The purpose of producing a texture on the rolled product is to achieve the triobological characteristics required such as forming strains, wear resistance, adhesion properties for the application of coating materials and general appearance. In general the SBT method generates the texture by plastically deforming the surfaces with the use of shot blasting medium, while the other three methods the textured is obtained by locally melting the roll surface.

Shot Blasting Texturing has many disadvantages, which gave rise to the new texturing technologies. Some of the disadvantages are the large variance, low peak density of strip roughness, bad working environment due to the shot blasting method and the difficulty of texturing high chromium cat iron

rolls. The Peak Density (PPI), in the range of 5 to 15 μm Rz, is 1.5 to 2 times higher in the EDT method in comparison to the SBT method [55].

The focus of this research is on EDT textured rolls which are mostly used in the automotive industry due to the stochastic pattern which is preferred by autobody manufacturers due to the improved paint adherence and smooth appearance of paint without any distinct pattern, which can be mostly visible in certain light conditions [57]. There is a need to replace the chrome plating of work rolls because of its carcinogenic properties, which led to a ban from industrial applications in the European Union. Various projects are in place to find alternative solutions to the use of chrome in the steel industry [58, 59], one of them being the electro-discharge coating (EDC), which in principle is an EDT technology where the electrodes may contain hardening elements that can be deposited directly onto the roll surface. Alternatively, with EDC the surface of the roll could be hardened by a reaction of the electrode elements with the dielectric oil, with materials on the oil or with the roll material itself. This eliminates the need for chrome plating and possibly increases the durability of the roll and texture. WC and VC electrodes were used by Sarclad Ltd., for the CrFreeRolls EU project [58] and the conclusions from trials resulted in producing a homogeneous surface with an improved performance. The requirement for average roughness (Ra) of 2.6 μm to 4.5 μm was also achieved. The EDC method could provide the same performance as the chrome plating of rolls and eventually replace the chrome plating method, however, the hardness that is achieved with EDC is limited to the a thin layer on the surface of the roll. Conclusions from testing the EDC technologies on a small scale rig are that the chrome-plated sample showed by far the best roughness retention, with respect to Ra evolution with rolling length. Other techniques such as using HSS rolls and HVOF coatings showed intermediate behaviour, better than bare steel but not as good as chrome plating. There is a need to replace chrome plating of rolls, mainly due to the carcinogenic properties of hexavalent chromium but also because of the high cost of typically €300-€400 per roll per campaign [59].

Laser cladding is studied here as an alternative, with the added benefit of producing thicker coatings that can be re-built, thus extending the loading limits and life of work rolls. Extending the life of the texture means extending the rolling campaign of each roll between re-grinding and re-texturing, resulting in increasing yield and profitability of the rolling mill.

Work rolls are harder than the material they roll and they mainly wear by abrasion due to the debris, however, in some cases rolling mills have back-up rolls of high hardness, which the work rolls come in contact with. Generally the work rolls experience Hertzian stress with normal and tangential forces which result in surface shear stresses of a complex form with the combination of pressurisation from lubricant/coolant and the presence of asperities [60]. Work rolls are made of cast and forged alloy steel, which requires to have high ductility and hardness through quenching and tempering and with the addition of key elements such Chromium (up to 5%wt-hardness, strength), Nickel (toughness, strength), Vanadium (hardness, toughness), Manganese (strength, through-hardness), Molybdenum and Cobalt (hardness, strength, yield point, carbide formation) [61]. For example the work roll material used in this study has a Cr5%wt, see items 14 and 15 in Table 5-2. Frolish et al. [62] tested work roll material made of high-speed steel (830 HV) and back-up roll material made of heat treated bainitic

roll steel (480 HV) on the Sheffield University ROlling Sliding (SUROS) machine. The SUROS machine has been used for texture testing in this study. Various parameters for rolling are summarised in Table 2-1 and some properties for forged steel used in making rolls is listed in Table 2-2. The test conditions for the SUROS testing were based on figures from industry and literature, specifically based on the work by Hilgenberg and Steinhoff [2] who performed similar twin disc tests for comparison of various texturing technologies with a focus on pulsed laser dispersing texture. Consideration was given to the test conditions and issues related to using opposing discs of very different hardness which can affect the results. Details of the experimental procedure are described in 5.4.

Table 2-1 Industrial and test rolling parameters

	Contact Pressure (MPa)	**Force (kN)**	**Disc1 Diameter (mm)**	**Disc2 Diameter (mm)**	**Disc Width (mm)**	**Slip (%)**	**Angular Velocity (rpm)**	**Duration (cycles) ($x10^3$)**
Literature [2]	1079, 1394, 1649	3, 5, 7	38	37.6	10	1.1	200	320 (3 kN), 520 (5 kN), 420 (7 kN)
Industry TM21 Mill at Ijmuiden NL, Tata [58]	936 (max rolls) 1313 (min rolls)	6000 (3 kN mm^{-1}, 2 m width work roll)	620 (max) 511 (min)	620 (max) 511 (min)	2000	1		
SUROS	1000	2.77	44.15	47.20	9	1	400	0.2 & 1

Table 2-2 Mechanical properties for forged roll grades [58]

Grade	**Ultimate Strength (MPa)**	**Tensile Yield Strength (MPa)**	**Elongation (%)**	**Impact (J)**
Forged Steel STD (Surface)	2400 – 2600	1900 – 2200	1 - 2	-
Forged Steel HSS (Surface)	2400 – 2600	1900 – 2200	1 - 2	-
Forged Steel (Core)	720 – 950	550 – 700	15 - 20	20 - 40

2.3.2 Descaling wear plates

In steel plate production steel slabs are reheated to over 1,000ºC prior to rolling. The steel slab is transferred onto a roller table from the reheat furnace to the rolling mill and during that time severe scale is formed on the surface of the slab, due to the exposure to the much colder oxygenated atmosphere. Descaler machines are used to remove the scale from the top and bottom of the slab, before (primary descaling) and during rolling (secondary descaling). For this purpose high pressure water jets produce a flat jet spray. Characteristics of the descaling spray are impact pressure (0.1-2 MPa), impact force (67-223 N), specific water impingement (3-40 l m^{-2}), descaling energy (0.2-85 kJ m^{-2}), spray width coverage (varies in mm), fluid velocity (120-212 m s^{-1}) and overlap (in mm or 8-15% of spray width) [63]. A typical steel plate descaler will be designed to have an impact pressure of about 1 MPa on the surface of the product at a standoff distance of about 150 mm from the nozzle. Typical water supply pressure is 200 Bar but there are industrial descaling systems that supply water from 100 Bar to 400 Bar. Typical flow is 130 lpm (litres per minute), which is very demanding in terms of pumping equipment and energy. Flat jet nozzles usually have a standoff distance (slab surface to nozzle) of around 150-200 mm and with a fan angle of 30º or 40º. Multiple jets are positioned in a row, with an offset angle in the vertical axis to create a continuous line of descaling water with a bit of overlap from each nozzle. This angle is typically 15º, but they are also offset 15º in the horizontal axis so that they do not impact the plate at 90º, but at 75º, which will aid in deflecting the water away from the nozzles, as in the example in Figure 2-22. The spray angles are usually tested by spraying on aluminium plate which wears easily and an imprint of the sprays can be obtain in seconds, Figure 2-23 is an example.

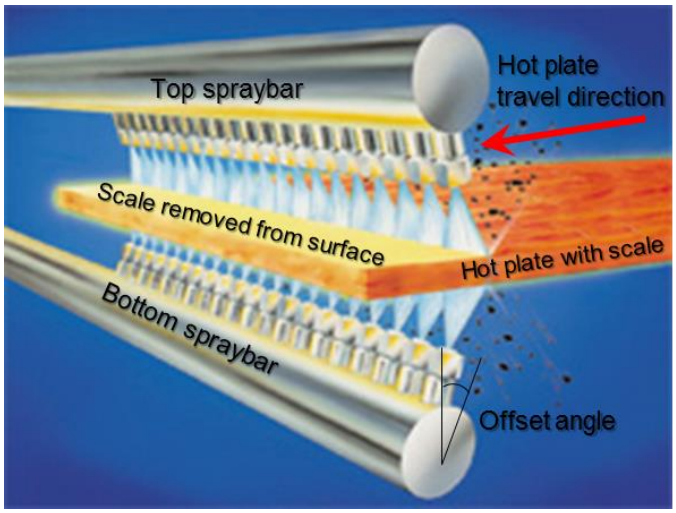

Figure 2-22 Descaler nozzle arrangement (top and bottom sprays) [64]

Figure 2-23 Two descaler jet imprints on aluminium plate (15º offset angle) and plan view shape of nozzle tip/orifice [63]

During normal descaling operation the water jets switch on before the plate enters the descaler and switch off after the plate has left the descaler. This short time that the plate is not present, the water jets impact the surrounding equipment which can cause erosion. Wear (deflector) plates are fixed in place to ricochet the water and act as sacrificial plates. Deflector plates are set at a 38^{o} impingement angle in order to deflect the water at a much wider angle. They are typically made of more durable material such as Hardox® 400, 450 or 550, which is more expensive than the rest of the equipment and which cannot be recovered once it has been damaged. The surface texture of these plates is untreated and the surface finish may vary. The plates are manufactured in accordance to EN 10 163-2, Class A, Sub-class 1 so in general the Hardox® plate on a descaler is as made surface finish. The hardness of Hardox® 450 would be between 425-475 Brinell which would equate to about 450-520 Vickers and has an approximate yield strength of 1,200 MPa and tensile strength of 1,400 MPa. The producer of Hardox®, SSAB have created the WearCalc™ 2.1 software which is a calculator for component wear in terms of erosion, impact and sliding wear, taking into account size, shape, impingement angle and velocity of the material. Furthermore, nozzle manufacturers like Lechler and Everloy produced their own software for calculating the various parameters for designing descaling systems, based on measurements on test rigs with the use of pressure transducers placed on the water jet impact zone [65].

The impact pressure on the deflector plates is an order magnitude lower than when it impacts the descaling area of the plate, with a larger contact area due to the widening angle of the fan jet and with a turbulence flow due to the distance from the nozzle where the jet flow is no longer laminar. This condition creates an erosive damage to the wear plates and surrounding equipment, along with scale debris that falling from the steel slabs and other damage from corrosion due to the cyclic exposure to oxygen.

The erosive wear mechanism can be studied in the laboratory in isolation, away from the harsh environment of a steel mill. For evaluating the performance of the clad plate the test conditions must be fixed in terms of the different parameters and mechanisms that affect erosion. Debris in the water jet and temperature variations will not be considered for the purpose of comparing the performance of materials, although they do have an effect in erosion and should be considered in other studies of damage by fluid erosion. Some of the parameters affecting erosion are the particle material, the angle of impingement, the impact velocity and particle size, where the damage is mostly abrasive wear with hard and solid particles and repetitive stress on impact for liquid particles [14]. Due to the high velocity of the water droplets, the wear on the deflector plates is by repetitive plastic deformation. A typical water droplet velocity for a descaler would be 200 m s^{-1}, which would result in a theoretical contact pressure of 300 MPa, using Equation 2-1 [14].

$$P_c = \rho v_s v_i \qquad \textbf{Equation 2-1}$$

where P is the contact pressure on impact [Pa]; ρ is the density of the fluid (1,000 for water) [kg m^{-3}]; vs is the speed of sound in fluid (1,500 for water) [m s^{-1}]; and v_i is the fluid velocity at impact (200 for a typical descaler) [m s^{-1}].

Research in other industrial applications is focused on droplet speeds similar to that found in descalers. For example in wind turbine blade tips, which experience wind speeds up to 90 m s^{-1}, with a need to operate at significantly higher speeds, in order to reduce the shaft torque and associated gearbox failures [66-68]. Another example is rotor blades on aircraft, such as the helicopter rotor blade, where the air (and rain droplet) velocity over the rotor blades can reach speeds of up to 200 m s^{-1}, with some aircraft speeds reported to 0.9 Mach (309 m s^{-1}), and where titanium and nickel coatings, as well as polyurethane tapes are used as protective coatings against solid and liquid particle erosion [69-71].

If we consider a drop in velocity by the time the droplets impact the deflector plates below/above the mill descaling area, then the impact pressure would be in the range of 100-150 MPa. The fluid velocity at impact in this research is at subsonic speeds; since the shock or pressure waves move at the speed of sound through the droplet during impact, the speed of sound in fluid is the limiting factor for this equation, where above supersonic speeds (in fluid) the effect of impact will be reduced and the equation will not be valid as other damage mechanism will dominate. Bowden and Brunton found that a liquid mass behaves in a compressible manner when colliding with a solid surface at velocities above 500 m s^{-1} and at sonic speeds a single impact may cause severe damage [72].

The contact pressure in Figure 2-24 illustrates the phenomenon of the liquid transient formation of shock waves which allow for release of the impact pressure. Until the shock waves have released the impact pressure through the liquid, the impact pressure is maintained as illustrated in the two middle images of Figure 2-24, where each image is the progression in time of a droplet impacting a surface. Bowden and Brunton [72] have shown this phenomenon through experiments in 1961 and Figure 2-25 is a photograph from one of their experiments showing the damage to stainless steel and aluminium surface from a high velocity droplet. The inner wall of the crater seems to have a different texture/damage to the centre, which is probably a result of the shockwave pressure forming a ring pressure patch as it rebounds back to the liquid in horizontal tension, opposing to the vertical tension in the middle of the impact zone.

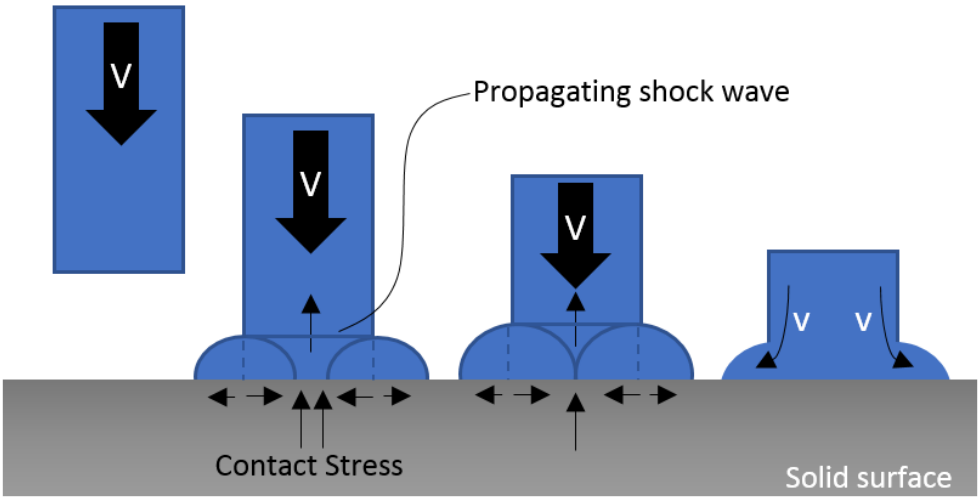

Figure 2-24 Liquid particle erosion mechanism on solid surface (adapted from Stachowiak [14])

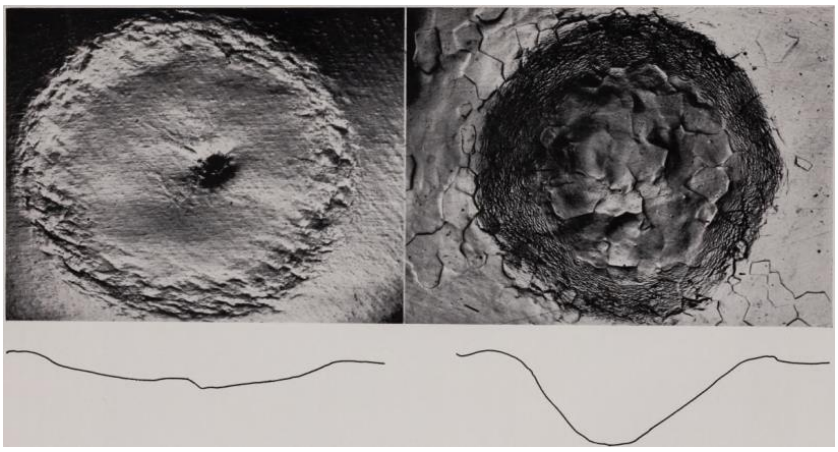

Figure 2-25 Deformation of stainless-steel (left) and aluminium (right) specimens by high velocity impact of a water jet (705 m s^{-1}) at x 17 magnification with their respective cross-section outline below each image [72]

Damage by liquid erosion wear is resulting from a large number of accumulative contact stresses from the impact of liquid droplets and the velocity as well as the duration of the impact have a big influence on the wear and the two parameters are dependent on each other. Subsequent impacts collapse the craters created by initial impacts and in that manner the damage increases, while in the case of brittle material the wear is by crack formation and fracture. It was found that an austenitic layer without carbides has a good resistance to erosion as well as the transformation from austenite to martensite at the surface, which generates surface compressive residual stresses [73].

Five stages can be identified for erosive or cavitation wear, according to Blau [74], which are also explained in 6.1.2 for rolling/sliding wear. The stages increase with time and the erosion rate increases after the incubation stage through an acceleration stage to reach the maximum rate stage. Deceleration follows to a steady state of wear rate, as shown in Figure 2-26.

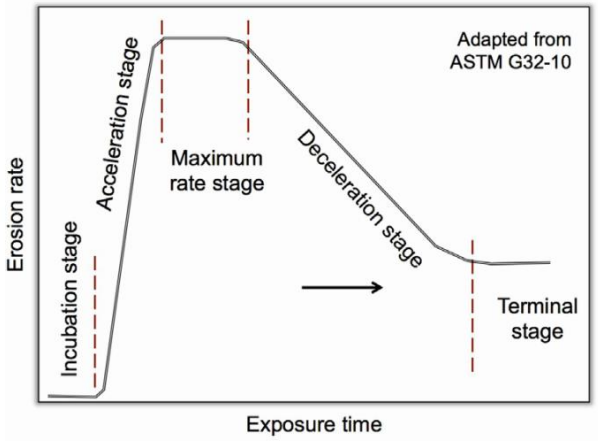

Figure 2-26 Liquid droplet erosion versus time [74]

Residual stresses that can be potentially created by the laser cladding process on the surface of the samples, may contribute to the erosion resistance and these should be evaluate and measured before testing. The wear mechanism is controlled by the characteristics of the erosive wear and as well as the material characteristics, for example the erosion resistance of materials depends on the

angle of impingement and the material's hardness, so with two variables in the systems, we cannot simply consider that materials with high hardness have high erosion resistance, as this might have the opposite result at high impingement angles. Materials can be very hard and tough, so that the impacting particle will not make an impression, or they could be tough, but with an extremely low elastic modulus so that the kinetic energy of the particle is dissipated. For steels, enhanced ductility rather than hardness can improve erosion wear resistance [14]. The deflector plates are designed based on very tough and hard steels and which have a high erosion resistance due to the low impingement angle they are placed in the mill. If this angle was to change then the erosion resistance would change.

Laser cladding has been considered in other applications for increasing erosion resistance. Examples are Stellite 6 clad on turbine blades made of martensitic stainless steel UNS 42000 which was tested on a cavitation erosion apparatus and in the field [75] and laser cladding of high-entropy alloy onto Q345 steel for slurry erosion testing [76]. Erosion experiments on laser clad materials have been performed by Singh et al. [3] on Stellite 6 which was clad on stainless steel 13Cr-4Ni and compared to AISI 304 stainless steel. The erodent was alumina of around 150 μm in size which were propelled by an air jet, according to ASTM G7607 standard. Cavitation erosion was tested by using a simple vibratory test method at a frequency of 20 ± 0.5 kHz in distilled water for approximately 30 hours in 3.5% NaCl solution at room temperature The conclusion was that the Stellite 6 cladding enhanced the erosion and corrosion resistance of the stainless steel.

There are various ASTM standards for erosion testing, however, due to the requirement of replicating the flat jet created by the descaler nozzle, which is designed specifically with a high impact pressure for removing scale, it was decided not to follow an erosion standard for testing and to build a custom test rig. A preliminary test is required to identify suitable pressure, stand off and angle for the chosen specimens, the expected pressure would be in the region of 200 Bar and with a flow of around 25 lpm. Following this, the materials will be tested under the same conditions and for variable time, depending on the wear rates.

2.3.3 Rod mill pinion

A pinion is a critical component used in the rolling of long products and it is part of a Cantilevered Mill. It is a pinion that drives the mill roll (see Figure 2-27), which is used to shape steel products such as round bar. The mill roll has grooves shaped into the running face and when two mill rolls are positioned close to each other and parallel to their rotational axis, together they form oval or round patterns from which the steel products can be shaped accordingly. Multiple pairs can be arranged in a production line, each producing different shapes that decrease in diameter towards the end of the production line, thus reducing the desired thickness of the round bar from start to end of the production line. Figure 2-28 is an example of a rod mill, showing two pairs of rolls arranged at 90^{o} offset in the rolling axis, which is a typical set-up in this type of mill to alternate the orientation of the roll pairs and with dozens of pairs in a single production line. Figure 2-27 is a diagram demonstrating the different components of the pinion assembly.

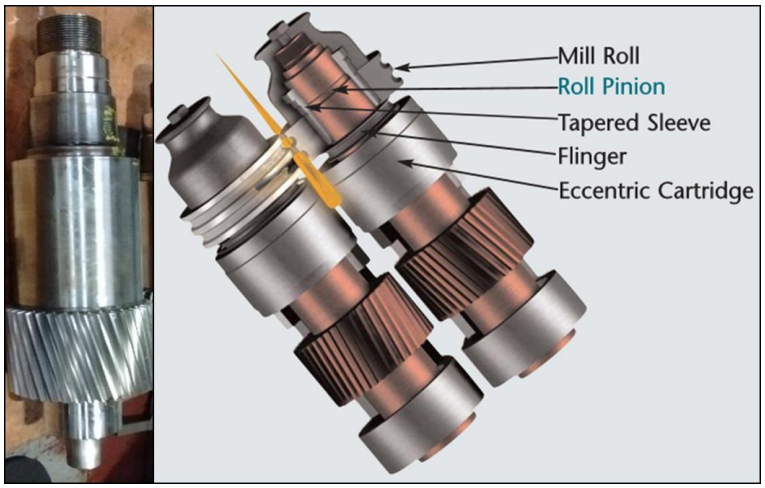

Figure 2-27 Image of the rod mill pinion and assembly diagram (courtesy of Primetals Technologies©)

The pinion is supported by two hydrodynamic bearings (eccentric cartridge in Figure 2-27) and it is driven by a spiral gear in the middle. Typical product temperatures exceed 750^{o}C in order to provide thermomechanical rolling, with typical round bar diameter of 5.5-28 mm and at maximum rolling speeds of 120 m s^{-1}. In addition the rolling force (mill roll separating force) can be up to 394 kN [77], but typically in hot rolling the separating force cam be lower. The mill rolls require replacing from time to time and production line downtime must be kept to a minimum. A taper sleeve is used to mount the mill rolls onto the pinion, with the use of a hydraulic tool that slides the sleeve into position by "wedging" it between mill roll and roll pinion to create an interference fit. This enables a quick removal, using the same tool, thus reducing downtime of the production line.

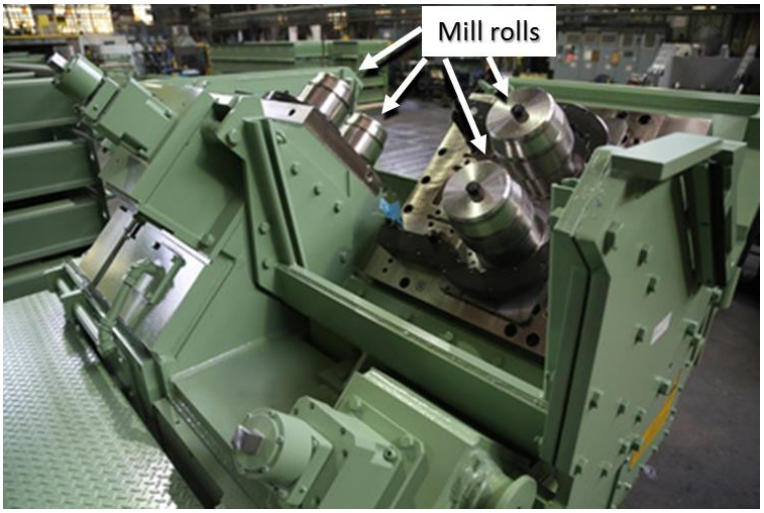

Figure 2-28 Pinions lined up for inspection (courtesy of Primetals Technologies©)

The pinions are made of durable forged steel in order to accommodate high rotational speeds with high bending loads. However, over time cracking and wear damage occurs on the taper surface of the pinion due to this sliding action of the taper sleeve during the regular replacement of the mill rolls. This "wedging" action caused by the sliding of the taper sleeve in the axial direction, could be a few millimetres. In addition, damage has been found on the contact surface with the bearings, which is caused by particle pick-up. To avoid replacing the whole pinion a solution is to apply chrome plating

on the surface of existing pinions, which provides a new, harder surface, thus extending the pinion life. Although the chrome plating layer can be repaired repeatedly, it is not a sustainable process with a limited number of possible repairs.

Chrome electroplating is used for decorative purposes with deposits below 0.80 μm, typically plated over nickel and for functional purposes when deposits exceed 0.80 μm for engineering coatings. The use for functional purposes is chosen for the special properties of chromium such as resistance to heat, hardness, wear, nongelling, nonwetting qualities, high melting point (around 1900^{o}C), corrosion, erosion and a low coefficient of friction [78]. It provides a surface with a low coefficient of friction that resists galling, abrasive and lubricated wear, and corrosion with typical thicknesses ranging from 2.5 to 500 μm and for certain applications to considerably greater thicknesses [79]. Products such as piston rings, shock absorbers, struts, brake pistons, engine valve stems, cylinder liners, and hydraulic rods benefit from chromium coatings, as well as aircraft landing gears, textile and gravure rolls, plastic rolls, dies and moulds [79].

The process involves the electrodeposition from a solution containing chromium trioxide (CrO3) and a catalytic anion (sulfate or fluoride) in proper proportion in specially designed baths. There can be many disadvantages such as “throwing power” of chromium (coating distribution over the part’s current density range) compared to other metals, low efficiency in maintaining plating bath conditions throughout the process and custom tank designs are required, limited coating thickness and environmental pollution and health hazards from the chemicals used during the electroplating process. Chromium deposits below 0.5 μm are normally crack free but porous, while thicker deposits may contain microcracks [78]. The microcrack density can be in the region of 200-1500 cracks / cm [80]. Figure 2-29 shows cracks in the chrome layer of a chrome plated spindle sample, which was tested and discussed in 6.5.

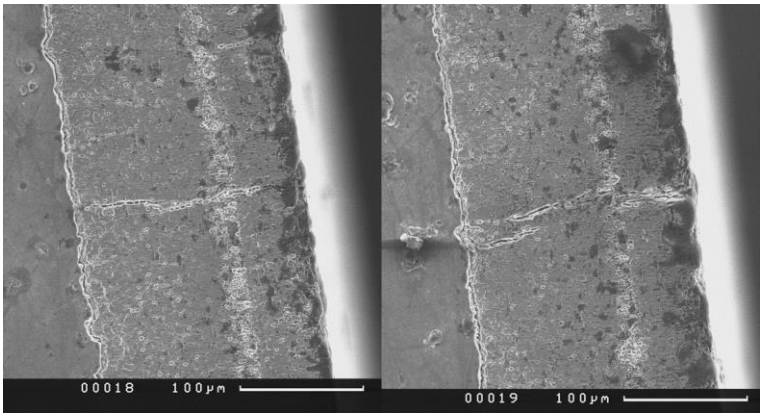

Figure 2-29 Microcracks on the chrome layer of the spindle

Elastic Modulus and Ultimate Tensile Strength values range from 103 GPa to 248 GPa and 103 MPa-482 MPa respectively, depending on the electroplating process [81]. The accurate control of the electroplating process is paramount to achieving the desired properties. Due to its carcinogenic properties a ban from industrial applications is in place in the European Union from September 2017 under the REACH regulation and an EU project initiative was investigating alternatives to the use of chrome in the steel industry [58, 59].

2.4 Summary

Five high load bearing interfaces and their associated failure mechanisms have been described in this chapter. Coatings applied with laser cladding onto the surfaces of components could provide multiple benefits, especially in extreme interfaces, which are highly loaded by impact or traction forces. Such benefits include increasing wear resistance and reducing crack propagation. In addition, due to the nature of the selected materials, corrosion resistance is readily available, although corrosion performance has not been investigated in this study. Laser clad coatings generally achieve these properties through the much higher hardness they possess, through a thicker layer than other coatings. However, other mechanisms of the laser cladding process, such as the rapid cooling and reduced heat affected zone, contribute to their advantageous properties. In order to answer the fundamental question of the thesis, whether laser cladding can increase the durability of these interfaces, multiple tests were designed accordingly.

Investigating multiple interfaces introduces complexity for this project, therefore only one clad material was applied in each interface. The failure mechanisms in each interface are different, so the appropriate material was chosen in each case. MSS was chosen for the rolling/sliding tests of railway materials, because this was proven a successful material on previous experiments by Lewis et al. [1]. For the water jet erosion test, Stellite 6 was chosen which is known for its cavitation erosion resistance and often used in hardfacing applications through plasma transferred arc (PTA) [82]. The same coating material was chosen for the impact test, a comparison with currently used railway materials for switches and crossings, without seeking to identify the most suitable material for this application as this was not the core purpose of the study. Finally, for the rolling/sliding texture and bending test, a combination of Technolase® with an intermediate layer of Inconel 625 was chosen. Issues with crack propagation associated with these interfaces, a softer intermediate layer was used to arrest cracks from propagating into the parent material, while a much harder coating was chosen mainly to reduce surface wear. The Technolase® coating achieves high harness and wear resistance properties from the inclusions of WC particles, which commonly used in other research [83-85].

A literature review was undertaken to form a wider picture of research in this field and a paper grading map was produced to help identify gaps in research (Chapter 3). Modelling (Chapter 4) was required to identify the contact conditions and help design the tests. The tests and assessment methods are summarised in Table 2-3.

Table 2-3 Test plan and assessment methods

Test	Activities / Conditions	Clad material	Modelling (to plan tests)	Assessment Methods					Upscale Modelling
				Chemical Analysis	Nanoindentation	Hardness Profile	Wear	DIC Strain	
Twin Disc	Benchmarking (1,10,20% slip)	MSS	✔	✔	✔	✔	✔		
	Work roll texture	Inconel 625 &Technolase®	✔	✔			✔		
Bending	Stress test of clad layer	Inconel 625 &Technolase®	✔	✔	✔	✔		✔	
Impact	Crossing Nose Test	Stellite 6	✔	✔		✔	✔		✔
Erosion	Hardox vs Clad	Stellite 6		✔		✔	✔		

This page was intentionally left blank

3 LASER CLADDING THEORY AND TRIBOLOGICAL PERFORMANCE

3.1 Introduction

Advances in the metals industry, and especially the steel industry, seem to be focused on the purification of the end products where good quality steel is produced with a big reduction in inclusions, as well as a variety of steel grades with characteristics to suit different applications. According to the World Steel Association there are 3,500 different grades of steel [86]. Advances in steel grades alone are not sufficient for increased performance, the surface quality must be considered too. For example the selection of appropriate material and surface finish on ball bearings in order to have a reduced coefficient of friction and to enable a longer life [87, 88]. Another example is the design of a surface to improve automotive coatings adherence [89]. In machine design it is important to define specific surface finish for all components interacting with each other, as this enables improved performance, such as longer life or working with selective friction coefficients. Different methods for improving the surface are coating techniques, such as plasma spraying, physical vapour deposition, hot pressing, spark plasma sintering, electroplating with phosphate, chromate or oxide coatings, galvanizing, porcelain enamelling, laser cladding, anodising, thermal spraying, high velocity oxygen fuel spraying, roller cladding/coating, spin coating and the list goes on. Other functions of these coatings are to optimise their surface properties such as adhesion, optical, protective, magnetic, electrical and others.

Coatings techniques have limited properties and therefore limited applications to mild contact conditions, while laser cladding is designed for severe contact conditions, aiming at load bearing properties through improved non-porous microstructure and higher thickness of the clad layer. For example, nickel electroplating can be produced to a up to a maximum thickness of 125 μm [79]. It has been applied on pistons and cylinder walls in automotive engines where surface shear stresses dominate to improve wear resistance, however, it would not be suitable in contact conditions with dominant normal stresses that extend beyond the coating thickness. Thermal sprays can be produced to several millimetres with added elements such as WC-Co to increase the coating bulk hardness and wear resistance. However, they are not ideal candidates for load bearing applications due to the mechanical bond with the substrate and varying levels of porosity that result in low strength and elastic modulus [90].

Selecting softer or harder cladding materials is a major factor when it comes to performance, whether it is for corrosion resistance, strength, toughness, or friction control. For example, in non-load bearing applications pure soft metals or oxides are used for corrosion and oxidation resistance. Laser cladding coatings are normally thicker than coatings from more established techniques and by this difference alone one could assume an improved performance over many coatings without further investigation. However, it is not purely the thickness of the coating that provides improved performance, but the sintering method which allows for more precision control over multiple materials in order to produce a better performing coating structure than the substrate or parent material. Improved hardness and ductility in the coating are key characteristics for improved performance in

load bearing applications. When designing the laser clad process for load bearing applications, it is important that the thickness of the clad layer is bigger than the depth of maximum Hertzian contact stresses, in order for the clad layer to be effective in arresting the loading stresses, thus protecting the substrate. Figure 3-1 [91] shows a comparison of coating processes in terms of coating thickness and process temperature. Laser cladding falls in the “Welding” category where each layer deposited is generally thicker than other typical coating processes.

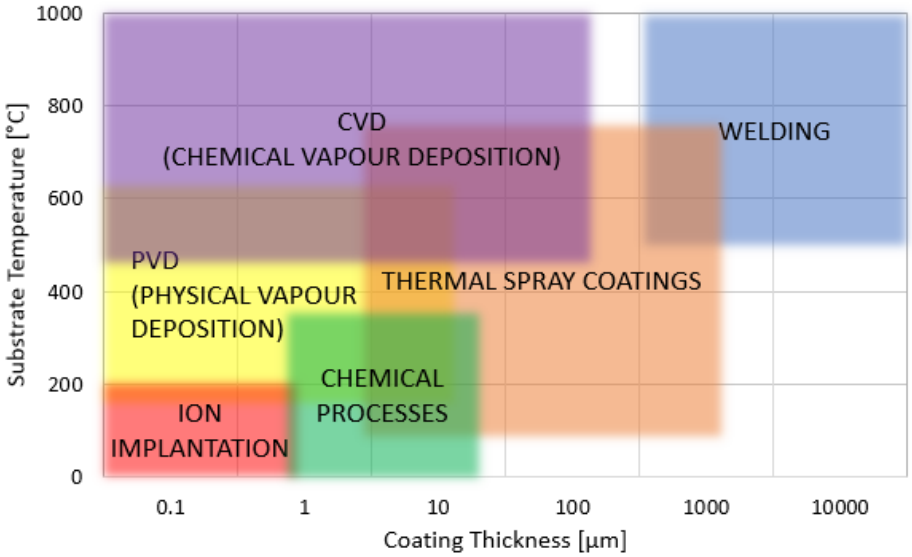

Figure 3-1 Coating process comparison map, adapted from Sulzer-Metco [91]

Early attempts in laser solidification of materials date back to the 1960’s [92] with the invention of the first working laser by Maiman [93], but since the mid-1980’s when additive manufacturing started to take off, there have been many advancements in metal additive technologies with a faster increase into the 1990’s. One of the main reasons for the sudden developments in the 1980’s and 1990’s was the introduction of powder feeders as well as modelling and better understanding of the process. Also, the invention of Stereolithography by Charles Hull at 3D Systems Inc. [92, 94], created a global technology competition and the need for metal additive manufacture, which forced further developments in laser cladding in the 1990’s. The wear and corrosion resistant applications of this technology were reported by many research groups in the 1980’s. The first jet engine components to be hard-faced using laser cladding were the RB-211 (Rolls-Royce 1981) and JT8-JT9 (Pratt and Whitney 1983), while in the automotive industry it was first introduced for engine valve seats (Fiat, Toyota and Mercedes Benz) [95].

A review of laser cladding in 2007, found that 580 patents were awarded between 1985 and 2007, which included automotive cylinder liners and valve seat coatings (Toyota, Nissan, Sulzer, Fuji Valve, Daimler-Chrysler, Hyundai); rebuilding of turbine blades (GE, Westinghouse, IHHI, Nippon Steel, Rolls Royce, Alstom); internal/external coating of tubes (Mitsubishi, IHHI), weapons (United Technologies, Volvo Aero, Rheinmetall) and other applications such as nuclear reactors (GE, Toshiba, Sumitomo, Harima Heavy etc.), prototyping, instruments/manufacturing processes for laser cladding and so on. It is estimated that the starting point of the laser cladding activities was at the

beginning of the 1980s, based on the filing of some of the earliest patents and this correlates with the emergence of the first high-power (above 1kW) CO_2 laser [96].

This was a natural progression for the development of metal coatings and it was not until the late 1990's that the laser cladding method was commercialised which enabled a high quality and distortion free process, with a huge range of material selection for alloy coating development. Figure 3-2 is a conceptual timeline of new technologies that led to the development of additive technologies. Other technological advancements that enabled a rapid progression of laser cladding were increase of computer power, advanced modelling and computer-numerical-control systems, as well as a demand for metal additive manufacture.

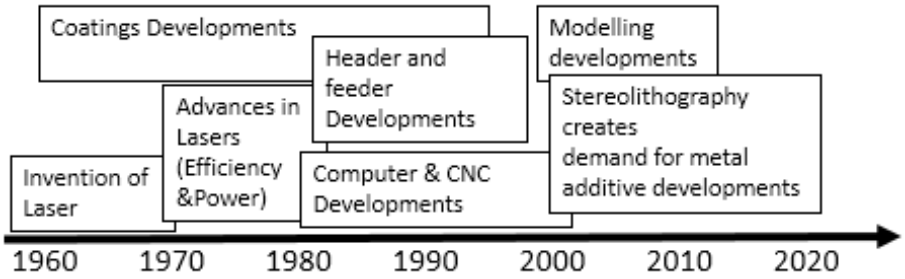

Figure 3-2 Laser Cladding Progress Curve

To identify original and important developments in the field, a literature review was undertaken. For identifying gaps in the current research, the papers were categorised and graded. The paper grading is discussed in this chapter, followed by detail explanation of the laser cladding process and a discussion on the significance of using laser cladding on extreme interfaces. The graded papers are referenced at the end of the chapter.

The literature identified here is limited in terms of the coating method and only papers with the laser cladding process were reviewed. Past reviews [97-99] were mainly on the use of laser cladding for surface protection from wear and corrosion, however, the main focus here is on laser cladding for load bearing applications which has not been addressed before. Thousands of laser cladding papers have been published in journals, of which many are limited to material science and alloying mechanisms. A total of 196 papers have been selected for grading in this review. Due to the increasing number of laser cladding research papers in recent years, fewer papers were selected between 2015 and March 2019, based on inclusion of wear testing and with reference to load bearing applications, which have taken a more mechanical applied view, especially for railways and the steel industry [P125-P196]. The search terms "laser cladding" and "wear" were used to filter the results for the period 2015-19, considering the wear test objectives of this research.

3.2 Quantitative paper grading methodology and trends

A number of papers were found from the early 1970's which were chosen for a review of the laser cladding technology, in order to outline the developments in this field and identify gaps in the research. The papers were published by Universities and Institutions all over the world up to the year 2015 and are listed at the end of this section [P1-P124]. For the purpose of sifting through the papers

in an organised way, the papers were split into several categories and a further grading system was added in order to prioritise according to paper relevance with regards to laser cladding research. The final grading was adjusted to indicate the impact of the papers and to put together a paper grading map to aid in visualising the research and to identify knowledge gaps.

Several categories were identified and narrowed down to eight more generic categories which describe the different fields of work covered in the papers. These are “General reviews”, “General cladding material tests”, “rolling contact fatigue (RCF) and wear testing”, “Modelling of cladding process”, “Cladding process control”, “Treatment and residual stress tests”, “Mechanics: Shakedown, Ratchetting, Plasticity and Fracture” and “Other”. The paper map in Figure 3-3 indicates the categories and associated score results in a visual format. The circle size is roughly proportional to the number of papers in each grade.

The grading was simplified to A, B or C which was calculated using a scoring system of one point if the attribute is applicable to the paper and no points if it is not. Grade A are the papers with the higher score of 3 or 4, grade B are the papers with a score of 2 and grade C are the papers with a score of 1 or 0. The different attributes are as follow:

1) **Peer Review** – Has the paper been reviewed by peers?
2) **Modelling** – Does the paper contain information on modelling by the authors?
3) **Testing** – Does the paper contain information on testing by the authors?
4) **Material and cladding parameters information** – Does the paper contain information on the substrate and the clad material and/or information on laser cladding parameters such as laser power, feed rate, pre-heating and so on?

Papers published between 2015-2019 which relate to “rail and wear” are also shown in Figure 3-3. A similar grading system was used for these papers with the exception of the modelling attribute, since the focus from the selected papers was on wear testing.

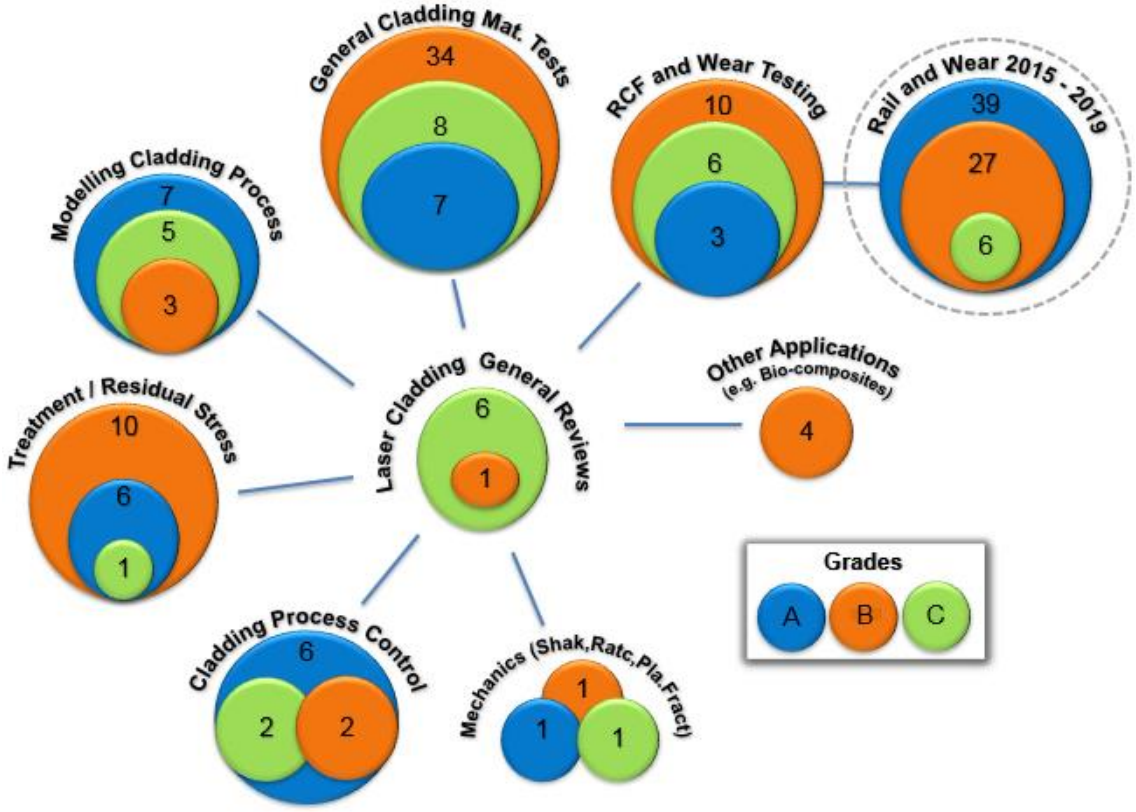

Figure 3-3 Paper Grading Map for papers published before 2015 and for Rail and Wear paper published between 2015 and 2019

The grading is used as a first identification of papers that might be useful in research and the quality of research has not been evaluated at this stage. It is clear from the paper map in Figure 3-3 that there is a lot of research in materials for laser cladding in comparison to the other aspects of modelling, control, mechanics etc. There are some commonalities in the papers, especially with the process control, modelling and treatment/residual stress papers. The institutions and organisations that lead developments in process control, develop offline and online models for a number of predictions around the cladding process. Offline models are mostly predictive and isolated from laser cladding equipment while online models are directly connected to the laser cladding equipment for feedback and control during the cladding process. These models are typically used in controlling heat treatment, and detection or prediction of the residual stresses in order to either avoid creating them or finding ways to remove them.

Figure 3-4 is a graph of all the laser cladding papers in this review according to the year they were published. A decline in laser cladding research in the near future would be unlikely, as shown by the increasing number of publish papers in Figure 3-4 and because the research so far is yielding a lot of promising results which feed and expand into further research and developments in other areas and into different industries.

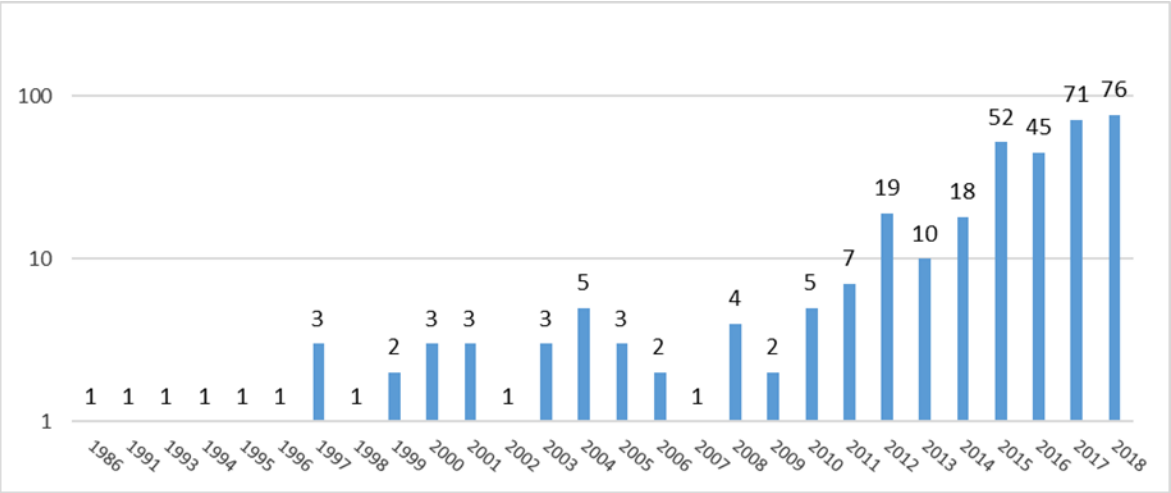

Figure 3-4 Increasing number of papers published per year (over 200 in recent years)

A number of trends were identified through the review and grading. Some of the technical topics mentioned here are discussed in the next section:

- With the UK and USA having started and promoted a lot of the research in the early years, they continue to invest heavily and to be leaders in the development of laser cladding coating technology and research. Other European countries gained great expertise in the field and China has contributed immensely in recent years.
- Although cladding with powder has many benefits and it seems to be an established method, there is still ongoing work with wire feed cladding, which indicates that the advantages are attractive enough to justify interest in improving on the drawbacks of wire cladding.
- Hybrid laser cladding has been shown to lead to accurate and reliable cladding equipment/process. This includes assistive technologies such as heating the substrate and clad material, aid of plasma, vibration, electromagnetics, supersonic (cryogenic) and the RECLAIM Project (combination of other processes, machining-inspection).
- The speed of cladding is of great importance in order for this process is to be part of mainstream manufacturing. Additional equipment for process control, feedback during cladding and modelling are needed to improve reliability and speed of the cladding process.
- Biomedical applications could benefit from using laser cladding because of its many advantages over other coating techniques. Such advantages are the precision of alloying elements and good substrate bonding, ability to clad ceramics which are biocompatible (and brittle) and bond to titanium (which is strong and light) and create textured surfaces which could help bones bind onto stronger structures.
- Another cladding technology that was observed was the Friction Surface Cladding [100] which although it uses a frictional method instead of lasers to deposit a coating onto a surface, it has similar benefits to the laser cladding method over other coating processes, such as low heat transfer with minimal dimensional and microstructural changes of the substrate. Currently the thickness of the FSC coating is lower than that achieved by laser

cladding, however, it seems to be an intermediate between other coating processes and laser cladding. Future research in the field should be monitored as this technology seems promising.

3.3 Laser cladding process

Laser devices are used for the various methods for coating and treating surfaces. The laser energy can be concentrated in the small beam area, resulting in a relatively high power (after some energy loss in the system), making it an efficient way of heating any component. Developments in lasers over the recent decades, enabled lasers to be more efficient, economic and powerful, capable of providing the same power as welding equipment in melting metal surfaces for material bonding. Lasers have been used extensively to improve wear and corrosion resistance of mechanical components, either by laser hardening (post-heating, stress-releasing) or alloying of different powders as a coating on existing components.

Laser cladding could be classed as a “Solid Freeform Fabrication” technology, which is the same technology group that “Rapid Prototyping” belongs to and the main characteristic of SFF technologies is the production of net shape metal components without the aid of moulds by laser fusion of metal powder alloys [101]. It is also known by many other names such as Direct Metal Laser Deposition (DMLD), Direct Metal Deposition (University of Michigan - DMD™), Laser Engineered Net Shaping (Sandia National Laboratories - LENS™), Laser Direct Casting (University of Liverpool - LDC), Laser Consolidation (Integrated Manufacturing Technologies Institute, Canada), Direct Laser Powder Deposition (DLPD), Direct Laser Deposition Welding, Powder Fusion Welding, Laser Based Solid Freeform Fabrication, Direct Metal Casting, Laser Powder Forming (LPF) or Laser Powder Fusion (LPF) as used in the turbine blade repair industry and many more [95].

Similar to welding, laser cladding is a manufacturing process which metallurgically bonds materials or alloys onto a base material, but with a laser beam as a heat source which creates a melt pool with minimal heat affected zone (HAZ) due to the precise control of the heating parameters. The blown powder (one step method) system is the most preferred method due to the many advantages over not only the wire feed method, but also over a method of pre-placing the powder (two step method) onto the substrate surface. Placing the powder has many disadvantages, such as porosity and rough surface finish due to the evaporation or decomposition of binder residues; complex geometries make it difficult to apply a uniform coating and having a two-step process has lower productivity. One way to eliminate the two step process is to deposit the clad material as a paste in front of the melt pool, however, the porosity is still present due to incomplete evaporation of the binder [102]. Figure 3-5 is a schematic of some of the laser cladding methods.

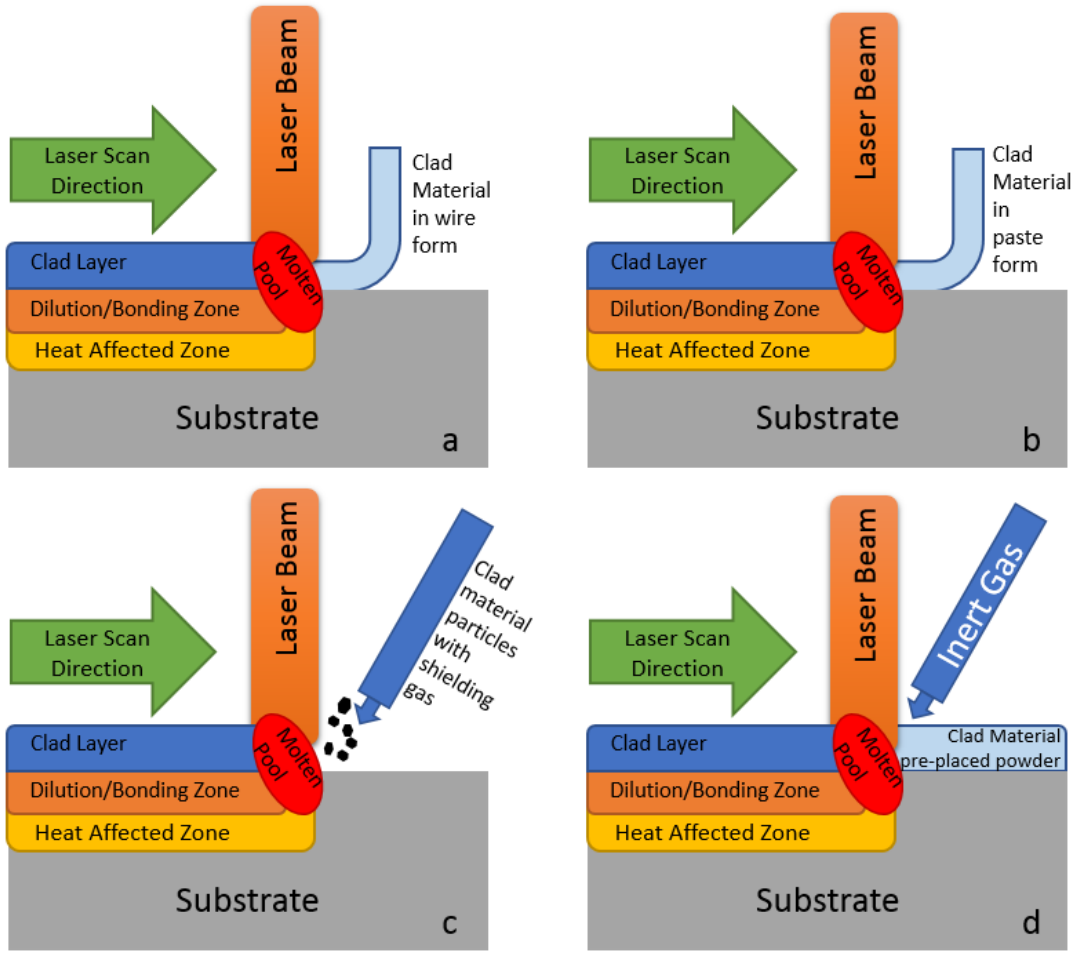

Figure 3-5 Laser cladding methods (a) wire, (b) paste, (c) blown powder, (d) pre-placed powder

The main disadvantage when cladding by feeding a wire of the chosen clad material to the melt pool, is the low laser energy absorption, which may be overcome by heating the wire. However, when heating the wire, the dilution increases [102] and this is considered a big drawback over the blown powder method. The well-established method of blowing the powder to the melt pool, as described in Figure 3-6, most commonly uses an inert carrier gas, that shields the melt pool to prevent oxidation, for example argon, nitrogen or helium. This method is not very efficient when it comes to material usage as some powder will bounce off and away from the melt pool, however, in a controlled environment the material can be collected and reused. It is important to protect nearby surfaces when cladding in-situ, for example repairs on turbine blades, where hot powder material may hit and bond with nearby surfaces or recently deposited tracks which are still hot, thus creating a rough surface. This rebound effect depends on the powder injection tube design and its jet divergence [102]. Overall, injecting powder gives better control over coating adherence, clad dilution and reproducibility [102].

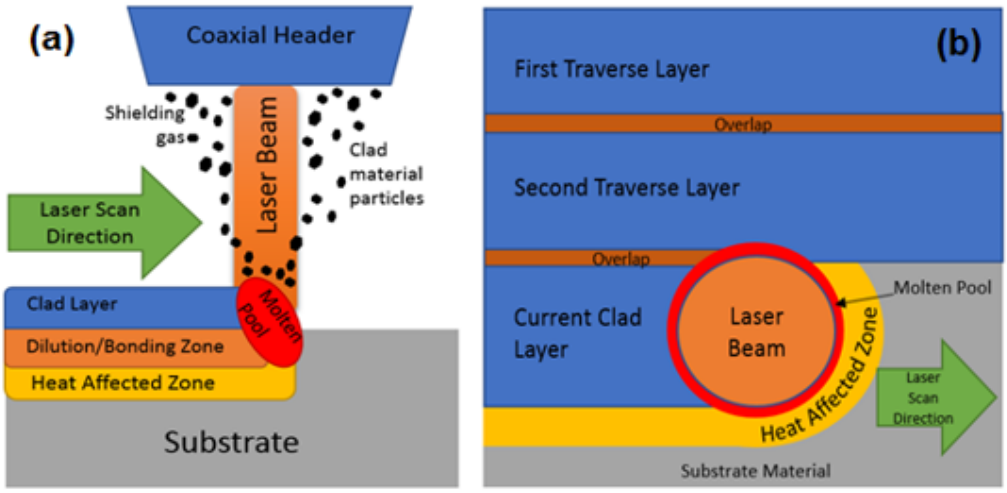

Figure 3-6 Laser cladding coaxial nozzle blown process

(a) side view, (b) top view

Typically, the laser traverses in a straight line and then in a “serpentine” motion to cover a flat area or in some cases in a circuitous motion winding from the centre outwards or vice versa. For cylindrical objects the laser clad head is designed to only move along the longitudinal axis of a turning machine, for example by attaching the laser clad head onto the frame of a modified lathe. In this set-up, the cylindrical component rotates while the laser clad head moves in a rectilinear motion parallel to the axis of rotation. This enables the melt pool to shift in a spiral motion around the component, thus covering the whole surface. Cladding conical components can be achieved by changing the rectilinear motion so that it is not parallel to the rotation axis. Lathes can also been modified accordingly or bespoke systems can be designed to enable repair on asymmetrical profiles along the axis of cylindrical or longitudinal components, for example crankshaft repair [103]. For in-situ repairs of complex geometries the laser clad head, typically a coaxial nozzle, can be retrofitted on to robotic arms, which can be programmed to follow specific profiles using computer numerical control.

Once a layer is deposited onto a substrate, more layers can be fused on top, creating a thicker coating. It is important to maintain the desired material properties throughout all the layers and to maintain a good metallurgical bond with each layer. This calls for control of many parameters and a very specific process, therefore it is extremely difficult to produce very thick clad layers. Currently one or two layers are common by many users of laser cladding and there is potential with improvements in control of the laser cladding process to enable build-up of many more layers for thick coating applications. With each new deposition in a layer, each time the laser nozzle traverses in the opposite direction to an existing clad line, the new line typically overlaps slightly the neighbouring deposited material to ensure material continuity. If the overlap is in the region of 50% to 60%, then sufficient low roughness can be obtained, thus avoiding or reducing post-cladding surface machining [102].

There are three different ways of implementing laser cladding processes on different materials. In general, the coating is referred to as a “cladding” when it has a different chemical composition to the substrate (Figure 3-7a). Another way is to clad with the same material as the substrate in terms of chemical composition (Figure 3-7b) which allows to rebuild thick layers of the substrate when severe

wear occurs when in services thus in theory extending its life by an infinite time. Cladding with the same material can also provide additional process benefits, such as controlling the microstructure near the surface by varying the laser parameters, for example to provide a harder surface or to release residual stresses near the surface. A third way would be to disperse hard particles such as carbides, cobalt or tungsten in the coating layer to form a composite (Figure 3-7c) [98]. This allows the average hardness of a surface to reach extreme values (e.g. 3000 HV), but this is topological hardness only available at the particle location while the surrounding volume of material could have fairly high hardness, much higher than the substrate. Multiple layers of cladding material allow for multiple materials to be cladded together providing various benefits. An example is to have a soft mass-produced substrate, a high ductile layer with an outer layer that has extreme hardness and perhaps reduced ductility. The outer material will provide the interface protection and cracks may generate, while the intermediate layer will arrest some of these cracks to prevent them from reaching the substrate. A multiple-powder feeder has the advantage of varying the ratios of each feeder, creating graded parts [97]. This opens new doors for development of custom alloy coatings of various grades at different areas on the same components or varying grade over the thickness of the coating to provide engineered coatings where the bottom section of the coating is designed for good mechanical bonding with the substrate and with increase hardness to withstand high loading, the next layer to block any external cracking from continuing into the substrate and the outmost layer for corrosion protection.

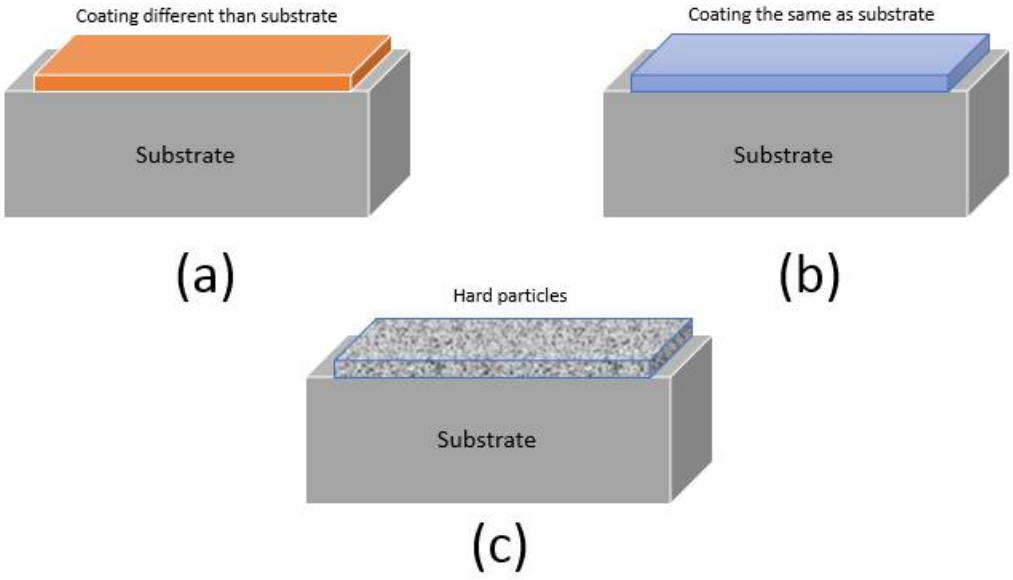

Figure 3-7 Types of coating

The structural integrity of a laser-deposited coating is determined by its mechanical properties, microstructure and the microstructure of the interface area. The latter consists of two distinctive zones, the dilution and the heat affected zone (HAZ). The dilution region is made of a mixture of the melted substrate and the coating material with the microstructure typically similar to the coating, while the heat affected zone lies in the substrate and its microstructure is different from the substrate due to the heat transfer from the melt pool [104] as shown in Figure 3-8. Several parameters play a dominant role in producing successful clad surfaces with a good mechanical bond and the desired

mechanical and metallurgical properties. The laser cladding process is very flexible in terms of adjusting these parameters at any stage of the deposition which means different areas or different layers of the clad surface can have bespoke parameters to suit the surface or application requirements. The laser parameters are the melt pool intensity, size and temperature, laser power, laser wavelength, laser focal point, laser distance to substrate and traverse/scanning speed. With regards to the material feeder, parameters include: powder feed rate, inert gas supply (including pressure and flow rate), material/alloy selection, powder particle shape and size. Process parameters are ambient temperature as well as temperature of the clad and substrate material, solidification rate, beam overlap, pre-heating or post-heating of substrate and clad material, amount of overspray, laser beam width to clad height ratio. Other parameters may apply depending on the type of laser clad equipment, such as the angle of powder feed or angle of laser beam to substrate and laser beam polarisation. The accurate control of these parameters would result in controlling the level of dilution, improving system efficiency, control of clad layer thickness, improve surface finish, reduce or even eliminate porosity and produce consistent and good quality clad material. Figure 3-9 demonstrates the different parameters on a corresponding laser cladding arrangement.

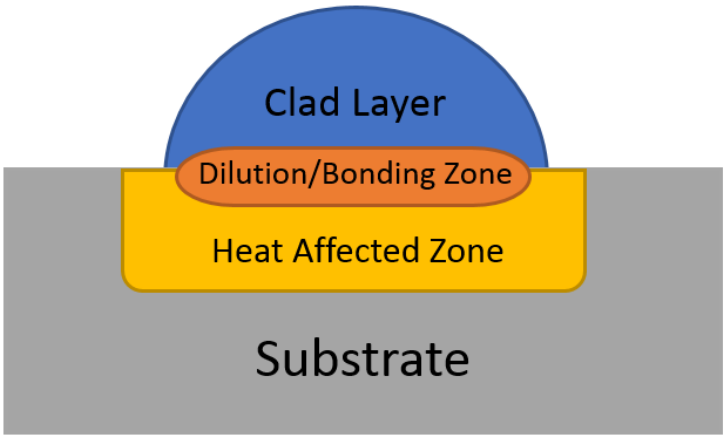

Figure 3-8 Interface area of substrate with a laser cladded bead

Several parameters play a dominant role in producing successful clad surfaces with a good mechanical bond and the desired mechanical and metallurgical properties. The laser cladding process is very flexible in terms of adjusting these parameters at any stage of the deposition which means different areas or different layers of the clad surface can have bespoke parameters to suit the surface or application requirements. These parameters are the melt pool intensity, size and temperature, laser power, laser wavelength, laser focal point, laser distance to substrate, traverse/scanning speed, powder feed rate, powder particle shape and size, ambient temperature as well as temperature of the clad and substrate material, material/alloy selection, solidification rate, inert gas supply (including pressure and flow rate), beam overlap, pre-heating or post-heating of substrate and clad material, amount of overspray, laser beam width to clad height ratio and more depending on the type of laser cladding technology, such as angle of powder feed or angle of laser beam to substrate and laser beam polarisation.

The accurate control of these parameters would result in controlling the level of dilution, improving system efficiency, control of clad layer thickness, improve surface finish, reduce or even eliminate porosity and produce consistent and good quality clad material. Figure 3-9 demonstrate the different parameters on a corresponding laser cladding arrangement.

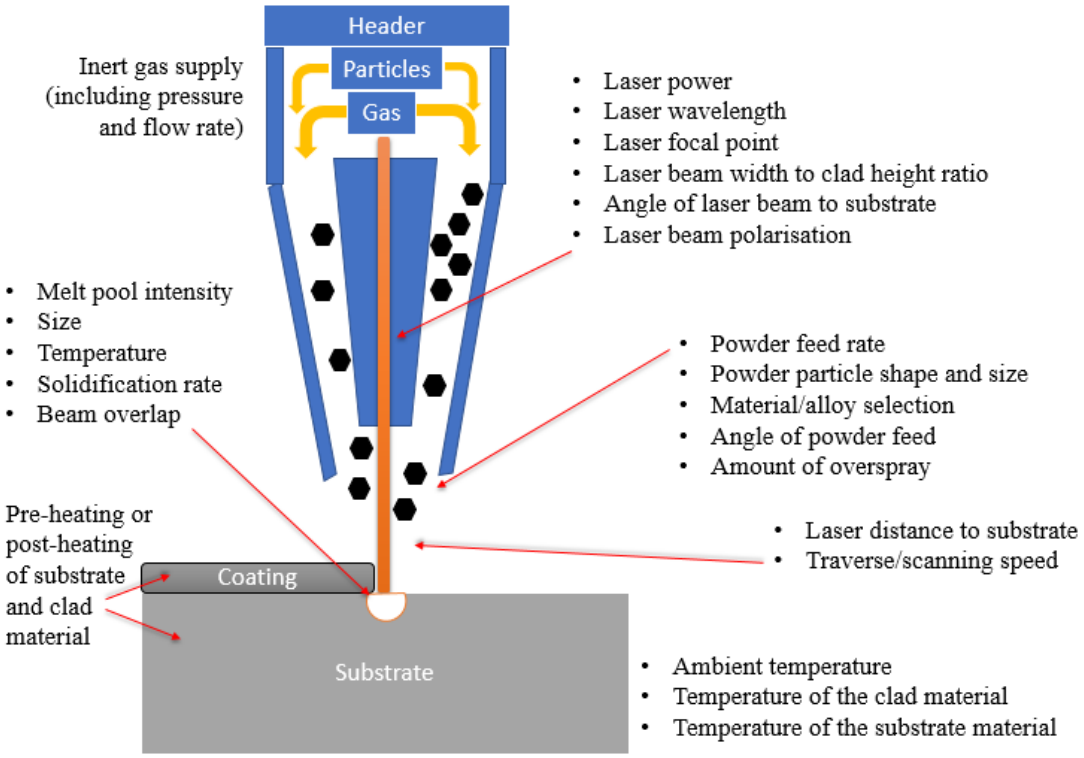

Figure 3-9 Some laser cladding parameters

Dilution is the ratio of the substrate diluted in a coating and it is considered as a percentage of diluted thickness over the clad coating thickness [98]. An example of the dilution zone can be seen in Figure 3-10, which is an optical microscope image of a Stellite 6 laser clad coating on Pearlitic steel. Kaierle et al. [97] refers to technologies where 2% dilution has been achieved with the use of plasma-transfer-arc for pre-heating the substrate and clad material and also concludes that dilution levels below 5% of the clad thickness lead to high quality coatings. Clad height is governed by the process speed and the powder feed rate while clad width is mainly affected by the laser beam diameter, however, changes in the gas supply, powder feed rate or process speed will affect its size, width and depth. The depth of dilution may be reduced by increasing the gas supply, but changes in the process speed seem to have little effect. Increasing the powder feed rate tends to increase the depth of dilution [105]. The maximum thickness of the coating that can be achieved depends on the set-up, but mostly on the clad material powders available. Typical clad layer thicknesses range from 0.5 mm to 2 mm or even thicker can be achieved.

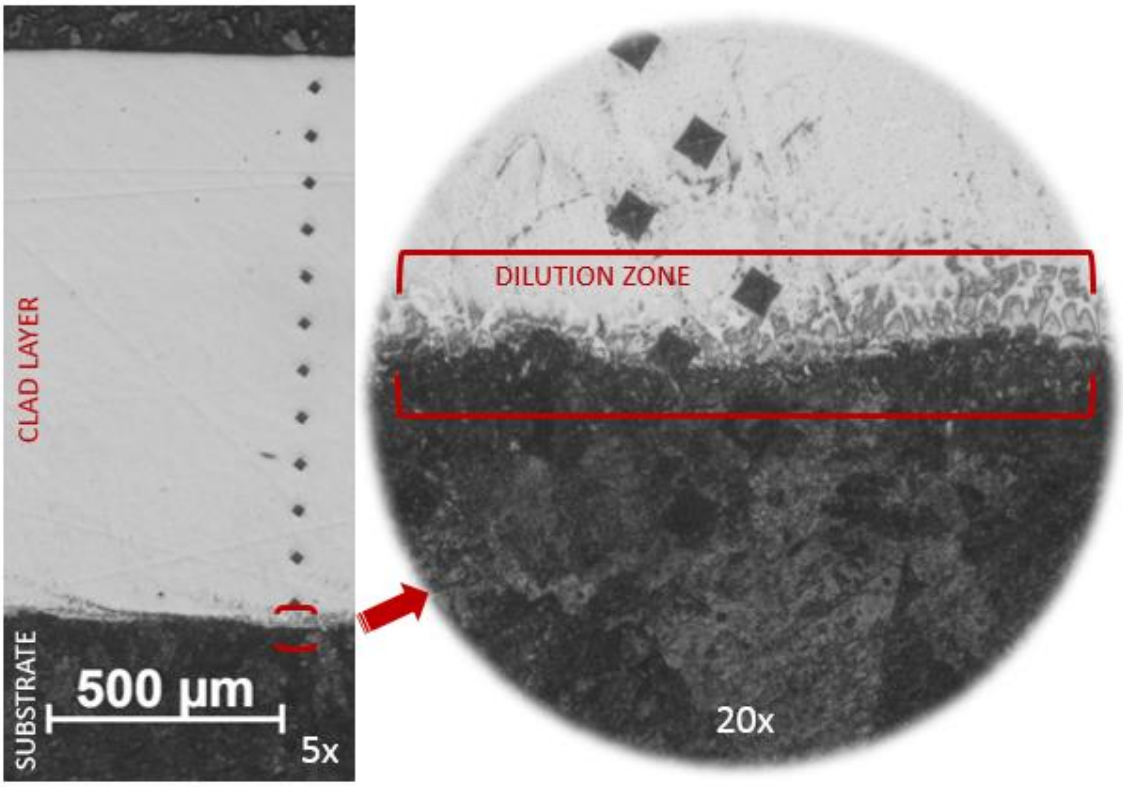

Figure 3-10 Optical image of Stellite 6 clad on pearlitic steel (R200) substrate with Vickers indentations visible

A lot of researchers refer to the exposure beam equations as a reference to the energy absorbed by the components during the cladding process. An example, is the simple description in Equation 3-1 [106]:

$$F' = \frac{P' E_t}{\pi r^2} \qquad where\ E_t = \frac{d}{f_r}(s) \qquad \textbf{Equation 3-1}$$

where F' is the laser beam fluence [J m^{-2}]; P' is the laser beam power [W]; r is the radius of the laser beam [mm]; E_t is the exposure time of laser beam on materials; d is the laser beam diameter [mm]; and f_r is the scanning speed [mm s^{-1}].

Several process models have been developed [107-121] to predict and control the laser cladding process, a lot of them involve thermal finite element models to estimate temperature and heat transfer based on cladding parameters in order to predict the heat affected zone, geometrical shape of clad bead or microstructure evolution.

An interesting approach for controlling the dilution is to measure the width of the bead live during the clad process and compare melt pool width ensuring that is smaller than a critical value, for example about 90% of the laser beam diameter. This method can not only control the dilution level, but could also reduce laser power consumption during cladding [119].

Similar processes are being developed by researchers for live feedback of the laser clad process in order to control the dilution, geometry, heat affected zone or microstructure, mostly with the use of CCD cameras [103, 122-130]. For example a fuzzy logic control from a CCD camera has been

developed to cope with the multiple parameters of the cladding process [116] and other CCD systems for example to measure the melt pool width as mentioned in the previous paragraph [123]. A very interesting development is the live detection of cracks during and after cladding using an acoustic emission technique, allowing for adjustment and fine tuning of the cladding parameters for good quality clad and repeatable production, making the process more reliable and efficient [128].

The practicalities of cladding surfaces using lasers are not straight forward due to the power demands of the laser equipment and its cooling requirements, simultaneous multi-feed powder system from different sources, three or five axis control mechanisms, gas supply control and so on. A lot of development is undertaken to design suitable laser cladding nozzles to cope with the demands of the cladding applications, whether it is a mobile cladding system or one mounted on a machine bed in a shop floor or even on a large industrial robotic arm for cladding complicated surfaces. Probably the most demanding challenge is to design a nozzle arrangement small enough to clad confined areas. It has been reported by Brückner et al. [131] that cladding nozzles have been used for internal cladding in bore diameter of 10cm and with an immersion depth into the bore hole of 1 metre.

Laser technological developments enable smaller in size, bigger in power, more efficient and accurate control laser to be commercially available for further research and industrial application of cladding. Lasers have been developed from CO_2 and Nd:YAG types to Disk, Diode and Fibre laser which among other benefits of high electro-optical efficiency they can produce a minimum reproducible track width in the range of 30μm and up to 22 mm enabling the use of powder particle sizes from 5 μm to 150 μm [97].

3.3.1 Advantages

The laser cladding method has many advantages over similar coating methods, such as minimised corrosion, longer part life, lower dilution levels, metallurgical bond with the substrate, minimal heat affected zone, minimal heat input (less distortion), large material selection (custom blending of alloys), thicker coatings possible than traditional methods, high deposition rates, improved wear resistance over conventional coating methods, greater impact resistance and most of the benefits come from a combination of the manufacturing method and the wide range of material selection. Traditionally the application of laser cladding as a hard-facing coating has been for wear and corrosion resistance, while in recent years the load bearing applications are of interest for example applications in the railways [132]. The increased hardness and proportionally yield/strength of the materials available for laser cladding allow for high load applications and it is the developments in laser cladding over the past two decades that enabled these materials to be successfully clad with metallurgical bonds, no or low porosity and maintain the desired microstructure as per the requirements. According to Kaierle et al. [97] “The significant advantage of laser cladding is the broad range of additive materials: Metals, Ceramics, Polymers and Compounds, nearly all weldable materials can be used. For instance, Steel, Aluminium and Titanium, have been used for laser cladding as well as Stellite, non-weldable rated nickel-based superalloys, shape memory alloys and nano composites.”

One of the main reasons why the laser cladding process has significant material advantages over conventional processes, is that it can exceed the tensile strength of conventionally produced parts without losses in the breaking strain because of the high thermal gradient during processing, which achieves a small-grained structure after solidification as explained by Gebhardt [133].

Stellites 6, 12 and 21 are commonly used in the in the conventional welding industry due to their beneficial attributes as coatings. Stellites are a common clad material for laser cladding and one of the main reasons is the Co-rich content. Diaz et al. [134] have tested Stellites® and Tribaloy® on Cr-Mo low alloy steel ASTM A182 F11 which is commonly used for steam circuit components. All the Stellites clad coatings had a dendritic microstructure and no visible cracks or porosity, while Stellite 12 had the smallest dendrites, which together with the higher content of C and W forming more carbides, made Stellite 12 the hardest of the Stellites tested. On the other hand, Stellite 21 had higher size of dendrites and lower content of carbides, which resulted in a lower hardness value.

On other tests a different coating Ni60A alloy powder on 45 steel substrate showed 2.6 times increase in hardness and increase in friction for the particular test than the substrate under the same load, where the wear rates were about 1 / 6.2 of the substrate wear rates under higher load. It was noticed that the wear mechanisms were different for the new coating compare to the uncoated substrate alone. The wear mechanisms of the uncoated substrate included: adhesive wear, abrasive wear, severe plastic deformation and oxidation wear, while that of the coating was merely a combination of mild abrasive wear and moderate oxidation wear [135].

3.3.2 Performance from composite coatings

Various combinations of readily available alloy powders for laser cladding applications can alter the hardness, friction coefficient and therefore wear mechanisms of the original component. With the appropriate selection of materials and process, they can produce laser clad coatings with more durable performance. Such performance would be applicable in non-conformal contact under rolling sliding conditions, as it is the case for railway contact examined in this research. The normal or shear forces in the contact determine whether the material will yield, especially near the surface when considering a Hertzian contact. Independent of the type of contact, the material properties near the surface are important and plain materials tend to have the same hardness through the thickness. More advanced materials are available that provide a composite hardness, where the hardness increases near the surface of the component. For example, heat treated materials such as R350HT, which is the heat treated version of the R260 rail, for which hardness is presented in 6.1.1. Of course, there is a limit to the maximum hardness and to the amount of control for the hardness gradient that can be achieved on uncoated surfaces through heat treatment or other surface hardening techniques such as carburizing, nitriding, cold working or work hardening. The limitations are attributed to the chemical, mechanical and thermal transformations of the uncoated material. The advantage of laser clad coatings is that material properties such as ductility, yield and hardness can be added to the surface over multiple layers, having more control over the distribution of these properties through the clad layers and achieving higher values and steeper gradients.

D'Oliveira et al. [136] explored the structural technique of cladding multiple layers, that influences hardness and microstructure, by testing and found that multilayer structures show alternate regions of fine and coarse dendrites. The latter being due to overlapping and overlaying, with coatings showed an increased interdendritic refinement close to the external surface. Because of the solidification contraction and the decreasing thermal gradients, with more layers deposited, surface residual stresses built-up and a non-uniform hardness across the coating, due to soft interfaces regions next to regions with interfaces harder than the surface.

Although high hardness relates to higher yield strength and could therefore increase the static strength of a coating or the fatigue strength of the same coating, it does not always imply that the wear resistance is applicable at high loads. At high load bearing applications there may be other characteristics in the microstructure that could reduce wear rates. It is important to look at each specific application as a separate isolated case and examine the conditions, the environment, the friction coefficients in the particular tribosystem and so on. Some other findings concluded that the wear resistance when comparing different Stellite coatings is proportional to the hardness and the carbide volume content of the coating [137].

An example of a powder designed for high load applications with high hardness is Sphérotène®. Sphérotène® comes as spheres with an extreme hardness of 3000 HV +/-500 HV and is obtained by spraying a liquid phase of Tungsten Carbide in a patented technique called a cold crucible electromagnetic levitation. According to the manufacturer Technogenia, Sphérotène® has a very fine metallurgical structure known as "tangled needles" and the absence of oxidation makes derived products highly weldable, improving wear and shock resistance compared to similar cladding powders made of crushed Tungsten Carbide particles.

3.3.3 Post treatment

Laser cladding has low energy efficiency, since the laser radiation used for the process is very small compared to the 88% of the overall electric power which is lost in the system [138]. Additional energy sources are used to compensate for the low efficiency, as mentioned previously by heating the wire for wire-fed systems, by the use of two laser beams simultaneously, by plasma pre-heating of the powder and substrate and pre-heating and post-heating of the substrate and clad layer using induction heating, where the latter is the most promising method where fast feed rates of up to 3 m min^{-1} and dilutions under 5% have been realised. Other process combinations are Plasma-Enhanced-Laser-Cladding (PALC), where a plasma-transferred-arc (PTA) is used to pre-heat the substrate surface and cladding material and it has shown to produce coatings with dilution of 2%.

In addition, a technology that bears low investment and operating cost than plasma or induction heating is the Laser Guided and Stabilised GMA-cladding (LGS-GMA) where an additional laser contributes energy for the stabilisation of the arc plasma and also preheats the substrate. This provides a dilution of 3% and high purity of the coating, which results to an average hardness of 63 HRc for a 1.4718 steel (MSS steel, X45CrSi9-3) coating onto mild steel substrate, however, this technology has only be proven to a few materials so far [97].

Laserline GmbH report on Ultra-High Speed Laser Material Deposition (Ultra-High Speed LMD) achieving 200 m min^{-1}, by focusing the primary energy deposition onto the clad powder rather than the substrate, having a particle temperature in the range of the melting temperature [139].

Due to the heating effect and the high thermal gradients of the laser cladding process, there are a few negative outcomes such as hardening or ductility reduction in the heat affected zone, the formation of cracks as well as large density changes which need to be suppressed, can all be counteracted by pre-heating the substrate accordingly [97].

Cracks in the coatings are usually generated by the function of the thermal stress and the structural stress, if the total thermal stress is larger than the tensile strength of the coating material, the coating will break and cracks are generated [140]. It is important to control the cladding process and heating conditions throughout, ensuring an appropriate cladding plan with pre- and post- treatment available to eliminate any crack generation in the clad layer, the dilution area or the substrate material. A method of providing live feedback of the temperature in the clad deposited region throughout the process can be beneficial, as a study shows, where micro-thermocouples were added to the clad to compare two different energy inputs by varying the scanning speed and characterise the thermal damage [141]. Feedback of the thermal condition during the cladding process can be characterised using vision systems as well [124, 125, 127, 129].

Regardless of preheating the clad area of the substrate, some residual stresses will remain in the clad components, either due to the large heat input or because of the different cooling rates of the dissimilar materials. Re-scanning with the laser over the previously worked area can be a way of post-heating the component in order to remove any residual stresses. Laser Shock Peening or Ultrasonic Impact Treatment are some of the many established processes for surface treatment to control residual stresses or to work-harden the coating surface after cladding.

Another reason for re-scanning the surface with the laser alone, is to partially re-melt the surface of the clad coating, in order to provide a desired surface texture. The introduction/creation of compressive stresses in the clad layer and part of the substrate can increase the fatigue life of the component, especially for components operating in cyclic loading conditions. Mechanical post-processed conditioning by deep rolling showed significant impact on the residual stress situation in low-alloy steel, inducing compressive residual stresses near the surface and an increase of tensile residual stress in the core of the part [142]. D'Oliveira et al. [143] explain how residual stresses are created due to the thermal gradient caused by the laser cladding process: "During heating the irradiated region expands. However, it is constrained by the cold surrounding area and becomes stressed in compression until melting occurs that relaxes the stresses in the liquid state. It is during the re-solidification and cooling down curve that the final stress state is determined. Tensile stresses are formed during shrinkage of the melt pool limited by the metallurgical bonding with the substrate. Clearly, these residual stresses affect the mechanical properties, such as fatigue, creep and brittle fracture behaviour. Stress is an extrinsic property and it cannot be measured directly but only calculated from the experimentally detected displacements converted into elastic strains by using elastic constants".

From their tests they found that residual tensile stress for Stellite 6 was around 450 MPa which is acceptable considering that it is around 60% of the yield stress and also concluded that the residual stress increases with scanning speed, track overlapping and change from flat to round (turning) shape of the substrate.

Residual stresses, which affect the fatigue strength negatively, were still induced in a process where the peak temperature was constant during cladding using close loop control, despite achieving a highly homogeneous cladding quality [144]. It is not an easy task to avoid the creation of residual stresses during the cladding process, but some post-processing methods have been shown to relieve the residual stress state in the substrate or clad layers. Post-cladding stress-relieving treatments such as tempering are suggested that they could significantly influence the magnitude and direction of resultant residual stress in the clad region [145].

3.3.4 The use of lasers

Laser is an acronym for "Light Amplification by Stimulated Emission of Radiation" and it was first built by Theodore H. Maiman at Hughes Research Laboratories in 1960 [93] based on previous theoretical work by Charles H. Townes and his colleagues after they have tested the Maser in 1954 (Microwave Amplification by Stimulated Emission of Radiation") [146]. The original theory of stimulated emission was first proposed by Albert Einstein in 1917 based on the theory of Max Planck in 1900, so it took 60 years to prove the theory which led to the discovery of lasers.

Different types of lasers used for laser cladding applications are CO_2, Nd:YAG, Diode, Disk and Fibre lasers with power capacities from 500 W to 15 kW for diode laser [147] and also 16 kW fibre laser is used in research for cladding applications, as well as 3D production of parts by laser deposition when mounted on a 6-axis robotic arm. Laserline GmbH report of lasers up to 20kW used for cladding [139].

Some important laser parameters for laser cladding applications are the wavelength, power, type, irradiance, spatial coherence, polarization, efficiency and so on. The width of the laser beam is of importance when it comes to cladding small components or having accurate control over the cladding process for quality purposes and different laser and optic technologies play a role in this. It is reported that the smallest width of laser beam used for laser cladding is in the region of 30 µm and currently researchers are aiming to achieve cladding with a laser beam width of 5 µm [97].

Laser cladding has low energy efficiency, not only because of the laser support equipment (cooling, CNC arms etc.), but also from the heat being absorbed in the substrate, Kaierle et al. [97] cite a study by IWS Dresden which shows 88% of the electric power is lost so it is of benefit to have additional technologies to improve efficiency, such as induction heating of the area to be cladded or further improvements in laser technology.

3.3.5 Hybrid

The laser cladding technology has been developed further to allow for a hybrid method of combining the laser deposition of new material with intermittent machining between layers or final machining to enable better forming to reduce porosity or improve the mechanical properties. An example of such development is a UK-based research project named RECLAIM (REmanufacture of high value products using a Combined LAser cladding, Inspection and Machining system) with multiple collaborators from industry and academia [148].

The outcome of RECLAIM are multiple-axis machines that combine CNC control of multiple machining heads, inspection heads, as well as laser cladding heads, resulting in a single, efficient machine that combines conventional and unconventional (additive) manufacture.

Hybrid laser cladding is another term that might refer to additional processes that combine with the traditional laser cladding equipment to enhance the performance and improve efficiency. Such a process is the induction heating of the substrate and pre- and/or post- heating of the substrate and clad material.

Zeng et al. [149] report on a hybrid fibre laser with induction heating being 3.7 times more efficient than a conventional CO_2 laser, with overall 64% efficiency. In addition, there is a tendency to have a lower cladding efficiency when the laser speed is increased, however, their findings indicate that with high induction pre-heating, high cladding efficiency could be achieved at high laser scan speeds.

References have been cited in literature where electromagnetic fields, vibration or other assisted measures in laser cladding process were introduced to obtain improved microstructures and properties [99].

3.3.6 Laser techniques

Supersonic laser deposition (SLD) is a very promising technique where a cold spray nozzle is combined with a laser to raise and control the temperature of the impact zone, where it softens the substrate and deposited particles thus facilitating the deposition of a wide range of materials at slower impact speeds, allowing the use of cheaper nitrogen gas. The advantages of cold spray are solid state deposition, no dilution, low oxidation and high build rates. In addition the SLD coating displayed submicron-scale microstructure while the laser clad coating had carbide dendrites of approximately 10 µm in thickness [150]. The traditional cold spray process disrupts the thin surface oxide films that are present on all metals and alloys and the projected particles experience extreme and rapid plastic deformation, unlike thermal spray process which uses thermal energy to melt or soften the particles causing thermal degradation and partial oxidation of the coating material which may be undesirable.

Research on different laser parameters found that pulse instead of continuous laser irradiation yields a more refined microstructure with the same phase aggregate (martensite, carbide and retained austenite) and that post-cladding thermal treatment increases volume fraction of carbides by tempering of martensite or conversion of retained austenite into pearlite/bainite. The same research

found that laser cladding of hardened and tempered AISI H13 tool steel with clad powder of the same material, develops residual compressive stresses on the surface. They explain that the state of residual stress arises due to the formation of large volume fraction of martensite during the cladding operation, despite liquid to solid transformation involved in cladding. Normally there are tensile residual stresses in the clad layer. Other findings were that the surface hardness increased significantly up to 45% compared to that of the hardened and tempered AISI H13 tool steel substrate, similarly for the microhardness after laser reheating was consistently higher than the substrate, however, post-cladding isothermal tempering lead to marginal reduction in hardness, though still higher than the substrate [151]. Surface treatment techniques, for example laser shot peening, are designed to induce compressive stresses on high value components in order to increase the surface fatigue strength [152]. A similar approach takes place with laser cladding, where the final surface stress state preference is compressive. In either case when multiple layers are to be cladded, careful consideration must be given to the recently cladded surface to ensure a good base for cladding the next layer, free of unwanted stress. A recent study [153] investigated the effects of synchronous rolling, where a ceramic roller was used to apply pressure and “roll” the newly solidified cladding layer, thus improving the uniformity of the microstructure with grain refinement. In addition, the cladding layer hardness was increased, due to the precipitation of strengthening phases caused by the residual plastic energy of the rolling action.

3.4 Significance for extreme interfaces

A gap identified in the research literature is for high load bearing applications. Examples such as machinery equipment experiencing severe wear and in construction for use in seismic isolators and friction pendulum bearings experiencing high loads from the gravitational weight of buildings. The same advantages, harder materials with metallurgical bond and customised alloying of the coating could find use in sports equipment, where high load contact and wear conditions dominate on equipment designed for superior performance. It is also affected by the environmental conditions which must be considered whether the equipment is a bicycle in hot and dry climate, a rowing boat in wet conditions or ski/sledge and climbing equipment in near freezing conditions. The bespoke laser clad coatings might be able to increase the working envelope of some components for all year performance under different conditions, increasing durability and therefore safety.

Some areas of research that could be developed further belong to the category of mechanics, in particular for understanding and classifying clad materials based on their mechanical performance. Such developments could produce data such as fracture toughness measurements, fatigue under different conditions, basic mechanical properties such as yield and tensile stress, shakedown and ratcheting diagrams and other non-linear data. The main issue is that laser cladding is producing coatings rather than whole components and any type of testing as described here must be standardised in a way that it ensures consistency in the use of the data. For example, some of the existing fatigue tests include a tensile test specimen for which there are different designs depending on the standard testing against, however, with the laser cladding, a coating is added over the specimen and this must be consistent when comparing different tests, in terms of thickness, location,

size, porosity and so on. This also extends to crack initiation and propagation and especially rolling contact fatigue (RCF) testing, which is more difficult to design a standard test due to the many parameters involved, such as different load ranges and different speed ranges as well as different size specimens depending on the organisation or institution's size of testing equipment.

So far research of laser cladding has been focused on solid contact wear, however, erosion might be a wear mechanism which laser cladding coatings might excel and prove to increase wear resistance. Stellite 6 is a good candidate material for enhancing erosion resistance along with other alloys that have a significantly high hardness [3]. Coatings which are shown to have good erosion resistance may be beneficial to industries where high pressure water is used that erodes surrounding equipment. In addition, impact wear is another mechanism that laser cladding could increase the wear resistance, for example at railway switches and crossings where the wheel is impacting the rail at various speeds and loads.

In various papers the clad surface was tested as made and in other papers there is a reference to machining or grinding the surface to a final finish. It is of interest whether the texture on the surface can be controlled by the laser cladding process directly without further (or extensive) post work. This is of interest not only for creating a designated texture but a more durable texture. This could be applicable to areas mentioned earlier such as textured ceramics on titanium for allowing the bone to bond to or it could be new areas of research such as work rolls in the cold mill industry, where traditionally rolls are textured with different established methods and the advantages of this process could make the texture more durable than the established methods of texturing work rolls.

With regards to wear testing a lot of the tests are standard tribological tests and because they interact with the surface of the components, therefore the coating, it seems straight forward to test laser clad components. Testing at high loads, for example in-situ with realistic loads, would be the real challenge for such coatings. Wear tests in most papers in this review are "generic" and do not consider the interface which may influence the performance greatly, for example the wheel-rail interface which cannot be characterised by a pin-on-plate wear test. When characterising the cladding material, the dilution zone and the resultant microstructure of the cladding is dependant of the substrate. In many papers, the choice of steel is mentioned, for example mild or stainless, without giving further details of the specific grade of the substrate.

3.4.1 Tribological performance

The laser cladding method has many advantages, similar to surface treatment techniques and coatings such as chrome plating, carburizing, nitriding, HVOF, CVD, PVD and others. Advantages such as minimised corrosion, longer part life, lower dilution levels, metallurgical bond with the substrate, minimal heat affected zone, minimal heat input (less distortion) and large material selection (custom blending of alloys). Unlike other techniques, laser clad coatings can benefit from all these advantages. This is mostly attributed to the ability to produce thicker non-porous coatings, high deposition rates, improved wear resistance over conventional coating methods and greater impact resistance. Most of the benefits come from a combination of the manufacturing method and the wide

range of material selection. Traditionally the application of laser cladding as a hard-facing coating has been for wear and corrosion resistance, mostly in equipment that is affected by sliding wear, such as drilling heads, engine valves or abrasive wear from particle erosion, for example turbine blades. In recent years load bearing applications with rolling-sliding wear have been of interest for applications in the railways [1] for example. Materials available for laser cladding allow for high load applications, because the driving factor is hardness increase and by increasing the hardness of the clad alloys, the yield point of the material also increases, since there is a relationship between yield and hardness. It is the developments in laser cladding over the past two decades that enabled these materials to be successfully clad with metallurgical bonds, without or low porosity and to maintain the desired microstructure as per the requirements. Kaierle et al. [97] identified that the significant advantage of laser cladding is the broad range of additive materials where nearly all weldable materials can be used, metals, ceramics, polymers, compounds, non-weldable rated nickel-based superalloys, shape memory alloys and nano composites.

One of the reasons why the laser cladding process has significant material advantages over conventional processes, is that it can exceed the tensile strength of conventionally produced parts of the same composition because of the high thermal gradient during processing, which achieves a small-grained structure after solidification as explained by Gebhardt [133].

3.4.2 Railway research

There are a great number of reports on rail testing, whether it is with laser clad coatings or without. Laser cladding for railway materials has been tested at the University of Sheffield, as part of a wider industry collaboration project named RailCLAD [1]. Some of the materials and their corresponding micro-hardness that has been achieved during the twin disc trials is shown in Table 3-1, while the wear rate is shown in Figure 3-11.

Table 3-1 Materials used in railway research as part of RailCLAD project [1]

Commercial Name / Category	Clad Material	Hardness (Vickers)	
Hardfacing Alloys – Cobalt based	Stellite 6	564	682 (work hardened)
	Stellite 12	673	787 (work hardened)
Manganese –Molybdenum Steel	MN-Mo	640	
Twin Induced Plasticity Steel	TWIP (5-20%Mn)	240	581 (work hardened)
Ultrahigh Strength Steel	300M (Q&T)	Failed to adhere to substrate	
Martensitic Stainless Steel	MSS	630-766	
Composite powder	NiCrSiB	850	

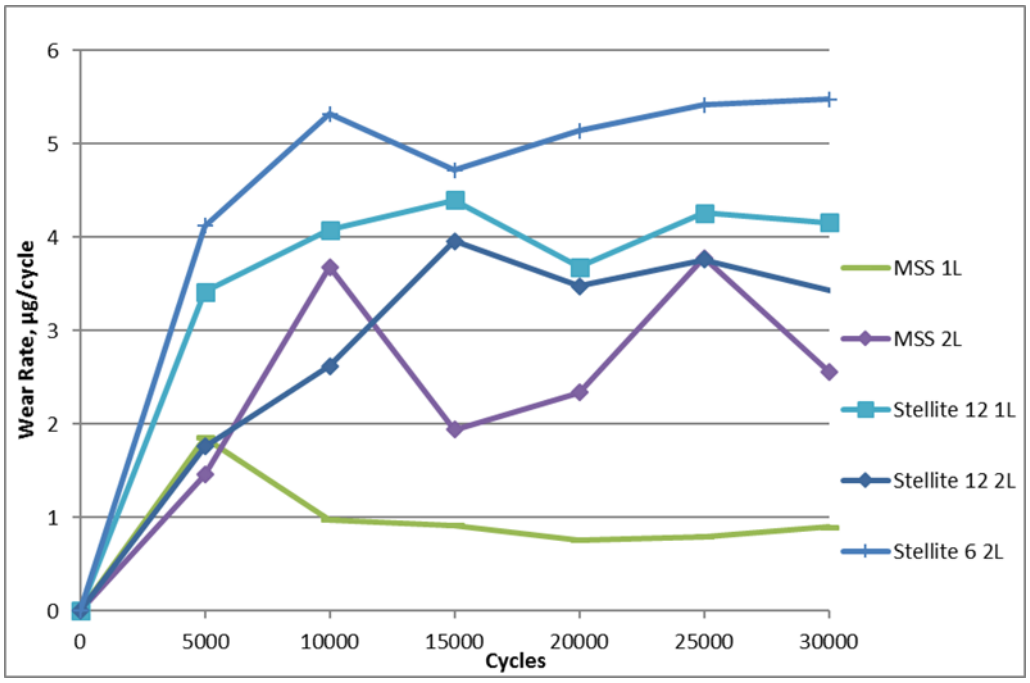

Figure 3-11 Clad rail twin discs wear rate - 1L and 2L are one and two layers of cladding [1]

Another report on Insulated Block Joints (IBJ) indicate lipping of the rail over the insulating gap causing electrical failure and a comparison was made between tougher and harder steel and laser clad steel, where the laser clad layer on tougher material gave the greatest resistance to lipping [154]. Lipping is the material flow by plastic deformation of the railhead over the endpost and in severe cases it closes the insulating gap, thus causing electrical failure. The R350 and laser clad (Stellite 6 on R260) disc samples are shown in Figure 3-12, after a 96,000 cycle test at a maximum contact pressure of 1,500 MPa and a slip of 0.5%.

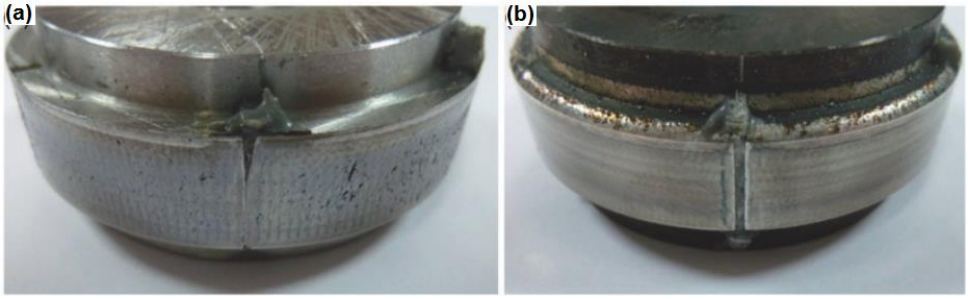

Figure 3-12 IBJ twin disc images after 96,000 cycles testing (a) R350 rail steel, (b) R260 rail steel with a laser clad layer of Stellite 6 [154]

The cross-sectional etched images of these discs are shown in Figure 3-13. In both images it is clear that the insulation has failed in the unclad disc due to lipping, while in the laser clad disc the insulation gap was maintained. Other studies on improving railway material found some promising behaviour after tensile testing for fatigue, mainly because the local crack formation in the clad during fatigue testing did not shorten the fatigue lifetime. This is based on a Co-Cr coating, which might not be very cost-effective for cladding rails [155]. Another publication from the same authors from Chalmers University, indicates further mechanical properties from these tests [156]. The same researchers

have developed a thermal and phase transformation model as a first step towards judging the resulting microstructure and hardness in the heat affected zone [112]. Further research from Monash Universities in Australia has been focused on laser cladding parameters and heat treatments for the Hypereutectoid rail R400HT [157-159]. Universities in the USA and Saudi Arabia have developed fully pearlitic laser clad weld as an alternative to thermite welds which was successfully tested in the field [53]. Research by Chinese Universities was focused on laser clad repair of railway axles, which indicated an improvement in the fatigue life of EA4T steel axle with Kf311 cladding material (17.5% Cr and 10.5% Ni) [160].

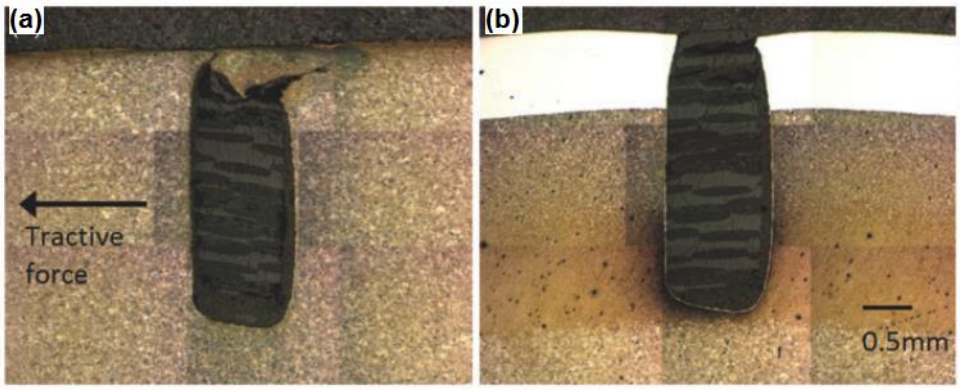

Figure 3-13 Cross-sectional etched images of IBJ twin disc samples after 96,000 cycles testing (a) R350 rail steel, (b) R260 rail steel with a laser clad layer of Stellite 6 [154]

3.4.3 Load bearing performance and material selection

When considering laser cladding on all kinds of metals, the obvious working solution would be to clad with powder (or wire) of the same material as the substrate, with the exception that the clad layer will have minor differences in its mechanical properties than the substrate due to the cladding process. This will ensure good compatibility and fusion in the melt pool since both materials have the same melting point and bonding properties. The next step is the use of metal alloys different to the substrate. Similarly to welding and other coating techniques, each element in the alloy will serve a purpose, whether this is for achieving adherence, corrosion protection or other purpose such as wear resistance. There must be some compatibility in the materials, for example the different melting points of materials prohibits certain combinations, although some polymers might be compatible with other polymers or ceramics [161]. Some ceramics though provide desirable properties and are suitable for metal alloys [162]. Intermetallic compounds are also introduced into laser cladding on metals and nowadays, the most popular research focuses on the cermet (i.e. ceramics–metal composites). There is a great interest in bio-compatible materials such as Hydroxyapatite and Fluorapatite which have been clad with titanium alloys [99]. The benefits of laser cladding bio-compatible materials would be preferable over established coating techniques, due to its accurate control of coating area/thickness and decreased level of dilution.

There have been developments in cladding of softer metals, such as yellow metals, specifically copper, however, this is not always successful when applied directly. Sometimes an intermediate coating layer of a different alloy is needed, for example when cladding aluminium on mild steel, and this is due to the different coefficients of thermal expansion of both materials which build up stresses when cooled, leading to failure of the coating. On a successful trial the intermediate coating was made up of a thick layer of nickel with a high melting (1455°C) point which could be easily applied to mild steel as a homogeneous coating via the electroless nickel plating process. This proved challenging though since the aluminium clad broke through the Ni coating [163]. In recent years there are reports of cladding pure aluminium onto 304 stainless steel, as a proof of concept [164].

There are many established alloys which have been used for coating applications and which are suitable for use with the laser cladding process. For example, Stellite 6 is an ideal hardfacing alloy because the chromium provides corrosion resistance, while carbides add strength to the alloy. In addition, Molybdenum and Tungsten are solid solution hardening elements and also contribute to the strength of Stellite 6 via precipitation hardening, forming carbides and intermetallic phases such as Co (Mo, W) [3].

Most papers refer to the clad layer having a higher hardness or micro hardness than the substrate. It is a common theme that the materials chosen for most of the clad applications in this review are aiming at increasing load bearing performance on the substrate with the addition of a harder clad layer. A separate study involving titanium alloys, indicated that higher cooling rates of the clad layer, for example when the substrate is not heated, led to more uniform TiC particle distribution, however, this also means potential micro-cracking in the clad layer [165]. Whether cladding is performed for corrosion or to increase hardness, it is important to achieve an ideal clad surface with a uniform distribution of the selected particles and without any cracks present. Cracks can be generated during the cladding process due to many factors, such as rapid heating and cooling, presence of residual stresses, non-uniform distribution of particles, porosity in the clad layer and so on. For high load bearing applications, however, the potential for generating cracks might not be acceptable due to the loading conditions which will propagate the cracks and possibly result in failure.

Another study explored cladding with the use of hot wire. A comparison was made with the un-clad substrate and with additional cladding of TiC particles over the hot wire clad layer. The tensile strength was almost equivalent to that of the substrate, but ductility and impact toughness deteriorated a lot in the hot-wire clad. However, the ductility and toughness improved to the equivalent of those of the substrate although the strength dropped a little when the specimen was tempered by re-scanning the sample with the laser. By adding TiC nanoparticles, the overall mechanical properties were improved and the ductility and impact toughness were even better than those of the substrate [166].

In terms of material selection, a study on cladding wheel and rail surfaces found that the addition of lanthanum oxide in the laser clad material refines the microstructure and significantly reduces wear, while there is no obvious influence on hardness. The wear mechanism transforms from severe spalling to slight peeling, with homogeneous wear debris with the inclusion of lanthanum oxide in the coating compared to without lanthanum oxide being present in the coating [167].

Ceramics show great potential for increasing hardness and improving wear resistance, for example a VC-Cr_7C_3 ceramic coating exhibited very good metallurgical bond on A3 mild steel substrate where it achieved a high hardness of 1000 HV, significantly higher than 150 HV of the substrate. It also exhibited four times the wear resistance of the substrate due to the distribution of the VC-Cr_7C_3 particles which were strongly bonded in the matrix [168]. Niobium content in a Fe-Cr-C cladding on low carbon Q235 steel plate, indicated an increase in hardness, strength and wear resistance at 0.71wt.%, with hardness increasing from 560 HV to 620 HV, tensile strength increasing from 1209 MPa to 1588 MPa, yield strength increasing from 957 MPa to 1344 MPa, abrasive wear weight loss reduced from 0.33 g h^{-1} to 0.15 g h^{-1} and coefficient of friction of adhesive wear reduce from 0.6 to 0.47 [169]. This study highlighted that the positive increase in material properties was related to the increase of Niobium content and how specific elements can influence material properties. Aluminium oxide (Al_2O_3) ceramic particles are often used as an addition to the laser cladding coatings due to their high hardness and melting point [170].

A table of typical laser clad materials can be a useful reference for selecting clad materials for specific applications. Such a table was not found in the literature, therefore Table 3-2 and Table 3-3 were put together, consisting of materials found mainly in the literature review presented here. It is not an exhaustive list of all the materials used in laser cladding research and for industrial applications.

The first column is the category for the group of materials, while the second column is the name of the material. The third column is the nominal composition followed by a description of the characteristics for each material. The information was obtained from the research literature or it was sourced from commercial brochures, where information was not available in research papers. For some materials, the specific grade or composition was not available, however, a description for the characteristics of the material category has been included. Furthermore, where applicable, the hardness range of the clad material has been included in the referenced scale.

In Table 3-2 various steel-based materials have been identified, mostly stainless steels as they are desirable for corrosion resistant applications. A range of other alloys have been categorised, with ceramics coatings and biocompatible alloys to show promising results when used with the laser cladding process. The materials in Table 3-3 are mostly materials that in their powder or wire form have been used for decades as traditional hardfacing coatings. These are now deemed to be established laser clad materials, as they have been tried and tested in the industry for many years.

Table 3-2 Common materials used in laser cladding

Cat.	Clad Material	Nominal Composition	Characteristics	
Steel Based	304 Stainless Steel	Fe 12Ni 20Cr 0.75Si 2Mn 0.08C	Practical stainless steel, economical, non-magnetic, not suitable for demanding post-clad machining	Chromium based steels with superior corrosion in comparison to other steels. Five types: 200 and 300 series are Austenitic, 400 series are Ferritic and Martensitic, 2000 series for Duplex (mixed microstructure of ferrite and austenite) and Precipitation Hardening (PH), also known as Maraging.
	308 Stainless Steel	Fe 9.5Ni 19.9Cr 0.58Si 2Mn 0.024C	Ductile, excellent heat resistance, very good weldability	
	316/316L Stainless Steel	Fe 12Ni 17Cr 2.5Mo 1Si 2Mn 0.08C	Corrosion resistance in marine environments, resistance to pitting and cavitation, creep and stress rupture at elevated temperatures	
	420 Stainless Steel	Fe 1Ni 14Cr 1Si 1.3Mn 0.036C	Very durable, hardenable to 500 BHN. Typical applications: dental instruments, surgical instruments, hospital equipment, gears, molds, dies, knife blades, valve parts, and bushings	
	431 Stainless Steel	Fe 3Ni 18Cr 1Si 2Mn 0.2C	High strength, high toughness and tensile properties. Typical applications: Fasteners, bolts and nuts, pump and propeller shafts	
	4140 Steel	Fe Ni 1.2Cr 0.35Mo 0.4Si 1.1Mn 0.44C	High fatigue strength, abrasion and impact resistance, toughness, and torsional strength. Typical applications in aerospace, oil and gas, and steel industry components	
	Martensitic Stainless Steel	Fe 10Cr 2Ni 1Co 1Mn 0.5W 0.2Mo 0.2Si 0.2C	**Custom material used on rail as part of this research**	
	Maraging Steel	Fe 19Ni 9Co 5Mo 1Ti 0.15Al	High strength and high hardness derived from precipitation of intermetallic compounds. Also, high fatigue strength and good machinability	
Tool Steel	CPM REX 20	10.5Mo 6.25W 3.75Cr 2V 1.3C 0.35Mn 0.25Si	Cobalt-free high speed steel, high red hardness, high abrasion resistance and good toughness. Typical clad hardness 300 HV. Typical applications: end mills, forming tools, mill cutters, special taps	
	CPM 9V	1.3Mo 5.55Cr 9.1V 1.9C	High toughness with high crack resistance, suitable for severe wear applications, but not intended for applications requiring high compressive strength	
Titanium Based	CP Titanium	Ti 0.18-0.4O 0.2-0.5Fe 0.08C 0.03-0.05N	Pure Titanium with higher strength-to-weight ratio and ability to osseointegrate within the human body, making it ideal for medical applications such as medical implants	
	Ti6Al-4V	Ti 5.5-6.5Al 3.5-4.5V 0.13O 0.25Fe 0.08C 0.05N	Most popular alloy in industry and for research. Light, bio-compatible, low thermal and electrical conductivity, high corrosion and stress-corrosion resistance. Poor surface wear properties. Typical applications: motorsport, marine, energy (turbine blades), aerospace (blades, airframe, engine cases) and medical implants	
Alum. alloys	e.g. Al-Mg-Si		Typically the same alloys (or similar alloys with additions) as the substrate are cladded for surface repair. Additions may contribute to improving the coating strength, ductility and wear resistance	
Ceramic coatings		Al_2O_3	Low specific weight, low electrical and thermal conductivity, good tribological properties and widely used in plasma sprayed application	
		$VC\text{-}Cr_7C_3$	Enhanced resistance against thermal, corrosion and mechanical wear, with high hardness and good wettability with the bonding metal. Hardness up to 1050 HV	
Copper alloys	Copper-Silver		The antimicrobial activity of copper-silver alloys could improve materials used in the health sector. Other applications of copper alloys are intended to make use of the electrical and thermal conductivity of copper by using minimal quantities of copper alloy with laser cladding	
Biocompatible alloys	Hydroxyapatite (HA)		Chemically and crystallographically similar to the bone with good adhesive properties with bones, however, naturally brittle. With titanium alloys as suitable substrates, they are used as replacements of hip and knee joints and in dentistry	
	Fluorapatite (FA)		Higher chemical stability and improved biocompatibility than Hydroxyapatite (HA), with better corrosion resistance in body fluids or acidic solutions	
	45S5/S520 bioactive glass		Bioactive glass and glass-ceramics have potential use in tissue-engineering applications due to their osteoconductivity and bone bonding ability. The laser cladding process can be applied to complex shape geometries like those found in the middle ear and other low load-bearing craniofacial prostheses	

Table 3-3 Common materials used in laser cladding from traditional hardfacing applications

Cat.	Clad Material	Nominal Composition	Characteristics
Tungsten Carbide based	MetcoClad™ 52001	W 3.5C	Hard phase constituent, blended with a metallic matrix, for applications where high hardness, wear resistance and resistance to slurry erosion is needed. Typical hardness 2700-3500 HV. Applications: Down hole tools such as stabilizers and drill collars, slurry pump impellers, conveyor screws used for manufacturing of plastics
	MetcoClad™ 52052, 53003	WC 40(NiCrBSi)	High hardness, wear resistance and resistance to slurry erosion, 53003 provides good abrasion resistance with fair impact resistance. Applications: Down hole tools such as stabilizers and drill collars, Slurry pump impellers, conveyor and extruder screws used for manufacturing of plastics or ceramics, agricultural shearing blades, drill collars and tool joints used for oil exploration and drilling equipment
	Technolase®40s-400	60% Sphérotène® (WC) 40% Matrix (Ni/Cr)	Increased anti-wear and erosion protection with the use of spherical WC particles. Other grades available with varying levers of WC. Typical hardness 3000 HV ± 500 HV. **Used in this research for steel industry applications in rolling/sliding and texture evolution tests**
Cobalt based	Stellite™ 6	Co 27-32Cr 4-6W 2.5Ni 0.9-1.4C Ni Fe Si Mn	Most popular alloy with a good balance of the overall Stellite™ alloys properties. Typical hardness 380-490 HV. **Used for impact and erosion tests in this research**
	Stellite™ 12	Co 27-32Cr 7.5-9.5W 1.4-1.7C Ni Fe Si Mn	Typical hardness 435-590 HV
	Stellite™ 21	Co 26-29Cr 4.5-6Mo 0.2-0.35C 2-3Ni Fe Si Mn	Typical hardness 290-430 HV
	Stellite™ 32 (X40)	Co 26.5Cr 8W 0.55C 11.5Ni 2Fe 1Si 1Mn	Typically used for atmospheric plasma spray offering wear resistance to abrasive grains, hard surfaces, fretting and particle erosion at high temperatures up to 850 °C
			They are resistant to cavitation, corrosion, erosion, abrasion and galling. The lower carbon alloys are generally recommended for cavitation, sliding wear, or moderate galling. The higher carbon alloys are usually selected for abrasion, severe galling, or low-angle erosion. Exceptional surface finish with low coefficient of friction, suitable for sliding wear and excellent oxidation resistance to temperature range of 315 – 600 °C
	Triballoy® T800	50Co 18.5Cr 3NiFe 30Mo 3.8Si 0.08C	Developed for applications in which extreme wear is combined with high temperatures up to 800–1000 °C and corrosive media. They are very suitable for use in adhesive (metal-to-metal) wear situations due to their high molybdenum content, which accounts for the excellent dry-running properties. Typical hardness 700 HV
Nickel Based	Eatonite®	39Ni 29Cr 1Si 8Fe 2.4C	Designed for protection of hydraulic cylinder rods from salt water environment (marine and offshore rig applications). Typical hardness 42HRc
	Inconel® 625	Ni 20-23Cr 8-10Mo 5Fe 1Co 3-5Ni+Ta 0.4Ti 0.4Al 0.5Mn 0.5Si	High strength with excellent fabricability and outstanding corrosion resistance. Suitable for sea-water applications, such as wire rope for mooring cables, propeller blades, submarine quick disconnect fittings, exhaust ducts on utility boats, undersea communication cable sheathing, aircraft ducting and exhaust systems, fuel and hydraulic line tubing, bellows, turbine shroud rings and heat exchangers. Typical hardness range 120-240 HV. Service temperature up to 982 °C
	Inconel® 718	Ni+Co 17-21Cr 3.3Mo Fe 5.5Ni+Ta 1.15Ti 0.8Al 0.3Mn 0.25Si 0.3Cu	Age hardening alloy with outstanding welding characteristics with good tensile, fatigue, creep and rupture strength. It is widely used in liquid fuelled rockets, rings, casings and various formed sheet metal parts for aircraft and land-based gas turbine engines. In addition in cryogenic tankage, fasteners and instrumentation parts. Typical hardness range 150-600 HV. Service temperature range -217 to 704 °C
	Hastelloy® C276	Ni 2.5Co 16Cr 16Mo 5Fe 4W 1Mn 0.35V Si C Cu	Widely accepted material in the chemical process and associated industries in reactors, heat exchangers and columns, due to its ductility, formability and weldability with exceptional resistance to stress corrosion cracking in chloride-bearing solutions. Typical hardness around 180 HV
	Hastelloy® X	Ni 1.5Co 22Cr 9Mo 18Fe 0.6W 1Mn 0.15Ti 1Si 0.1C 0.5Al 0.5Nb	Exceptional oxidation resistance, fabricability and high-temperature strength. Used for combustion zone components in gas turbine engines and in afterburners, tailpipes and cabin heaters. In addition, it is used in furnace applications due to its unusual resistance to oxidation, while in the chemical process industry for retorts, muffles, catalyst support grits, furnace buffles etc. Typical hardness around 180 HV
	Wall Colmonoy® 69	Ni 16.5Cr 3.6B 4.8Si 0.55C 3Fe 3.5Mo 2.1Cu	Designed for spraywelder and HVOF applications, it has more chromium and molybdenum for better corrosion resistance. Improved plastic range makes overlays easier to fuse without sagging, suitable for marine and petro-chemicals applications and finished by grinding. Typical hardness >800 HV
	Wall Colmonoy® 88	Ni 17.3W 15Cr 4Si 3.5Fe 3B 0.8C	Unique alloy containing chromium and tungsten borides and carbides for maximum abrasion and corrosion resistance. For high-temperature, highly abrasive applications, glass mould plungers, pump plungers and sleeves, valve seats, plastics extrusion screws. Finished by grinding or CBN tools. Typical hardness 750 HV
	Deloro 60®	Ni 17.3W 14-15Cr 2-4.5Si 4Fe 3.-3.5B 0.7C	Suitable for sprayfuse and powder welding applications due to their low melting point, available in a range of hardnesses. Typical hardness of grade 60, is 56 Rock"C", used in severe wear applications of up to 315 °C and offer good oxidation resistance

3.4.4 Summary

A literature review [P1-P124] identified gaps in laser cladding process research and paper grading of the literature helped identify original and important developments in the field. Key process trends that were identified through this review and paper grading: cladding with powder is an established method which has many benefits while there is ongoing research for wire feed cladding; hybrid laser cladding is leading the research with the use of assistive technologies such as plasma, vibration, electromagnetics, supersonic (cryogenic) and a combination of machining with inspection; the speed of cladding is of great importance for commercialisation with research focusing on process control, feedback during cladding and modelling for improving speed and reliability; there are many advantages of laser cladding that could benefit biomedical applications, especially the ability to clad ceramics which are biocompatible (and brittle) that bond to titanium (which is strong and light) and to create textured surfaces which could help bones bind onto stronger structures.

It was identified that lasers have been used for the texturing of metal surfaces but never in combination with the laser clad process. Incorporating the two processes into one may result in cost savings for certain applications. Similarly, for fluid erosion conditions, laser clad materials seem to excel, yet not a lot has been found in literature, with some industrial examples from the mining industry.

Two future trends were identified, the ability to customise the cladding material and parameters at any time during the cladding process and the ability to apply different materials alternatively on the same surface. The first refers to coatings with varying material grade through the thickness or in selected regions of the coating, while the second refers to the application of alternating thick layers of known material grades that form a lamellar structure, which introduces new possibilities in terms of performance.

Laser cladding technology can benefit from new areas of research besides surface protection, for example load bearing applications. In addition, extensive mechanical testing will characterise the mechanical properties of the various clad materials and their intrinsic mechanical behaviour, but also as part of a cladded component.

New techniques for cladding might provide ground-breaking solutions applicable to existing and new applications.

1) The ability to customise the cladding material and parameters at any time during the cladding process could allow for manufacturing components with varying material grade on the same surface and therefore varying performance over the surface area of a component.

2) This ability to vary the material and performance could extend not only on the surface coating of a component but through the thickness of the surface coating, providing engineered coatings where the bottom section of the coating is designed for good mechanical bonding with the substrate and with increase hardness to withstand high loading, the next layer or layers to block any external cracking from continuing into the substrate and the outmost layer

for corrosion protection. It is not an easy task to achieve, but there is an opportunity as different materials exhibit different abilities to withstand the conditions described here.

3) An effort was made to grade and categorise published papers. This alone is not enough to provide a full picture and a technological update since some additional information came from an internet search and a patent search. Some papers consider cladding materials used in steel industry component, however, only one paper was found that included industrial testing of mould foot rollers in continuous casting [171]. A comparison was made between laser clad and resurfacing weld repair of foot rollers, with the laser clad repair performing significantly better with minimal cracking, wear, corrosion and deformation. A patent search highlighted engineering organisations that suggested laser cladding solutions, which indicated that some sort of research or development in the steel industry has taken place prior to applying for a patent. An example is a process by Eaton, also advertised on Eaton's website [172], where they laser clad their own custom material on hydraulic cylinder rods, mainly for corrosion protection.

3.5 Paper Grading References

Papers up to year 2015:

[P1] J. Ahlstrohm, B. Karlsson, and S. Niederhauser, "Modelling of laser cladding of medium carbon steel - a first approach," *Journal De Physique Iv,* vol. 120, pp. 405-412, Dec 2004, doi: 10.1051/jp4:2004120046.

[P2] J. M. Amado, M. J. Tobar, J. C. Alvarez, J. Lamas, and A. Yáñez, "Laser cladding of tungsten carbides (Spherotene®) hardfacing alloys for the mining and mineral industry," *Applied Surface Science,* vol. 255, no. 10, pp. 5553-5556, 2009, doi: 10.1016/j.apsusc.2008.07.198.

[P3] F. Arias-González *et al.*, "Fiber laser cladding of nickel- based alloy on cast iron," *Applied Surface Science,* vol. 374, pp. 197-205, 2016, doi: 10.1016/j.apsusc.2015.11.023.

[P4] T. Baldridge *et al.*, "Laser cladding of Inconel 690 on Inconel 600 superalloy for corrosion protection in nuclear applications," *Optics and Lasers in Engineering,* vol. 51, no. 2, pp. 180-184, 2013, doi: 10.1016/j.optlaseng.2012.08.006.

[P5] M. Bamberger, W. D. Kaplan, B. Medres, and L. Shepeleva, "Calculation of process parameters for laser alloying and cladding," *J. Laser Appl.,* vol. 10, no. 1, pp. 29-33, Feb 1998.

[P6] D. Bartkowski, A. Młynarczak, A. Piasecki, B. Dudziak, M. Gościański, and A. Bartkowska, "Microstructure, microhardness and corrosion resistance of Stellite- 6 coatings reinforced with WC particles using laser cladding," *Optics and Laser Technology,* vol. 68, pp. 191-201, 2015, doi: 10.1016/j.optlastec.2014.12.005.

[P7] P. Beaty, B. Temple, M. B. Marshall, and R. Lewis, "Experimental modelling of lipping in insulated rail joints and investigation of rail head material improvements," *Proc. Inst. Mech. Eng. Part F-J. Rail Rapid Transit,* Article vol. 230, no. 4, pp. 1375-1387, May 2016, doi: 10.1177/0954409715600740.

[P8] P. Bendeich *et al.*, "Residual stress measurements in laser clad repaired low pressure turbine blades for the power industry," *Materials Science & Engineering A,* vol. 437, no. 1, pp. 70-74, 2006, doi: 10.1016/j.msea.2006.04.065.

[P9] F. Brückner, D. Lepski, and E. Beyer, "Modeling the Influence of Process Parameters and Additional Heat Sources on Residual Stresses in Laser Cladding," *J Therm Spray Tech,* vol. 16, no. 3, pp. 355-373, 2007, doi: 10.1007/s11666-007-9026-7.

[P10] A. Calleja, I. Tabernero, A. Fernández, A. Celaya, A. Lamikiz, and L. N. López de Lacalle, "Improvement of strategies and parameters for multi- axis laser cladding operations," *Optics and Lasers in Engineering,* vol. 56, pp. 113-120, 2014, doi: 10.1016/j.optlaseng.2013.12.017.

[P11] J. Chen, S.-H. Wang, and L. Xue, "On the development of microstructures and residual stresses during laser cladding and post- heat treatments," *J Mater Sci,* vol. 47, no. 2, pp. 779-792, 2012, doi: 10.1007/s10853-011-5854-4.

[P12] J. Y. Chen, K. Conlon, L. Xue, and R. Rogge, "Experimental study of residual stresses in laser clad AISI P20 tool steel on pre- hardened wrought P20 substrate," *Materials Science & Engineering A,* vol. 527, no. 27, pp. 7265-7273, 2010, doi: 10.1016/j.msea.2010.07.098.

[P13] Y. Chew, J. H. L. Pang, G. Bi, and B. Song, "Thermo- mechanical model for simulating laser cladding induced residual stresses with single and multiple clad beads," *Journal of Materials Processing Tech.,* vol. 224, pp. 89-101, 2015, doi: 10.1016/j.jmatprotec.2015.04.031.

[P14] G. Chryssolouris, S. Zannis, K. Tsirbas, and C. Lalas, "An experimental investigation of laser cladding," *Cirp Annals-Manufacturing Technology,* vol. 51, no. 1, pp. 145-148, 2002 2002, doi: 10.1016/s0007-8506(07)61486-3.

[P15] E. J. Chun, H. Baba, K. Nishimoto, and K. Saida, "Effect of sodium on repair weldability of SUS316FR for a fast breeder reactor," *Welding International,* pp. 1-12, 2015, doi: 10.1080/09507116.2014.921086.

[P16] R. Comesaña *et al.*, "Three- dimensional bioactive glass implants fabricated by rapid prototyping based on CO 2 laser cladding," *Acta Biomaterialia,* 2011, doi: 10.1016/j.actbio.2011.05.023.

[P17] R. Cottam *et al.*, "The role of microstructure in the stress relaxation and tempering of laser clad Ti– 6Al– 4V," *Materials Science & Engineering A,* vol. 601, pp. 65-69, 2014, doi: 10.1016/j.msea.2014.02.034.

[P18] J. L. de Mol van Otterloo and J. T. M. De Hosson, "Microstructure and abrasive wear of cobalt-based laser coatings," *Scripta Materialia,* vol. 36, no. 2, pp. 239-245, 1997, doi: 10.1016/S1359-6462(96)00346-6.

[P19] U. de Oliveira, V. Ocelík, and J. T. M. De Hosson, "Residual stress analysis in Co- based laser clad layers by laboratory X- rays and synchrotron diffraction techniques," *Surface & Coatings Technology,* vol. 201, no. 3, pp. 533-542, 2006, doi: 10.1016/j.surfcoat.2005.12.011.

[P20] E. Diaz, J. M. Amado, J. Montero, M. J. Tobar, and A. Yanez, "Comparative study of Co-based alloys in repairing low Cr-Mo steel components by laser cladding," *Laser Assisted Net Shape Engineering 7 (Lane 2012),* vol. 39, pp. 368-375, 2012 2012, doi: 10.1016/j.phpro.2012.10.050.

[P21] L. Dubourg and J. Archambeault, "Technological and scientific landscape of laser cladding process in 2007," *Surface & Coatings Technology,* vol. 202, no. 24, pp. 5863-5869, 2008, doi: 10.1016/j.surfcoat.2008.06.122.

[P22] M. Ellis, D. Xiao, W. M.Steen, K. G. Watkins, and W. P. Brown, "Processing aspects of laser cladding an aluminium alloy onto steel," *Journal of Materials Processing Tech.,* vol. 52, no. 1, pp. 55-67, 1995, doi: 10.1016/0924-0136(94)01443-5.

[P23] A. Emamian, M. Alimardani, and A. Khajepour, "Correlation between temperature distribution and in situ formed microstructure of Fe-TiC deposited on carbon steel using laser cladding," *Applied Surface Science,* vol. 258, no. 22, pp. 9025-9031, 2012, doi: 10.1016/j.apsusc.2012.05.143.

[P24] A. Emamian, S. F. Corbin, and A. Khajepour, "Effect of laser cladding process parameters on clad quality and in-situ formed microstructure of Fe-TiC composite coatings," *Surface & Coatings Technology,* vol. 205, no. 7, pp. 2007-2015, Dec 25 2010, doi: 10.1016/j.surfcoat.2010.08.087.

[P25] P. Farahmand and R. Kovacevic, "An experimental-numerical investigation of heat distribution and stress field in single- and multi-track laser cladding by a high-power direct diode laser," *Optics and Laser Technology,* vol. 63, pp. 154-168, Nov 2014, doi: 10.1016/j.optlastec.2014.04.016.

[P26] F. J. Franklin, G. J. Weeda, A. Kapoor, and E. J. M. Hiensch, "Rolling contact fatigue and wear behaviour of the infrastar two- material rail," *Wear,* vol. 258, no. 7, pp. 1048-1054, 2005, doi: 10.1016/j.wear.2004.03.054.

[P27] A. Frenk and W. Kurz, "High speed laser cladding: solidification conditions and microstructure of a cobalt- based alloy," *Materials Science & Engineering A,* vol. 173, no. 1, pp. 339-342, 1993, doi: 10.1016/0921-5093(93)90240-F.

[P28] A. Frenk and W. Kurz, "Microstructural effects on the sliding wear resistance of a cobalt-based alloy," *Wear,* vol. 174, no. 1, pp. 81-91, 1994, doi: 10.1016/0043-1648(94)90089-2.

[P29] F. Fu, Y. Zhang, G. Chang, and J. Dai, "Analysis on the physical mechanism of laser cladding crack and its influence factors," *Optik,* vol. 127, no. 1, pp. 200-202, 2016 2016, doi: 10.1016/j.ijleo.2015.10.043.

[P30] G. Fu, S. Liu, and J. Fan, "The design of cobalt- free, nickel- based alloy powder (Ni- 3) used for sealing surfaces of nuclear power valves and its structure of laser cladding coating," *Nuclear Engineering and Design,* vol. 241, no. 5, pp. 1403-1406, 2011, doi: 10.1016/j.nucengdes.2011.01.020.

[P31] Z. K. Fu, H. H. Ding, W. J. Wang, Q. Y. Liu, J. Guo, and M. H. Zhu, "Investigation on microstructure and wear characteristic of laser cladding Fe- based alloy on wheel/rail materials," *Wear,* vol. 330-331, pp. 592-599, 2015, doi: 10.1016/j.wear.2015.02.053.

[P32] B. Graf, A. Gumenyuk, and M. Rethmeier, "Laser Metal Deposition as Repair Technology for Stainless Steel and Titanium Alloys," *Physics Procedia,* vol. 39, pp. 376-381, 2012, doi: 10.1016/j.phpro.2012.10.051.

[P33] H.-M. Guo, Q. Wang, W.-J. Wang, J. Guo, Q.-Y. Liu, and M.-H. Zhu, "Investigation on wear and damage performance of laser cladding Co- based alloy on single wheel or rail material," *Wear,* vol. 328-329, pp. 329-337, 2015, doi: 10.1016/j.wear.2015.03.002.

[P34] Y. Guo *et al.*, "Microstructure evolution of Fe- based nanostructured bainite coating by laser cladding," *Materials and Design,* vol. 63, pp. 100-108, 2014, doi: 10.1016/j.matdes.2014.05.041.

[P35] M. Hans *et al.*, "Laser cladding of stainless steel with a copper– silver alloy to generate surfaces of high antimicrobial activity," *Applied Surface Science,* vol. 320, pp. 195-199, 2014, doi: 10.1016/j.apsusc.2014.09.069.

[P36] M. Hao and Y. Sun, "A FEM model for simulating temperature field in coaxial laser cladding of TI6AL4V alloy using an inverse modeling approach," *International Journal of Heat and Mass Transfer,* vol. 64, pp. 352-360, Sep 2013, doi: 10.1016/j.ijheatmasstransfer.2013.04.050.

[P37] I. Hemmati, V. Ocelík, and J. T. M. De Hosson, "The effect of cladding speed on phase constitution and properties of AISI 431 stainless steel laser deposited coatings," *Surface & Coatings Technology,* vol. 205, no. 21, pp. 5235-5239, 2011, doi: 10.1016/j.surfcoat.2011.05.035.

[P38] I. Hemmati, V. Ocelík, and J. T. M. De Hosson, "Dilution effects in laser cladding of Ni– Cr– B– Si– C hardfacing alloys," *Materials Letters,* vol. 84, pp. 69-72, 2012, doi: 10.1016/j.matlet.2012.06.054.

[P39] E. J. M. Hiensch *et al.*, "Prevention of RCF damage in curved track through development of the INFRA-STAR two- material rail," *Fatigue & Fracture of Engineering Materials & Structures,* vol. 26, no. 10, pp. 1007-1017, 2003, doi: 10.1046/j.1460-2695.2003.00663.x.

[P40] M. Hiensch *et al.*, "Two- material rail development: field test results regarding rolling contact fatigue and squeal noise behaviour," *Wear,* vol. 258, no. 7, pp. 964-972, 2005, doi: 10.1016/j.wear.2004.03.067.

[P41] J. T. Hofman, D. F. de Lange, B. Pathiraj, and J. Meijer, "FEM modeling and experimental verification for dilution control in laser cladding," *Journal of Materials Processing Tech.,* vol. 211, no. 2, pp. 187-196, 2011, doi: 10.1016/j.jmatprotec.2010.09.007.

[P42] J. T. Hofman, B. Pathiraj, J. van Dijk, D. E. de Lange, and J. Meijer, "A camera based feedback control strategy for the laser cladding process," *J. Mater. Process. Technol.,* vol. 212, no. 11, pp. 2455-2462, Nov 2012, doi: 10.1016/j.jmatprotec.2012.06.027.

[P43] Y. Huang, "Characterization of dilution action in laser-induction hybrid cladding," *Optics and Laser Technology,* vol. 43, no. 5, pp. 965-973, Jul 2011, doi: 10.1016/j.optlastec.2010.12.005.

[P44] N. Hutasoit, W. Yan, R. Cottam, M. Brandt, and A. Blicblau, "Evaluation of Microstructure and Mechanical Properties at the Interface Region of Laser- Clad Stellite 6 on Steel Using Nanoindentation," *Metallogr. Microstruct. Anal.,* vol. 2, no. 5, pp. 328-336, 2013, doi: 10.1007/s13632-013-0093-5.

[P45] M.-C. Jeng, L.-Y. Yan, and J.-L. Doong, "Wear behaviour of cobalt- based alloys in laser surface cladding," *Surface & Coatings Technology,* vol. 48, no. 3, pp. 225-231, 1991, doi: 10.1016/0257-8972(91)90008-K.

[P46] Z. J. Jing, H. Zhou, P. Zhang, C. W. Wang, C. Meng, and D. L. Cong, "Effect of thermal fatigue on the wear resistance of graphite cast iron with bionic units processed by laser cladding WC," *Applied Surface Science,* vol. 271, pp. 329-336, Apr 2013, doi: 10.1016/j.apsusc.2013.01.193.

[P47] S. Kaierle, A. Barroi, C. Noelke, J. Hermsdorf, L. Overmeyer, and H. Haferkamp, "Review on Laser Deposition Welding: From Micro to Macro," *Physics Procedia,* vol. 39, pp. 336-345, 2012, doi: 10.1016/j.phpro.2012.10.046.

[P48] Y. P. Kathuria, "Some aspects of laser surface cladding in the turbine industry," *Surface & Coatings Technology,* vol. 132, no. 2, pp. 262-269, 2000, doi: 10.1016/S0257-8972(00)00735-0.

[P49] P. Kattire, S. Paul, R. Singh, and W. Yan, "Experimental characterization of laser cladding of CPM 9V on H13 tool steel for die repair applications," *Journal of Manufacturing Processes,* vol. 20, pp. 492-499, 2015, doi: 10.1016/j.jmapro.2015.06.018.

[P50] F. Klocke, C. Brecher, M. Wegener, D. Heinen, B. Fischer, and D. Do-Khac, "Scanner- based Laser Cladding," *Physics Procedia,* vol. 39, pp. 346-353, 2012, doi: 10.1016/j.phpro.2012.10.047.

[P51] H. Köhler, K. Partes, J. R. Kornmeier, and F. Vollertsen, "Residual Stresses in Steel Specimens Induced by Laser Cladding and their Effect on Fatigue Strength," *Physics Procedia,* vol. 39, pp. 354-361, 2012, doi: 10.1016/j.phpro.2012.10.048.

[P52] H. Köhler, R. Rajput, P. Khazan, and J. R. Kornmeier, "On the Influence of Laser Cladding and Post- processing Strategies on Residual Stresses in Steel Specimens," *Physics Procedia,* vol. 56, pp. 250-261, 2014, doi: 10.1016/j.phpro.2014.08.169.

[P53] A. Kusmoko, D. Dunne, and H. Li, "Effect of Heat Input on Stellite 6 Coatings on a Medium Carbon Steel Substrate by Laser Cladding," *Materials Today-Proceedings,* vol. 2, no. 4-5, pp. 1747-1754, 2015 2015, doi: 10.1016/j.matpr.2015.07.010.

[P54] A. Kusmoko, D. Dunne, H. Li, and D. Nolan, "Effect of Two Different Energy Inputs for Laser Cladding of Stellite 6 on P91 and P22 Steel Substrates," *Procedia Materials Science,* vol. 6, pp. 26-36, 2014, doi: 10.1016/j.mspro.2014.07.005.

[P55] J. Leunda, V. Garcia Navas, C. Soriano, and C. Sanz, "Effect of laser tempering of high alloy powder metallurgical tool steels after laser cladding," *Surface & Coatings Technology,* vol. 259, pp. 570-576, Nov 25 2014, doi: 10.1016/j.surfcoat.2014.10.028.

[P56] S. R. Lewis, R. Lewis, and D. I. Fletcher, "Assessment of laser cladding as an option for repairing/ enhancing rails," *Wear,* vol. 330-331, pp. 581-591, 2015, doi: 10.1016/j.wear.2015.02.027.

[P57] K. Li, D. Li, D. Liu, G. Pei, and L. Sun, "Microstructure evolution and mechanical properties of multiple- layer laser cladding coating of 308L stainless steel," *Applied Surface Science,* vol. 340, pp. 143-150, 2015, doi: 10.1016/j.apsusc.2015.02.171.

[P58] M. Li, J. Huang, Y. Y. Zhu, and Z. G. Li, "Effect of heat input on the microstructure of in-situ synthesized TiN-TiB/Ti based composite coating by laser cladding," *Surface & Coatings Technology,* vol. 206, no. 19-20, pp. 4021-4026, May 25 2012, doi: 10.1016/j.surfcoat.2012.03.082.

[P59] C.M. Lin, "Parameter optimization of laser cladding process and resulting microstructure for the repair of tenon on steam turbine blade," *Vacuum,* vol. 115, pp. 117-123, 2015, doi: 10.1016/j.vacuum.2015.02.021.

[P60] Y. Lin, Y. Lei, H. Fu, and J. Lin, "Mechanical properties and toughening mechanism of TiB2/ NiTi reinforced titanium matrix composite coating by laser cladding," *Materials and Design,* vol. 80, pp. 82-88, 2015, doi: 10.1016/j.matdes.2015.05.009.

[P61] B. Liu and S. Dong, "Stress evaluation of laser cladding coating with critically refracted longitudinal wave based on cross correlation function," *Applied Acoustics,* vol. 101, pp. 98-103, 2016, doi: 10.1016/j.apacoust.2015.08.015.

[P62] H. Liu, C. Wang, X. Zhang, Y. Jiang, C. Cai, and S. Tang, "Improving the corrosion resistance and mechanical property of 45 steel surface by laser cladding with Ni60CuMoW alloy powder," *Surface & Coatings Technology,* vol. 228, pp. S296-S300, 2013, doi: 10.1016/j.surfcoat.2012.05.115.

[P63] X.-L. Lu *et al.*, "Effects of heat treatment on microstructure and mechanical properties of Ni60/h- BN self- lubricating anti- wear composite coatings on 304 stainless steel by laser cladding," *Applied Surface Science,* vol. 355, pp. 350-358, 2015, doi: 10.1016/j.apsusc.2015.07.138.

[P64] F. Luo *et al.*, "Performance comparison of Stellite 6® deposited on steel using supersonic laser deposition and laser cladding," *Surface & Coatings Technology,* vol. 212, pp. 119-127, 2012, doi: 10.1016/j.surfcoat.2012.09.031.

[P65] F. Luo, J.-h. Yao, X.-x. Hu, and G.-z. Chai, "Effect of Laser Power on the Cladding Temperature Field and the Heat Affected Zone," *Journal of Iron and Steel Research International,* vol. 18, no. 1, pp. 73-78, Jan 2011, doi: 10.1016/s1006-706x(11)60014-9.

[P66] N. K. Mandal, "Ratchetting of railhead material of insulated rail joints (IRJs) with reference to endpost thickness," *Engineering Failure Analysis,* vol. 45, pp. 347-362, 2014, doi: 10.1016/j.engfailanal.2014.07.003.

[P67] F. Meriaudeau, F. Truchetete, C. Dumont, E. Renier, and P. Bolland, "Acquisition and image processing system able to optimize laser cladding process," vol. 2, ed, 1996, pp. 1628-1631.

[P68] F. K. Mirzade *et al.*, "Kinetic approach in numerical modeling of melting and crystallization at laser cladding with powder injection," *Physica B: Physics of Condensed Matter,* vol. 423, pp. 69-76, 2013, doi: 10.1016/j.physb.2013.04.053.

[P69] B. N. R. Munjuluri, S. Agarwal, and F. W. Liou, "Process modeling, monitoring and control of laser metal forming," 2001.

[P70] S. Niederhauser and B. Karlsson, "Mechanical properties of laser cladded steel," *Materials Science and Technology,* vol. 19, no. 11, pp. 1611-1616, Nov 2003, doi: 10.1179/026708303225008103.

[P71] S. Niederhauser and B. Karlsson, "Fatigue behaviour of Co–Cr laser cladded steel plates for railway applications," *Wear,* vol. 258, no. 7, pp. 1156-1164, 2005, doi: 10.1016/j.wear.2004.03.026.

[P72] V. Ocelik, M. Eekma, I. Hemmati, and J. T. M. De Hosson, "Elimination of Start/Stop defects in laser cladding," *Surface & Coatings Technology,* vol. 206, no. 8-9, pp. 2403-2409, Jan 2012, doi: 10.1016/j.surfcoat.2011.10.040.

[P73] A. S. Oliveira, P. S. Da Silva, and R. M. Vilar, "Microstructural features of consecutive layers of Stellite 6 deposited by laser cladding," *Surface & Coatings Technology,* vol. 153, no. 2, pp. 203-209, 2002, doi: 10.1016/S0257-8972(01)01687-5.

[P74] L. Pawlowski, "Thick laser coatings: A review," *J Therm Spray Tech,* vol. 8, no. 2, pp. 279-295, 1999, doi: 10.1361/105996399770350502.

[P75] H. Paydas, A. Mertens, R. Carrus, J. Lecomte-Beckers, and J. Tchoufang Tchuindjang, "Laser cladding as repair technology for Ti– 6Al– 4V alloy: Influence of building strategy on microstructure and hardness," *Materials & Design,* vol. 85, pp. 497-510, 2015, doi: 10.1016/j.matdes.2015.07.035.

[P76] J. Pereira, J. Zambrano, M. Licausi, M. Tobar, and V. Amigó, "Tribology and high temperature friction wear behavior of MCrAlY laser cladding coatings on stainless steel," *Wear,* vol. 330-331, pp. 280-287, 2015, doi: 10.1016/j.wear.2015.01.048.

[P77] M. Pleterski, T. Muhic, B. Podgornik, and J. Tusek, "Blanking punch life improvement by laser cladding," *Engineering Failure Analysis,* vol. 18, no. 6, pp. 1527-1537, Sep 2011, doi: 10.1016/j.engfailanal.2011.05.010.

[P78] H. Qi, J. Mazumder, and H. Ki, "Numerical simulation of heat transfer and fluid flow in coaxial laser cladding process for direct metal deposition," *J. Appl. Phys.,* vol. 100, no. 2, 2006, doi: 10.1063/1.2209807.

[P79] M. Qian, L. C. Lim, Z. D. Chen, and W. I. Chen, "Parametric studies of laser cladding processes," *Journal of Materials Processing Tech.,* vol. 63, no. 1, pp. 590-593, 1997, doi: 10.1016/S0924-0136(96)02689-1.

[P80] R. Qin, X. Zhang, S. Guo, B. Sun, S. Tang, and W. Li, "Laser cladding of high Co– Ni secondary hardening steel on 18Cr2Ni4WA steel," *Surface & Coatings Technology,* vol. 285, pp. 242-248, 2016, doi: 10.1016/j.surfcoat.2015.11.032.

[P81] C. Rathod, D. Wexler, T. Chandra, and H. Li, "Microstructural characterisation of railhead damage in insulated rail joints," *Thermec 2011, Pts 1-4,* vol. 706-709, pp. 2937-2942, 2012, doi: 10.4028/www.scientific.net/MSF.706-709.2937.

[P82] J. W. Ringsberg, F. J. Franklin, B. L. Josefson, A. Kapoor, and J. C. O. Nielsen, "Fatigue evaluation of surface coated railway rails using shakedown theory, finite element calculations, and lab and field trials," *International Journal of Fatigue,* vol. 27, no. 6, pp. 680-694, 2005, doi: 10.1016/j.ijfatigue.2004.11.002.

[P83] J. W. Ringsberg, A. Skyttebol, and B. L. Josefson, "Investigation of the rolling contact fatigue resistance of laser cladded twin- disc specimens: FE simulation of laser cladding, grinding and a twin- disc test," *International Journal of Fatigue,* vol. 27, no. 6, pp. 702-714, 2005, doi: 10.1016/j.ijfatigue.2004.10.006.

[P84] A. Riveiro *et al.*, "Optimization of Laser Cladding for Al Coating Production," *Physics Procedia,* vol. 41, pp. 327-334, 2013, doi: 10.1016/j.phpro.2013.03.085.

[P85] B. Rottwinkel, C. Noelke, S. Kaierle, and V. Wesling, "Crack repair of single crystal turbine blades using laser cladding technology," *Proceedings of the 3rd International Conference in through-Life Engineering Services,* vol. 22, pp. 263-267, 2014 2014, doi: 10.1016/j.procir.2014.06.151.

[P86] J. W. Sears, "Direct laser powder deposition - State of the Art," *ASTM/TMS Materials Week, Cincinnati,* 1999.

[P87] C. L. Sexton, G. Byrne, and K. G. Watkins, "Alloy development by laser cladding: An overview," *J. Laser Appl.,* Article vol. 13, no. 1, pp. 2-11, Feb 2001.

[P88] S. Shang *et al.*, "Laser beam profile modulation for microstructure control in laser cladding of an NiCrBSi alloy," *Surface & Coatings Technology,* vol. 248, pp. 46-53, 2014, doi: 10.1016/j.surfcoat.2014.03.018.

[P89] R. Singh, D. Kumar, S. K. Mishra, and S. K. Tiwari, "Laser cladding of Stellite 6 on stainless steel to enhance solid particle erosion and cavitation resistance," *Surface & Coatings Technology,* 2014, doi: 10.1016/j.surfcoat.2014.04.008.

[P90] I. Smolina, P. Szymczyk, E. Chlebus, I. Ivashchenko, and T. Kurzynowski, "Composite Laser-Clad Coating on Titanium Substrate Using Pure Hydroxyapatite Powder," *Powder Metallurgy and Metal Ceramics,* vol. 54, no. 5-6, pp. 318-323, 2015, doi: 10.1007/s11106-015-9716-5.

[P91] I. Smurov, M. Doubenskaia, and A. Zaitsev, "Complex Analysis of Laser Cladding based on Comprehensive Optical Diagnostics and Numerical Simulation," *Physics Procedia,* vol. 39, pp. 743-752, 2012, doi: 10.1016/j.phpro.2012.10.096.

[P92] I. Smurov, M. Doubenskaia, and A. Zaitsev, "Comprehensive analysis of laser cladding by means of optical diagnostics and numerical simulation," *Surface & Coatings Technology,* vol. 220, pp. 112-121, Apr 15 2013, doi: 10.1016/j.surfcoat.2012.10.053.

[P93] A. Suárez, J. M. Amado, M. J. Tobar, A. Yáñez, E. Fraga, and M. J. Peel, "Study of residual stresses generated inside laser cladded plates using FEM and diffraction of synchrotron radiation," *Surface & Coatings Technology,* vol. 204, no. 12, pp. 1983-1988, 2010, doi: 10.1016/j.surfcoat.2009.11.037.

[P94] N. Sun *et al.*, "Friction and wear behaviors of compacted graphite iron with different biomimetic units fabricated by laser cladding," *Applied Surface Science,* vol. 258, no. 19, pp. 7699-7706, 2012, doi: 10.1016/j.apsusc.2012.04.125.

[P95] Y. Sun and M. Hao, "Statistical analysis and optimization of process parameters in Ti6Al4V laser cladding using Nd:YAG laser," *Optics and Lasers in Engineering,* vol. 50, no. 7, pp. 985-995, 2012, doi: 10.1016/j.optlaseng.2012.01.018.

[P96] I. Tabernero, A. Lamikiz, S. Martínez, E. Ukar, and L. N. L. D. Lacalle, "Geometric Modelling of Added Layers by Coaxial Laser Cladding," *Physics Procedia,* vol. 39, pp. 913-920, 2012, doi: 10.1016/j.phpro.2012.10.116.

[P97] G. Telasang, J. D. Majumdar, G. Padmanabham, M. Tak, and I. Manna, "Effect of laser parameters on microstructure and hardness of laser clad and tempered AISI H13 tool steel," *Surface & Coatings Technology,* vol. 258, pp. 1108-1118, Nov 15 2014, doi: 10.1016/j.surfcoat.2014.07.023.

[P98] A. Tiziani, L. Giordano, P. Matteazzi, and B. Badan, "Laser stellite coatings on austenitic stainless steels," *Materials Science and Engineering,* vol. 88, pp. 171-175, 1987, doi: 10.1016/0025-5416(87)90082-6.

[P99] M. J. Tobar, J. M. Amado, A. Yáñez, J. C. Pereira, and V. Amigó, "Laser Cladding of MCrAlY Coatings on Stainless Steel," *Physics Procedia,* vol. 56, pp. 276-283, 2014, doi: 10.1016/j.phpro.2014.08.172.

[P100] T. Torims, G. Pikurs, A. Ratkus, A. Logins, J. Vilcans, and S. Sklariks, "Development of Technological Equipment to Laboratory Test In-Situ Laser Cladding for Marine Engine Crankshaft Renovation," *25th Daaam International Symposium on Intelligent Manufacturing and Automation, 2014,* vol. 100, pp. 559-568, 2015, doi: 10.1016/j.proeng.2015.01.405.

[P101] E. Toyserkani, A. Khajepour, and S. Corbin, "Application of experimental-based modeling to laser cladding," *J. Laser Appl.,* vol. 14, no. 3, pp. 165-173, Aug 2002, doi: 10.2351/1.1494079.

[P102] E. Toyserkani, A. Khajepour, and S. Corbin, "3-D finite element modeling of laser cladding by powder injection: effects of laser pulse shaping on the process," *Optics and Lasers in Engineering,* vol. 41, no. 6, pp. 849-867, Jun 2004, doi: 10.1016/s0143-8166(03)00063-0.

[P103] W. C. Tseng and J. N. Aoh, "Simulation study on laser cladding on preplaced powder layer with a tailored laser heat source," *Optics and Laser Technology,* vol. 48, pp. 141-152, 2013, doi: 10.1016/j.optlastec.2012.09.014.

[P104] B. Valsecchi, B. Previtali, E. Gariboldi, and A. Liu, "Characterisation of the Thermal Damage in a Martensitic Steel Substrate Consequent to Laser Cladding Process," *11th International Conference on the Mechanical Behavior of Materials (Icm11),* vol. 10, 2011 2011, doi: 10.1016/j.proeng.2011.04.474.

[P105] R. Vilar, "Laser cladding," *J. Laser Appl.,* vol. 11, no. 2, pp. 64-79, 1999, doi: 10.2351/1.521888.

[P106] D. Wang, Q. Hu, Y. Zheng, Y. Xie, and X. Zeng, "Study on deposition rate and laser energy efficiency of Laser- Induction Hybrid Cladding," *Optics and Laser Technology,* vol. 77, pp. 16-22, 2016, doi: 10.1016/j.optlastec.2015.08.019.

[P107] F. Wang, H. Mao, D. Zhang, and X. Zhao, "The crack control during laser cladding by adding the stainless steel net in the coating," *Applied Surface Science,* vol. 255, no. 21, pp. 8846-8854, 2009, doi: 10.1016/j.apsusc.2009.06.066.

[P108] F. Wang, H. Mao, D. Zhang, X. Zhao, and Y. Shen, "Online study of cracks during laser cladding process based on acoustic emission technique and finite element analysis," *Applied Surface Science,* vol. 255, no. 5, pp. 3267-3275, 2008, doi: 10.1016/j.apsusc.2008.09.039.

[P109] L. Wang, J. Zhou, Y. Yu, C. Guo, and J. Chen, "Effect of powders refinement on the tribological behavior of Ni-based composite coatings by laser cladding," *Applied Surface Science,* vol. 258, no. 17, pp. 6697-6704, Jun 15 2012, doi: 10.1016/j.apsusc.2012.03.141.

[P110] P.-Z. Wang, Y.-S. Yang, G. Ding, J.-X. Qu, and H.-S. Shao, "Laser cladding coating against erosion- corrosion wear and its application to mining machine parts," *Wear,* vol. 209, no. 1, pp. 96-100, 1997, doi: 10.1016/S0043-1648(97)00018-5.

[P111] W. J. Wang, Z. K. Fu, X. Cao, J. Guo, Q. Y. Liu, and M. H. Zhu, "The role of lanthanum oxide on wear and contact fatigue damage resistance of laser cladding Fe- based alloy coating under oil lubrication condition," *Tribology International,* vol. 94, pp. 470-478, 2016, doi: 10.1016/j.triboint.2015.10.017.

[P112] W. J. Wang, J. Hu, J. Guo, Q. Y. Liu, and M. H. Zhu, "Effect of laser cladding on wear and damage behaviors of heavy- haul wheel/ rail materials," *Wear,* vol. 311, no. 1-2, pp. 130-136, 2014, doi: 10.1016/j.wear.2014.01.011.

[P113] P. Wen, Z. Cai, Z. Feng, and G. Wang, "Microstructure and mechanical properties of hot wire laser clad layers for repairing precipitation hardening martensitic stainless steel," *Optics and Laser Technology,* vol. 75, pp. 207-213, 2015, doi: 10.1016/j.optlastec.2015.07.014.

[P114] F. Weng, C. Chen, and H. Yu, "Research status of laser cladding on titanium and its alloys: A review," *Materials & Design,* vol. 58, pp. 412-425, Jun 2014, doi: 10.1016/j.matdes.2014.01.077.

[P115] Q. Wu, W. Li, N. Zhong, W. Gang, and W. Haishan, "Microstructure and wear behavior of laser cladding VC– Cr7C3 ceramic coating on steel substrate," *Materials and Design,* vol. 49, pp. 10-18, 2013, doi: 10.1016/j.matdes.2013.01.067.

[P116] Z. Xiong, G. X. Chen, and X. Y. Zeng, "Effects of process variables on interfacial quality of laser cladding on aeroengine blade material GH4133," *J. Mater. Process. Technol.,* vol. 209, no. 2, pp. 930-936, Jan 2009, doi: 10.1016/j.jmatprotec.2008.03.004.

[P117] M. Xu, J. Li, J. Jiang, and B. Li, "Influence of Powders and Process Parameters on Bonding Shear Strength and Micro Hardness in Laser Cladding Remanufacturing," *Procedia CIRP,* vol. 29, pp. 804-809, 2015, doi: 10.1016/j.procir.2015.02.088.

[P118] Z. Xu, K. H. Leong, P. G. Sanders, and D. Technology, "Laser surface alloying of silicon into aluminum casting alloys," *J. Laser Appl.,* vol. 12, no. 4, 2000, doi: 10.2351/1.521928.

[P119] W. Ya, B. Pathiraj, and S. J. Liu, "2D modelling of clad geometry and resulting thermal cycles during laser cladding," *J. Mater. Process. Technol.,* vol. 230, pp. 217-232, Apr 2016, doi: 10.1016/j.jmatprotec.2015.11.012.

[P120] M. Zeinali and A. Khajepour, "Development of an adaptive fuzzy logic-based inverse dynamic model for laser cladding process," *Engineering Applications of Artificial Intelligence,* vol. 23, no. 8, pp. 1408-1419, Dec 2010, doi: 10.1016/j.engappai.2009.11.006.

[P121] C. Zeng, W. Tian, W.-H. Liao, and L. Hua, "Study of laser cladding thermal damage: A quantified microhardness method," *Surface & Coatings Technology,* vol. 236, pp. 309-314, 2013, doi: 10.1016/j.surfcoat.2013.10.005.

[P122] J. Zhang, Y. Hu, X.-J. Tan, L. Guo, and Q.-M. Zhang, "Microstructure and high temperature tribological behavior of laser cladding Ni60A alloys coatings on 45 steel substrate," *Transactions of Nonferrous Metals Society of China,* vol. 25, no. 5, pp. 1525-1532, 2015, doi: 10.1016/S1003-6326(15)63754-2.

[P123] M. Zhong, C. Mayer, and A. Becker, "Microstructural evolution in high power laser cladding of Stellite 6+ WC layers," *Surface & Coatings Technology,* vol. 157, no. 2, pp. 128-137, 2002, doi: 10.1016/S0257-8972(02)00165-2.

[P124] C. Zhou, S. Zhao, Y. Wang, F. Liu, W. Gao, and X. Lin, "Mitigation of pores generation at overlapping zone during laser cladding," *Journal of Materials Processing Tech.,* vol. 216, pp. 369-374, 2015, doi: 10.1016/j.jmatprotec.2014.09.025.

Papers between 2015-2019, with reference to load bearing applications in railways and steel industry:

[P125] O. Adesina, A. Popoola, S. Pityana, and D. Oloruntoba, "Microstructural and tribological behavior of in situ synthesized Ti/ Co coatings on Ti- 6Al- 4V alloy using laser surface cladding technique," *The International Journal of Advanced Manufacturing Technology,* vol. 95, no. 1, pp. 1265-1280, 2018, doi: 10.1007/s00170-017-1300-3.

[P126] R. Awasthi *et al.*, "Wear Characteristics of Ni- Based Hardfacing Alloy Deposited on Stainless Steel Substrate by Laser Cladding," *Metallurgical and Mat. Transactions A,* vol. 46, no. 3, pp. 1237-1252, 2015, doi: 10.1007/s11661-014-2719-x.

[P127] D. Bartkowski and A. Bartkowska, "Wear resistance in the soil of Stellite- 6/ WC coatings produced using laser cladding method," *International Journal of Refractory Metals & Hard Materials,* vol. 64, p. 20, 2017.

[P128] V. Biryukov, E. Khriptovich, and A. Fishkov, "Determination of influence of laser welding modes and powder material composition on wear resistance of coatings," *Journal of Machinery Manufacture and Reliability,* vol. 46, no. 1, pp. 53-56, 2017, doi: 10.3103/S1052618817010034.

[P129] Y. Cai, Z. Luo, M. Feng, Z. Liu, Z. Huang, and Y. Zeng, "The effect of TiC/ Al2O3 composite ceramic reinforcement on tribological behavior of laser cladding Ni60 alloys coatings," *Surface & Coatings Technology,* vol. 291, pp. 222-229, 2016, doi: 10.1016/j.surfcoat.2016.02.033.

[P130] Z. Cai, X. Cui, Z. Liu, Y. Li, M. Dong, and G. Jin, "Microstructure and wear resistance of laser cladded Ni- Cr- Co- Ti- V high- entropy alloy coating after laser remelting processing," *Optics and Laser Technology,* vol. 99, pp. 276-281, 2018, doi: 10.1016/j.optlastec.2017.09.012.

[P131] T. Chen, D. Liu, F. Wu, and H. Wang, "Effect of CeO 2 on microstructure and wear resistance of TiC bioinert coatings on Ti6Al4V alloy by laser cladding," *Materials,* vol. 11, no. 1, 2017, doi: 10.3390/ma11010058.

[P132] W. Chen, H. Chen, C. Li, X. Wang, and Q. Cai, "Microstructure and fatigue crack growth of EA4T steel in laser cladding remanufacturing," *Engineering Failure Analysis,* vol. 79, pp. 120-129, 2017, doi: 10.1016/j.engfailanal.2017.03.005.

[P133] P. Deng *et al.*, "Enhanced wear resistance of laser cladded graphene nanoplatelets reinforced Inconel 625 superalloy composite coating," *Surface & Coatings Technology,* vol. 335, pp. 334-344, 2018, doi: 10.1016/j.surfcoat.2017.12.047.

[P134] D. Deschuyteneer, F. Petit, M. Gonon, and F. Cambier, "Processing and characterization of laser clad NiCrBSi/ WC composite coatings — Influence of microstructure on hardness and wear," *Surface & Coatings Technology,* vol. 283, pp. 162-171, 2015, doi: 10.1016/j.surfcoat.2015.10.055.

[P135] L. Ding, S. Hu, X. Quan, and J. Shen, "Effect of Mo and nano-Nd 2 O 3 on the microstructure and wear resistance of laser cladding Ni- based alloy coatings," *Materials Science & Processing,* vol. 122, no. 4, pp. 1-7, 2016, doi: 10.1007/s00339-016-9905-1.

[P136] L. Ding, S. Hu, X. Quan, and J. Shen, "Effect of Ti on the microstructure evolution and wear behavior of VN alloy/ Co- based composite coatings by laser cladding," *Journal of Materials Processing Tech.,* vol. 252, pp. 711-719, 2018, doi: 10.1016/j.jmatprotec.2017.10.042.

[P137] Y. Ding, R. Liu, J. Yao, Q. Zhang, and L. Wang, "Stellite alloy mixture hardfacing via laser cladding for control valve seat sealing surfaces," *Surface & Coatings Technology,* vol. 329, p. 97, 2017.

[P138] X. Duan *et al.*, "Reinforcement mechanism and wear resistance of Al2O3/ Fe- Cr- Mo steel composite coating produced by laser cladding," *Surface & Coatings Technology,* vol. 291, pp. 230-238, 2016, doi: 10.1016/j.surfcoat.2016.02.045.

[P139] H. El-Labban, E. Mahmoud, and A. Algahtani, "Microstructure, Wear, and Corrosion Characteristics of TiC- Laser Surface Cladding on Low- Carbon Steel," *Metallurgical and Materials Transactions B,* vol. 47, no. 2, pp. 974-982, 2016, doi:10.1007/s11663-016-0602-4.

[P140] L. Fang, H. Yan, Y. Yao, P. Zhang, Q. Gao, and Y. Qin, "Reactive Fabrication and Effect of NbC on Microstructure and Tribological Properties of CrS Co- Based Self- Lubricating Coatings by Laser Cladding," *Materials (Basel, Switzerland),* vol. 11, no. 1, 2017, doi: 10.3390/ma11010044.

[P141] P. Farahmand and R. Kovacevic, "Corrosion and wear behavior of laser cladded Ni– WC coatings," *Surface & Coatings Technology,* vol. 276, pp. 121-135, 2015, doi: 10.1016/j.surfcoat.2015.06.039.

[P142] K. Feng *et al.*, "Improved high- temperature hardness and wear resistance of Inconel 625 coatings fabricated by laser cladding," *Journal of Materials Processing Tech.,* vol. 243, pp. 82-91, 2017, doi: 10.1016/j.jmatprotec.2016.12.001.

[P143] N. Hashemi *et al.*, "Oxidative wear behaviour of laser clad High Speed Steel thick deposits: Influence of sliding speed, carbide type and morphology," *Surface & Coatings Technology,* vol. 315, pp. 519-529, 2017, doi: 10.1016/j.surfcoat.2017.02.071.

[P144] H. He, T. Zhang, M. Ma, and W. Liu, "Microstructure and wear resistance of laser cladding particulate reinforced Fe- based composite coating on railway steel," *J. Laser Appl.,* vol. 29, no. 2, 2017, doi: 10.2351/1.4983232.

[P145] C. Huang *et al.*, "Microstructure and dry sliding wear behavior of laser clad AlCrNiSiTi multi-principal element alloy coatings," *Rare Metals,* vol. 36, no. 7, pp. 562-568, 2017, doi: 10.1007/s12598-017-0912-y.

[P146] X. Ji, H. Duan, H. Zhang, and J. Ma, "Slurry erosion resistance of laser clad NiCoCrFeAl 3 high entropy alloy coatings," *Tribology Transactions,* vol. 58, no. 6, pp. 00-00, 2015, doi: 10.1080/10402004.2015.1044148.

[P147] L. Jiahong and K. Dejun, "Micro- Structures and High- Temperature Friction- Wear Performances of Laser Cladded Cr- Ni Coatings," *Materials (Basel, Switzerland),* vol. 11, no. 1, 2018, doi: 10.3390/ma11010137.

[P148] J. Jiang, Y. Zhou, M. Kang, and J. Wang, "Optimization of Process Parameters, Microstructure, and Properties of Laser Cladding Fe- Based Alloy on 42CrMo Steel Roller," *Materials,* vol. 11, no. 10, 2018, doi: 10.3390/ma11102061.

[P149] X. Jiao, J. Wang, C. Wang, Z. Gong, X. Pang, and S. M. Xiong, "Effect of laser scanning speed on microstructure and wear properties of T15M cladding coating fabricated by laser cladding technology," *Optics and Lasers in Engineering,* vol. 110, pp. 163-171, 2018, doi: 10.1016/j.optlaseng.2018.05.024.

[P150] Q. Lai *et al.*, "Effects of preheating and carbon dilution on material characteristics of laser-cladded hypereutectoid rail steels," *Materials Science & Engineering A,* vol. 712, pp. 548-563, 2018, doi: 10.1016/j.msea.2017.12.003.

[P151] Q. Lai *et al.*, "Investigation of a novel functionally graded material for the repair of premium hypereutectoid rails using laser cladding technology," *Composites Part B,* vol. 130, pp. 174-191, 2017, doi: 10.1016/j.compositesb.2017.07.089.

[P152] Q. Lai *et al.*, "Influences of depositing materials, processing parameters and heating conditions on material characteristics of laser-cladded hypereutectoid rails," *Journal of Materials Processing Tech.,* vol. 263, pp. 1-20, 2019, doi: 10.1016/j.jmatprotec.2018.07.035.

[P153] X. Lan *et al.*, "Microstructures and tribological properties of laser cladded Ti- based metallic glass composite coatings," *Materials Characterization,* vol. 120, pp. 82-89, 2016, doi: 10.1016/j.matchar.2016.08.026.

[P154] Q. Li, H. Qiao, H. Fu, and Y. Lei, "Microstructure and wear resistance of laser cladding Fe-based coatings reinforced by in situ synthesized TiB2+TiC," Optoelectronics and advanced materials-rapid communications, vol. 9, no. 11-12, pp. 1544-1548, 2015.

[P155] D.-y. Lin, N.-n. Zhang, B. He, G.-w. Zhang, Y. Zhang, and D.-y. Li, "Tribological properties of FeCoCrNiAlB x high- entropy alloys coating prepared by laser cladding," *Journal of Iron and Steel Research International,* vol. 24, no. 2, pp. 184-189, 2017, doi: 10.1016/S1006-706X(17)30026-2.

[P156] H. Liu, Q. Xu, C. Wang, and X. Zhang, "Corrosion and wear behavior of Ni60CuMoW coatings fabricated by combination of laser cladding and mechanical vibration processing," *Journal of Alloys and Compounds,* vol. 621, pp. 357-363, 2015, doi: 10.1016/j.jallcom.2014.10.030.

[P157] D. Lu, S. Liu, X. Zhang, and W. Zhang, "Effect of Y2O3 on microstructural characteristics and wear resistance of cobalt- based composite coatings produced on TA15 titanium alloy surface by laser cladding," *Surface and Interface Analysis,* vol. 47, no. 2, pp. 239-244, 2015, doi: 10.1002/sia.5697.

[P158] S. Lu, X. Wei, J. Zhao, and X. Ling, "Wear resistance of nickel- based alloy coating formed by multilayer laser cladding," *Materials Research Express,* vol. 5, no. 12, p. 126508, 2018, doi: 10.1088/2053-1591/aae01b.

[P159] S. X. Luo, S. S. Liu, X. H. Wang, and M. Zhang, "Effect of Molybdenum on the Wear Properties of (Ti,Mo)C-TiB 2 -Mo 2 B Particles Reinforced Fe-Based Laser Cladding Composite Coatings," *Journal of tribology.,* vol. 140, no. 5, p. 051603, 2018, doi: 10.1115/1.4039411

[P160] A. Makarov, N. Soboleva, and I. Malygina, "Role of the strengthening phases in abrasive wear resistance of laser- clad NiCrBSi coatings," *Journal of Friction and Wear,* vol. 38, no. 4, pp. 272-278, 2017, doi: 10.3103/S1068366617040080.

[P161] L. Meng *et al.*, "A comparison of microstructure and mechanical properties of laser cladding and laser- induction hybrid cladding coatings on full- scale rail," *Materials Science & Engineering A,* vol. 748, pp. 1-15, 2019, doi: 10.1016/j.msea.2019.01.068.

[P162] B. A. Obadele, A. Andrews, P. A. Olubambi, M. T. Mathew, and S. Pityana, "Effect of ZrO2 addition on the dry sliding wear behavior of laser clad Ti6Al4V alloy," *Wear,* vol. 328-329, pp. 295-300, 2015, doi: 10.1016/j.wear.2015.02.056.

[P163] G.-k. Qin, X.-l. Xing, X. Lu, and C.-x. Liu, "Preparation and Tribological Properties of Carbide-free Bainite Coatings by Laser Cladding," *CHINA SURFACE ENGINEERING,* vol. 31, no. 4, pp. 160-168, 2018, doi: 10.11933/j.issn.1007-9289.20180129001

[P164] M. M. Quazi, M. A. Fazal, A. S. M. A. Haseeb, F. Yusof, H. H. Masjuki, and A. Arslan, "Effect of rare earth elements and their oxides on tribo- mechanical performance of laser claddings: A review," *Journal of Rare Earths,* vol. 34, no. 6, pp. 549-564, 2016, doi: 10.1016/S1002-0721(16)60061-3.

[P165] F. C. Robles Hernández, A. O. Okonkwo, V. Kadekar, T. Metz, and N. Badi, "Laser cladding: The alternative for field thermite welds life extension," *Materials & Design,* vol. 111, pp. 165-173, 2016, doi: 10.1016/j.matdes.2016.08.061.

[P166] T. Roy *et al.*, "Effect of deposition material and heat treatment on wear and rolling contact fatigue of laser cladded rails," *Wear,* vol. 412-413, pp. 69-81, 2018, doi: 10.1016/j.wear.2018.07.001.

[P167] K. Sobiyi and E. Akinlabi, "Microstructure and Wear Properties of Laser- Cladded cBN/Ti [173] 3 Al on Pure Titanium," *Arabian Journal for Science and Engineering,* vol. 42, no. 11, pp. 4597-4604, 2017, doi: 10.1007/s13369-017-2585-0.

[P168] Y. Sui, F. Yang, G. Qin, Z. Ao, Y. Liu, and Y. Wang, "Microstructure and wear resistance of laser- cladded Ni- based composite coatings on downhole tools," *Journal of Materials Processing Tech.,* vol. 252, pp. 217-224, 2018, doi: 10.1016/j.jmatprotec.2017.09.028.

[P169] H. Tan, Z. Luo, Y. Li, F. Yan, R. Duan, and Y. Huang, "Effect of strengthening particles on the dry sliding wear behavior of Al2O3– M7C3/ Fe metal matrix composite coatings produced by laser cladding," *Wear,* vol. 324-325, pp. 36-44, 2015, doi: 10.1016/j.wear.2014.11.023.

[P170] H. Torres, S. Slawik, C. Gachot, B. Prakash, and M. Rodríguez Ripoll, "Microstructural design of self- lubricating laser claddings for use in high temperature sliding applications," *Surface & Coatings Technology,* vol. 337, pp. 24-34, 2018, doi: 10.1016/j.surfcoat.2017.12.060.

[P171] J. Tuominen, J. Näkki, H. Pajukoski, L. Hyvärinen, and P. Vuoristo, "Microstructural and abrasion wear characteristics of laser- clad tool steel coatings," *Surface Engineering,* vol. 32, no. 12, pp. 923-933, 2016, doi: 10.1080/02670844.2016.1180496.

[P172] M. Vostřák, Š. Houdková, M. Bystrianský, and Z. Česánek, "The influence of process parameters on structure and abrasive wear resistance of laser clad wc-nicrbsi coatings," *Materials Research Express,* vol. 5, no. 9, p. 096522, 2018, doi: 10.1088/2053-1591/aad859.

[P173] C. Wang, Y. Gao, Z. Zeng, and Y. Fu, "Effect of rare- earth on friction and wear properties of laser cladding Ni- based coatings on 6063Al," *Journal of Alloys and Compounds,* vol. 727, pp. 278-285, 2017, doi: 10.1016/j.jallcom.2017.08.101.

[P174] C. Wang, S. Zhang, C. H. Zhang, C. L. Wu, J. B. Zhang, and A. O. Abdullah, "Phase evolution and wear resistance of in situ synthesized V8C7 particles reinforced Fe-based coating by laser cladding," *Optics and Laser Technology,* vol. 105, pp. 58-65, 2018, doi: 10.1016/j.optlastec.2018.02.019.

[P175] K. Wang, B. Chang, Y. Lei, H. Fu, and Y. Lin, "Effect of Cobalt on Microstructure and Wear Resistance of Ni-Based Alloy Coating Fabricated by Laser Cladding," *Metals,* vol. 7, no. 12, p. 551, 2017, doi: 10.3390/met7120551.

[P176] W. J. Wang, Z. K. Fu, J. Guo, Y. Q. Zhang, Q. Y. Liu, and M. H. Zhu, "Investigation on Wear Resistance and Fatigue Damage of Laser Cladding Coating on Wheel and Rail Materials under the Oil Lubrication Condition," *Tribology Transactions,* pp. 1-8, 2016, doi: 10.1080/10402004.2015.1107926.

[P177] Y. Wang, Z. Liang, J. Zhang, Z. Ning, and H. Jin, "Microstructure and Antiwear Property of Laser Cladding Ni- Co Duplex Coating on Copper," *Materials (Basel, Switzerland),* vol. 9, no. 8, 2016, doi: 10.3390/ma9080634.

[P178] Y. Wang, B. Liu, and Z. Guo, "Wear resistance of machine tools' bionic linear rolling guides by laser cladding," *Optics and Laser Technology,* vol. 91, pp. 55-62, 2017, doi: 10.1016/j.optlastec.2016.12.015.

[P179] F. Weng, H. Yu, C. Chen, and J. Dai, "Microstructures and wear properties of laser cladding Co- based composite coatings on Ti– 6Al– 4V," *Materials and Design,* vol. 80, pp. 174-181, 2015, doi: 10.1016/j.matdes.2015.05.005.

[P180] Z. Weng, A. Wang, X. Wu, Y. Wang, and Z. Yang, "Wear resistance of diode laser- clad Ni/ WC composite coatings at different temperatures," *Surface & Coatings Technology,* vol. 304, pp. 283-292, 2016, doi: 10.1016/j.surfcoat.2016.06.081.

[P181] F. Wu, T. Chen, H. Wang, and D. Liu, "Effect of Mo on Microstructures and Wear Properties of In Situ Synthesized Ti(C, N)/ Ni- Based Composite Coatings by Laser Cladding," *Materials (Basel, Switzerland),* vol. 10, no. 9, 2017, doi: 10.3390/ma10091047.

[P182] H. Xiangchun, D. Dong, W. Kaiming, H. Yuxiang, and C. Baohua, "Microstructure and Wear Resistance of Fe- Cr- Mo- Co- C- B Amorphous Composite Coatings Synthesized by Laser Cladding," *Metals,* vol. 8, no. 8, p. 622, 2018, doi: 10.3390/met8080622.

[P183] H. Yan, P. Zhang, Z. Yu, Q. Lu, J. Guo, and Z. Chen, "Laser cladding NiCrBSi/TiN/h-BN self-lubricating wear resistant coating on Ti–6Al–4V surface," *Materials Research Express,* vol. 6, no. 6, p. 066537, 2019, doi: 10.1088/2053-1591/ab0d76

[P184] C. Yang, X. Cheng, H. Tang, X. Tian, and D. Liu, "Influence of microstructures and wear behaviors of the microalloyed coatings on TC11 alloy surface using laser cladding technique," *Surface & Coatings Technology,* vol. 337, pp. 97-103, 2018, doi: 10.1016/j.surfcoat.2017.12.058.

[P185] J. Yang, J. Huang, D. Fan, and S. Chen, "Microstructure and wear properties of Fe–6wt.%Cr–0.55wt.%C–Xwt.%Nb laser cladding coating and the mechanism analysis," *Materials & Design,* vol. 88, pp. 1031-1041, 2015, doi: 10.1016/j.matdes.2015.09.108.

[P186] J. Yao, J. Zhang, G. Wu, L. Wang, Q. Zhang, and R. Liu, "Microstructure and wear resistance of laser cladded composite coatings prepared from pre-alloyed WC-NiCrMo powder with different laser spots," *Optics and Laser Technology,* vol. 101, pp. 520-530, 2018, doi: 10.1016/j.optlastec.2017.12.007.

[P187] J. Yin, D. Wang, L. Meng, L. Ke, Q. Hu, and X. Zeng, "High- temperature slide wear of Ni- Cr-Si metal silicide based composite coatings on copper substrate by laser- induction hybrid cladding," *Surface & Coatings Technology,* vol. 325, pp. 120-126, 2017, doi: 10.1016/j.surfcoat.2017.06.063.

[P188] C.-C. Zang, Y.-Z. Wang, Y.-D. Zhang, J.-H. Li, H. Zeng, and D.-Q. Zhang, "Microstructure and wear-resistant properties of NiCr–Cr 3 C 2 coating with Ni45 transition layer produced by laser cladding," *Rare Metals,* vol. 34, no. 7, pp. 491-497, 2015, doi: 10.1007/s12598-015-0492-7.

[P189] J. Zeisig *et al.*, "Microstructure and abrasive wear behavior of a novel FeCrMoVC laser cladding alloy for high- performance tool steels," *Wear,* vol. 382, pp. 107-112, 2017, doi: 10.1016/j.wear.201.X04.021.

[P190] H. Zhang, H. Yu, and C. Chen, "Microstructure and wear resistance of composite coating by laser cladding Ni60A/B 4 C pre- placed powders on Ti- 6Al- 4V substrate," *Science and Engineering of Composite Materials,* vol. 24, no. 4, pp. 541-546, 2017, doi: 10.1515/secm-2015-0032.

[P191] L. Zhang, C. S. Wang, S. Qian, Q. Yu, and C. Dong, "Microstructure and Wear Resistance of Laser- Clad (Co, Ni)(61.2) B26.2Si7.8Ta4.8 Coatings," *Metals,* vol. 7, no. 10, 2017, doi: 10.3390/met7100419.

[P192] Z. Zhang and R. Kovacevic, "Laser cladding of iron- based erosion resistant metal matrix composites," *Journal of Manufacturing Processes,* vol. 38, pp. 63-75, 2019, doi: 10.1016/j.jmapro.2019.01.001.

[P193] J. Zhao, A. Ma, X. Ji, J. Jiang, and Y. Bao, "Slurry Erosion Behavior of AlxCoCrFeNiTi0.5 High-Entropy Alloy Coatings Fabricated by Laser Cladding," *Metals,* vol. 8, no. 2, p. 126, 2018, doi: 10.3390/met8020126.

[P194] W. Zhao, G. Zha, M. Xi, and S. Gao, "Effects of Synchronous Rolling on Microstructure, Hardness, and Wear Resistance of Laser Multilayer Cladding," *Journal of Materials Engineering and Performance,* vol. 27, no. 4, pp. 1746-1752, 2018, doi: 10.1007/s11665-018-3286-x.

[P195] Q. Zhuang, P. Zhang, M. Li, H. Yan, Z. Yu, and Q. Lu, "Microstructure, Wear Resistance and Oxidation Behavior of Ni-Ti-Si Coatings Fabricated on Ti6Al4V by Laser Cladding," *Materials,* vol. 10, no. 11, p. 1248, 2017, doi: 10.3390/ma10111248.

[P196] S. R. Lewis *et al.*, "Improving rail wear and RCF performance using laser cladding," *Wear,* vol. 366, pp. 268-278, Nov 2016, doi: 10.1016/j.wear.2016.05.011.

4 MODELLING

Mathematical models are used in mechanics and tribology for prediction of material behaviour undergoing a process, for example during operation such as the wheel-rail contact interface in railways. Other processes may include the manufacturing of coatings or heat treatment of materials to achieve certain material and mechanical properties. Typical operational models result in an approximation of the stress state of material and damage in terms of wear, elastic and plastic deformation, as well as crack damage. Crack damage can be characterised in different stages such as crack initiation and propagation. Cracks exist in various scales from microns to millimetres and may propagate to the point of total failure where irreversible damage deems the component unsuitable for service. Modelling in tribology is mainly concerned with the wear of material resulting in profile deformation and/or material loss. Crack modelling was excluded from this study and the majority of the evaluation work for laser cladding materials was conducted through physical testing. It was not the aim of this research to produce complete material models, so the modelling work was exploratory as illustrated by the modelling map in Figure 4-1. This chapter contains an overview of basic concepts on the material behaviour of steel, followed by modelling and basic calculations for each interface, and concluding with a discussion on predictive tools used in the selection of materials and coatings in industry.

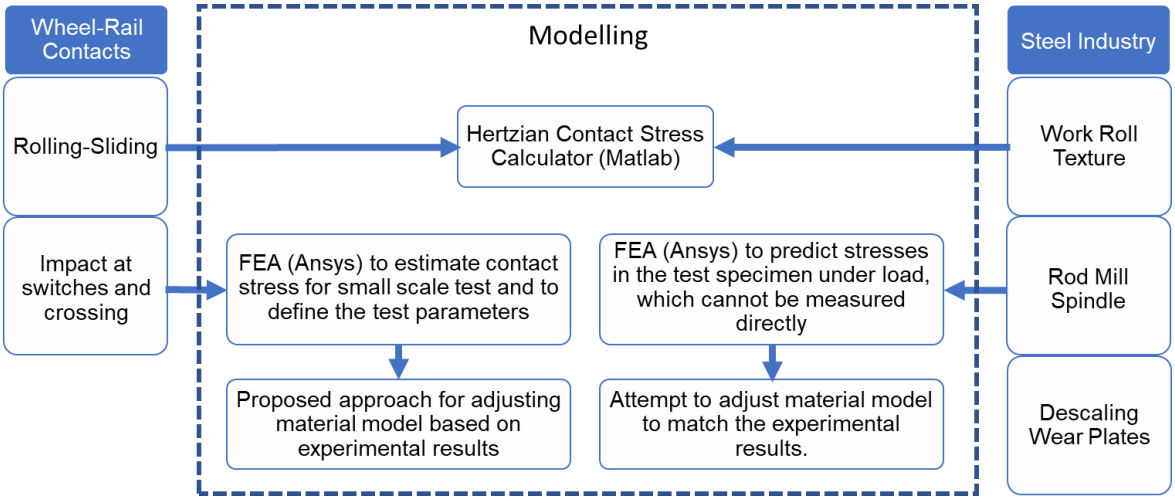

Figure 4-1 Modelling map

4.1 Material behaviour of steel

The material behaviour of steel is complex, governed by various phenomena such as stress-strain dependent phase transformations, its interactions with plasticity and Transformation-Induced Plasticity (TRIP) [174]. These phenomena are studied by experiments in isolated situations in micro, meso and macro levels. For example, cyclic loading tests can produce material models that characterise the behaviour of these materials which can then be used in modelling. Cyclic loading concepts for rail materials are explained here and illustrated in Figure 4-2. Rail materials can strain-harden (plastic flow) and form protective residual stresses when the applied load exceeds the elastic limit of the material. Where the applied load does not exceed the elastic shakedown limit there will

be some initial plastic flow, but ultimately the load will be supported elastically, and it will fail only by high cycle fatigue. If the applied load exceeds the elastic shakedown limit then there will be some plastic flow and if the load remains between the elastic and plastic shakedown limit can cause closed cycle of plasticity where the material fails by low cycle fatigue with no net accumulation of plastic strain. For loads that exceed the plastic shakedown limit then an open cycle of plastic strain accumulates, leading to failure by low cycle fatigue or ductility exhaustion [23, 26].

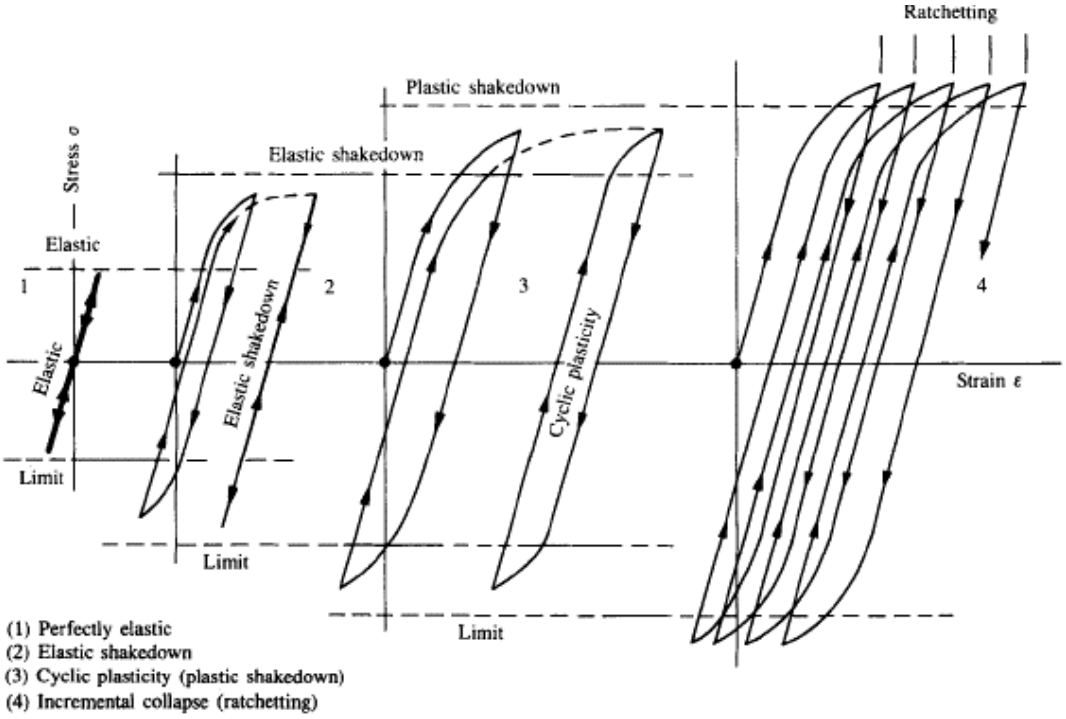

Figure 4-2 Cycling loading response [26]

There are various material models which govern the outcome of analytical modelling and computer simulations, for example Finite Element Analysis (FEA). Material model could include isotropic or kinematic hardening models, which are often obtained from tests. A description of these models is shown in Figure 4-3 with their corresponding Mohr's circle beneath each diagram that describes how the stress state at a given point changes according to each model.

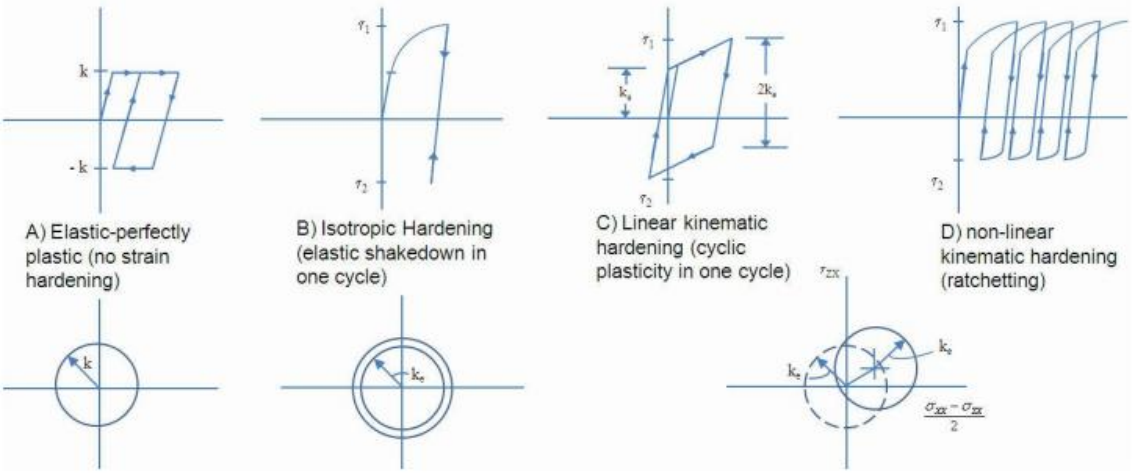

Figure 4-3 Different modes for yielding of materials [9]

Nonlinear kinematic hardening simulates the Bauschinger effect (when loading in tension and compression the elastic region remains the same size and the total of yield in tension and reduced yield in compression is now equal to twice the initial yield) and it is suitable for large strains and cyclic loading, thus modelling ratchetting and shakedown [175]. Examples are the Armstrong-Frederick, Prager-Ziegler, Chaboche, Ohno-Wang, and Guionnet kinematic hardening models. The main difference between linear and non-linear kinematic hardening models is that linear models cannot capture ratchetting. A single nonlinear kinematic model for the Chaboche model can capture ratchetting, while the addition of a second kinematic model will model shakedown. Temperature and strain-rate sensitivity is also important when obtaining data for material modelling since they can shift the yield stress criterion and change the flow stress behaviour. “Viscoplasticity” and “Creep” are terms used for rate-dependent plasticity and time-dependent irreversible deformation respectively, where the dominant deformation process in the former is crystallographic slip, enhanced by thermally-activated processes such as diffusion-activated dislocation climb. The mechanism for the latter is either diffusion controlled or influenced by diffusion with some crystallographic slip may still occur [176]. The Johnson-Cook model is a typical example of flow stress model used in FEA.

Strain-hardening concepts apply to the wheel-rail interface, for example rolling contact fatigue (RCF), where the main damage mechanism is ratchetting. In RCF, the increments of plastic flow accumulate until the stain hardening material cannot strain anymore and shallow cracks initiate. RCF has three crack initiation and propagation phases. This is illustrated in Figure 4-4, during initiation (phase I) there is a rapid growth for the new-born crack, followed by growth into millimetres deep in phase II, featuring acceleration and deceleration. Finally, in phase III the cracks are not influenced by the surface rolling contact stresses. Cracks may continue to develop under the influence of rail bending, thermal and residual stresses into the interior of the rail head and could contribute to a rail break [32].

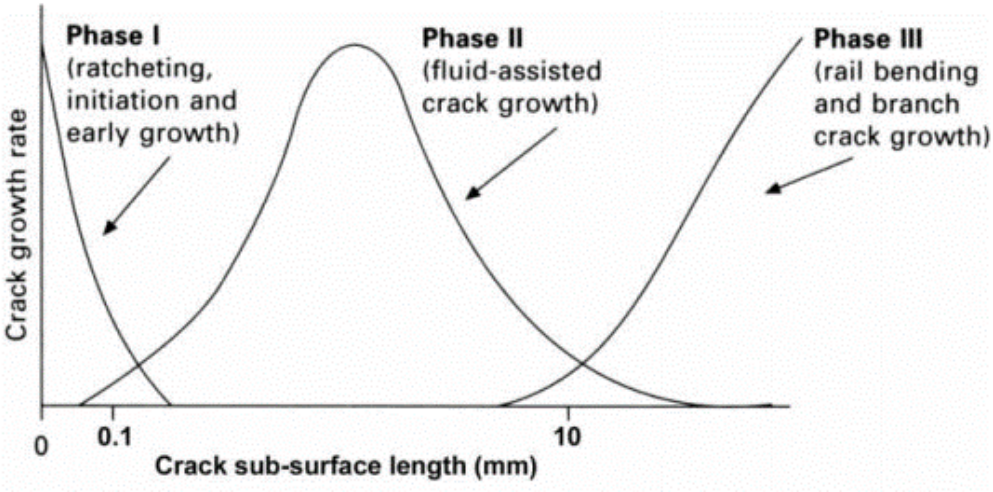

Figure 4-4 Three stages of RCF crack growth [13]

Beyond studying the mechanical behaviour of the steel samples, the wear and tribological performance is also examined by this research. Tribology is the highly interdisciplinary study of interacting surfaces in relative motion, concerning friction, lubrication and wear and which dates to 1493, as evident by Leonardo Da Vinci’s notebooks [177]. Friction is the dissipation of energy

between sliding bodies and it is governed by four basic empirical laws for dry friction: there is proportionality between the maximum tangential force before sliding and the normal force when a static body is subjected to increasing tangential load, the tangential friction force is proportional to the normal force in sliding, friction force is independent of the apparent contact area, and kinetic friction is independent of the sliding velocity [14]. The second and third laws were put forward by Leonardo Da Vinci and enunciated by Guillaume Amontons (1699), while the fourth law by Charles-Augustin de Coulomb (1781). Wear can be attributed to a number of mechanisms either chemical or mechanical.

Only mechanical wear is concerned in this research. Typical wear mechanisms are adhesive or abrasive wear, percussive impact, erosive and oxidation. Contact mechanics are essential in defining the interface in order to be used in wear models for estimating wear and wear rates, critical in the design of tribological interfaces. Numerous wear models have been developed over the years, Meng and Ludema have identified 182 equations from the journal Wear between 1957 and 1992, and Wear of Materials (WOM) conferences from 1977 to 1991 [178]. A significant contribution in the 1950's was the Archard wear equation, as described in Equation 4-1 [179]:

$$V = \frac{KW'L}{p_m} \qquad \textbf{Equation 4-1}$$

where V is worn volume [m^3]; K is a dimensionless wear coefficient; W' is applied load [N]; L is sliding distance [m]; and p_m is flow pressure of the softer material, which is approximately equivalent to hardness.

Continuum theory of matter is used to model solid contact and it is limited to asperities with a contact area of linear dimension of at least 10 to 100 atoms at loads of order the macroscopic hardness and typical temperatures. Modelling of smaller contact areas should be based on discrete particulate atoms joined by elastic bonds and molecular dynamics simulations should be used [180].

Wear modelling for the rail industry is discussed in section 2.2.1.1, with a focus on wear rates which are key for characterising the wear behaviour of the wheel-rail interface. The modelling discussed for the rail industry can apply to other industries as well, either in the form of Tγ/A wear maps or with the use of Archard's wear law. Early experiments from 1956 by Archard and Hirst [181] found that wear rates of materials are independent of the apparent area of contact, with wear rates being proportional to the applied load unless a change in the load causes the surface conditions to change. They concluded that the numerical application of simple theories of wear are based on the assumption of plastic deformation of surface asperities, however, paradoxically they yield values for the probability of surface damage. This suggests that with some materials the asperities would deform elastically. It is challenging to understand and predict wear particles at an asperity encounter. Meng and Ludema [178] identified in 1995 the slow pace of translating microscopic observations into macroscopic models and suggested to develop full descriptions of the evolution of macroscopic events on sliding surfaces, including the formation and movement of fragmented particles on the interface.

4.2 Representation of physical characteristics using analytical tools

Wear and plastic deformation are the main damage mechanisms that are being investigated in this research. The behaviour of cracks present in samples tested is not characterised or modelled. Modelling in this research was used prior to testing, to determine the test parameters, for example by predicting the contact patch size. In addition, an attempt was made to adjust the material models used in modelling based on experimental results, as a way to estimate the damage for industrial interfaces based on the small-scale test results.

4.2.1 Twin disc modelling

A Hertzian contact stress calculator was programmed using Matlab as a quick tool to calculate and extrapolate contact conditions from small scale to large scale and vice versa. An example of the calculator GUI is shown in Figure 10-2, in the Appendix. The calculator is not complete and therefore not discussed in detail here, however, it is mentioned as it was developed during this project and it was used to calculate the load conditions for the small scale tests.

The key results generated from the railway twin disc tests were the wear rates in the form of Tγ/A which is Tγ (traction force) normalised using area. Because the results are normalised using area, it means that they can be extrapolated to any dimension, so they can be used with standard industry modelling tools for wear prediction. Tγ/A has more advantages over the use of Archard's wear coefficients for modelling. An explanation is given in section 5.2 along with the need for modelling data, as an introduction to the test procedure.

4.2.2 Erosion

The outcomes from this study for evaluating the performance of the materials were based on physical testing. The methodology from a commercial code ANSYS Fluent, which is based on a typical erosion model is described in Equation 4-2 as a reference to better understand the complex underline mechanisms of erosion wear [182].

$$\boldsymbol{ER = \sum_{p=1}^{N_{trajct}} \frac{\dot{m}_p C(d_p) f(a) v_p^n}{A_{face}}} \qquad \textbf{Equation 4-2}$$

where $\dot{m}$ is the mass flow rate of particles; $C(d_p)$ is the particle diameter function; $f(a)$ is the impact angle function; v_p is the particle impact velocity; n is the velocity exponent; and A_{face} the impacted area.

The ductility or brittleness of the material is important when using erosion models, since this can influence the damage in relation to the impingement angle. For example, in Figure 4-5 the ductile material erosion is much higher at a shallow angle and less damaging at 90°, while the brittle material is more damaging at 90° impingement angle from the surface of the material.

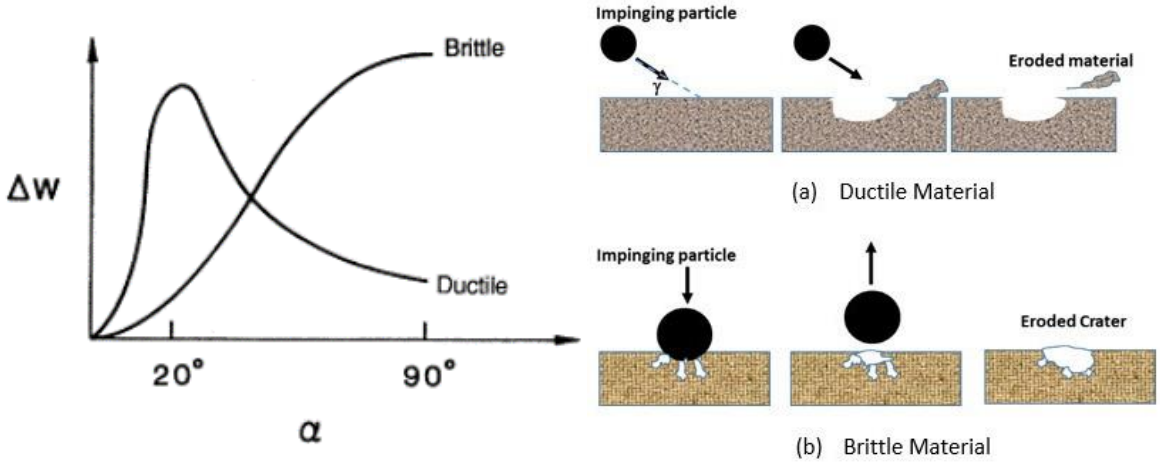

Figure 4-5 Wear damage versus impingement angle for ductile and brittle materials [182]

Additional models are considered in commercial codes, for example the Finnie [183] erosion model which is more suited for ductile materials, the Oka [184] model which considers the effect of wall material hardness and the McLaury [185] erosion model which is developed for predicting the erosion rates of solid particles in water, for example analysis of slurry.

Although the data produces from testing have not been used directly in modelling, an effort was made to understand the parameters required for modelling and to correlate these to the test conditions. The spray parameters (impingement angle, stand off, flow rate, pressure, spray pattern etc.) from the tests are made available and results in the form of volume wear for various steel samples of which one is coated with a laser clad materials are available in section 6.4.1. The test conditions can be used as input parameters in erosion modelling tools, thus replicating the current tests for comparison of the materials used in testing. Modelling beyond these limited test conditions should only be used with caution and with verification with further tests, as the behaviour exhibited from these tests may not be linear for all conditions.

4.2.3 Impact

The analysis was produced to identify the weight and drop height for the impact, which would produce contact stress in the interface similar to that of the wheel impacting on a crossing nose. The intention was to simulate various material models for comparison, however, only one effort was made to simulate full scale wheel-rail impact with an approximation in the material properties. The modelling was not a main objective set out in the thesis but complimentary.

A drop test rig for composites was used for the experimental data. The rig was modified to accommodate a new solid base and a pin/dart that could be replaced after each test. The experimental procedure is described in 5.3. A Finite Element Analysis (FEA) was performed where basic parameters that were produced under idealistic and simplified conditions, with the following assumptions; air resistance, friction from the linear guides, rig stiffness and dynamic effects were not considered, while mass was estimated and rounded up.

For the impact calculations “Explicit” analyses were performed in Ansys Workbench 19.1. Typical Finite Element Analyses are solved “Implicitly”, with time integration using a series of linear approximations with small iterative time steps in order to achieve convergence. “Explicit” in Ansys is solved with time integration, using uncoupled equations that can be solved directly (explicitly), using tiny time steps to solve the equations once. Explicit is ideal for extremely large distortions and deformations, material failure and extreme nonlinear materials [186]. Material models are key for describing the material behaviour and solving the problem accurately, typically the Johnson-Cook model is used for ductile materials while the Johnson-Holmquist model is used for brittle materials [187]. Input parameters for the material models include the elastic model (Young’s modulus and Poisson’s ratio), the plasticity model (plastic deformation behaviour) and the damage model, where the latter is used as a criterion for failed elements, which can then be removed from the model, thus simulating wear and material loss by erosion. Parameters for such models are obtained through experiments such as the split Hopkinson torsion bar test [187]. Additional influences such as residual stresses may affect the results. Simple material parameters available in the Ansys material library were used in this study and listed in Table 4-1, “non-linear structural steel” for the specimen and “explicit 4340 steel” for the ball and overall weight, while a softer “non-linear copper alloy” for the pin/dart. The non-linear material properties assigned to the specimen and pin included simplistic bilinear isotropic hardening information, while the explicit material model assigned to the ball included additional information such as Johnson-Cook parameters. To account for the overall weight of the dropping frame without modelling the whole frame, a small cylinder was added on top of the pin. The density of the material assigned to this small cylinder was altered in such a way that the overall weight of the pin/dart and the cylinder components would equate to 1.4 kg.

The velocity at impact was required as an input parameter for the simulation and the kinetic energy as a way of validating the simulation. The energy of the raised mass (around 1.4 kg by 1.58 m) was calculated by Equation 4-3 and found to be 21.7 J.

Energy $$(\boldsymbol{P.E.})\boldsymbol{mgh} = (\boldsymbol{K.E.})\frac{\boldsymbol{1}}{\boldsymbol{2}}\boldsymbol{mv^2}$$ **Equation 4-3**

The velocity at impact is found to be 5.56 m s^{-1} (Equation 4-4) and the drop time at 0.28 s (Equation 4-5) from the moment the pin/dart is released from the height of 1.58 m.

Speed $$\boldsymbol{v} = \sqrt{\boldsymbol{2gh}}$$ **Equation 4-4**

Time $$\boldsymbol{t} = \frac{\boldsymbol{h}}{\boldsymbol{v}}$$ **Equation 4-5**

The drop height in the FEA was in the region of microns, to save computational time of simulating 0.28 s, by initiating the simulation with a velocity of 5.56 m s^{-1}. An axisymmetric quarter model was used in the analysis to reduce computational time and finer mesh was selected near the contacting faces and a coarse mesh was selected away from highly loaded areas to reduce the overall mesh size. Figure 4-6 shows the mesh of the quarter model with a closer view on the right side of the figure. Figure 4-7 illustrates how the model was constrained. The base and cylindrical face of the specimen

were fixed in space. The pin, ball and weight had an initial velocity at the start of the simulation of 5.56 m s^{-1}. The falling components were placed very close to the specimen surface, but not in contact with it. Earth gravity effects applied to all components and displacement control was used to constraint the components from moving normal to the axisymmetric faces, where the symmetrical sections of the components would be, thus representing a full model in the analysis.

Table 4-1 Drop test and FEA parameters

Drop weight (pin and slider)	1.4 kg	Nodes	86,759
Height	1.58 m	Elements	388,627
Hemispherical diameter	6 mm	Frictional contact	0.3
Initial Velocity	5.56 m s^{-1} dart/pin quarter model weight 0.35 kg (1.4 kg full model)		
Maximum vertical travel from first contact	1.85 mm at 0.57 ms	Material flow height over the surface (from FE results)	0.3 mm
Maximum contact pressure with the specimen	1 GPa at 0.35 ms	Max value at singularity	4.86 GPa
Time step	2.28x10^{-9} s	Total cycles	299,066
Solve time	13 hours on UoS Iceberg HPC cluster	Total run time	0.74 ms
Specimen material: Structural Steel NL		Pin material: Copper Alloy NL	
Density	7850 kg m^{-3}	Density	8300 kg / m^3
Elastic Modulus	200 GPa	Elastic Modulus	110 GPa
Poisson's Ratio	0.3	Poisson's Ratio	0.34
Bilinear Isotropic Hardening		Bilinear Isotropic Hardening	
Yield Strength	250 MPa	Yield Strength	280 MPa
Tangent Modulus	1.45 GPa	Tangent Modulus	1.15 GPa
Ball and Weight material: STEEL 4340 Explicit			
Density	7830 kg m^{-3}		
Johnson Cook Strength			
Initial Yield Stress	792 MPa	Thermal Softening Exponent	1.03
Hardening Constant	510 MPa	Reference Strain Rate	1 / s
Hardening Exponent	0.26	Bulk Modulus	159 GPa
Strain Rate Constant	0.014	Shear Modulus	81.8 GPa

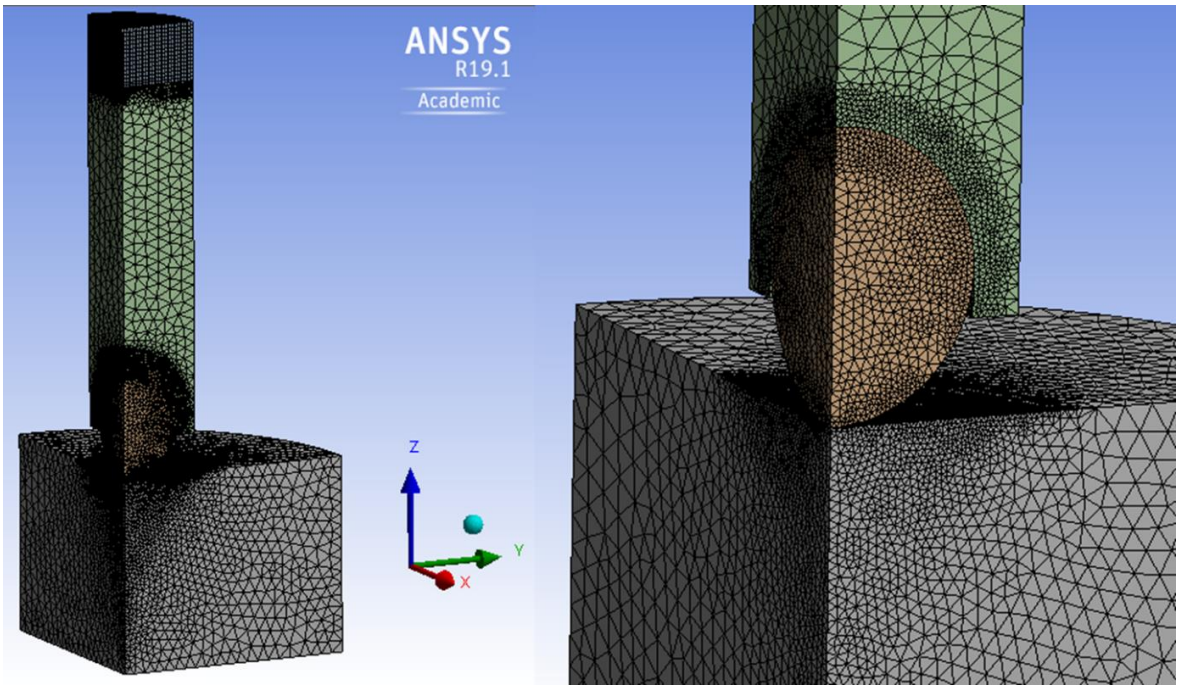

Figure 4-6 Mesh detail of the quarter model

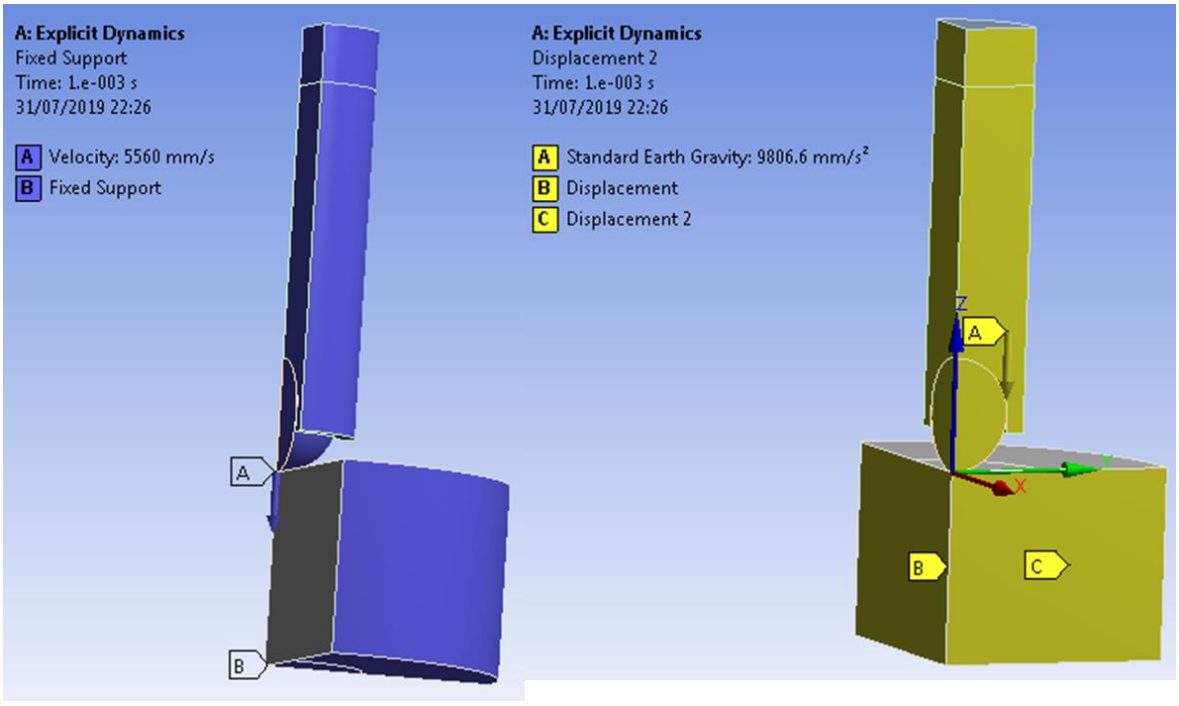

Figure 4-7 FEA model constraints and forces

Figure 4-8 is a plot from the simulation showing the kinetic and internal energy against simulation time, whereby the kinetic energy was converted into internal energy as the pin velocity goes to zero and the contact between the pin and specimen increases. The zero velocity point is when the kinetic energy has been converted to internal energy, about 0.55 ms from the start of the simulation. It is verified that the initial velocity and mass were calculated correctly since the kinetic energy at start for the quarter model is 5.4 J, which is a quarter of the 21.7 J total energy, as calculated in Equation 4-3.

Hourglass energy is zero which means no hourglass effect deformation of the mesh took place and contact energy goes from zero to -253 mJ at zero velocity where full contact conditions dominate.

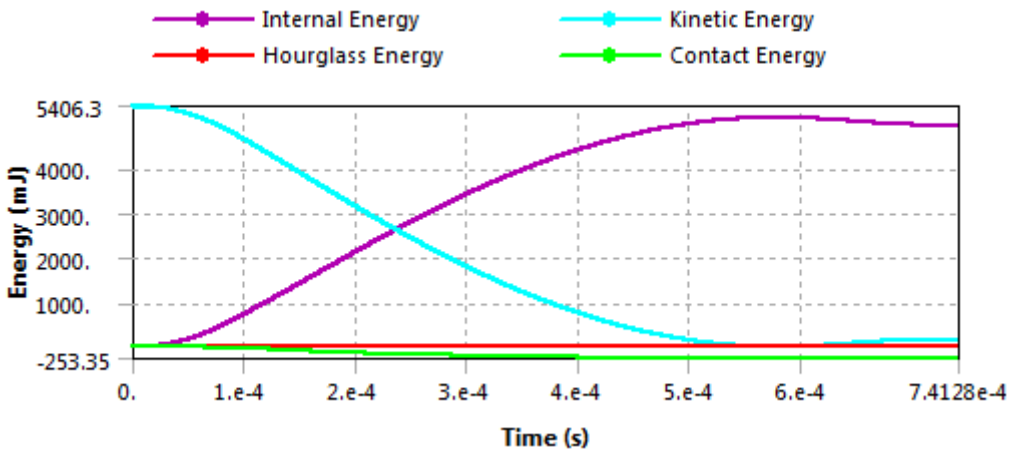

Figure 4-8 Energy summary from the pin/disc FEA in Ansys

After full contact the kinetic energy starts to rise again and the internal energy is reduced, however, after a very short time both energies run constant as opposed to continuing on their corresponding trajectory. This may be due to gravity effects acting in the opposite direction than the rebound force. The impact time can be identified by the compression and rebound time, before the impacting bodies separate, and the rebound time could be longer than the compression time, depending on the elastic properties of the impacting bodies. The simulation was computationally intensive, so it was decided not to run the analysis further to investigate this.

Among the various FEA results produced, the key result information was the normal and shear stresses, Equivalent and Principal stresses, strain and deformation. Some of these were chosen for discussion. Minimum principal stress is representing compressive forces in the model, Figure 4-9 shows a maximum compressive stress in the region of 4.86 GPa, 0.2 ms prior to zero velocity time and a maximum deformation in the vertical axis of 1.85 mm at the zero velocity time of 0.55 ms. The steel ball penetrates the specimen by 0.6 mm, while the brass pin is deforming around the shape of the undeformable ball. The maximum deflection of 1.85mm is attributed to the top section of the pin (highlighted in blue), which is the volume of material that has not been deformed and exhibits the highest vertical movement.

Images of the deformed pin are shown in Figure 4-10, where one of the pins was sectioned to remove the ball and to examine the internal geometry of the pin, but also any damage on the ball that was not visible when held by the pin. Images of the undeformed pin and the pin holder are shown in Figure 5-27, in section 5.3 where the test procedure is described. The pin holder was not considered in the FEA, which has a cylindrical pocket to hold the pin, the constraint faces of the pin holder are illustrated by the red lines in Figure 4-10. This would have had an effect in the deformation of the pin resulting in a sharp transition in the bulging of the brass around the ball due to higher plasticity induced by the edges of the pin holder. Instead a smoother transition occurred, with a deformation shape, not far off from the physical pin deformation.

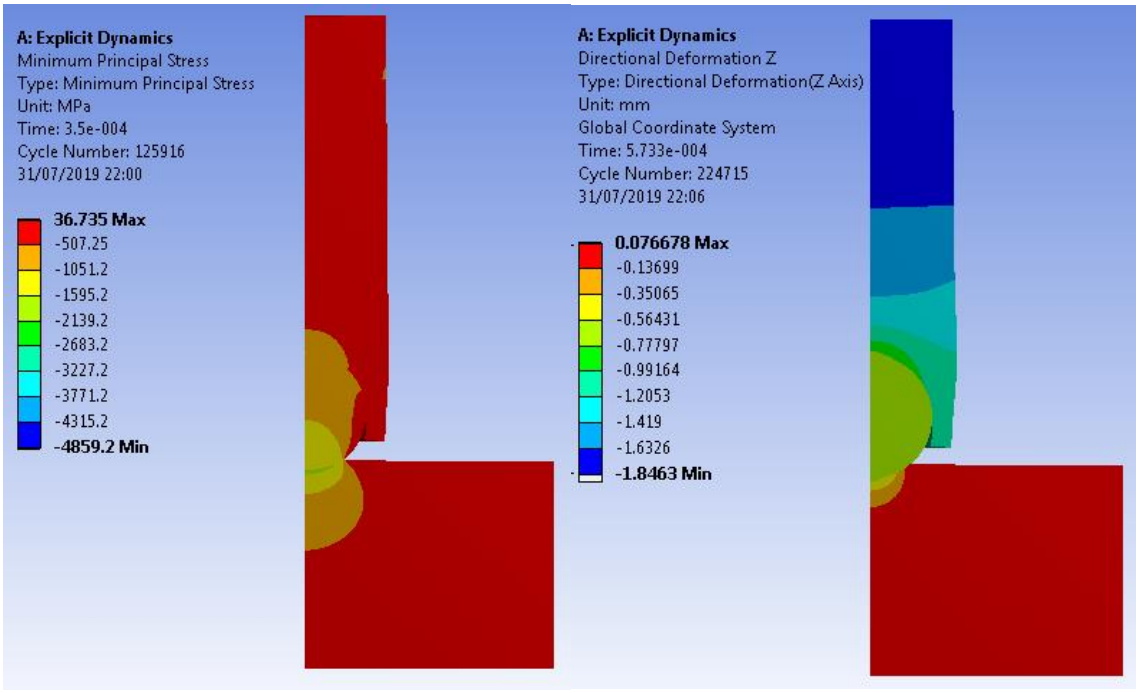

Figure 4-9 Minimum Principal Stress (left) and Vertical deformation (right)

Figure 4-10 Steel ball in brass cartridge (dart)

To validate the contact stress on of 4.86 GPa shown in Figure 4-9, a closer look at the contact area was obtained in Figure 4-11, which reveals that the maximum compressive stress is most likely caused by a mesh singularity. This is because most of the contact surface area has stress values in the region of 1 GPa. Analytical calculations were produced to validate these results. It was assumed that the impact was inelastic collision, meaning that although the pin bounced back, some energy was absorbed by the sample and the pin, which was converted into strain energy in the sample and pin, through plastic damage. It was assumed that the ball damage was negligible.

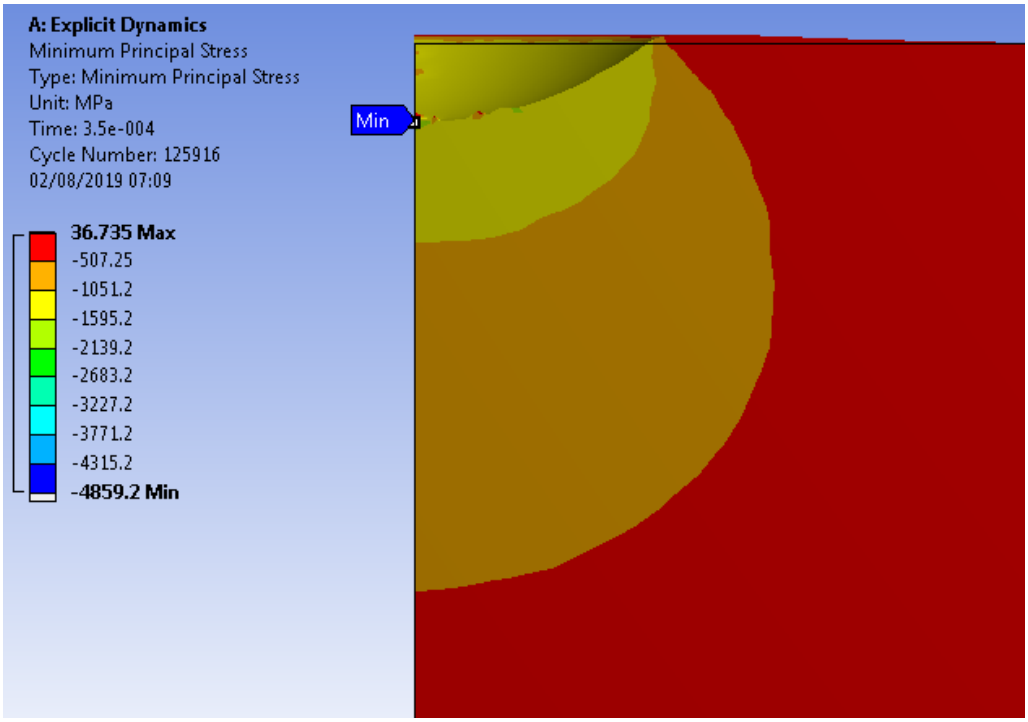

Figure 4-11 Specimen Minimum Principal Stress (compressive impact) just before kinetic energy=0J

Contact stress calculations using Hertzian contact equations were performed, however these are valid for a fraction of time after impact. This is because these equations are valid for elastic behaviour not exceeding the yield of the materials and for non-conformal contact, where tangential and frictional forces are not included. Hertzian contact is valid for contacting solids at rest and in equilibrium for contact area that is small compared to the size of the curved bodies. However, it appears that most if the impact parameters can be predicted accurately from experiments [188, 189].

The geometrical and physical parameters required for the equations are known, the key parameter is the impact force, something that it is difficult to calculate in dynamic situations with very short duration, in which time the force changes amplitude, direction and distribution many times. In an ideal elastic collision the kinetic energy would not be absorbed, the pin would rebound at the same speed, reaching the drop height (assuming no gravity) where the kinetic energy would be converted to potential energy and there would be no conversion to strain energy in either body during the collision. Opposite and equal forces would act at impact time on the contacting surfaces to allow a full rebound and momentum would be maintained in the opposite direction. If the impacting body (a softer sample) was severely damaged by absorbing the pin without rebounding, then the impacting force would be analogous of the elastic energy of the sample, since most of the kinetic energy has been converted into strain energy and deformed the (very soft) sample. In this study, three objects were affected by the collision, which complicates understanding. These were the sample, the brass pin and the steel ball. The steel ball has been unaffected, in comparison to the steel sample and brass pin deformation.

This explains that most of the kinetic energy has not been converted to the strain energy in the sample alone, but to the brass pin as well from a reaction force during the collision. The Hertzian contact

calculation here considers the contact between the steel ball and sample only, which is that of a “sphere on plate contact”, lasting 0.35 ms, as per the time referenced in the FEA.

For elastic impact Equation 4-6 can be used to calculate the impact force, where twice the mass times velocity has been divided by the collision duration [188, 190]. The mass and velocity were multiplied by 1.1 instead of 2, assuming that only 10% of them energy was applied to changing the momentum direction and the rest absorbed by the colliding bodies. A force of 24,464N was used in conjunction with equations Equation 4-7 to Equation 4-10, to calculate the resultant contact radius (α) peak (Po) and average (Pavg) contact pressures.

Force $$P = \frac{2\,m\,v}{tc}$$ **Equation 4-6**

Reduced radius $$R' = \left(\frac{1}{R\,(sphere)} + \frac{1}{\infty}\right)^{-1}$$ **Equation 4-7**

Reduced Elastic Modulus $$E^* = \left(\frac{1-v^2}{E_1} + \frac{1-v^2}{E_2}\right)^{-1}$$ **Equation 4-8**

Contact radius $$a = \sqrt[3]{\frac{3\,P\,R'}{4\,E^*}}$$ **Equation 4-9**

Peak Contact Pressure $$Po = \frac{3P}{2\pi\alpha^2}$$ **Equation 4-10**

Average Contact Pressure $$Pavg = \frac{P}{\pi\alpha^2}$$ **Equation 4-11**

Assumptions regarding the reduced radius (Equation 4-7) and reduced elastic modulus (Equation 4-8) were based on approximate values and may affect the results slightly. The results are also sensitive to the collision time, if assumed a collision time an order magnitude shorter, then the resultant impact force would be and order magnitude higher and vice versa. Results are plotted in Table 4-2 for various collision durations ranging from 50 µs to 10 ms.

Table 4-2 Hertzian contact results for various collision durations

	Collision duration				
	50 µs	200 µs	350 µs	500 µs	10 ms
Impact force (N)	171,248	42,812	24,464	17,124	8,562
Contact radius (mm)	1.519	0.957	0.794	0.705	0.56
Peak Contact Pressure (GPa)	35.4	22.3	18.5	16.4	13
Average Contact Pressure (GPa)	23.6	14.8	12.3	10.9	8.7

The calculated average contact pressures in Table 4-2 are extremely high, in all cases. High stresses in small contact areas may be valid for the very early stages of contact, resulting in sever plastic deformation to a very small volume below the contacting surface area. As the contact bodies deform, the contact area expands along with the stress distribution, thus the stress intensity drops to the values predicted by the FEA, below 5 GPa.

Results from other research discussed in section 2.2.2, showed that the contact stress resulted from simulations of wheel and crossing nose was in the region of 1-1.3 GPa. The average stresses predicted from the FEA are in agreement with other research, therefore, the small scale test conditions were close to the scale-up conditions, in terms of contact stress. There are limitations to how many physical parameters can be simulated, and adjustments can be made in the constraints or material model to account for these effects. In various forms of testing for obtaining material properties (i.e. uniaxial tensile, torsion, thermo-mechanical fatigue etc.), the results are applicable under the test conditions and may not be suitable to use on larger geometries, loads or different environmental conditions without further validation. An example of elasto-plastic material properties produced by tensile tests are shown in Figure 10-1 in the Appendix. Pletz et al. [191] produced a wheel-rail impact simulation based on three materials, one of which was Manganese steel (Mn13), with yield of around 250 MPa (see Figure 10-1). The stress-strain curve for the Manganese steel is nearly the same as the “Structural Steel NL” material used in this study (see Table 4-1). The damage on the specimen was in the form of an impact cavity. The simulation resulted in a cavity width of just under 4mm, when compared the cavity to the scale bar in Figure 4-12. This cavity width is close to the cavity width of the Manganese test piece, as measured from the sectioned test specimen and found to be 3.7mm (see 6.2.1).

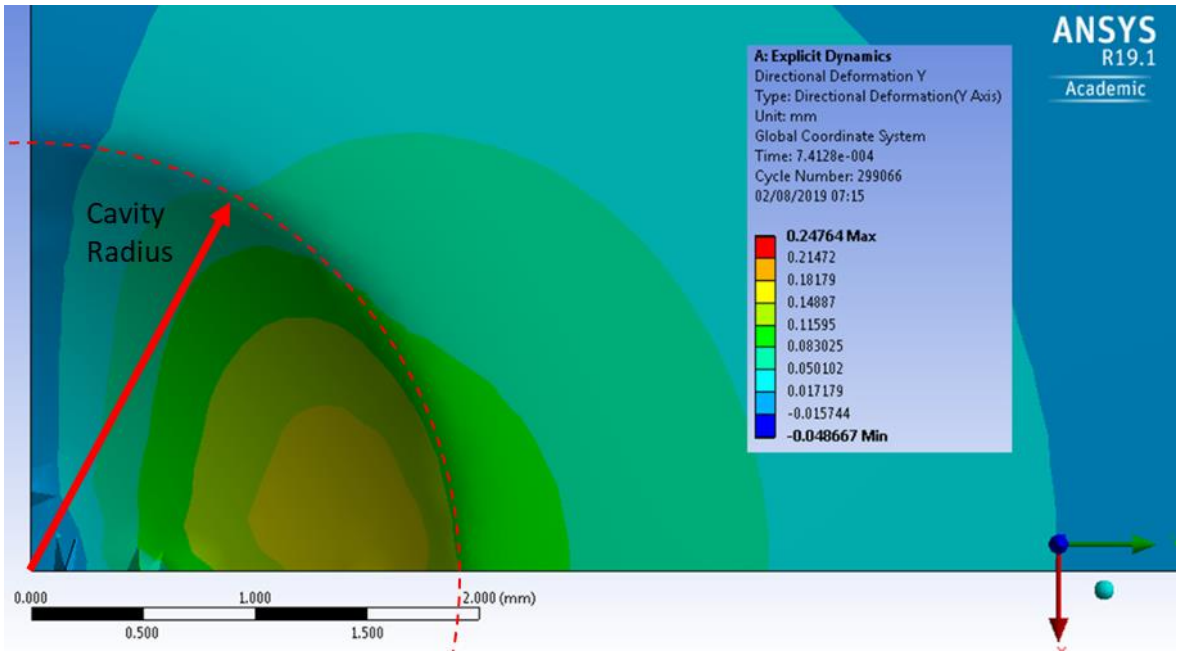

Figure 4-12 Vertical deformation on disc sample (normal view)

This is a good approximation to a realistic material model, however, as with material data obtained from tensile tests used in impact simulations, it may not be as precise as it could be. The hypothesis

in this study is that the damage information from impact tests can be used to compare the various materials, but it could also be used as material information for modelling. For example, tweaking the material properties used in the simulation would result in a deformation and plastic strain damage that would resemble the experimental results. Adjusting the “Structural Steel NL” material in Ansys, eventually the resultant width would be approximate 3.7 mm, as per the experimental result and the modified material model would then represent the materials in the conditions tested.

The calculated equivalent plastic strain is shown in Figure 4-13, where the maximum damage is in the contact area between the ball and the specimen, normal to the velocity trajectory. The strain is reduced gradually outwards from this contact region, in a pattern as expected from a non-conforming contact. Plastic strain ranges from 800,000 με in the contact surface to around 90,000 με, a few millimetres away from the contact surface. Contained plastic deformation is the state where the plastic deformation remains confined below the surface for pressures between 1.1 and 2.8 times the yield stress of the material [192]. The stress in the contact is well above 2.8 times the yield of the material, which results in plastic deformation that covers the contact area and expand outwards. The specimen plastic damage form the simulation is shown in Figure 4-14, where the bulging of the surface raised at the circumference of the cavity is marked by two red dashed lines. The bulging is lowered back to the surface height in a smooth, gradual fashion, at a distance almost equal the cavity diameter, as indicated by the red arrows A and B. The depth and width of the cavity as well as the plastic damage can be measured from the microstructure grain deformation, by sectioning the specimen. The proposed exercise of adjusting material models to match experimental results should be combined with measurements of the cavity width, the plastic strain damage and depth of cavity as well as. The successful validation of the material models for larger geometries and loads could then be used for impact simulations in industry.

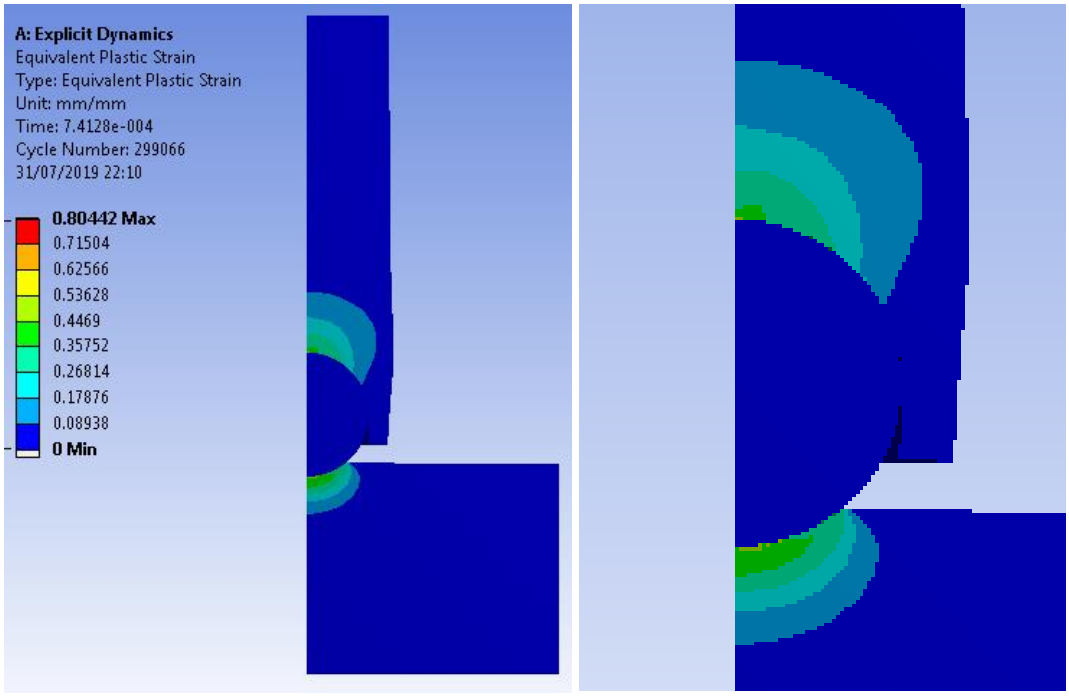

Figure 4-13 Equivalent Plastic Strain (enlarged area of interest on the right)

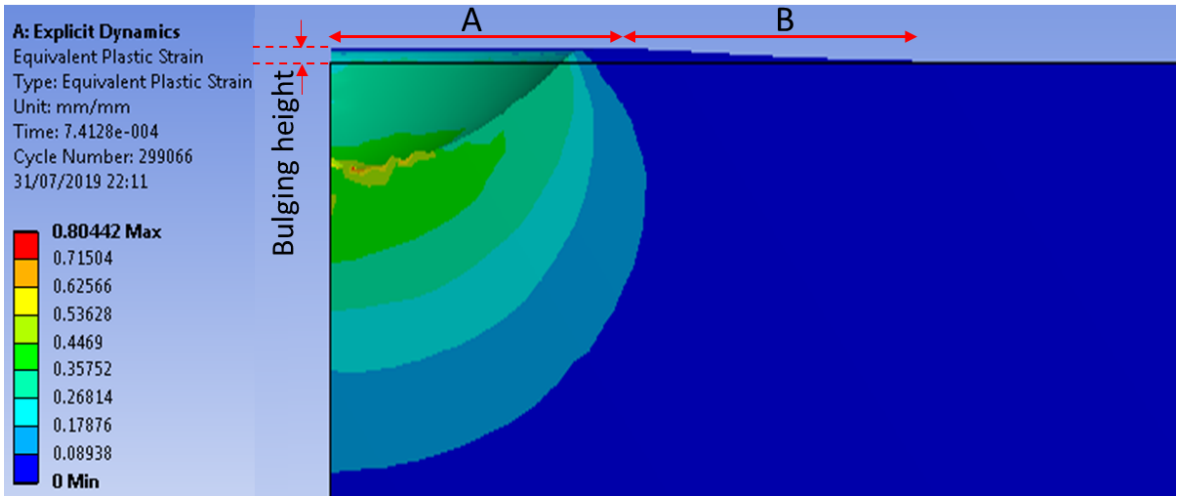

Figure 4-14 Specimen Equivalent Plastic Strain after rebound

An effort was made to simulate a larger model of a wheel and crossing nose. The analysis was performed purely to understand the computational requirements and limitations of running such an analysis and to obtain an idea of the contact patch based on the given geometry and estimated material properties. Non-linear materials from Ansys were used and the elastic modulus was changes to190 GPa for the rail and 170 GPa for the wheel. The mesh in Figure 4-15 has 110,602 nodes and 602,481 elements. An explicit simulation was performed with 10,499 cycles and a timestep of 3.8×10^{-8} s, representing 0.4 ms total simulation time and the analysis was solved in three hours on a standard laptop (Windows 7, 64-Bit, 4-core, i5-6200 CPU@2.30 GHz, 8 GB RAM). The speed of the wheel was set to 36 m s^{-1} and a small "weight" cylinder was added in the centre of the wheel, having the same initial speed as the wheel. The density of the "weight" cylinder was altered so that its total weight was 7,500 kg. This represents 1/8th of the weight of a 30 tonne carriage and the contact with the wheel was set to frictional as opposed to bonded. This is to ensure that the carriage mass initial trajectory would not be affected by the wheel halting from the impact, while the mass would still interact with the wheel with regards to momentum effects. The initial speed of train was estimated based on average speed that trains will go over crossing noses. Various train speeds were used in modelling research discussed in section 2.2.2, from 60 km h^{-1} to 160 km h^{-1} and with reaction forces of 75 kN to 310 kN respectively for the speed range, where the force is proportional to the impact speed. A speed of 36 m s^{-1} (129.6 km h^{-1}) was used in this simulation, slightly higher than the average speed used in other research to ensure that sufficient damage would occur. The reaction force from the impact in this simulation was 230 kN with an initial contact stress of 1 GPa, as shown in Figure 4-16. This is in agreement with the other research data mentioned here. The contact stress/reaction force fluctuates significantly due to the small timesteps of the calculation. The contact is better established at 0.3 ms and the corresponding stress/force at that timestep is quoted here. Plastic stain on the rail is shown in Figure 4-17 as a reference of what the contact patch damage from one cycle may look like. Repeating the simulation multiple times where each time the wheel impacts a different area on the rail, may result in rail surface deformation similar to that in the field.

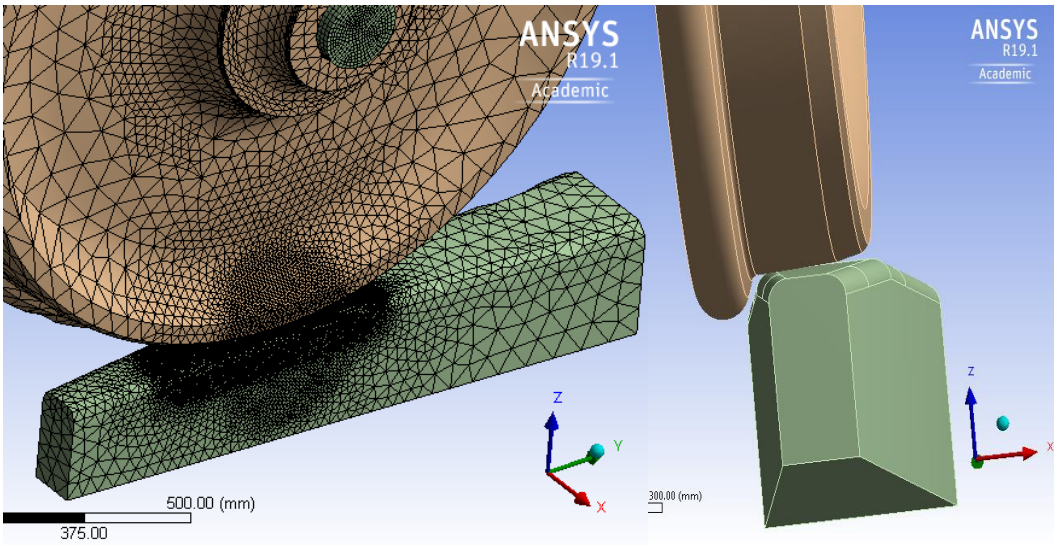

Figure 4-15 Mesh of the wheel and crossing nose FEA model in Ansys

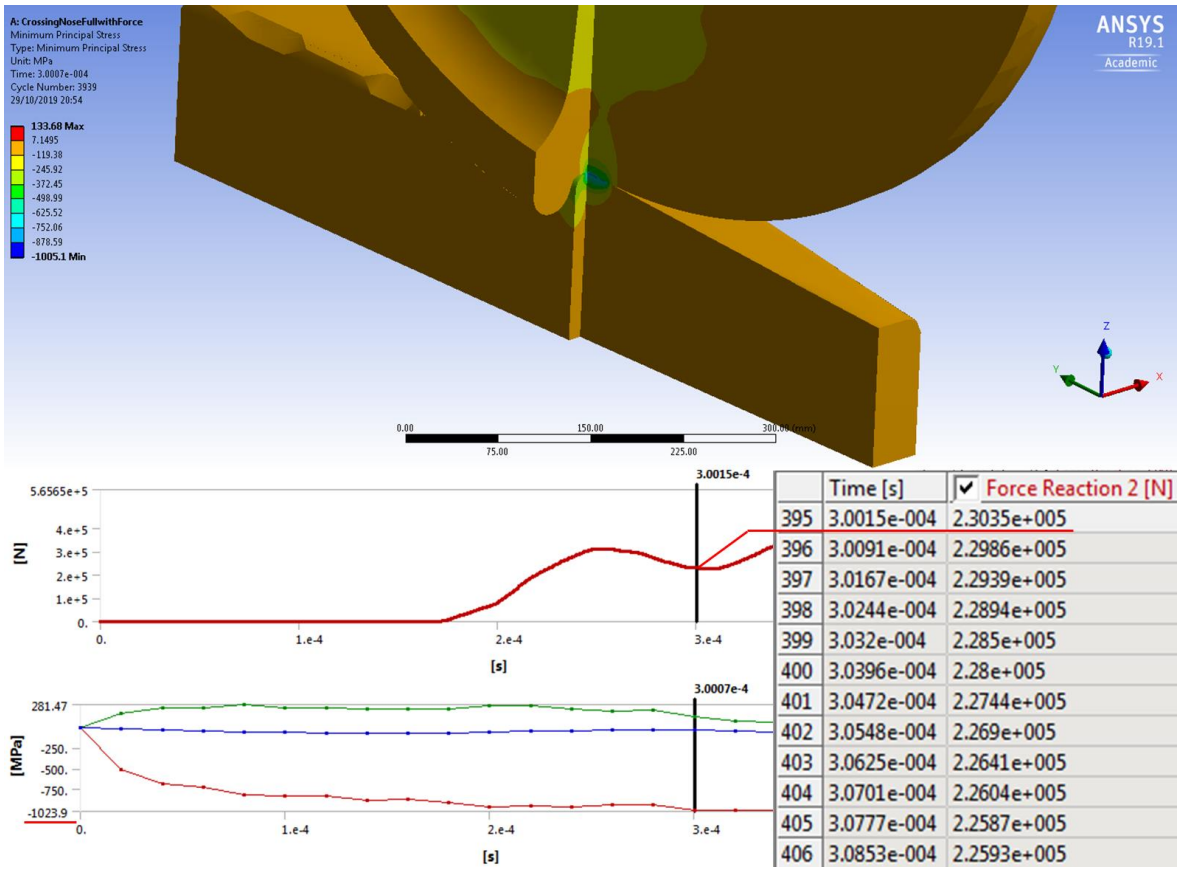

	Time [s]	Force Reaction 2 [N]
395	3.0015e-004	2.3035e+005
396	3.0091e-004	2.2986e+005
397	3.0167e-004	2.2939e+005
398	3.0244e-004	2.2894e+005
399	3.032e-004	2.285e+005
400	3.0396e-004	2.28e+005
401	3.0472e-004	2.2744e+005
402	3.0548e-004	2.269e+005
403	3.0625e-004	2.2641e+005
404	3.0701e-004	2.2604e+005
405	3.0777e-004	2.2587e+005
406	3.0853e-004	2.2593e+005

Figure 4-16 Minimum Principal Stress on rail and wheel (cross-section) and corresponding reaction force on rail

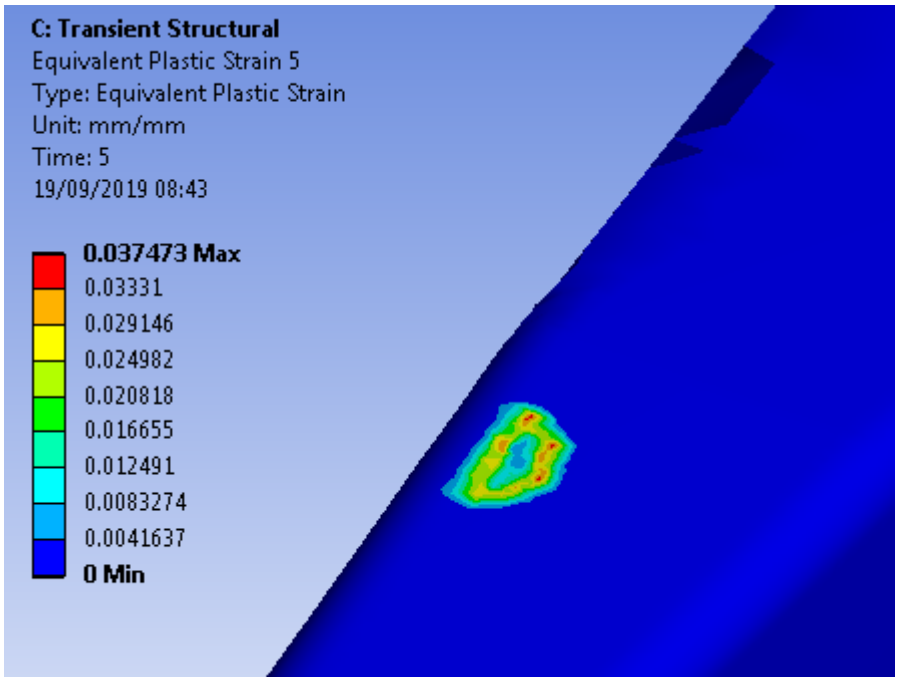

Figure 4-17 Plastic strain on rail

4.2.4 Bending

Bending tests of laser clad and chrome plated coatings are discussed in section 6.5. In standard tensile test specimens that have a simplistic dog-bone shape, the stress is calculated using the width of the gauge (therefore area) and the force applied during testing. This is not possible with three-point bending, due to the complicated geometry, where the stress does not flow through a well defined and measurable area. The preliminary FEA modelling in Ansys was produced in order to estimate the stresses acting on the sample during the bending tests. Furthermore an effort was made to adjust the material model used in the simulation to represent the experimental results as discussed in the previous section, however, this was done only for the elastic part of the test. Severe plastic deformation was not modelled. The basic parameters used in the simulation are listed in Table 4-3. The simulation was modelled based on the geometry of the larger clad specimen used in the UTM bend tests, see Figure 5-49 for geometry details.

Table 4-3 FEA parameters

Nodes	102,744
Elements	55,859
Frictional contact	0.3
Load Steps	1 kN, 4 kN, 8 kN and 10 kN

The material properties used in the model were taken from nanoindentation tests, which are described in section 5.1. The material properties are listed in Table 4-4.

Table 4-4 Material properties used in Ansys for FEA calculation

	Theoretical / Nanoindentation (see section 5.1)	**Unit**
	Substrate (Forged Steel)	
Density	7850	*Kg m^{-3}*
Elastic Modulus	**173.9**	*GPa*
Poisson's ratio	0.3	
Yield Strength	400	*MPa*
	Inconel 625	
Density	7850	*Kg m^{-3}*
Elastic Modulus	**160.8**	*GPa*
Poisson's ratio	0.3	
Yield Strength	400	*MPa*
	Technolase®	
Density	7850	*Kg m^{-3}*
Elastic Modulus	**269.1**	*GPa*
Poisson's ratio	0.3	
Yield Strength	400	*MPa*

The mesh is shown in Figure 4-18 where the two clad layers were modelled as individual bodies which are bonded to the substrate. Figure 4-19 illustrates the loads and constraints. The collinear pins were fixed in space, while the force was applied on the forming pin. Frictionless support was added on outer sections of the specimen and on flat faces on the pin, in order to stabilise the analysis by controlling the movement in the vertical direction only.

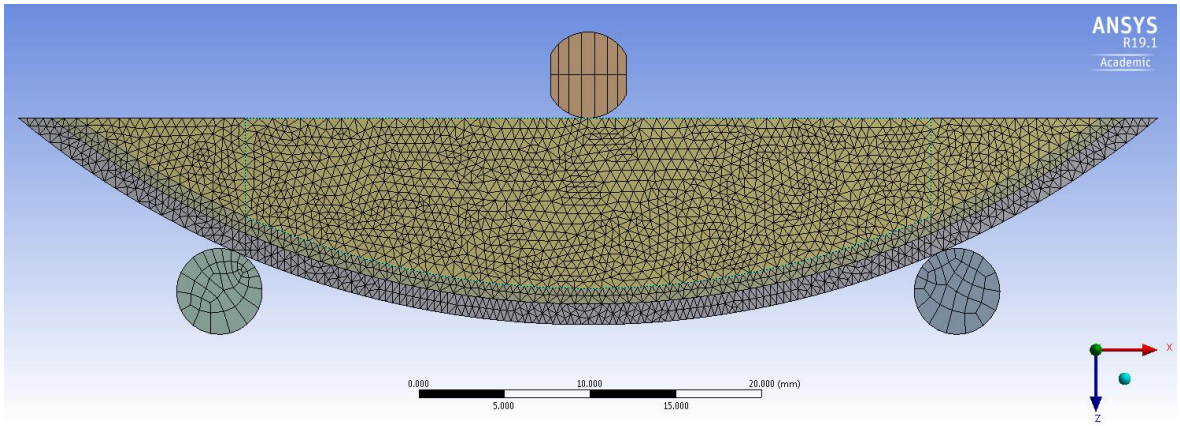

Figure 4-18 Mesh geometry

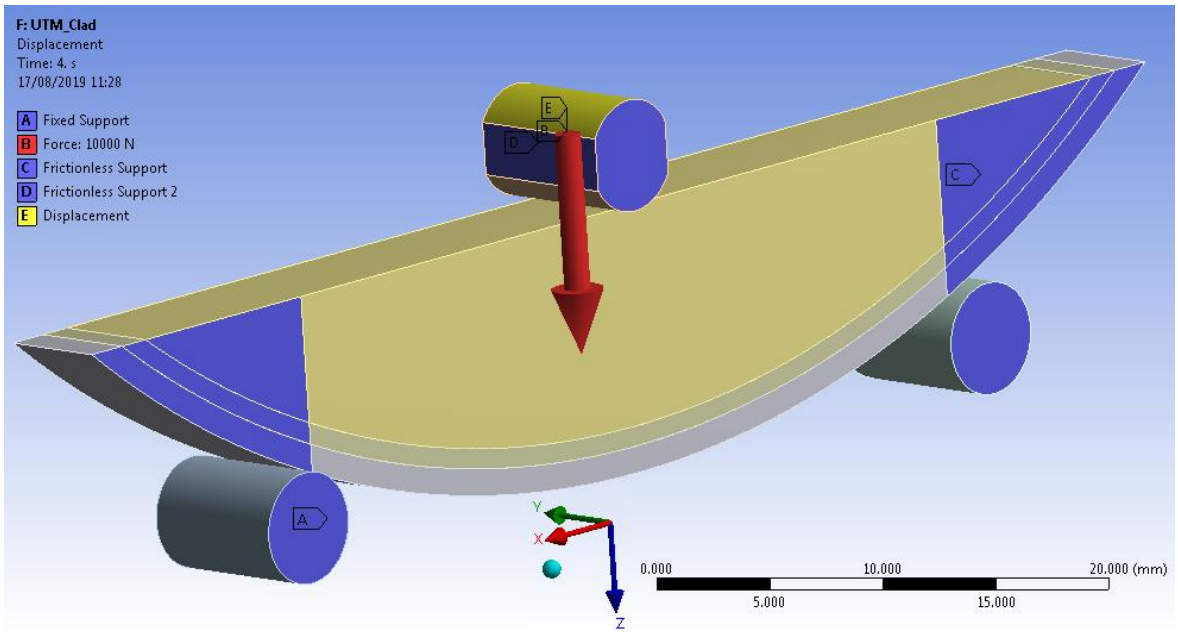

Figure 4-19 Loads and constraints

The following results are for 10 kN load, for which the resultant stresses are within the elastic limit of the composite clad material. The elastic limit is verified by Figure 4-25, which is the experimental data from the UTM test, a detailed description of the tests is in section 5.6. The Equivalent (von-Mises) stress is shown in Figure 4-20 while the Maximum (tensile) and Minimum (compressive) Principal stresses are shown in Figure 4-21 and Figure 4-22 respectively. Figure 4-23 shows the Maximum Principal Elastic strain, where the highest elastic strain area coincides with the highest tensile stress, as intended by the three point bend test design.

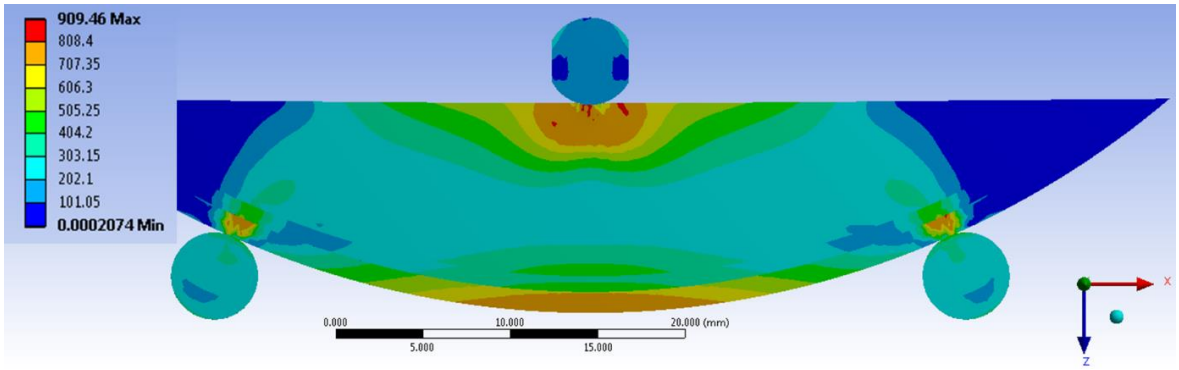

Figure 4-20 Equivalent (von-Mises) Stress

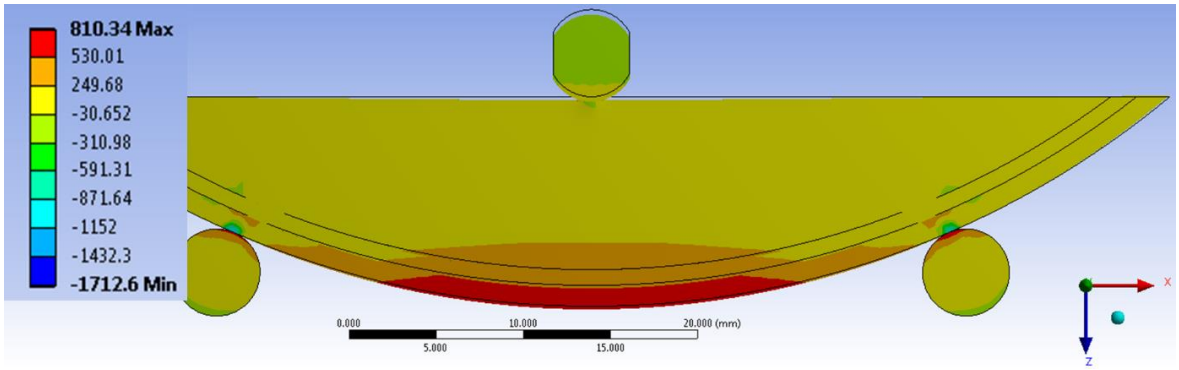

Figure 4-21 Maximum Principal Stress

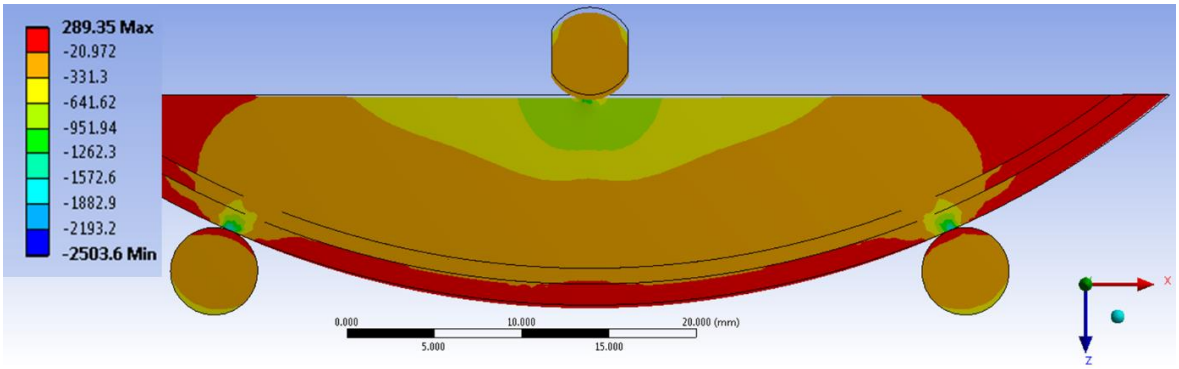

Figure 4-22 Minimum Principal Stress

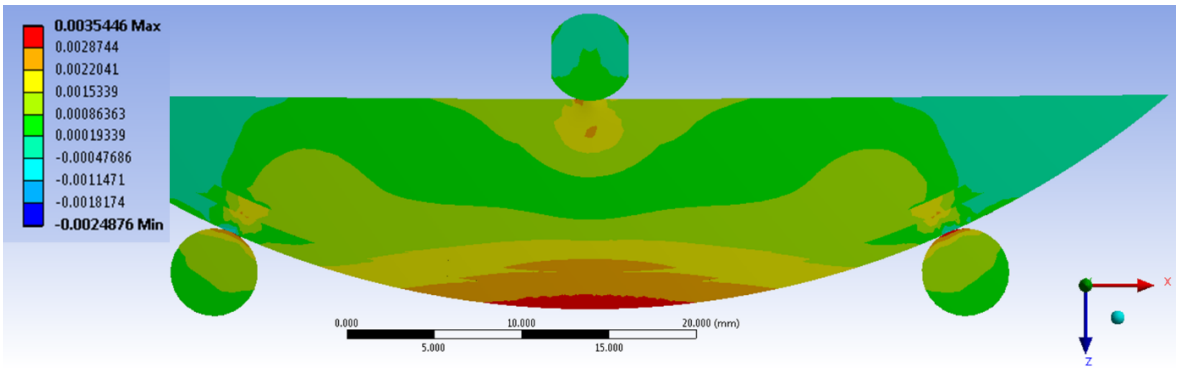

Figure 4-23 Maximum Principal Elastic Strain

The maximum vertical displacement figure in Figure 4-24 is the same as the displacement measured on the UTM by the movement of the forming pin and displayed as the x-axis in Figure 4-25.

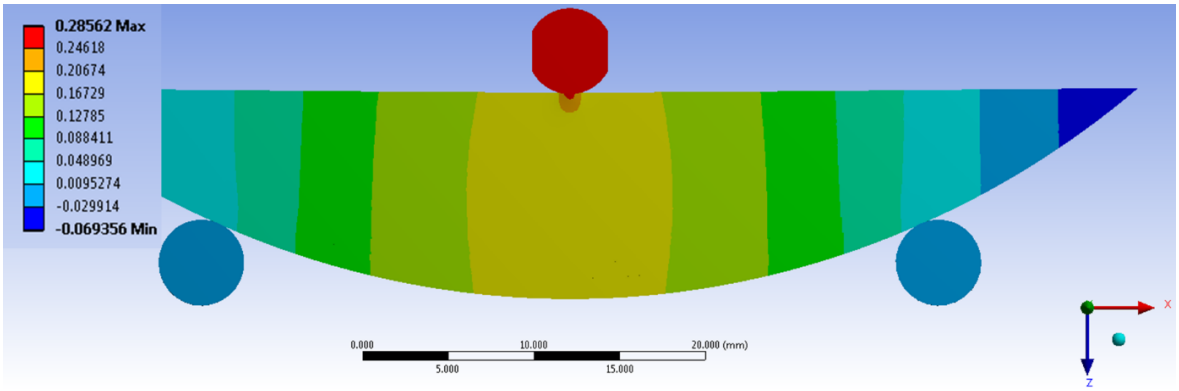

Figure 4-24 Deformation in the vertical (Z) direction

However, the figures measured for various loads do not match the displacement figures measured during the test. The “Clad FEA” curve in Figure 4-25 was expected to overlap “Clad 1” and “Clad 2“. An effort was made to modify the Elastic Modulus for each material so that the elastic behaviour of the specimen under load would adjust accordingly. The Elastic Modulus values that adjusted the curve anywhere near the expected position was for an order magnitude smaller. Certainly this indicates the difficulty in predicting material properties by simple adjustment of material properties.

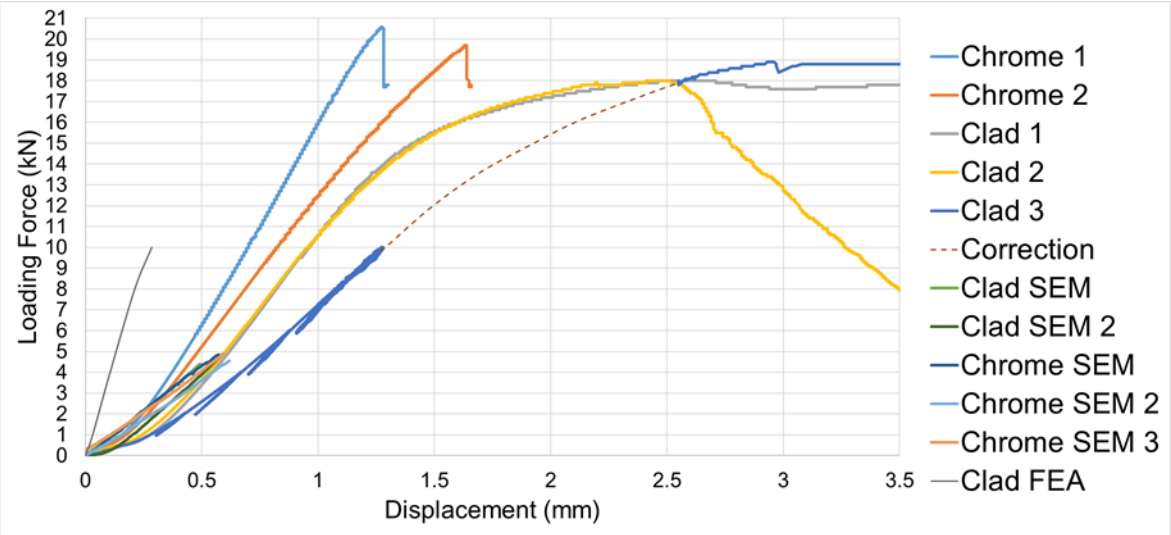

Figure 4-25 UTM test results including FEA results

One hypothesis for this issue is that plasticity was induced in the specimen. Plastic strain was estimated by the modelled in small regions near the pin contact area. The yield stress for all materials was set to a nominal 400 MPa. This was not measured by nanoindentation or other method. The mismatch of the simulation and experimental results hints that the yield values must be higher than 400 MPa, since the specimen in the simulation should behave more elastically, thus matching the experimental curves.

4.2.5 Modelling summary

Exploratory modelling work was performed to understand the requirements for producing or manipulating material models. Results for contact stress were produce with the Hertzian calculator to determine twin disc test conditions. Results from FEA (Ansys) were used to determine the test parameters of the impact test, with regards to drop height and weight. The damage on the specimen was in the form of an impact cavity and the simulation resulted in a cavity close to the width of the Manganese test piece. An effort was made to simulate in FEA a larger model of a wheel and crossing nose of which resulted in reaction force and contact stress in agreement with the other research in literature. The FEA method was also used to visualise the stresses in the bending test specimen which cannot be calculated directly from the test.

An effort was made to adjust the material model used in the bending simulation to represent the experimental results, however, this resulted in material properties with an order magnitude lower than expected. This is possibly attributed to plastic deformation occurring, which was not accounted for in the simulation performed in the elastic load range. There is great difficulty in predicting material properties by simple adjustment of material properties, due to the multiple parameters involved. In the bending simulation plasticity was induced, while in the impact simulation deformation of the pin introduced an uncertainty.

There is a hesitation in industry to adopt new and niche technologies, especially when the manufacturing or investment cost is high and traditional manufacturing techniques are established

and cost effective. This is the case with laser cladding and the production of wear properties and material models could convey confidence in the use of laser cladding in industry. Predictive tools can complement the selection of materials and coatings suited for specific applications, for example cladding materials on railway lines that experience high wear. With the correct material models the simulations produced here can predict the performance of such materials in other industries with similar interfaces.

This page was intentionally left blank

5 EXPERIMENTAL PROCEDURE

Five laboratory tests were performed for five interfaces, where three laser clad coating materials have been tested. The first part in this chapter is a summary of the parameters for all the materials used in the tests. The rest of the chapter is the experimental procedure for each interface test. The analysis of the results and discussions for each test is included in chapter 6 and a general discussion on all tests in chapter 7.

5.1 Materials characterisation

The materials used for this study are summarised in Table 5-1. A summary of the chemical composition for each material and coating is listed in Table 5-2, followed by nanoindentation test results for the MSS coating used in the rail tests, Technolase® and Inconel 625 coatings used in the steel industry interfaces. The Stellite 6 material was not investigated with nanoindentation, figures from literature are quoted in this section. Surface roughness was measured using the Alicona IFM SL G1 Vb6, which was calibrated within a year of obtaining the results. Micro-hardness was obtained with the Struers Durascan automated tester, using a Vickers indenter with 0.3kg load, while nanoindentation tests were performed using the Hysitron Ti-Premier, using a Berkovich diamond indenter with an Elastic Modulus of 1140 GPa and Poisson's Ratio of 0.07. The nanoindentation equipment was calibrated with fused quartz and polycarbonate calibration samples prior to testing.

Table 5-1 List of specimens tested with OES

	Name	Area	Identifier
1	Stellite 6	From literature	SAEJ467b(1968) Special Purpose alloys
2		OES - as clad on S275JR plate	
3	MSS	From literature	Chromecore DN-S (EN14700:TZFe7)
4		OES - as clad	on R260 (R9)
5			on R200 (R3)
6	R260	From literature	EN13674-1:2017
7	R400HT	OES – rail samples	
8	Mn Steel	OES – rail sample (although the crossing nose material may have been explosion hardened [193] or work hardened through its service life, test samples were taken away from the railhead due to machining restrictions)	
9	R8 Wheel	From literature	EN 13262:2004 Standard ER8
10		OES – wheel specimens	WBW-7 (ex-service wheel from Wabtech)
11			LC (ex-service wheel from other source)
12		From literature	Wheel ER8, EN 13262 (Colombian report)
13	Rod Mill Pinion	OES ex-service	
14	Work Roll	OES, forged-not from service	
15	Work Roll	OES, forged-not from service, heat treated	

Chemical composition results from optical emission spectroscopy (OES) for all materials, with the exception of Technolase®. The OES method requires a flat surface of at least 12 mm in width, in order to vaporise atoms on the sample's surface for capturing their unique emission spectrum with a

detector. The Technolase® sample was narrow (9mm) and on a curved surface, therefore it was not possible to obtain its chemical composition with this method. The tests were performed by Rotech Laboratories, which is a UKAS accredited laboratory. The materials that were analysed are shown in Table 5-1. Rail materials R260 and R400HT were analysed while R350HT has the same chemical composition as R260 and it was decided not to analyse the chemical composition of the premium rail material since this would identify their commercial name, for which no permission was given to do so by the manufacturer. The R8 wheel and rod mill pinion taken from industrial service, as well as forged work roll material samples were also analysed. The work roll material was analysed before and after heat treatment, to observe if any changes in chemical composition had occurred during the heat treatment. Copper and Aluminium values were measured as being lower and higher respectively after heat treatment. This could be attributed to the fact the two separate samples were used and their composition may differ slightly. It should not be ruled out that the chemical composition could be altered during heat treatment, however, this was not obvious from this analysis.

In Stellite 6, chromium provides corrosion resistance, while strength is achieved with hardening elements such as Molybdenum and Tungsten, whereby they contribute to hardening via precipitation hardening in carbides and intermetallic phases such as Co (Mo,W) [3].

Table 5-2 Results from OES analysis

	Name	C [%]	Si [%]	Mn [%]	Cu [%]	Ni [%]	Cr [%]	Mo [%]	V [%]	Al [%]	Co [%]	W [%]	N [%]	Fe Balance [%]
1	Stellite 6	1.15	0.55	0.45	--	1.50	29	0.75	--	--	62.10	4.5	--	--
2		1.24	1.17	0.30	0.04	2.07	29.64	0.40	0.06	0.008	56.77	4.92	--	3.37
3	MSS	0.05	0.80	1.20	--	3.00	14.50	0.50	0.50	--	1.80	0.80	0.05	76.80
4		0.34	0.20	0.91	<0.01	2.27	9.51	0.25	0.28	--	1.22	0.45	--	84.56
5		0.22	0.18	0.87	<0.01	2.25	9.53	0.24	0.27	--	1.22	0.46	--	84.75
6	R260	0.60-0.82	0.13-0.60	0.65-1.25	--	--	<0.15	--	0.0300	0.0040	--	--	0.01	99.90
7	R400HT	0.931	0.251	1.269	0.017	0.015	0.275	0.0068	0.0035	0.0002	0.005	0.150	--	97.05
8	Mn Steel	1.11	0.28	12.07	0.18	0.35	0.45	0.18	<0.01	0.011	--	0.10	--	85.26
9	R8 Wheel	0.56	0.400	0.800	0.300	0.300	0.300	0.08	0.06	--	--	--	--	97.17
10		0.55	0.30	0.74	0.040	0.07	0.28	<0.01	<0.01	0.018	--	--	--	97.98
11		0.53	0.31	0.74	0.170	0.10	0.16	<0.01	<0.01	0.026	--	--	--	97.95
12		0.54	0.232	0.745	0.225	0.114	0.172	0.05	--	--	--	--	--	97.90
13	Rod Mill Pinion	0.16	0.21	0.50	0.170	1.38	1.60	0.28	0.01	0.029	--	--	--	95.64
14	Work Roll	0.84	0.72	0.24	0.42	0.21	5.02	0.33	0.02	0.006	--	--	--	92.19
15	Work Roll (treated)	0.85	0.71	0.25	0.06	0.22	5	0.32	0.02	0.024	--	--	--	92.54

An interesting aspect to testing of laser clad components is nanoindentation testing, which unlike microhardness and hardness testing allows the measurement of mechanical properties, such as elastic modulus, from load versus displacement curves, at fine spacings through the material. Nanoindentation was performed in three areas on the MSS mounted sample. Figure 5-1 is a schematic of the indentation pattern, showing areas A, B and C. Each area is a matrix of three rows by twenty indentations. Indentations in area A were taken on the MSS coating, near the edge of the specimen, area B was a crossover between the MSS coating, dilution zone and substrate and

area C was indentation of the R260 substrate material. These properties were obtained with 10 mN force and using the Oliver-Phar method [194]. The root mean square value of three indentation measurements at the same horizontal position was calculated for each region and shown as datapoints in Figure 5-2 to Figure 5-4. The line connecting the datapoints is for visualisation purposes only. The horizontal plot lines in each figure indicate the root mean square of all the datapoints for each dataset, as the average measurement of the dataset.

The hardness on the MSS clad layer was in the region of 724 HV, as shown in Figure 5-2. The hardness was found to be increasing near the dilution zone, as marked in Figure 5-3, while the substrate hardness was found to be around 300 HV, as shown in Figure 5-4. Average elastic modulus values were around 177 GPa for the clad material and 168 GPa for the R260 material. The elastic modulus of the dilution zone ranges between 177 GPa and 168 GPa, and not in a linear fashion, as this region is not homogeneous.

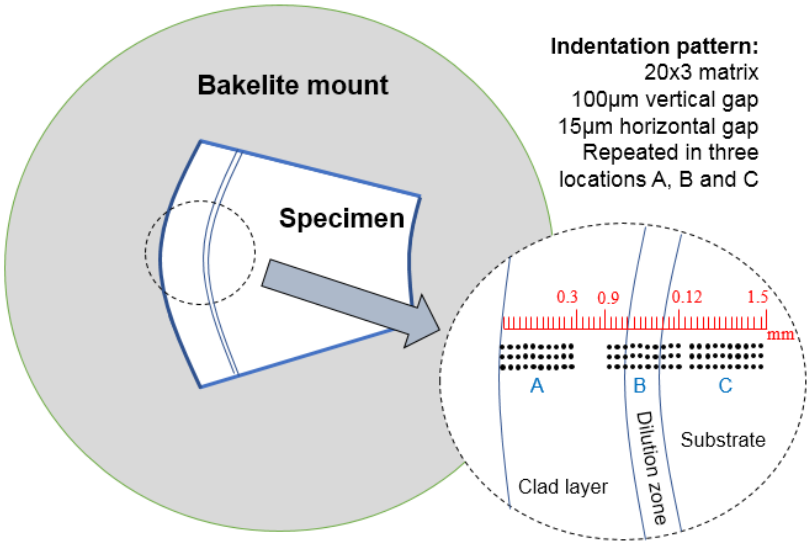

Figure 5-1 Schematic of indentation pattern

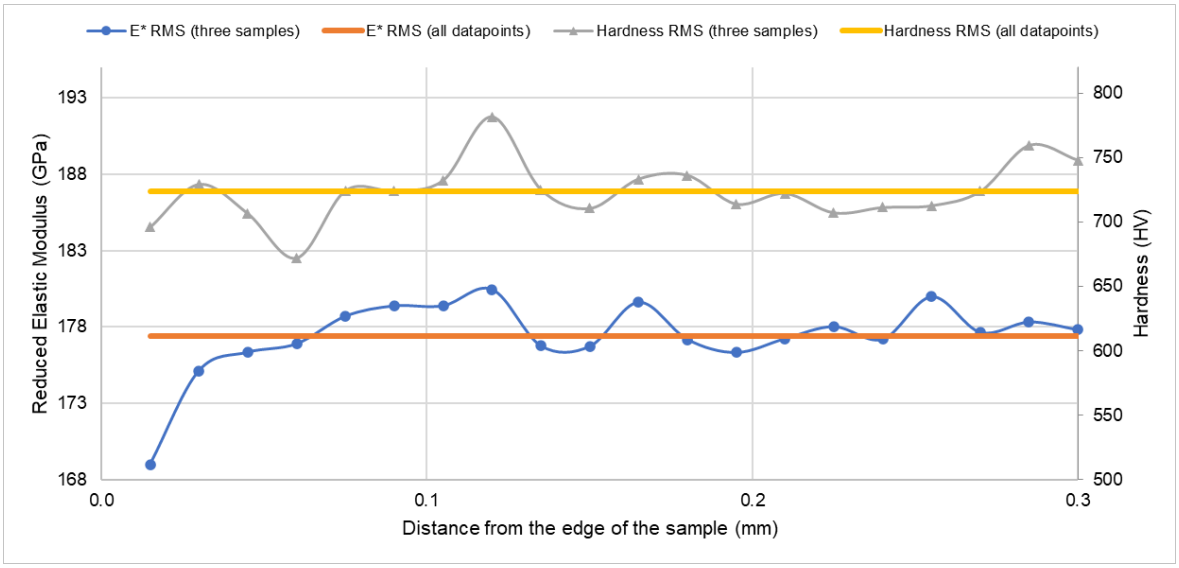

Figure 5-2 Location A results (MSS clad)

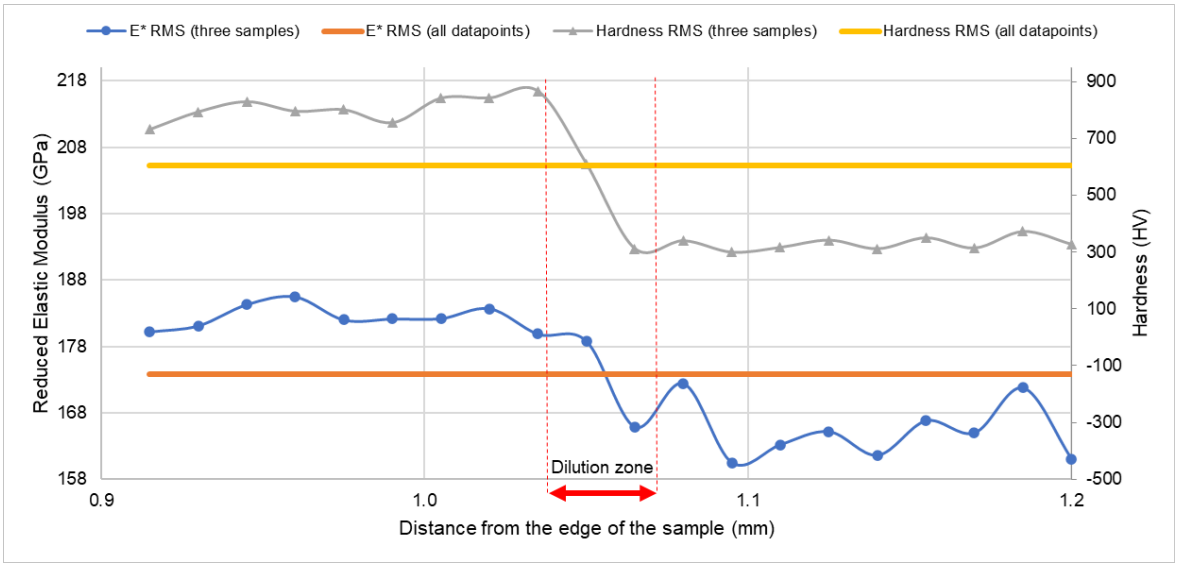

Figure 5-3 Location B results (MSS clad, dilution zone and R260 substrate)

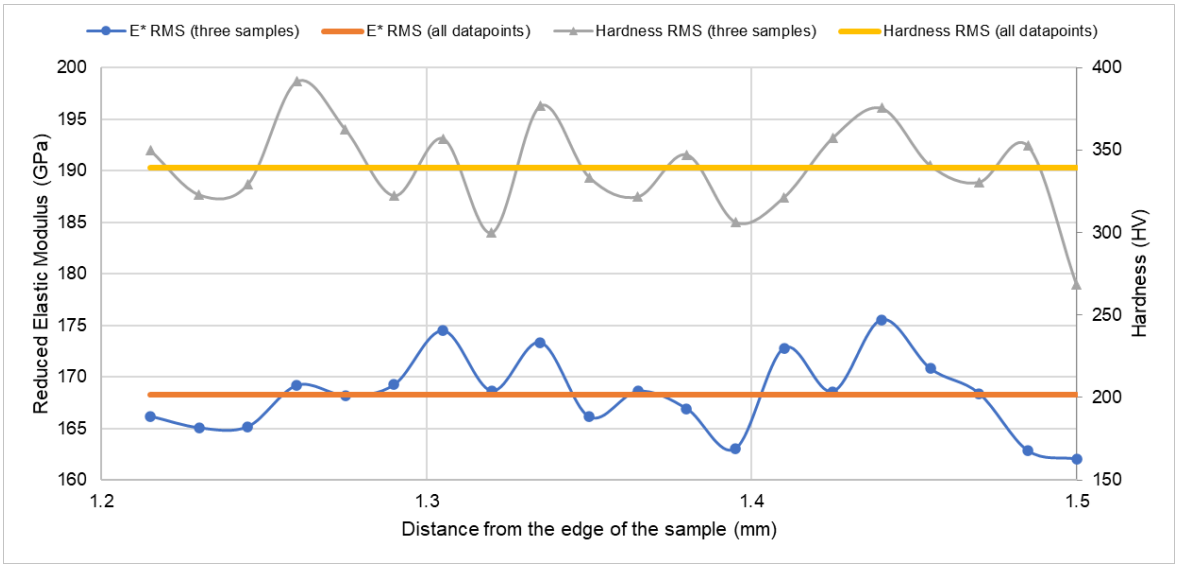

Figure 5-4 Location C results (R260 substrate)

Sets of four nanoindentation measurements were obtained from five regions in the sample cladded with Technolase® and Inconel 625. The regions include the WC spherical particle centre, the Technolase® material (excluding the WC particles), the dilution zone between the Technolase® and Inconel 625, the middle of the Inconel 625 layer and the substrate (pinion forged steel). The force vs displacement graphs shown in Figure 5-5 were illustrated using different colours for each repeat nanoindentation measurement taken. The spread of the result indicates the variation of properties in each coating, which is significant for understanding the role of each material in the coating matrix, especially when these results are used in modelling and computer simulations.

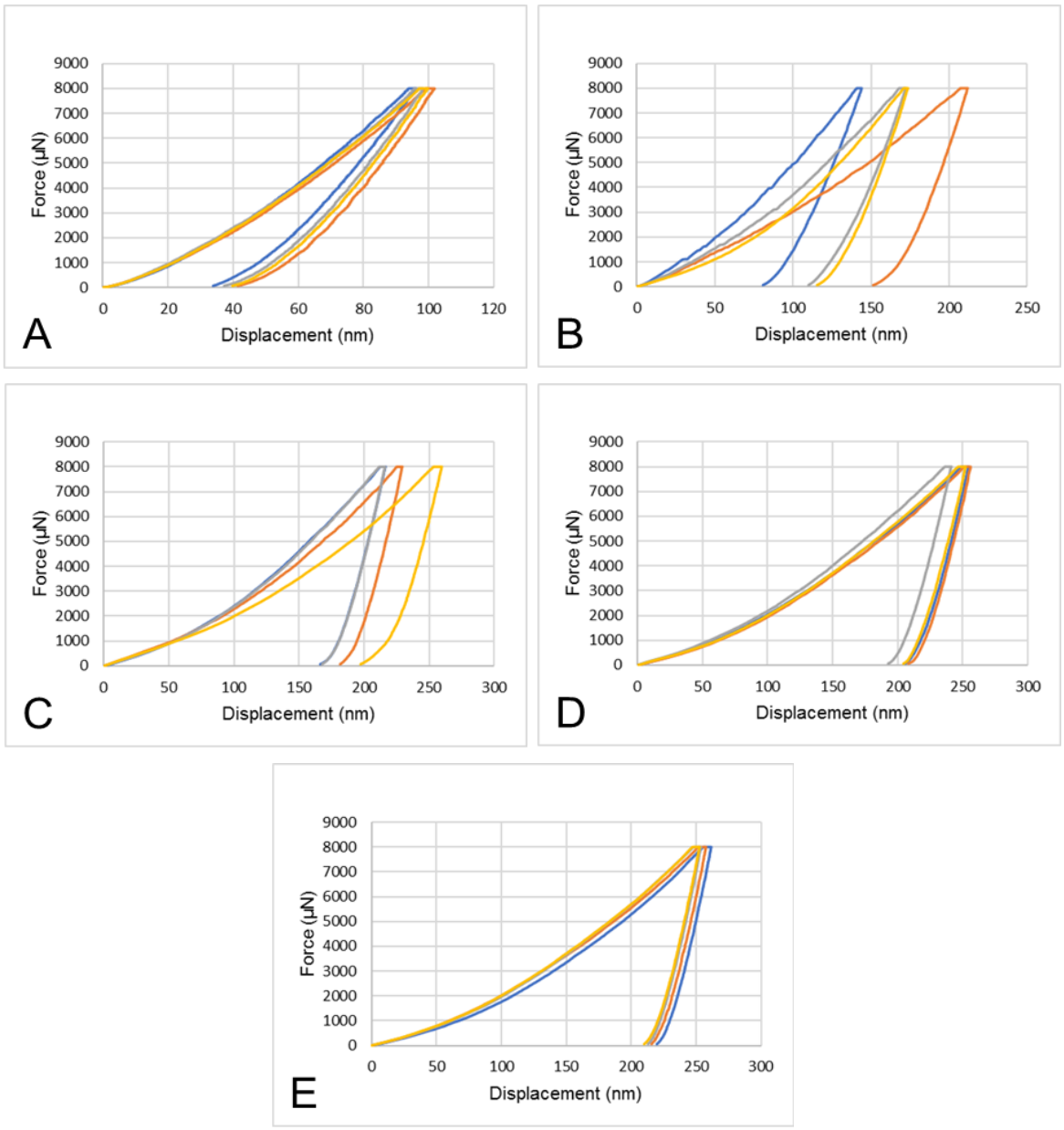

Figure 5-5 Nanoindentation Force vs Displacement graphs - A: WC particle, B: Coating, C: Dilution between Technolase and Inconel 625, D: Inconel 625 and E: Substrate of forged steel

Table 5-3 (2 x 2 matrix) and Table 5-4 (20 x 1 matrix) are summaries of the mean average of four and twenty nanoindentations respectively, on various locations on the sample. The substrate and Inconel 625 have similar reduced elastic modulus (161 and 174 GPa) and hardness (431 and 459 HV), in comparison to the Technolase® that has a reduced elastic modulus of 250 GPa and a hardness of 1770 HV. The Technolase® is about four times harder and 50% stiffer than the Inconel 625 and substrate. This is due to the WC particles which have a stiffness value of 341 GPa and their surrounding alloy which has a value of 196.7 GPa as opposed to 160-174 GPa for the Inconel and substrate. The hardness of the WC particles is exceeding 3000 HV which makes it ideal for abrasive applications. The hardness of the surrounding material is around 1000 HV which results in an average coating hardness of around 2000 HV, significantly higher than other coatings compared in this research, such as chrome plating hardness.

Table 5-3 Mean average Elastic Modulus and Hardness for 2 x 2 matrix (20 µm spacing) nanoindentation test at 8 mN force in various locations

	WC	Coating	Dilution	Inconel	Substrate	Mean average
E* (GPa)	341.4	196.7	179.4	160.8	173.9	210.4
E* (GPa)	341.4	196.7	----	----	----	**269.1**
H (GPa)	31.9	10.4	5.4	4.5	4.2	11.3
H (HV)	3251	1057	549	459	431	1149
H (HV)	3251	1057	----	----	----	**2154**

Table 5-4 Average Elastic Modulus and Hardness for 20 x 1 array (20 µm spacing) nanoindentation test at 8 mN force in various locations

	Technolase®	Dilution Technolase® / Inconel 625	Dilution Inconel 625 / Substrate	All
E* (GPa)	252.8	218.2	174.1	215.0
H (GPa)	17.4	13.1	5.7	12.0
H (HV)	1769.8	1338.5	577.7	1228.7

The through thickness hardness of the two coatings and substrate has also been captured with a micro-hardness test as shown in Figure 5-6. The graph is split into three distinct regions, the first is the Technolase® coating where the average hardness is 550 HV. The Sphérotène® spherical particles hardness measurements were excluded from this graph and shown in Figure 5-7. The middle region in Figure 5-6 is the intermediate coating layer of Inconel 625, with an average hardness of 272 HV and the region on the right belongs to the substrate material with an average hardness of 325 HV. Two regions have been highlighted, which indicate a transition from one coating to the next, these are the dilution zones. They are characterised by either a sharp rise in hardness or a sharp drop, followed a sharp rise. The laser clad coatings (Technolase® and Inconel 625) exhibit the desired hardness of a harder outer coating with a softer intermediate coating and their dilution zones are in the region of 5% of the coating thickness.

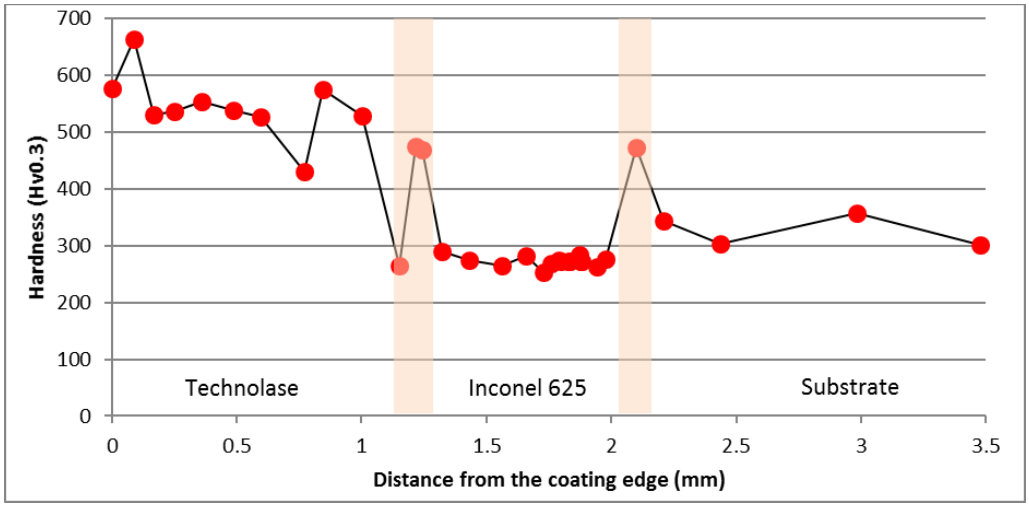

Figure 5-6 Through thickness microhardness (excluding WC particles). The line connecting the datapoints is for visualisation purposes only.

The hardness measurements on WC spherical particles are shown separately in Figure 5-7, with an average hardness of 2500 HV. On the same graph the dilution zone hardness between the two clad

layers and the corresponding image is shown. This includes one measurement of a WC particle that lies close to the dilution zone, which corresponds to the spike on the graph. The hardness changes in stages, with values exceeding 500 HV on the Technolase®, in the region of 450 HV on the dilution zone (highlighted area) and below 300 HV on the Inconel 625.

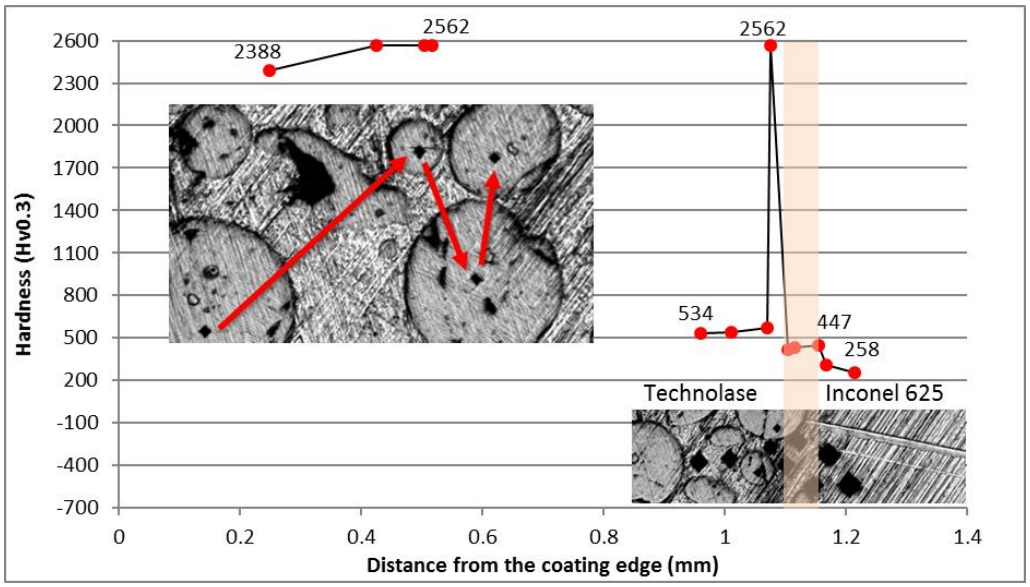

Figure 5-7 Through thickness microhardness (including (WC particles). The line connecting the datapoints is for visualisation purposes only.

Figure 5-8 is a hardness mapping of a small region on the Technolase® coating. The average hardness is 1300 HV, while the maximum hardness measured on the WC spherical particles is 2971 HV. There is a sharp rise in hardness, with no smooth transition between the nickel-based alloy and the WC particles. In some regions, the WC particle shape has not formed a sphere, for example values 1961 HV and 1844 HV in Figure 5-8. Some pitting is evident due to smaller WC particles flaking off during polishing of the specimens, this is highlighted by a red arrow in Figure 5-8.

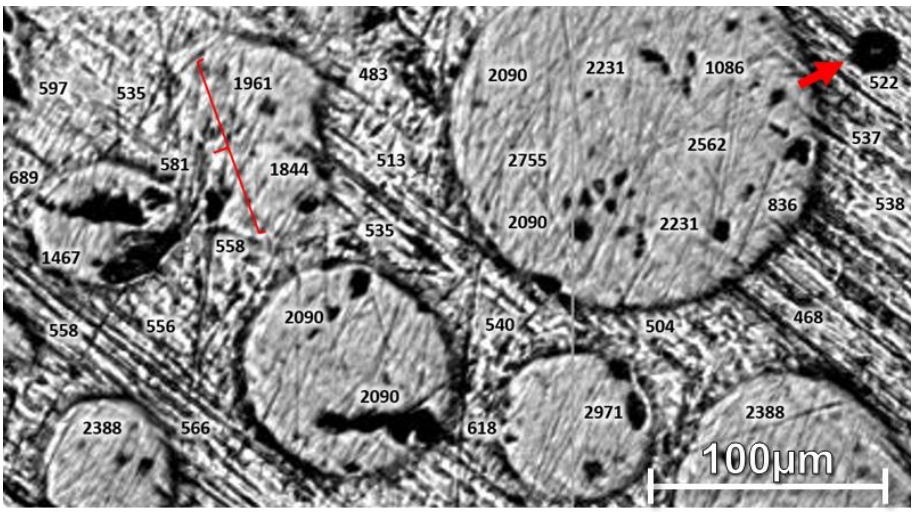

Figure 5-8 Hardness mapping on Technolase® (0.3 kg load)

It is important that the clad coatings have a smooth surface roughness, particularly for the roll mill pinion application. This is due to the hydrodynamic effect on the surface of the pinion during service,

it was advised by Primetals that a surface roughness in the region of Ra 0.6 µm would be acceptable. A much rougher surface may contribute to crack initiation, since the hydrodynamic effects could be amplified by captive bearing fluid in the rougher morphology. The current chrome coating Surface roughness for characterising the Technolase® material was obtained by scanning an area of 20mm x 10mm using the Alicona. The laser clad pinion sample is shown in Figure 5-9. The 2D image of the scan is shown at the bottom of the same figure. In Figure 5-9, two clad areas were identified, 1 and 2, where surfaces A, B and C from area 2 were used for roughness and micro-hardness measurements. The three surfaces are shown in Figure 5-10 as a 3D scan image taken with the Alicona. A graph of the depth measurement, obtained by scanning the primary profile (without filtering) is shown on the same figure, indicating that surface A (Technolase®) thickness was 1.2 mm and surface B (Inconel 625) thickness was 0.8 mm. Surface C was the substrate and used as the reference point for estimating the clad height. All three surfaces have been ground on a cylindrical grinding machine, using diamond grinding discs, and wiped clean with acetone prior to mounting the cylindrical sample onto the Alicona. The stepped surfaces between A-B and B-C, in the 2D image of Figure 5-9, are the untreated clad surfaces and hence why they are shown to have a rough texture.

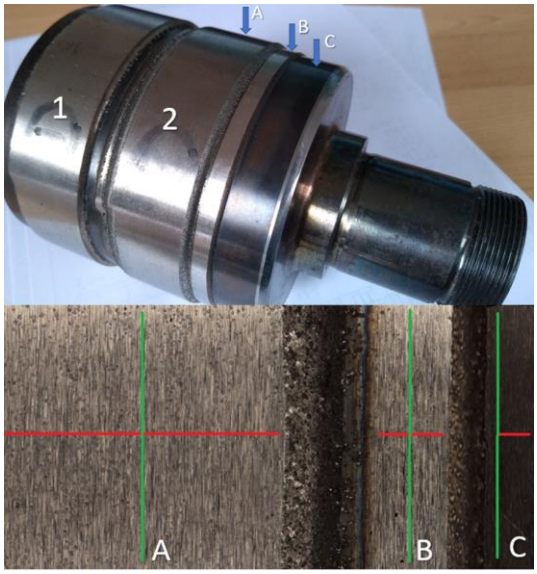

Figure 5-9 Image of pinion with laser cladded coatings and corresponding Alicona scan of surfaces

Surface roughness measurements were obtained for Rz, Ra and Rq, where Ra and Rq are more significant in most applications as they are average results for a chosen set of measurements. Rq is the root mean square of the measurements, whereby all measurements turn positive since they are squared, which means it will always produce positive values, slightly higher than Ra. However, Ra will indicate if there are a lot of negative values, for example more valleys than peaks. Rz is the average of the peak measurements only, it can be important in applications where the peaks of the asperities may alter the tribological performance. Since the cladding was applied in a spiral motion around the cylindrical face of the component, and since the grinding was conducted in a similar fashion, the line scans for surface roughness was taken in two directions, axial (parallel to the part's axis) and parallel to the circumference/perpendicular to the pinion's central axis. These are marked in Figure 5-9, red for axial and green for circumferential.

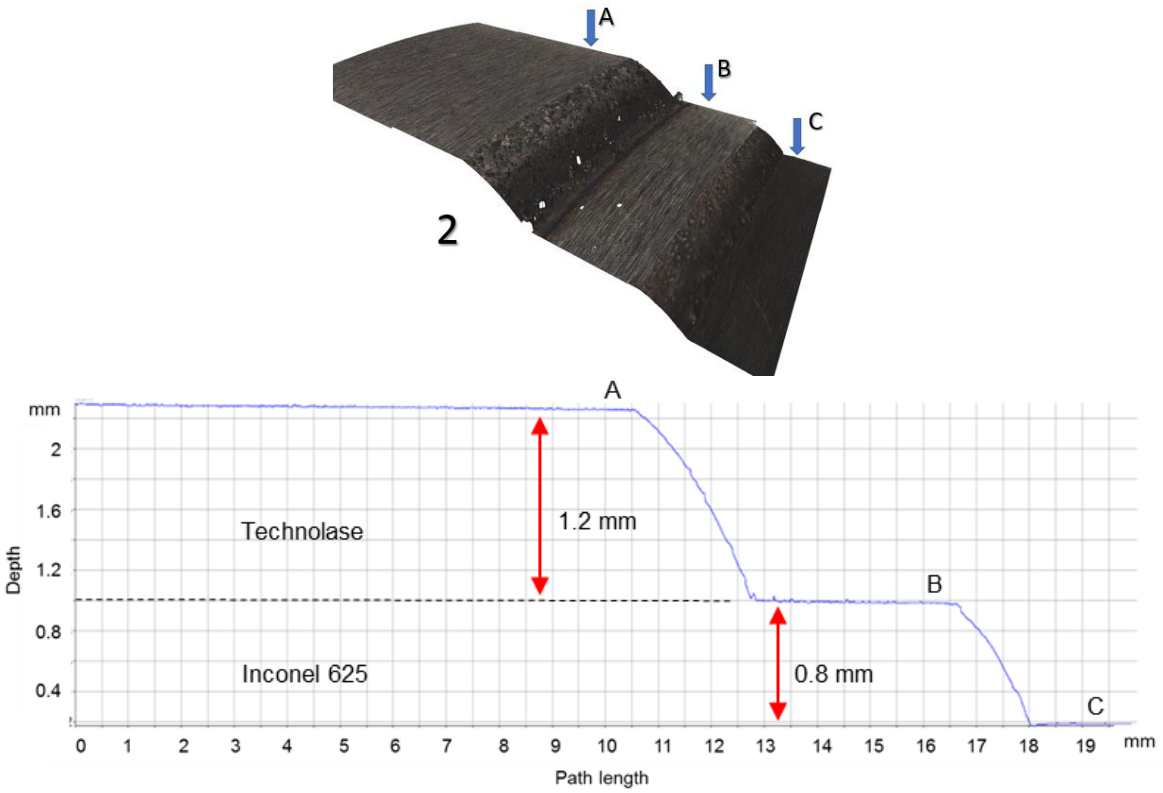

Figure 5-10 Alicona scan of surface A, B and C and corresponding primary profile graph showing the depth of the clad layers

Rz, Rq and Ra results are shown in Figure 5-11, using a cut off value of Lc=800 µm, for the filtering process in the Alicona. An additional sample was also included in Figure 5-11 for comparison, the "Work roll material", which is Technolase® and Inconel 625 clad on cylindrical specimens of work roll steel material, with a diameter of 45 mm. The sample is from parallel tests described in 6.3. Measuring the surface roughness on samples with different substrate material and diameters is significant for evaluating the quality of the clad surface and its application on similar components. Also, the surface on the work roll specimens was ground using a ceramic grinding discs, as opposed to a diamond disc. The Ra values in the circumferential directions are around 0.9 µm for both the work roll clad and roll mill pinion clad (Technolase® top surface). In the axial direction, the work roll Ra value is low at 0.62 µm, while Ra value for the roll mill pinion is much higher to 1.6 µm. Similarly, the axial Rz value of the work roll clad is significantly lower at 3.7 µm, as opposed to 10.4 µm for the pinion clad. Measurements in the circumference direction are very close between work roll and pinion clad, as observed with the Ra values. This is probably due to higher grinding forces in the circumferential direction, rather than the axial direction, as these cylindrical components were span around their central axis in order to perform the grinding. Values of Rz 10.4 µm may not be acceptable for many applications, so the surface finish of the work roll clad material is preferable as it is significantly smoother in both directions. Surface texture tests were undertaken with the work roll clad material only, so the roughness values observed here were acceptable.

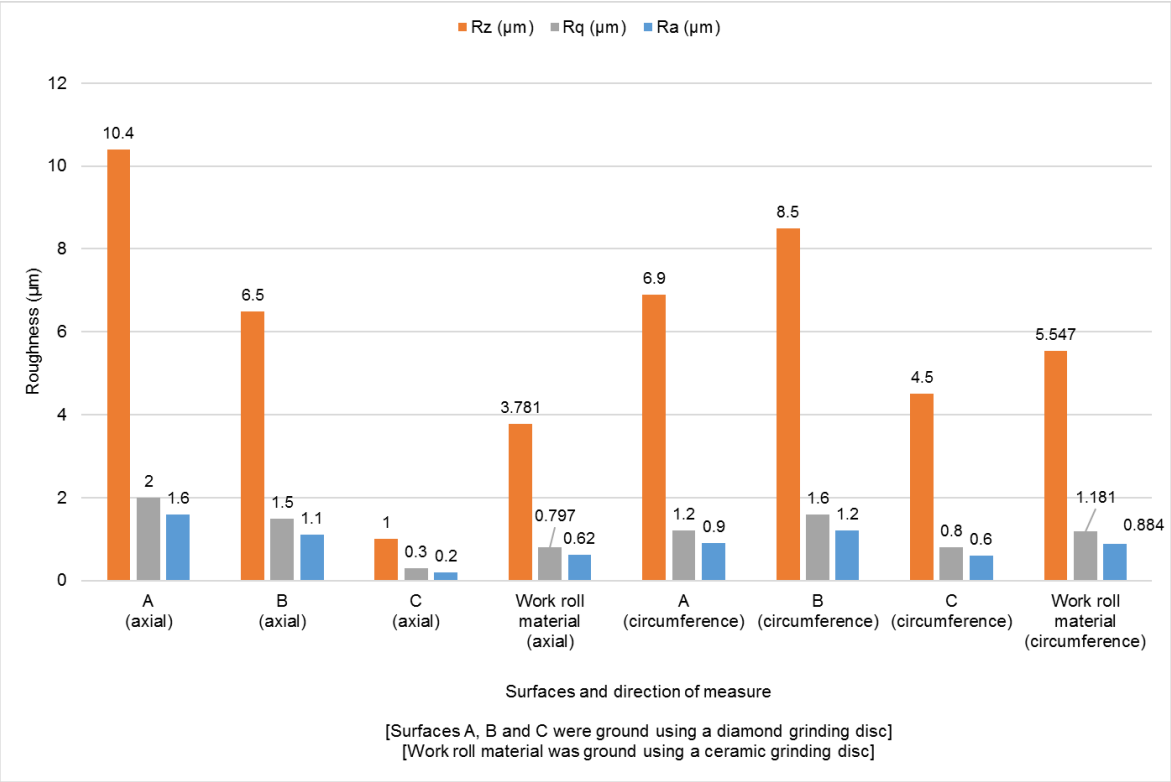

Figure 5-11 Roughness measurements

SEM images of mounted specimens revealed the morphology of the clad layers. Preparation of the samples involved sectioning samples and mounting on Bakelite material suitable for use in the SEM. Grinding was conducted manually with standard polishing pads and to a final 1200 grid paper, while polishing was conducted with 3 µm and 1 µm diamond suspension. It was challenging to remove a lot of the surface markings from sectioning and initial grinding process, mainly due to the sample diverse morphology of very hard (WC) particles and range of hardness through the sample. The diversity of steel grades on the same sample also introduced difficulty with etching. Typically, 2% Nital solution would be sufficient for the substrate steel material, however, a more powerful etchant was required for the Inconel 25 and Technolase clad layers, such as a solution with 4.76% Nitric acid, 47.62% Hydrochloric acid and 47.62% distilled water. The etchant was used to reveal the grain boundaries and substructures of the microstructure. In Figure 5-12 the substrate and two clad layers are clearly visible, where the Technolase® material is identified by the WC spherical particles. The clad was successful with no porosity, while the “pores” that can be seen in Figure 5-12 are cavities that were created by the loss of WC particles during polishing of the specimen. A breakdown of the different regions is shown in Figure 5-13, in various magnifications, starting with the image on the left. The microstructure in the substrate changes towards the dilution zone with the Inconel, and this highlights that the heat affected zone in the forged steel resulted from the cladding process (bottom right of Figure 5-13). No heat affected zone was observed in the intermediate layer, this may be attributed to the chosen etching process. However, if the desired microstructure has not been achieved in the intermediate layer, it is expected to fail under testing by delamination and by promoting cracking through the intermediate layer.

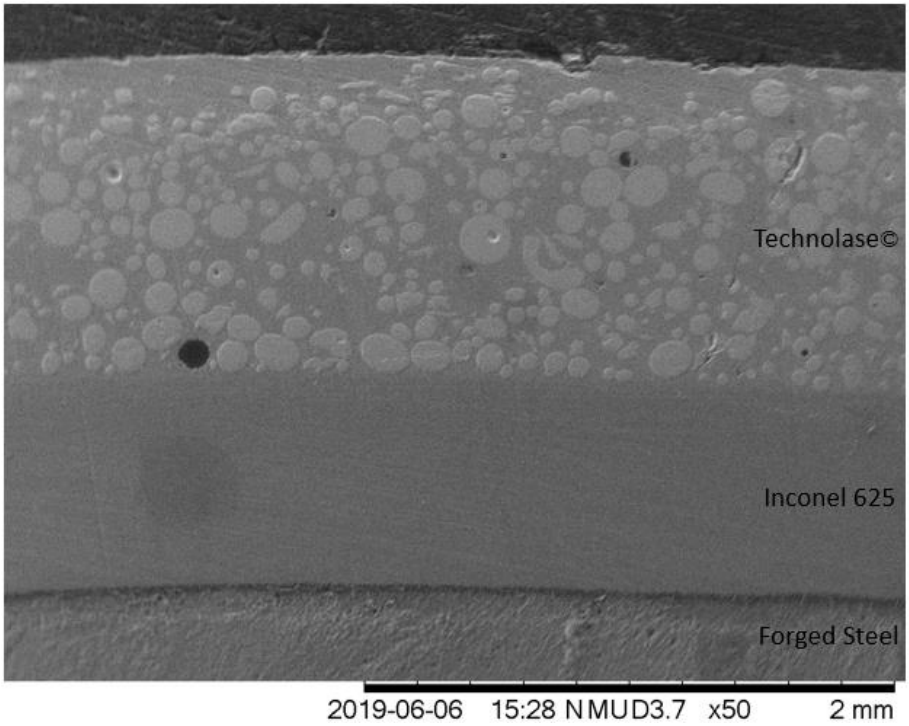

Figure 5-12 Cross-section image of the clad layers (taken with SEM Hitachi TM3030Plus at 50x magnification)

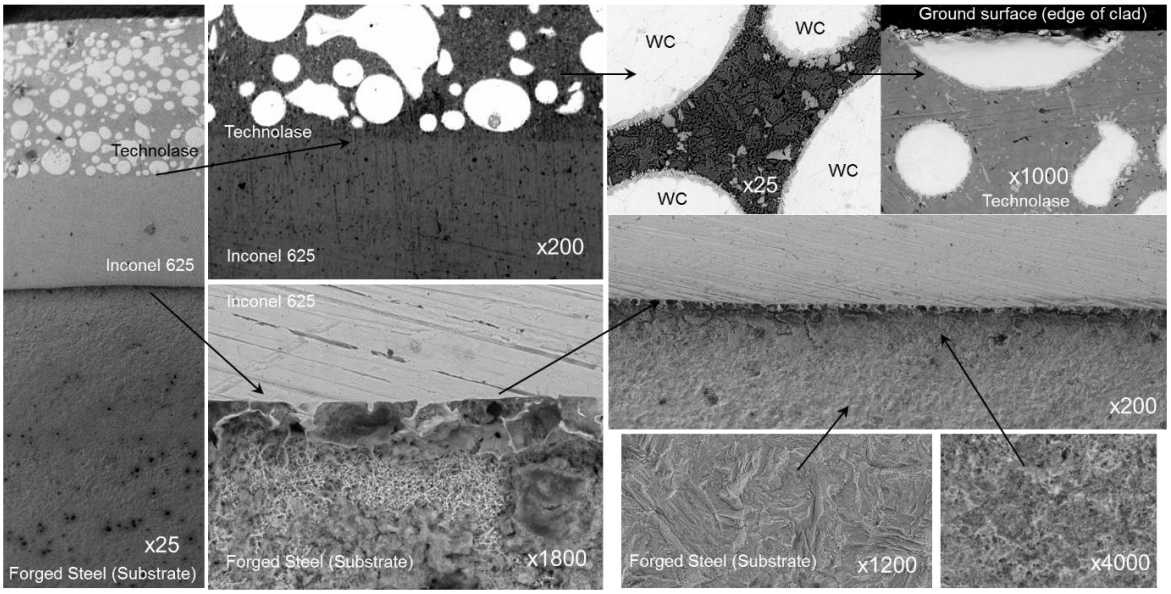

Figure 5-13 SEM images of various regions on a laser clad sample prior to testing

The concentration of the spherical particles is scarce near the surface of the outer layer, perhaps this is due to the particles sinking during the solidification of the molten pool. A few particles remain near the surface, of which some have either been ground successfully or they have popped out of the surface, thus leaving a cavity, which results in a pitted surface, see Figure 5-14. An example of one of the largest cavities was found to have a diameter of 200 μm and a depth of 50 μm, as shown in Figure 5-15.

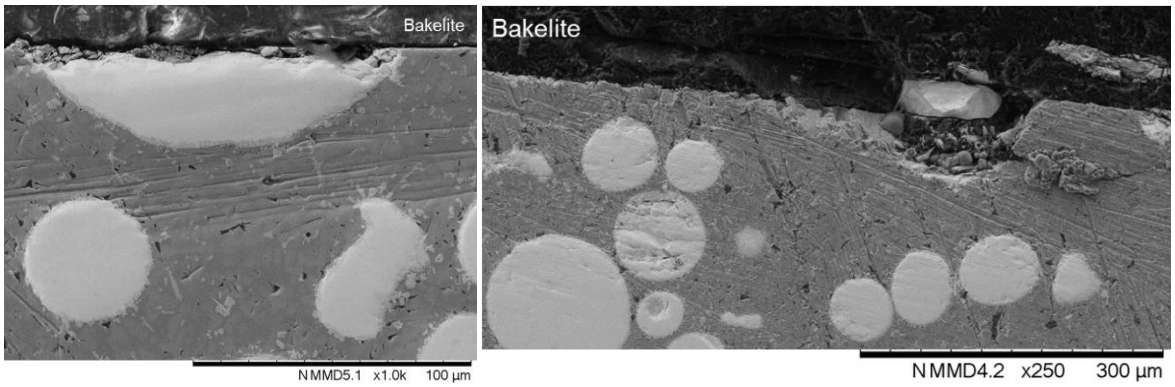

Figure 5-14 Surface of Technolase® coating shown on mounted sample, ground WC particle (left) and WC particle cavity (right) after the surface has been machine ground

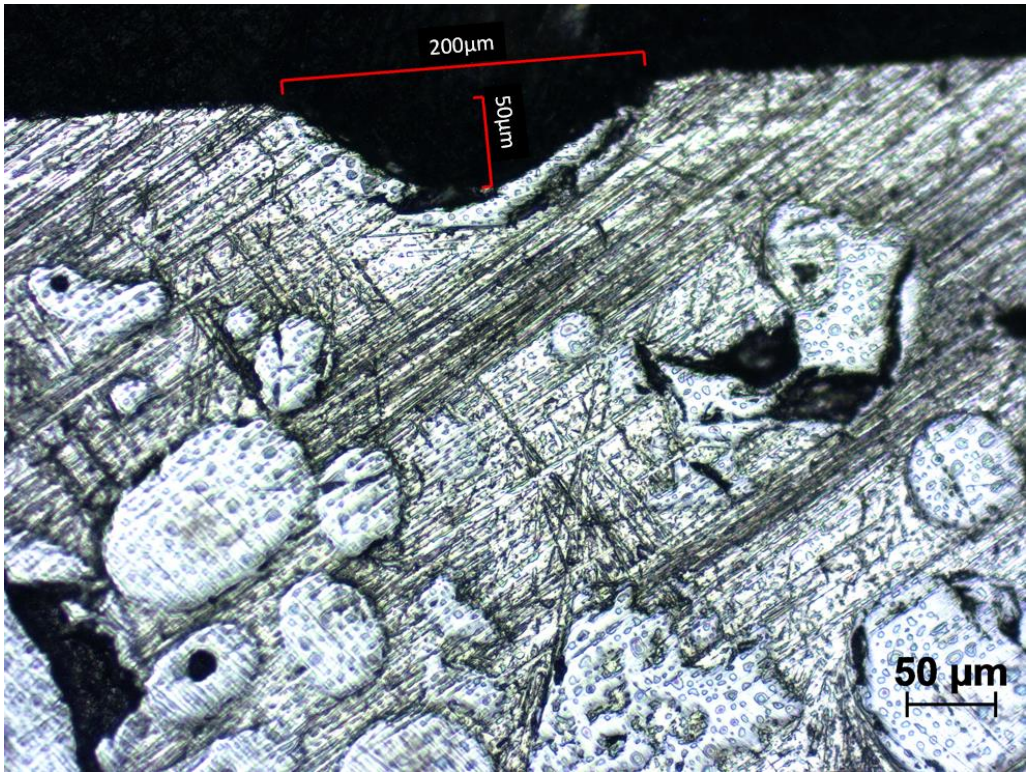

Figure 5-15 Typical surface cavity size as measured with an optical microscope

SEM images in Backscattered-Electron (BSE) mode were obtained to reveal the microstructural features of the Technolase® clad material. Figure 5-16 shows a sharp transition between the WC particles and Ni-alloy (green dashed lines), as well as detail of the microstructure. The brittle nature of the WC particles resulted in severe cracking of the particle after the cladding process, from micro-cracks to larger pieces ready to break off. Some of these cracks are identified with red arrows in Figure 5-16.

Dendritic microstructure features were revealed in Figure 5-17, in a low intensity exposure in the Ni-alloy, however, investigation into the metallurgy of the coatings was not pursued further to avoid diverting from the tribological investigation of this study.

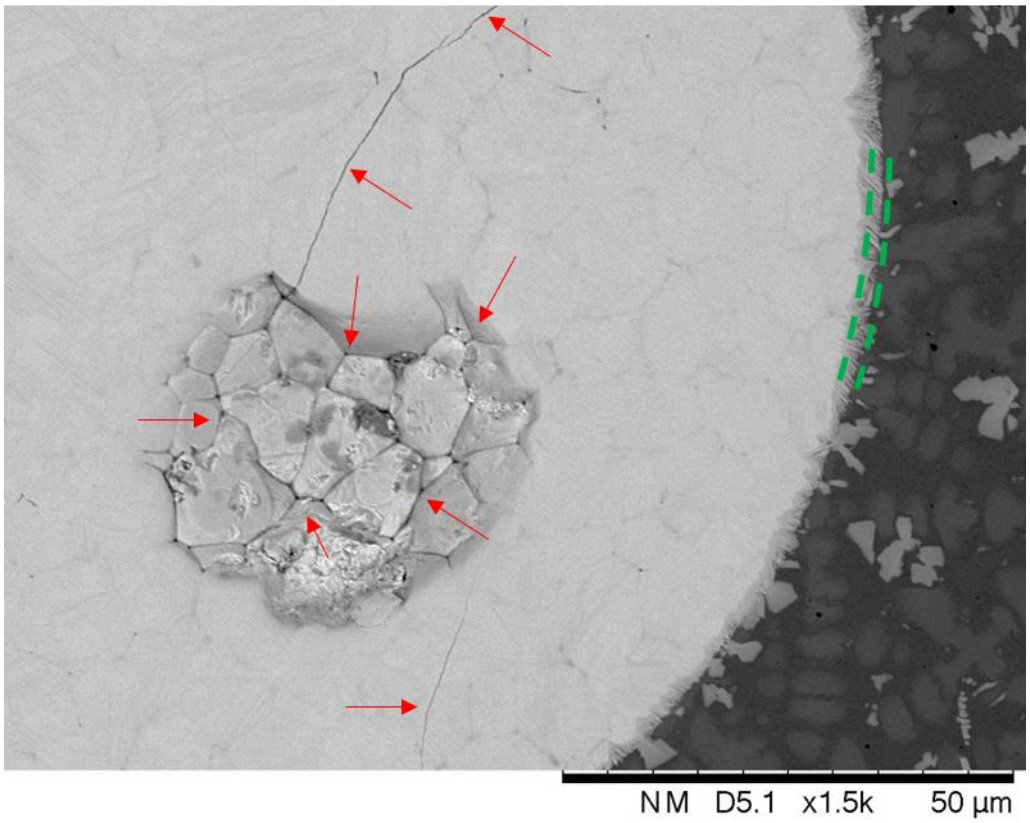

Figure 5-16 WC particle: detail of microstructure formation (polished sample, BSE mode)

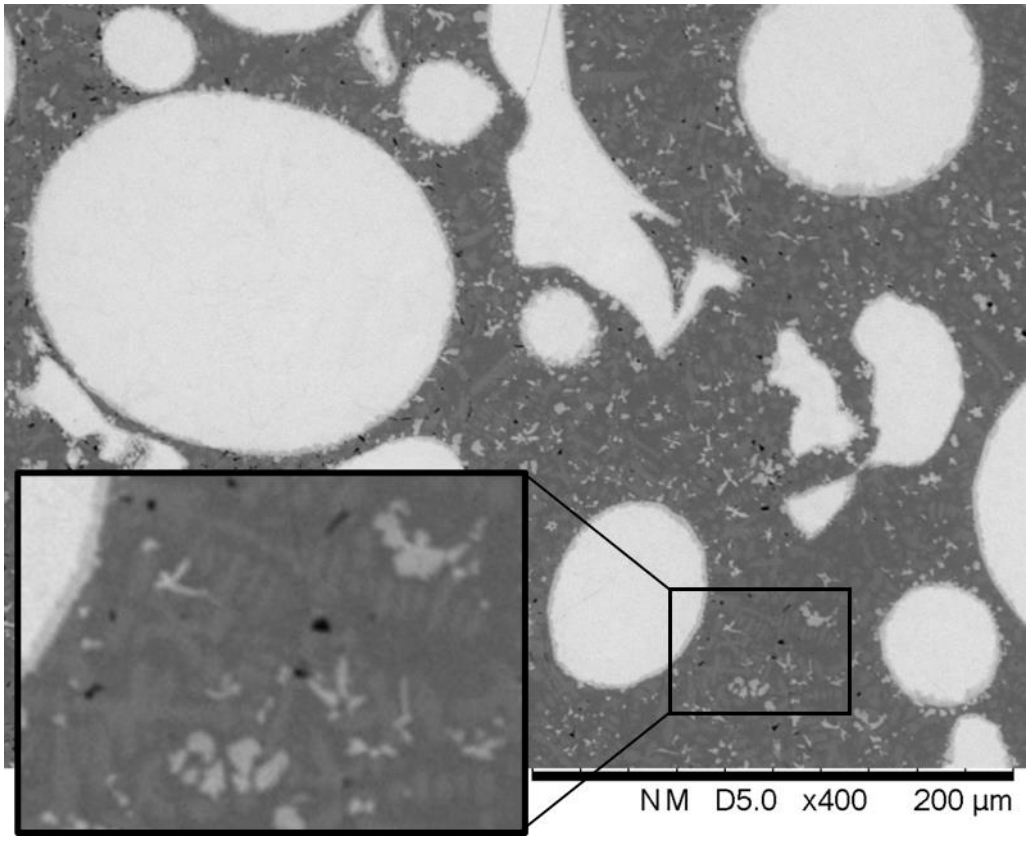

Figure 5-17 WC particles in the Technolase® coating (polished sample, BSE mode)

Cracks on the surface of the Technolase® prompt to investigate this further, to understand the severity of the cracks. After the cladding process there were no obvious cracks on the surface of the Technolase®. New cracks appeared on the test specimens after they have been sectioned using the EDM. The cracks seem to be superficial and when observed carefully, the crack surface path seems to be parallel to the pinnion's axis, as seen in Figure 5-18, which is a close view of a surface crack using an optical microscope. White arrows in Figure 5-18 point out individual surface cracks, where the distance between the surface cracks was measured and found to be between 3.5 mm-5 mm. An observation on the surface is that the crack path appears to be diverted towards the nearest pitting cavities, as this is highlighted by the red arrows in Figure 5-18.

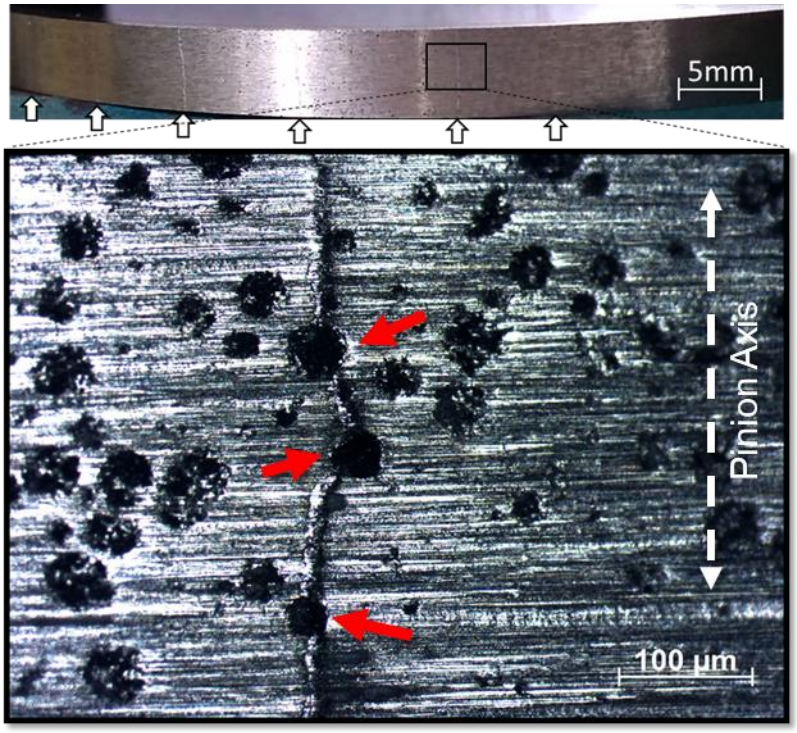

Figure 5-18 Optical microscope of the clad surface, focusing on a surface crack

Figure 5-19 highlights one of the small cracks that were found on the cross-section of a mounted specimen, using the SEM. In terms of the crack depth, it extends from the surface to the dilution zone with the intermediate clad layer (Inconel 625), but the crack does not penetrate the intermediate clad layer. WC particles seem to have split in alignment with the crack path. This indicates a solid bond between the Ni-alloy and WC, where the hard and brittle WC particles crack as opposed to unbound from the matrix when exposed to various stresses. In this case, it is assumed that residual stresses were formed during the cladding process, which were released during sectioning. The depth of crack indicates that the stresses were present in the top clad layer only, probably due to the presence of the WC particles that may affect the cooling rates. Near the surface of the clad, it was observed that the surface is slightly raised where the crack terminates. The raised surface crack is closed, as opposed to an open crack. A closed crack is preferable, as an open crack may contribute to crack propagation, under hydrodynamic forces.

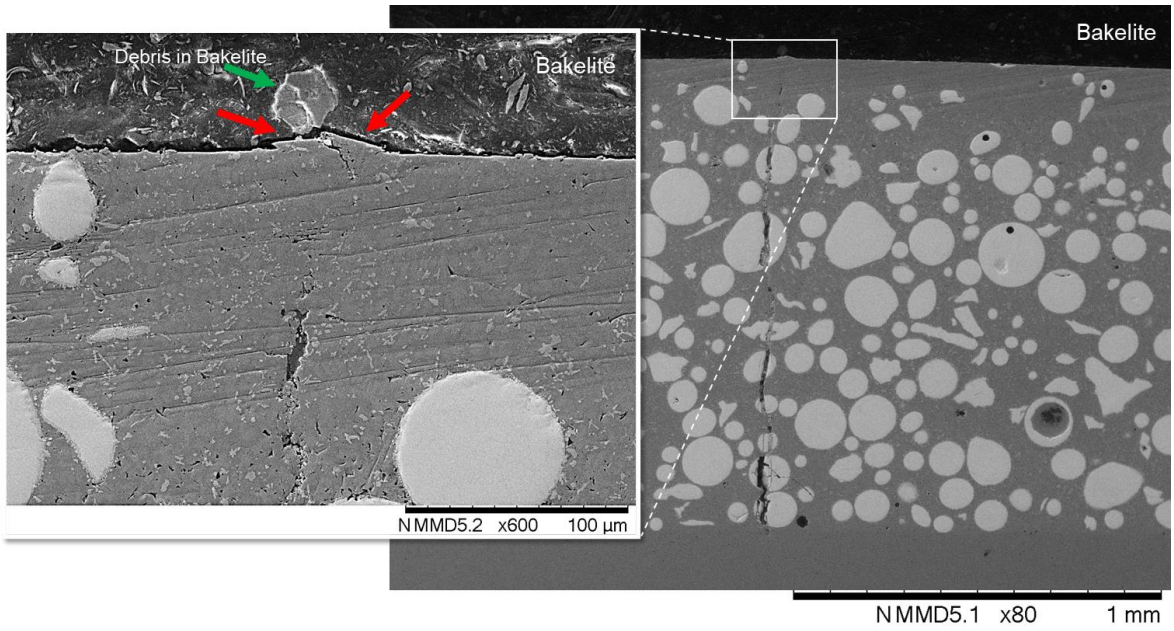

Figure 5-19 Crack through the Technolase® (prior to testing)

5.2 Railway materials twin disc - Procedure

The demand for faster and safer railways promotes the development of railway rails with greater quality and extended life. Such rails include newly developed steel compositions, heat treated steels, or rails with additively manufacturing wear resistant layers, for example with non-steel materials applied using laser cladding and are described by the industry as “premium” rail. They are mainly used on areas of rail networks where accelerated wear, rolling contact fatigue (RCF) or other rail related damage phenomena prevail. It is important to evaluate new materials used for rail since its performance may affect the other component of the interface, the wheel. Different types of wheel material and dimensions/profiles are being used on railways with a combination of varying loads and wheel-rail contact conditions. Wear mapping of materials is common practice in research [195, 196] and enables tribologists to identify material wear behaviour for example by mapping wear rate (mg/m/mm^2 – mass loss/distance rolled/contact area) against Tγ/A (normalised Tγ using area) or using an Archard wear coefficient approach [197]. The traction force is the shearing force responsible for wear, in the Tγ form, it is the creep force of the flowing material, which is derived by the traction force multiplied by the slip in the rolling/sliding contact. Wear mapping provides a standalone tool for understanding the likelihood of wear in different wheel/rail contact conditions. In combination with data from dynamic simulations, the wear data can also be used in prediction tools for comparison with other materials and contact conditions. Currently there is a lot of small scale data available for standard grade materials [196], but not so much on premium grades, making the prediction of their performance in the field difficult.

In this study the wear performance of four premium rail grades against R8 wheel material was measured in a laboratory environment. Twin disc testing was performed using the SUROS (Sheffield University ROlling Sliding) machine [198, 199]. Material loss from wheel and rail discs was measured

as well as friction in order to document the relationship of wear to Tγ/A curves. Conditions for testing were constant, with the exception of slip, which enabled variation of Tγ/A so that a benchmark wear map for a range of slip ratios could be established. Not all premium rail grades can be disclosed for this publication so rather than results specific to individual steels we focus on higher level conclusions relevant to premium grades in comparison to standard grade. The premium materials are referred to as R350HT, A, B and C.

Standard rail material R260 is the basis against which the premium material is compared. The R260 and one of the premium materials (R350HT) are manufactured in accordance with EN 13674-1:2011+A1:2017, which specifies Vignole rails of linear mass 46 kg m^{-1} and above, with a hardness range of 200-440 HBW. The rest of the premium materials are based on manufacturers' own standards. All premium materials in this study are designed for 40-60 kg m^{-1} linear mass for conventional and high speed railway track. Material R350HT has wear and RCF resistant properties and it is designed for use on curved and heavy haul tracks. Material A is designed to be wear and RCF resistant in comparison to similar steel grade, commonly used in curved track and high duty areas, while material B is designed to be the most wear resistant grade with exceptional resistance to RCF, aimed for tightly curved and heavy haul tracks. Material C is mainly designed for RCF resistance and for use in critical areas such as switch blades.

Laboratory tests were the preferred method of evaluating the wear performance of the premium rails because it is a quick and economical way to obtain results relative to field measurements. In addition, the use of a small scale twin-disc tester allows for replication of the tests under the same conditions, which can be difficult to achieve with field trials. Tests were planned in line with the good practice as described by Lewis et al. [200], such as the continuous supply of air to the disc contact area for cooling and for removing generated debris and the appropriate selection of specimen material from wheel and rail material. For specimen selection, it is important to ensure that the position and orientation of the specimen in the parent material is such that the representative microstructure and hardness of the wheel and rail running faces are represented in the specimen and to manufacture the specimen discs with representative surface finish as the wheel and rail. Twin disc data under dry tests should not be compared with tests that involve third bodies or conducted under lubricated conditions, as these will affect the coefficient of friction, therefore cleanliness of the discs before and after testing is paramount. It is important that the contact patch is maintained in the twin discs, crowning of the discs that occurs from severe wear rate under extreme conditions or by long duration tests, is not representative of the full contact conditions found in the field. Finally, results are comparable once they have reached a steady state, as initial wear rate acceleration and deceleration always takes place, in the severe and catastrophic regime occurs at a very short duration.

The SUROS twin disc machine [198, 199] (see Figure 5-20) was set-up at a maximum Hertzian contact pressure of 1500 MPa and a rail disc rotational speed of 400 rpm. The slip between the wheel and the rail discs was controlled by increasing the wheel disc rotational speed by the appropriate percentage of 1%, 10% and 20% of the rail disc's rotational speed, thereby representing a driving wheel. A torque transducer positioned on the rail disc drive shaft was used to measure torque and

enabled calculation of the tractive force and therefore the Tγ for each test. Tests were performed in dry conditions for varying numbers of cycles (1,000 cycles for 20% and up to 30,000 cycles for 1% slip). The discs have a contact width of 10 mm and a diameter of 47 mm (see Figure 5-22). The laboratory is in the interior of the building with mechanical ventilation and no solar heat gain (although not climate controlled). The measured temperature and relative humidity varied between 22°C-28°C and 30%-60% respectively between different test days. An issue when testing at small scale, particularly at high slip levels, is the dissipation of the heat generated. In the field the large mass of the wheel and rail aids in dissipating heat, in combination with the airflow around the system while the train is moving. To partially compensate for this in the twin-disc tests, compressed air was supplied to each disc to aid in dissipating heat but also the duration of the tests was kept short with increasing slip, for example 10,000 cycles for 10% and 1,000 cycles for 20%. In addition, the compressed air was a way of removing the generated debris from the test machine, ensuring that the debris was not sticking to the discs.

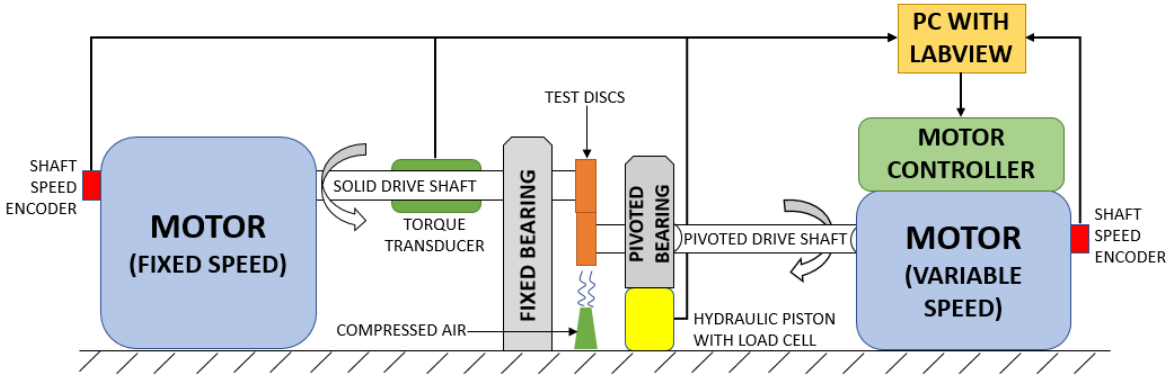

Figure 5-20 Schematic diagram of the SUROS twin disc testing machine

The specimens were cut from the rail head of each material and machined into SUROS discs, in the orientation shown in Figure 5-21. The hardness in each rail head may vary, since some premium rail grades are heat treated, hence having an increasing hardness from the centre towards the surface of the rail head. Also, the hardness will vary slightly at different parts of the rail head and through the thickness of the standard rail. This means that the hardness of the disc samples may vary slightly around their circumference. Similarly, the wheel disc was machined from the outer rim of an R8 wheel which complies with BS 5892:3, with specified hardness ranging from 241 HB to 285 HB (235 HV-300 HV). The SUROS discs were machined from the wheel flange and hardness tests with 1 kg load confirmed an average value of 300 HV. Typically, such wheels have a hardened running face but become softer towards the centre of the wheel. Samples used for the tests were selected from a range of rails of the same nominal grade, aiming to capture the variation that will be present between different batches of production. The tests took place over a ten-month period and in no particular order, to introduce statistical variation in the tests, as highlighted by Watson et al. [201]. Before commencing a test, the specimen discs were cleaned in acetone in an ultrasonic bath for two minutes. The weight of each disc was recorded using an Adam AAA-300L weighing balance with an output of four decimal points (0.1 mg resolution). For the tests done at 1% slip, the test was interrupted every 5k cycles up to 30k, in order to record the wear of each disc. This test approach was adopted from

[196] and used to monitor the wear evolution of the different materials. Before measuring the wear, the discs were cleaned again in the ultrasonic bath. For the tests done at 10% slip, the test was interrupted at 1k, 2k, 3k, 4k and 10k cycles. Finally, for the test done at 20% slip, the test was interrupted at 500 cycles and stopped at 1000 cycles. The wear rate for the 1% tests was calculated by dividing the mass loss for each 5k cycles by 5,000. The number of cycles for 10% and 20% tests was not as significant as the 1%, due to their short duration, their overall mass loss was divided by the number of cycles in each corresponding test interruption (i.e. 500 and 1,000 cycles for 20% test).

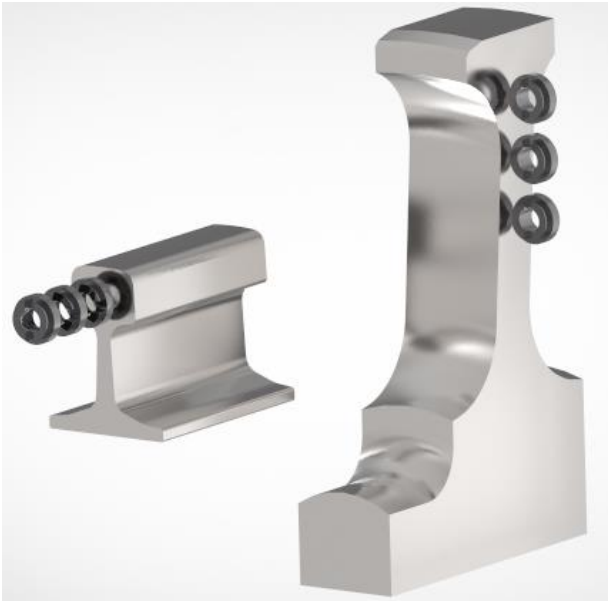

Figure 5-21 Representation of the sample orientation in sections of rail (left) and wheel (right)

After the tests were completed, the discs were sectioned in three cutting planes in order to expose an internal face of the disc in the middle of the outer rim (see Figure 5-22). The sectioned pieces were mounted and polished for further analysis including hardness testing. Micro-hardness testing took place with a load of 0.3 kg in multiple locations from the outer rim of the disc towards the centre of the section to observe any work hardening effects occurring near the running area of the disc (Figure 5-23). Surface images were also taken.

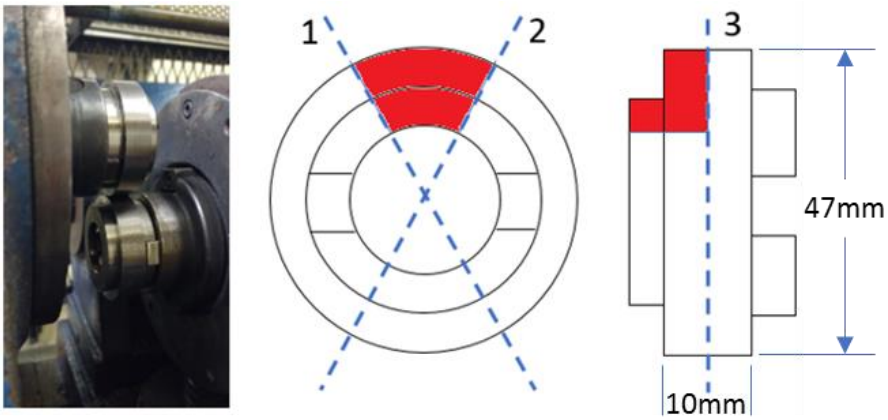

Figure 5-22 *(a)* Image of test discs mounted on the SUROS tester (b) Locations of the three section cuts (sample highlighted in red).

The main characteristic of premium rail grades is their fine lamellar pearlitic microstructure which impacts hardness and material strength, for example the higher the rail head hardness the more hard wearing the rail is expected to be. All premium rails tested in this study have a higher hardness than standard rail. Hardness mapping was obtained in this study for the purpose of identifying the hardness variations in the heads of the premium rails to show how this variation is represented in the twin disc specimens. Standard rail, for example R260, work hardens in the field and can eventually achieve similar surface hardness as some premium rail. That does not mean that it will perform the same as premium rail or rail with higher hardness, in terms of wear or RCF resistance and this can be seen from this comparative study. To benefit from the effects of increased hardness it must extend well below the surface. Increased hardness that exists superficially can be re-worked during operation and the rail head may experience multiple phases of plastic deformation, ratchetting and hardness fluctuations in comparison to materials designed for high wear resistance. Other methods to increase the hardness/wear resistant properties of the rail head is with the use of laser cladding. These methods are of interest due to the thicker coatings that can be produced in relation to more traditional coating techniques (mm versus μm). Figure 5-23 shows hardness profiles for R260 material, the four premium materials and a laser clad R260 with a coating of MSS steel of a 1 mm depth. The chemical composition of the martensitic stainless steel is given in Table 5-2. The hardness measurements were taken after the samples were tested in the SUROS machine at 1% slip for 30,000 cycles from the edge of the disc contact surface in a linear trajectory towards the centre of the disc up to 2 mm below the surface of the material. It is clear that all non-clad materials, with the exception of R260, have undergone hardening, affecting the material up to a depth of about 300 μm below the surface. The R260 material has had the greatest hardness change, increasing by approximately 390 HV near the surface but rapidly reducing to bulk hardness at a depth of approximately 900μm below the surface.

Comparing R260 to the MSS clad it can be observed that the higher hardness of the clad material runs to a depth of just over 1 mm from the surface and has protected the R260 substrate material from significant hardening. This protection depends on selection of a coating thickness that is deeper than locations at which sub-surface contact stress can drive ratchetting of the substrate. An area hardness measurement of the MSS Clad sample was conducted with 33 indentations. The resultant hardness map is shown in Figure 5-24, where the top of the figure is the area closer to the running edge of the SUROS disc. Figure 5-25 is the three-dimensional representation of Figure 5-24. There is a characteristic upwards and then downwards spike in the dilution zone (area highlighted in Figure 5-25 in which clad and substrate materials are mechanically mixed during cladding deposition), which is indicative of the interaction of the different material phases in this region, i.e., MSS and heat affected base material.

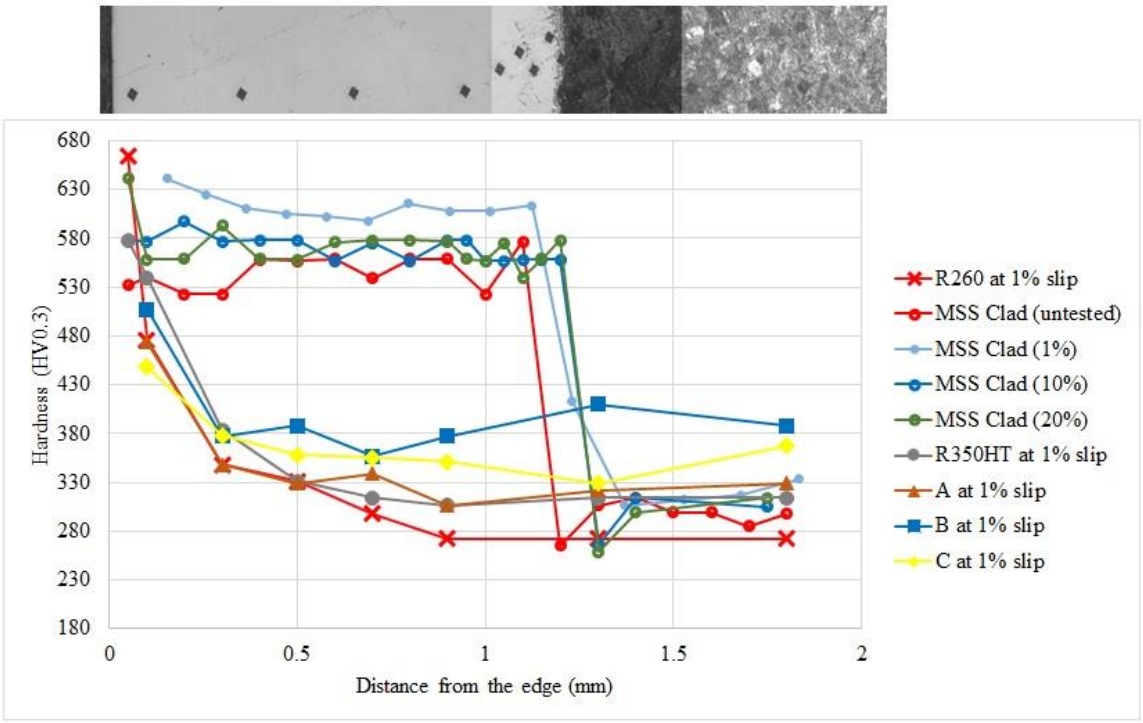

Figure 5-23 Hardness profile through the thickness of sectioned samples and stitched image of untested MSS Clad (using Struers DuraScan at HV 0.3 kg).

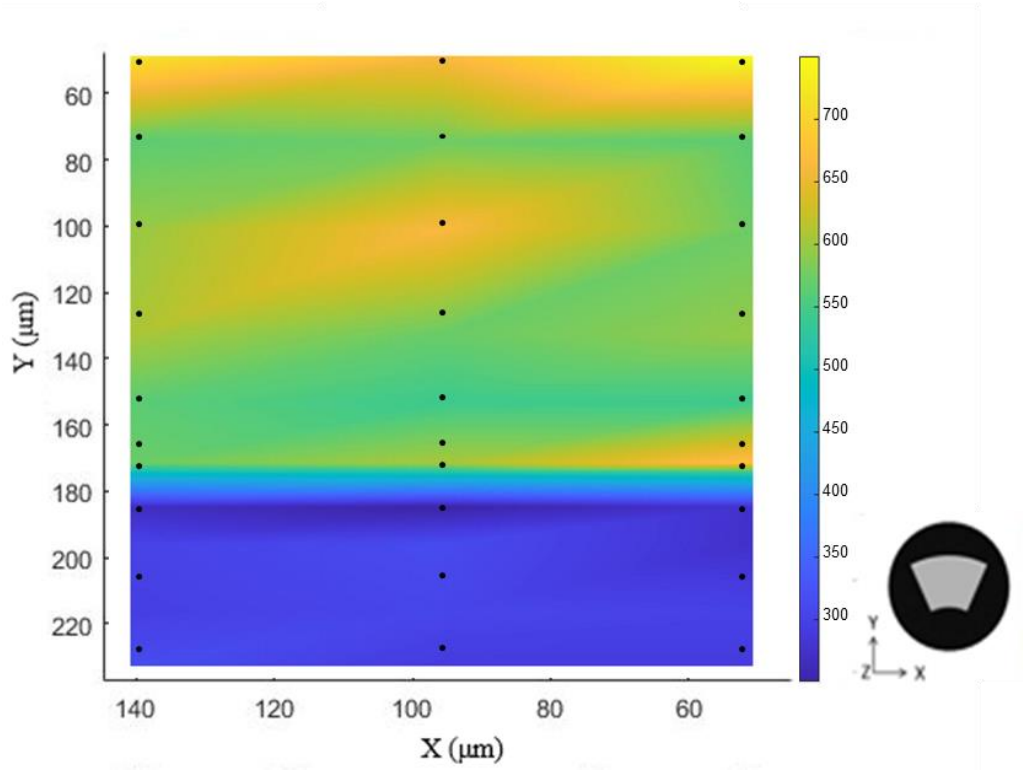

Figure 5-24 Vickers hardness mapping of the through the thickness of sectioned MSS Clad sample tested at 20% slip (using Struers DuraScan at HV 0.3 kg). Dimensions in µm, where the top of the graph is the running edge of the SUROS disc.

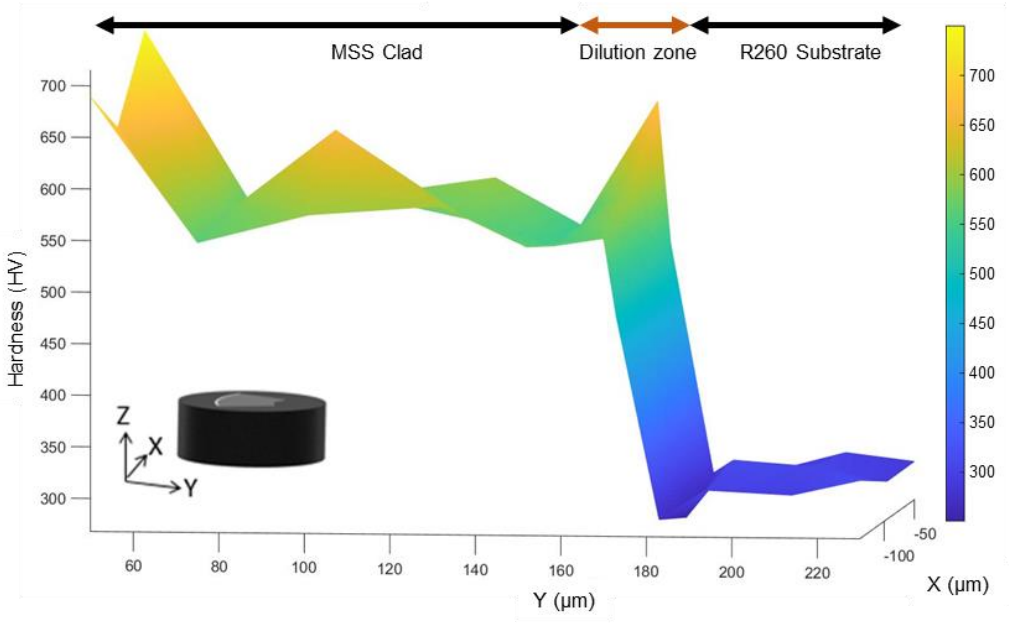

Figure 5-25 Hardness mapping in 3D view (Rotated Figure 5-24, hardness is now shown on the vertical axis). The characteristic spike upwards and downwards in the dilution zone is prevalent in the hardness mapping as first indicated by the hardness line profile in Figure 5-23. Horizontal axis in µm, vertical axis in HV 0.3 kg.

5.3 Impact - Procedure

There are various methods for testing impact damage, most common is the hammer type where a pivoting arm repeatedly hammers a material sample, for example an oscillating arm as used by Slatter et al. [202] at the University of Sheffield. The impact force can be easily calculated from the kinetic energy of the pendulum or pivoting arm. This type of test was considered for this study, however, it was decided to perform the test using an existing drop test rig, which was previously used for testing composites. Hammer type rigs are designed for small, precise and repetitive loads, while for the application of laser clad materials the test was simplified to a single impact in order to compare initial impact deformation for the various materials, including a laser clad coating. The drop test rig is made of a dart, where the mass and tip geometry are known and it is designed to drop from a known height, guided by two cylindrical sliders. To initiate the test, the dart/mass was released from a latch by a solenoid mechanism. For measuring the impact forces, a loadcell was included and “sandwiched” between the dart and the mass/moving frame. Figure 5-26 shows the rig, where the release mechanism is at a zero height, prior to raising it to the desired height. The base of the rig has a hole, which is larger than the dart and loadcell assembly. This is normally used to fix composite materials for testing by puncturing through. During preliminary test for the railway materials it was found that the base was not very stiff and the drop mechanism was bouncing to a significant height. It was decided to mount the rail samples onto a large base made of EN24 steel (see left image in Figure 5-26), which was then placed onto the concrete floor of the laboratory.

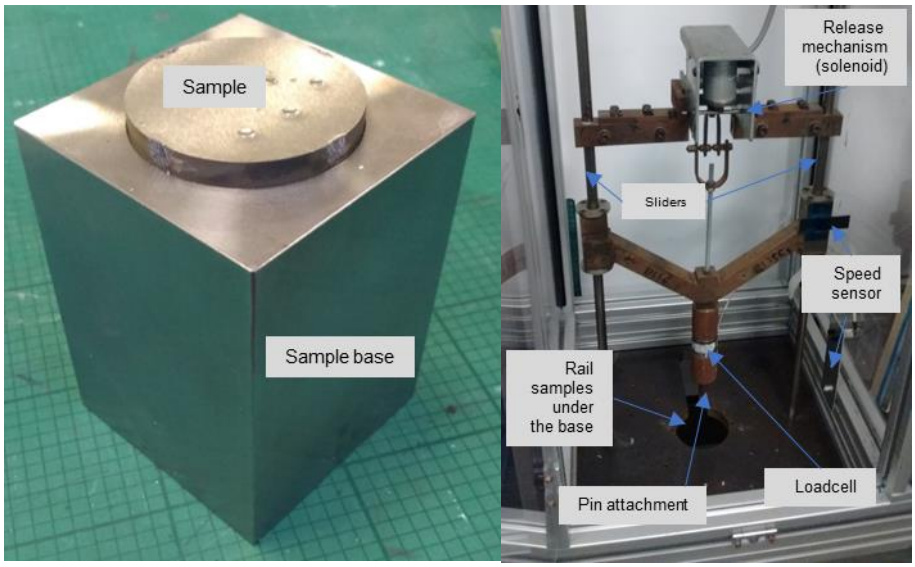

Figure 5-26 Rail sample mounted on base (left) and drop test rig at zero height adjust (right)

The kinetic energy from dropping the mass was now transferred to the sample and to the floor, instead of the flexible aluminium rig. Some of the impact energy was deforming the sample and some was reacting back to the dart/mass which then bounced upwards. The rebound height varied with the sample material and this was due to the variable stiffness of each sample. The original dart was only used for preliminary test, however, it was deforming severely. Darts made of R8T wheel material were deforming as well. The tip of the dart was round with a diameter of 12 mm. It was decided to use harder material such as AISI 52100 bearing steel which was already available in a 6 mm diameter ball and fitted in brass cylindrical pins. This type of pin is used for pin-on-disk tests and the ball hardness is in the region of 800 HV. A custom pin holder was made to hold the brass pin with a grub screw and to secure it to the drop frame, in line with the loadcell. Figure 5-27 shows a rail sample of 50 mm in diameter and 10mm in height, with the pin holder and pin resting on top of it. Three impact cavities can be seen on the rail sample. The pin shown fitted to the pin holder was deformed by testing, while the original undeformed pin is shown outside of the pin holder.

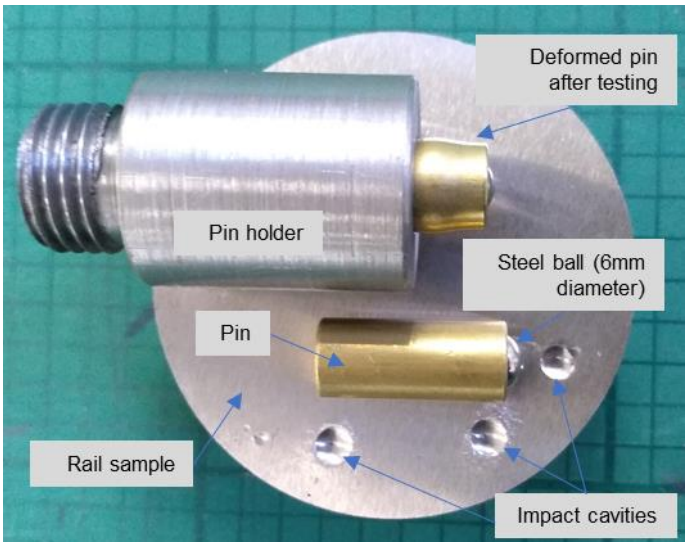

Figure 5-27 Pin holder, pin and rail sample

The ball remained undeformed in all tests, scratch marks were identified on the surface of the steel ball and brass, indicated by red arrows in Figure 5-28 (A). The outline of the brass pin had a cylindrical profile which held the steel ball tightly in place. After the test, the pin profile has been deformed, and the steel ball rests lower from the deformed rim and moves/spins freely. Green arrows indicate the gap between the ball and rim, which was not present on new pins, as well as the deformed profile in green dashed line in Figure 5-28 (B).

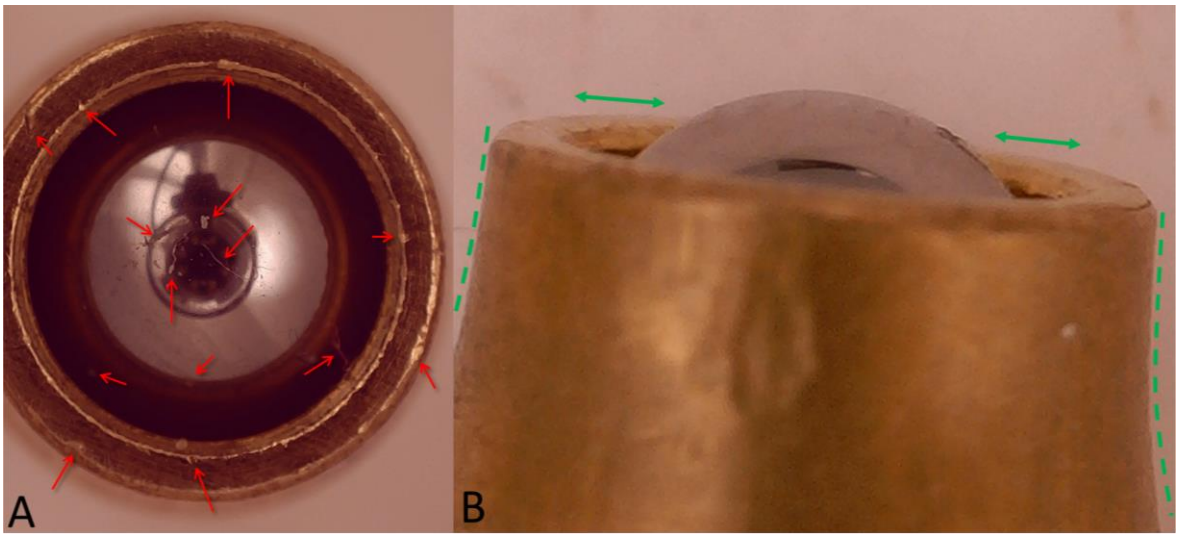

Figure 5-28 A: Scratch marking on a pin after impact test, B: Profile of the same pin

Four materials were chosen for the impact test, R260 standard rail, Manganese steel, R350HT and R260 rail with Stellite 6 laser clad material. The Manganese steel was obtained from an out of service crossing nose rail made in Sheffield by Edgar Allen. The materials were cut into 50 mm diameter discs with a 10 mm height using a waterjet cutting machine and they were machined ground on both sides to ensure clean and parallel faces. Bulk hardness measurements were taken from each sample disc using the Struers Durascan automated tester at 10 kg indentation load. The number of hardness indentation per samples is shown in a dashed square above the corresponding material in Figure 5-29, where the whiskers indicate the lower and upper hardness values that were measured. The cross markers indicate the mean hardness values, displayed on the side of each dataset and the box top and bottom faces indicate the upper and lower quartile. The Manganese steel is designed to work hardened, so it had a low hardness prior to the test, 223 HV for the mounted specimen and 300 HV for the impact test sample. The hardness difference in the two samples may be due to the mounted sample being obtained from a slightly softer part of the crossing nose rail. R350HT is a heat-treated steel, designed to have a higher hardness than the R260, at 363 HV, however, it was significantly softer than the Stellite 6 clad at 477HV, which was 60% harder than the standard R260 material of 283 HV.

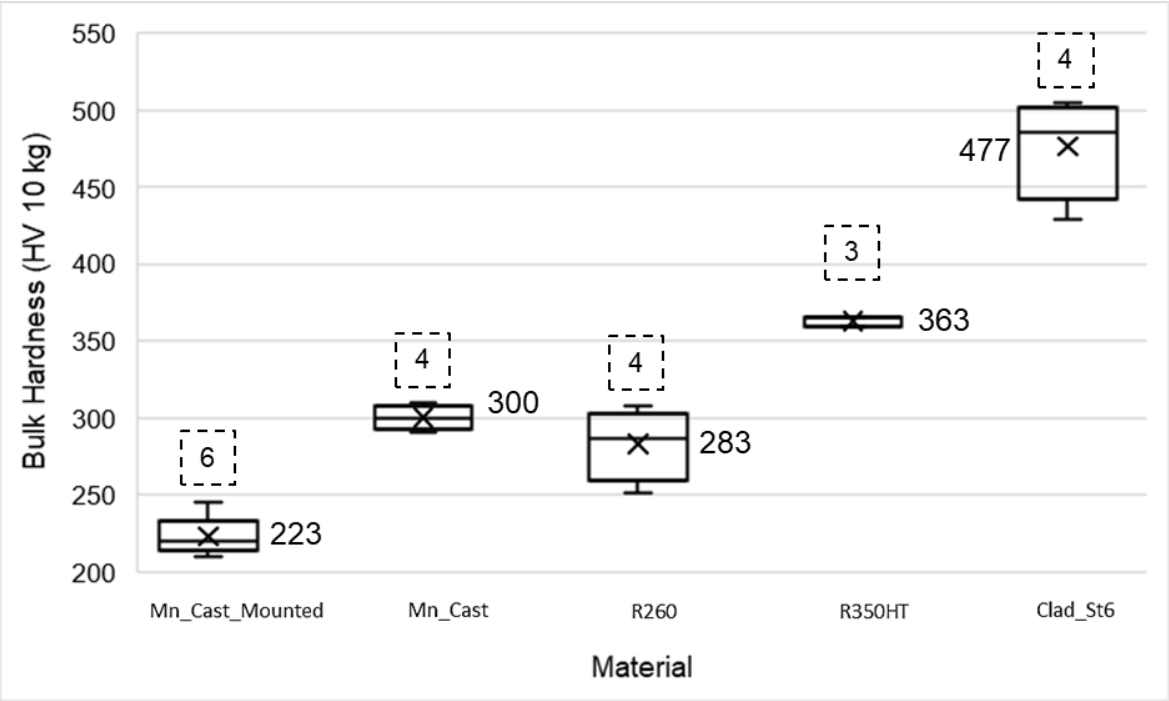

Figure 5-29 Bulk hardness measurements taken with 10 kg load

A new pin was used in each test and it was dropped onto the rail sample at least four times to ensure that the deformation of the pin has reached equilibrium state. After each drop the disc was rotated so that the next impact would hit a clean surface, away from any existing cavities. The deformation of the brass pin introduced an uncertainty to the test. From initial tests, it was decided that the first two to three impacts were responsible for the most severe deformation to the pin. Further impacts would only introduce minimal deformation to the pin, thus reaching an equilibrium state, where most of the impact energy would be absorbed by the rail sample in the form of cavities. A way to evaluate that the pin deformation has reached an equilibrium state was to observe how the initial depth of the cavities on the rail samples were not as deep as ones from later impacts, when the equilibrium state was achieved. However, during the test conditions trial, the load cell measurement was a good indicator that the equilibrium state was reached when, after subsequent impacts, the measured load "increase" between impacts was reduced. This means that the impact energy absorbed by the interface was transforming, higher impact force means less energy was converted into strain energy by deforming the materials. Strain and material deformation were still occurring, at smaller magnitudes than the initial impacts. The drop height was 1.58 metres and the total weight of the drop mass (pin, loadcell and frame) was about 1.4 kg. The drop height was decided based on modelling discussed in 4.2.3, which confirmed that the contact stress would be in the region of 1 GPa, similar to impact values found in the field from average train speeds. A Labview program was used to trigger the solenoid for initiating the drop and to record the speed and impact force.

After testing the surfaces were cleaned by applying acetone on cotton wool and wiping the impacted surface. The discs were analysed using the Alicona IFM SL G1, where the volume deformation of each impact cavity was recorded. Finally, the specimens were sectioned, mounted and polished for analysis of the microstructure and hardness measurement through the thickness of the impact cavity.

The polished mounted samples were etched using 2% Nital solution to expose the microstructure. As with the previous analysis of clad materials, 2% Nital solution was not sufficient to expose the microstructure of the Stellite 6, however, it was sufficient for the other materials of the impact test.

5.4 Textured rolling/sliding – Procedure

The textured test was a first attempt to investigate the suitability of laser clad coatings with the EDT process and to compare the durability of the texture with unclad material. The clad material chosen was Technolase® with an intermediate layer of Inconel 625, as discussed in 5.1. The aim was to perform a simple comparison on a twin disc testing machine. For this purpose the SUROS machine was used and the working principle and procedure for testing was similar to the description in 5.2 for the railway materials rolling/sliding tests. Tandem mill work roll material was provided by Forgemasters International in as forged state. The material required heat treatment in order to achieve the designed hardness. It was advised by Forgemasters that typical hardness for the tandem mill work roll would be around 800 HV on the barrel, while a skin pass mill barrel would be slightly higher at 830 HV. Due to the small size of the disc specimen used in the SUROS, it was preferable to laser clad a cylinder which would then be machined into individual discs. This would benefit the laser cladding process in many way, one of which is better heat retainment by the larger volume of material during the cladding process. Therefore the heat treatment of the work roll material was applied to cylinders of ø45 mm x 200 mm, prior to laser cladding and slicing into SUROS rings after cladding. The reason for producing rings as opposed to the “SUROS discs” (Figure 5-22), is because of the difficulties in machining the extremely hard cladding on the outer surface. Slicing the cylinder into rings was straight forward using an electrical discharge machining (EDM), whereby the rings would be mounted on the SUROS machine with the use of additional washers as per Figure 5-30. A spring washer (Qualfast 20 x 10.2 x 1.1 mm- Din 2093A/C) was added between the ring and the fixing bolt to ensure the ring would not slip during the rolling test. A tightening torque of 90 N m was applied for securing the disc and ring, which was the same torque value used successfully in previous twin disc tests on the SUROS, without any damage to the threads of the mounting shaft.

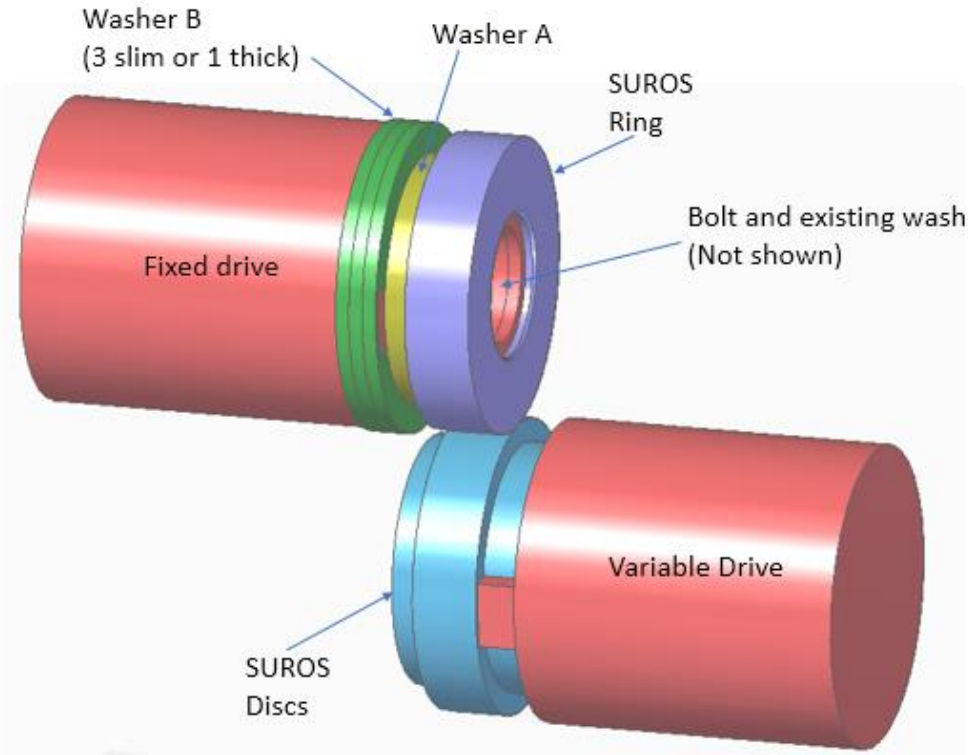

Figure 5-30 Schematic of SUROS "disc" and "ring" arrangement

The heat treatment took place using a laboratory oven (Elite Thermal Systems Ltd. - BCF11/8) which has a capacity of 8 Litres and a maximum heating temperature of 1,100^{o}C using 2 kW electrical heating elements. Figure 5-31 shows the heat treatment oven and cylinder specimens before and after heat treatment. Due to the small size of the cylinder in comparison to the full size work roll, a new treatment schedule had to be defined for the specific geometry and material volume. After trials on smaller specimens, the final treatment schedule involved soaking the cylinders upright for at least two hours at 980^{o}C, followed by quenching in a bath of cold water whilst stirring the water with the cylinder. Two baths were required where the quenching duration was about ten seconds in each bath. Following quenching, the oven temperature was turned down to 300^{o}C, which was achieved twenty minutes after quenching. The cylinders were then tempered at 300^{o}C for at least one hour and then left to air cool overnight.

Figure 5-31 A: Machined cylinders, B: hot laboratory oven with cylinder soaking, C: cylinder specimens after heating and quenching

Four hardness indentations were obtained from the flat face of the cylindrical samples, the mean hardness is displayed next to the datasets in Figure 5-32. With the chosen schedule the tandem mill work roll material hardness ranged from 400 HV in the centre to 600 HV near the edge of the cylinder. A significant difference from the original hardness of 244 HV. Before tempering a maximum hardness of 700 HV was measured, however, tempering reduced the hardness and this was in favour of making the specimen ductile and to remove residual stresses. Initially tempering was not applied, as a result large cracks appeared on the cylinder one hour after quenching, as shown in Figure 5-33 (left image). This was due to residual stresses from the heat treatment.

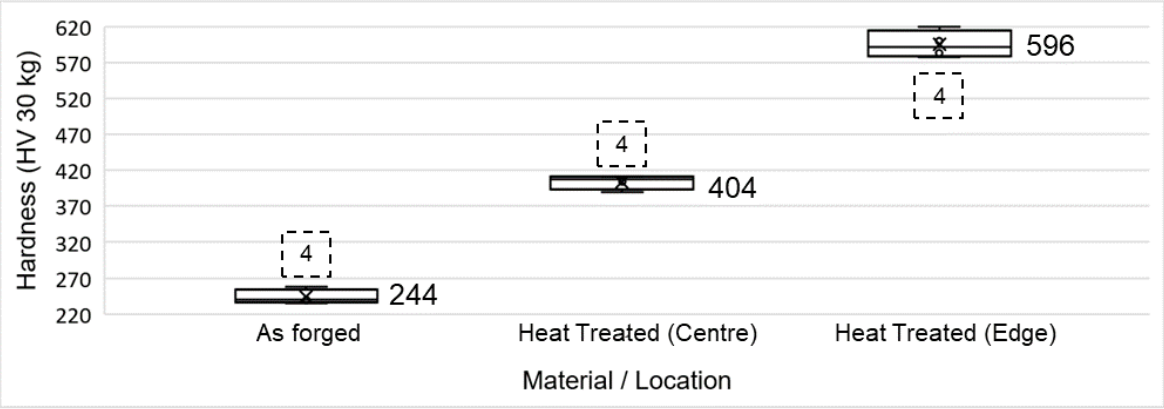

Figure 5-32 Hardness measurements on the flat face of the work roll cylinder samples

Five successful cylinders are shown in Figure 5-33 (right image) which were cut into twenty rings, using an EDM. Only ten out of twenty rings were used in this study while the rest were reserved for future testing. The dimensions for the rings and washers are shown in Figure 5-34.

Figure 5-33 Cracking of cylinder that has not been tempered (left) and five cylinders of various conditions prior to machining into rings and prior to cladding (right)

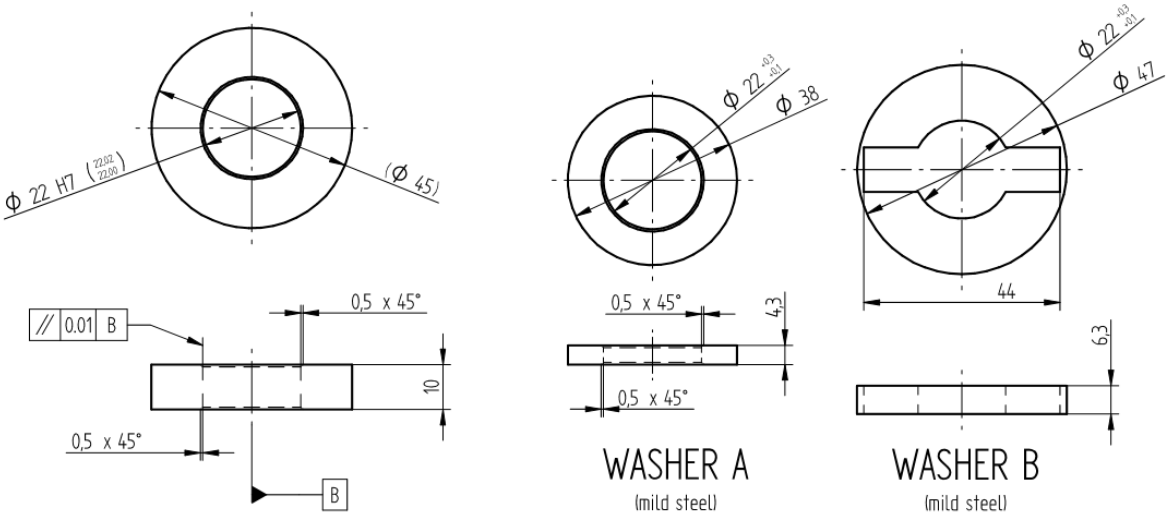

Figure 5-34 Drawing of the ring and washers for the ring adaptation in the SUROS

A mandrel was made out of EN24 steel, with centre holes at both ends to allow mounting on a cylindrical grinding machine. The mandrel can hold up to ten rings so that all rings can be ground at the same time using a ceramic grinding disc. This enabled all rings to have the same diameter and concentricity with regards to their internal hole and external face. EDT texture was applied directly to the mandrel arrangement, by Sarclad Ltd. The mandrel with rings is shown in Figure 5-35. The cladded rings can be identified in Figure 5-35 from their slightly dull texture, in comparison to the unclad rings and mandrel face.

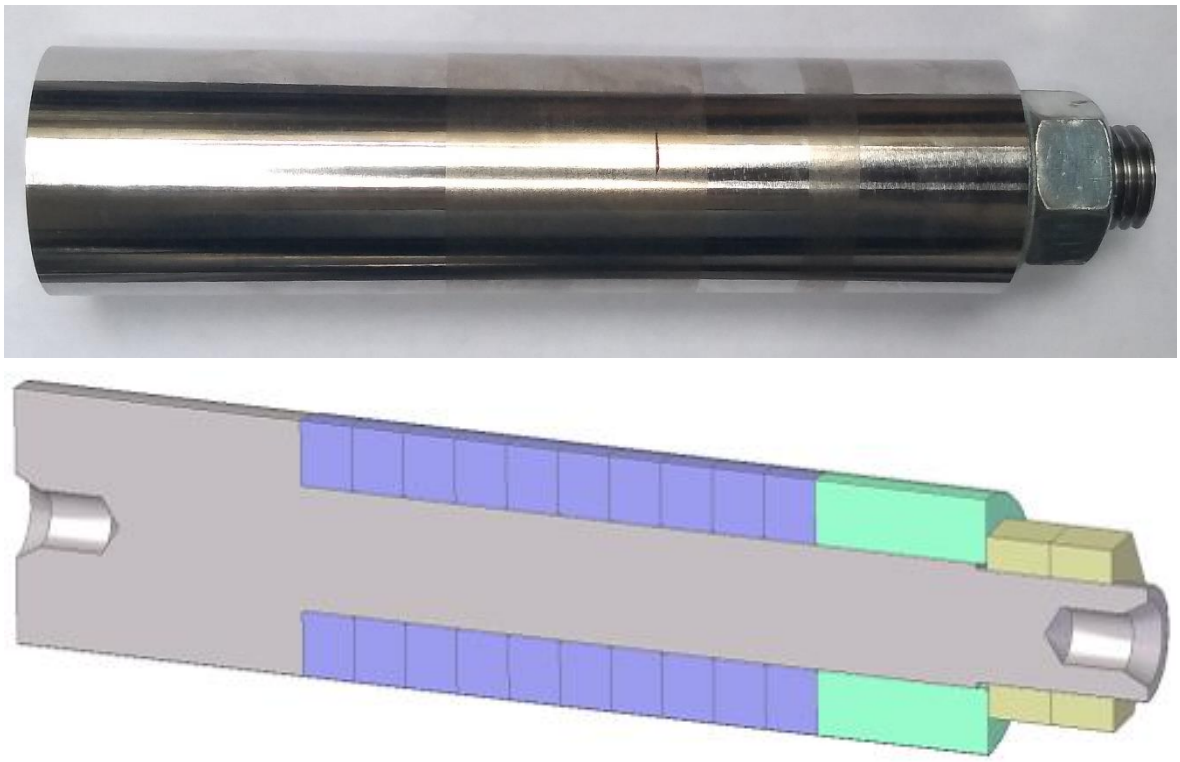

Figure 5-35 Mounting of rings onto a mandrel for cylindrical grinding (top) and sectioned view of its 3D model (bottom)

Kerosene and Somentor44 are typical oils used for flat rolling of aluminium products, along with additives for improving performance and surface finish. Due to the flash point of Kerosene/Somentor44, an alternative safer lubricant was selected, QWERL 4305 by Quaker Chemicals. The alternative lubricant is designed for rolling steel. Although work rolls are lubricated constantly during rolling, the wear tests were performed under dry conditions, in order to accelerate wear by introducing harsher conditions. The lubricant was only used during for transferring an impression of the texture to an aluminium sample, before and after the dry wear test. The work roll material that has been textured is referred to as “ring” and the other part of the interface is referred to as a “disc” or SUROS disc. All SUROS discs used in this test were made of R400HT rail material, with surface roughness values of Ra:1.7 μm, Rq:2.1 μm and Rz:11.1 μm. The roughness is similar to the roughness of the textured rings (Table 6-2 in page 153). However, the surface morphology is different, it consists of residue machining marks from the lathe tool used in manufacturing the discs, in the form of micro-grooves that run parallel to the disc circumference. The machine marks are visible in Figure 10-3, in the Appendix. The SUROS machine is a typical twin disc test machine for rolling/sliding and is described in 5.2. The ring was mounted on a drive shaft and operated at a constant rotational speed, while the disc was controlled by a motor inverter to operate at a slower speed. The bearing that supported the ring shaft was fixed in the machined, while the disc shaft bearing was supported in a sliding guide, allowing it to move up and down. See Figure 5-20 for a schematic of the SUROS and Figure 5-36 for an image of the ring and disc mounted in the SUROS machine prior to testing. The tests stages are described in Figure 5-37 for clarity.

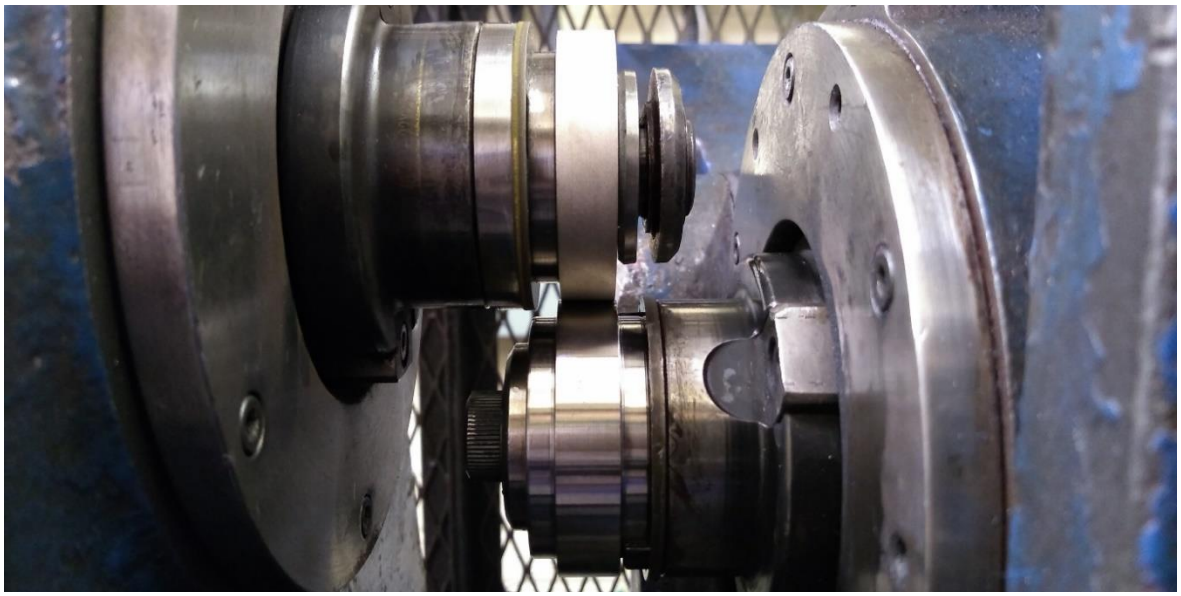

Figure 5-36 SUROS test machine (Top: Textured ring, Bottom: R400HT disc)

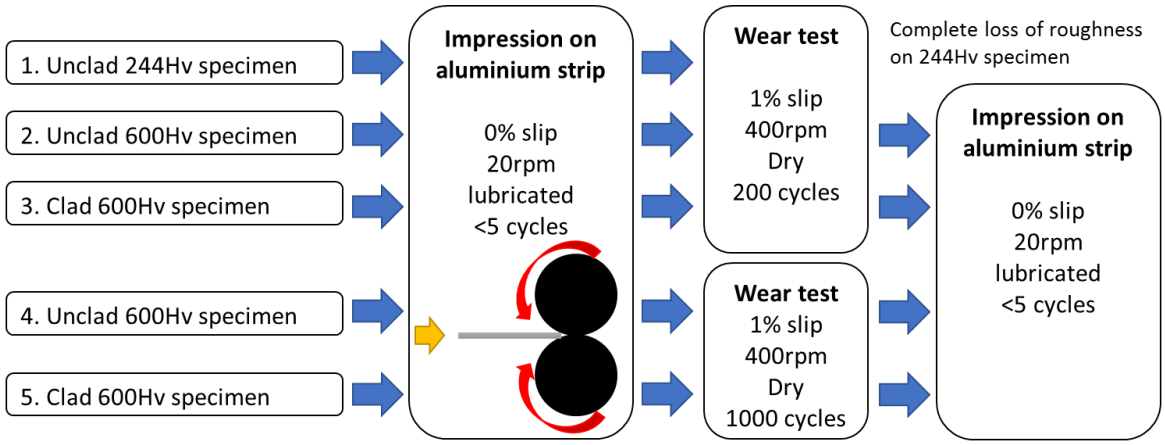

Figure 5-37 Schematic of the texture tests for five specimens

The rings and discs were cleaned in an ultrasonic bath using acetone for at least four minutes and their mass was recorded before and after the test using the Adam AAA-300L weighing balance with an output of four decimal points (0.1 mg precision). The first part of the test was the impression of the texture onto an aluminium strip. A 300 mm x 15 mm aluminium strip of 6082T6 aluminium (1.5 mm thickness) was rolled through the ring/disc interface, at a slow rotational speed of 20 rpm, in order to obtain impressions of the texture. Analysing the impression on samples is typical practice for evaluating the work roll performance in industry. Images of the textured discs and aluminium strip at various stages of the tests are shown in Figure 5-38. The contact pressure was 1000 MPa and the slip was 0%, meaning both the ring and disc were turning at 20 rpm. A generous amount of QWERL 4305 was applied on the ring, disc and strip using cotton wool. The ring and disc were then sprayed with acetone in situ and let to dry prior to performing the second part of the test, the wear test.

For the wear test, the speed of the work roll ring was set to 400 rpm and the SUROS disc at 396 rpm, to achieve 1% slip. The test contact pressure was based on information from industry, as discussed in section 2.3.1. The contact pressure was maintained at 1000 MPa for all tests, this was achieved

by applying a 2.77 kN force on the SUROS machine, which was calculated using the Hertzian calculator program discussed in 4.2.1. The width of the ring was 9 mm, while the SUROS R400HT disc had a wider width of 10 mm, therefore the contact width used for the calculation was 9 mm. The ring and disc diameters were around 44.2 mm and 47.2 mm respectively and none of the ring and disc diameters were less than 44.0 mm and 47.0 mm respectively. The Elastic Modulus of the materials used in the calculation was 212 GPa for all cases. The force applied during the test was calculated based on these parameters in order to achieve the chosen contact pressure.

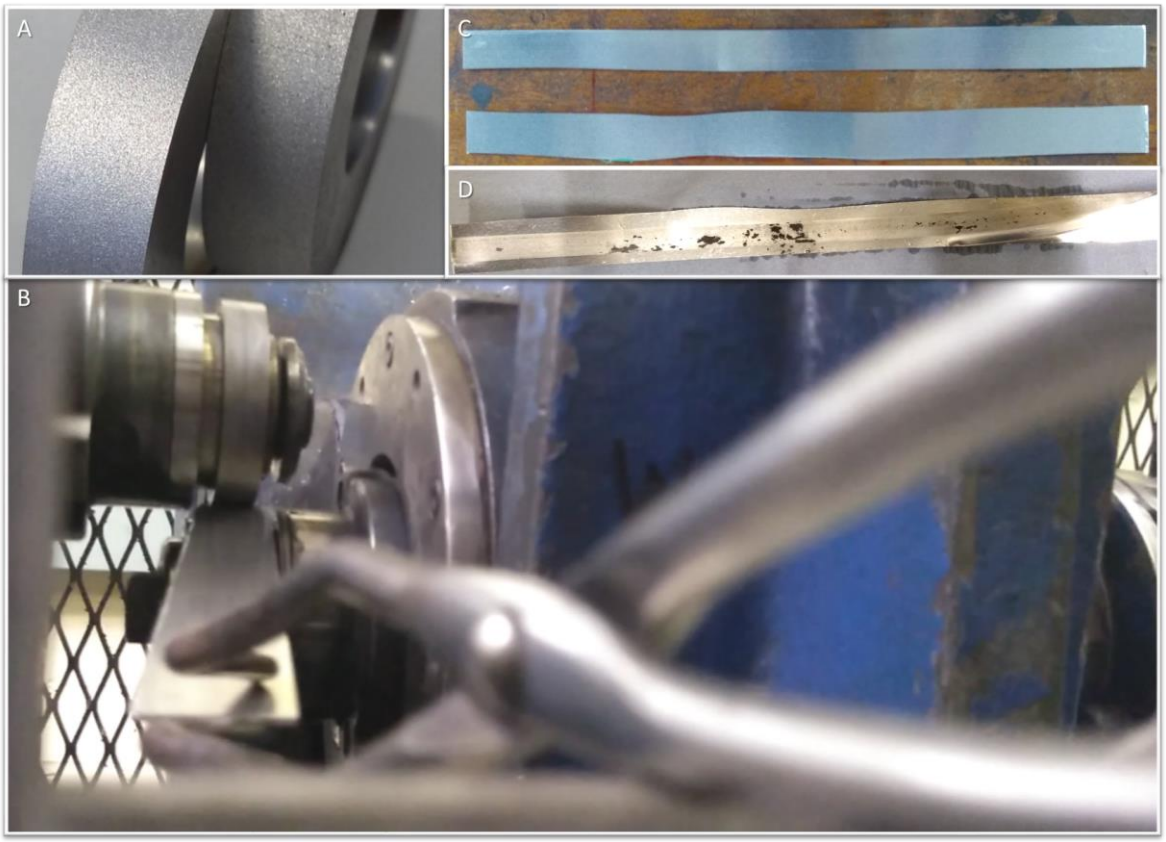

Figure 5-38 A: textured rings, B: feeding of the strip using tongs during rolling at slow speed, C: 6082T6 aluminium strips, D: aluminium strip after rolling with texture impression track shown in the middle of the strip

The third part of the test was another impression of the texture onto aluminium strip, after the wear test. The ring, disc and strip were lubricated once more and the procedure for the impression test was repeated as previously. Table 5-5 is a list of the samples prepared for testing and the coloured rows indicate the samples that were used in the test. A preliminary trial was conducted with a heat treated clad ring, not shown in Table 5-5. Following this, the first set of tests consisted of two unclad and one clad ring which had a duration of 30 seconds (200 cycles), while the second test consisted of one unclad and one clad ring and with a duration of 2.5 minutes (1,000 cycles). The unclad rings from the first test were chosen from one heat treated (600 HV) and one untreated (244 HV) ring. The untreated ring lost all its original texture and the machine marks from the disc's running face were imprinted onto the ring, since the disc hardness was significantly higher than the ring. The set of discs number 5.1 in Figure 6-33 shows this phenomenon, where both surfaces have the same texture of

machining marks after the test. Because the texture on the ring has been lost completely no more tests were performed using the untreated rings.

Table 5-5 List of test samples prepared for testing

Order on Mandrel	Marking	Treatment	Cladding	Average Hardness		Opposite Disc	Test duration
				Substrate	Surface	R400HT	
1	1.1	Heat treated	Unclad	600 HV	600 HV	430 HV	200 cycles
2	1.2	Heat treated	Unclad	600 HV	600 HV	430 HV	1000 cycles
3	2.1	Heat treated	Clad	600 HV	550-2500 HV	430 HV	200 cycles
4	2.2	Heat treated	Clad	600 HV	550-2500 HV	430 HV	1000 cycles
7	4.1	Heat treated	Clad	600 HV	550-2500 HV	430 HV	Initial trial
9	5.1	Untreated	Unclad	244 HV	244 HV	430 HV	200 cycles

Colour legend

Initial trial
First test 30 seconds/200 cycles
Second test 150seconds/1000cycles

5.5 Erosion – Procedure

An erosive wear comparison test between clad and unclad materials was performed with the HiPEr (High Pressure Erosion) rig. A test rig with a pump capable of supplying sufficient flow at high pressure was needed, so the HiPEr rig was designed and built for this purpose. The process to design, build and to provide suitable laboratory space in the in the University of Sheffield was a process that lasted over one year. A lot of work went into producing a document equivalent to a technical file that would allow the machine to comply with the Pressure Systems Safety Regulations 2000 (DIRECTIVE 2014/68/EU) and the Machinery Directive (DIRECTIVE 2006/42/EC). This compliance will enable the test machine to obtain a CE marking in the future, as this may be a requirement for all new equipment at the University. Further work involved completion of Essential Health and Safety Requirements, PUWER (Provision and Use of Work Equipment Regulations), Risk Assessments, Noise Level tests, producing Maintenance and Training Records as well as a Standard Operating Procedure/Manual for the operation of the equipment. Figure 5-39 is a schematic of HiPEr, showing the various components and nozzle arrangement against the specimen. Figure 5-40 is an image of the as-built rig shown in the laboratory.

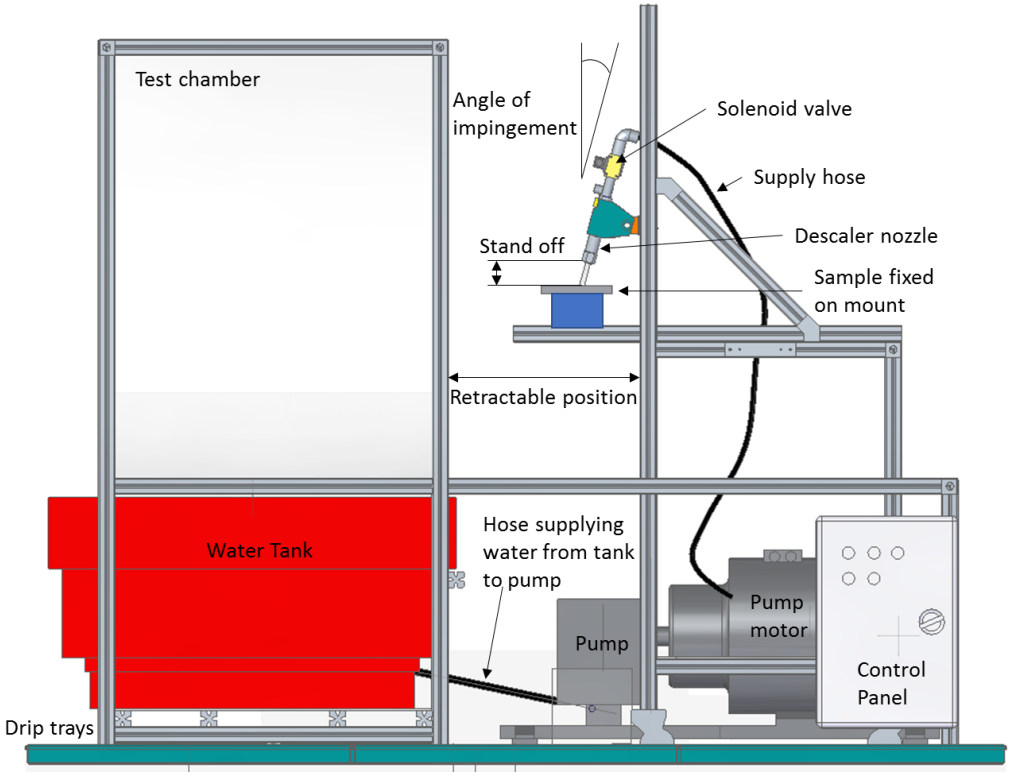

Figure 5-39 Schematic of HiPEr

The rig comprises of a motor inverter (ABB ACS580) which controls a motor pump (Interpump 66MPU M500-1051) that delivers high pressure water to a flat jet nozzle (PNR HWE-2162-F1AB) from an open top water tank. The water was fed to the pump by gravity while the water was collected into the open top tank during testing, so it is a closed-circuit system. Drip trays were used on the floor area of the rig to capture any leakages during commissioning or testing. The high pressure nozzle is typically a flat jet nozzle and it is located inside a chamber made up of durable aluminium frame and panels. Two panels on the frame are made of transparent polycarbonate sheet, in order to observe the test. The nozzle tips are inter-changeable to allow for different types of spray patterns and widths. The pressure is set by a pressure regulator valve, while the spray is controlled by a solenoid valve located near the nozzle. The on/off control can be made via a switch on the electrical panel or via a Labview program that was put together for use in any Windows PC, so that it can be run remotely. A pressure sensor is also located near the nozzle to record the pressure via the Labview program, ensuring repeatability over various tests. The nozzle arrangement is mounted onto a moving frame which retracts, to enable maintenance and replacement of the nozzle and specimen. Figure 5-40 is a descriptive image of the rig. A 3D model of the retracted frame (Figure 10-4), a drawing with general dimensions (Figure 10-5) and images of the motor inverter/pump (Figure 10-6) are shown in the Appendix.

Although the test rig was used successfully for these tests, some improvements are suggested here for future use. When testing for prolong periods, for example over two continuous hours, the water heats up from the pumping action due to it being in a closed circuit. The use of a water cooler would allow extensive testing and efficient use of the rig. Furthermore, slow leakage caused delays in

testing. It is recommended that the rig is sealed properly in the future, rubber seals were secured with tape which has stopped the leakage, however, these need to be secured with rivets and that a water cooler system is added to the tank, in case prolonged tests are required.

Typically, the specimens are flat plates and they are positioned 100-200 mm from the nozzle tip (stand off). Bigger stand off can be achieved if necessary. The angle of attack of the spray to the specimen can vary, depending on the test objectives, however, an incline as opposed to a perpendicular spray is recommended to deflect the water away from the nozzle. An image of the nozzle and water jet is shown in Figure 5-41, where the spray jet breaks down into smaller particles after impact and is reflected in a horizontal direction away from the nozzle position. As discussed in 4.2.2 the erosion wear is dependent on the particle velocity and impingement angle, but also by the ductility or brittleness of the material. It is difficult to control these parameters when comparing various materials so the impingement angle was set to an appropriate angle to deflect the water which is representative of the descaling jet interface. Similarly, maximum velocity was achieved by running the pump to the maximum possible speed/pressure. General HiPEr rig and test parameters are listed in Table 5-6.

The rig can achieve the same impact pressure as the majority of the descalers in the steel industry, around 200Bar. The flow rate is restricted to 40 lpm (litres per minute) by the pump or 25 lpm by the nozzle chosen for this test. Descalers would normally achieve flow rates in the region of 130 lpm. Regardless of the flow restrictions, the stand off can be adjusted to bring the specimen closer to the nozzle. In this way, the contact patch from the fan-shaped water jet becomes smaller, however, the impact pressure increases, due to the closer proximity with the nozzle which increased the impact force over a smaller contact area. Impact force over contact area for a given time can be described as the impact energy. By having these adjustments, the HiPEr rig can achieve impact energies equivalent to industrial descalers. The great benefit of replicating the same contact pressures on a smaller contact patch with reduced flows, is that it makes it practical to perform such tests outside of an industrial environment. The samples can be small enough for handling and for post-processing in a metallurgical laboratory, but also the equipment, such as the water tank and pump, are manageable in terms of size and maintenance.

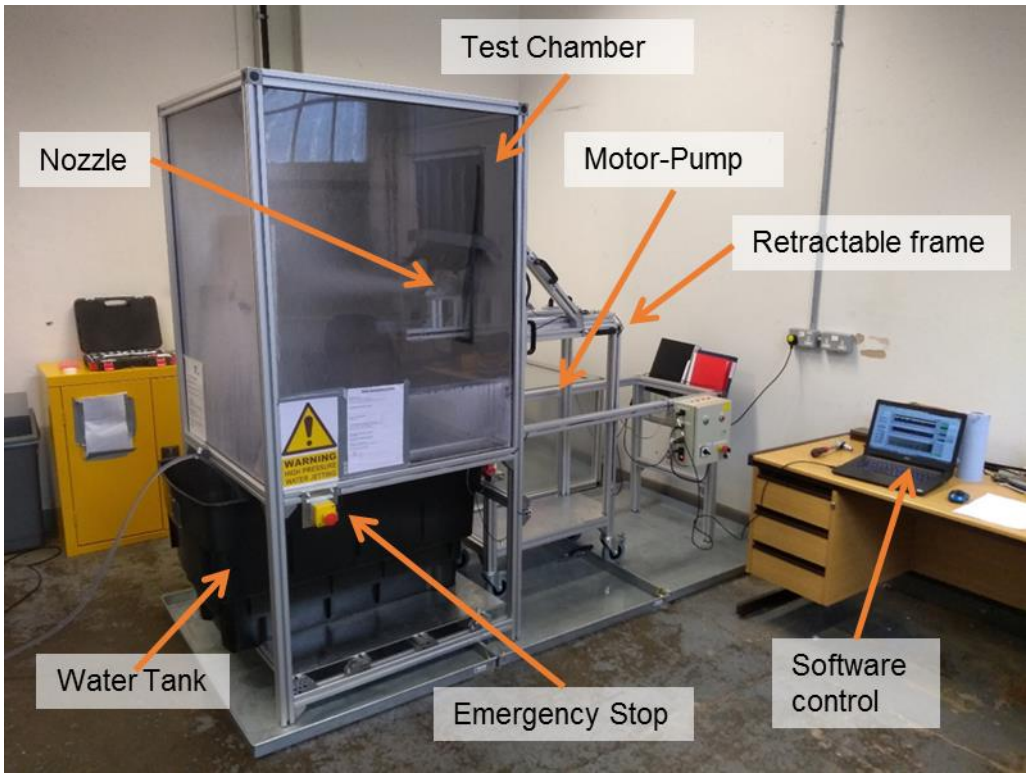

Figure 5-40 High Pressure Erosion rig (HiPEr)

Figure 5-41 Close up view of the descaling nozzle and jet (left) and sample secured with clamps before the test (right)

Table 5-6 General HiPEr rig and test parameters

Water pressure at nozzle	160 Bar	Preliminary test (measured)
Water pressure at nozzle	185 Bar	Comparative test (measured)
Flow	24 lpm	Estimated based on nozzle specification
Velocity	192 m s^{-1}	Estimated from simplified Bernoulli's equation $P + \frac{1}{2}\rho V^2 + \cancel{\rho g h} \equiv -V = \sqrt{\frac{2P}{\rho}} = \sqrt{\frac{2x18400000Pa}{997\frac{kg}{m^3}}}$
Angle of impingement	30º	From vertical axis
Stand off distance	30 mm	From nozzle tip to sample surface
Jet fan angle	26º	Defined by the nozzle tip geometry
Max flow	25.6 lpm @ 200 Bar	Defined by the nozzle tip geometry

Three materials were compared for the erosion test, as rolled S275JR steel, as rolled Hardox 500 and a Stellite 6 laser clad on S275JR substrate. The samples were cut to 50 mm x 150 mm specimens to make them convenient to load into the erosion rig and microscope equipment. The thickness of the samples was 15 mm and the laser clad sample was about 1mm thicker, due to the Stellite 6 coating. Only the Stellite 6 coating was machine ground, to ensure a surface roughness similar to the as rolled samples. Stellite 6 was clad in batches on a larger S275JR plate (Figure 5-42), followed by EDM cutting into smaller samples and finally grinding of the clad surface. The surface roughness before and after grinding of the Stellite 6 coating can be seen in Figure 5-43, next to the Hardox 500 as rolled surface.

Figure 5-42 S275JR plate with multiple laser clad batches prior to be cut into individual specimen plates

Figure 5-43 Specimen plates used in the erosion tests

A preliminary test was performed on an aluminium sample for 10 seconds, to ensure correct alignment of the nozzle, for which the results are shown for reference in Figure 5-44. The volume loss for aluminium is significant, 0.43 mm^3, considering that the test duration was 10 seconds. Some other features of the wear scar that can be seen in Figure 5-44 are the narrowing of the scar towards the edges due to the lower impact pressure of the flat jet. In addition, the primary and waviness profiles which were measured in the centre of the scar, show the scar inner surfaces not to be symmetrical. This indicates the angle of attack of the spray, in this case it was directed from the top right hand side towards the centre of the scar, hence the steeper angle of the scar surface on the right hand side, which eroded that side more than the opposing side.

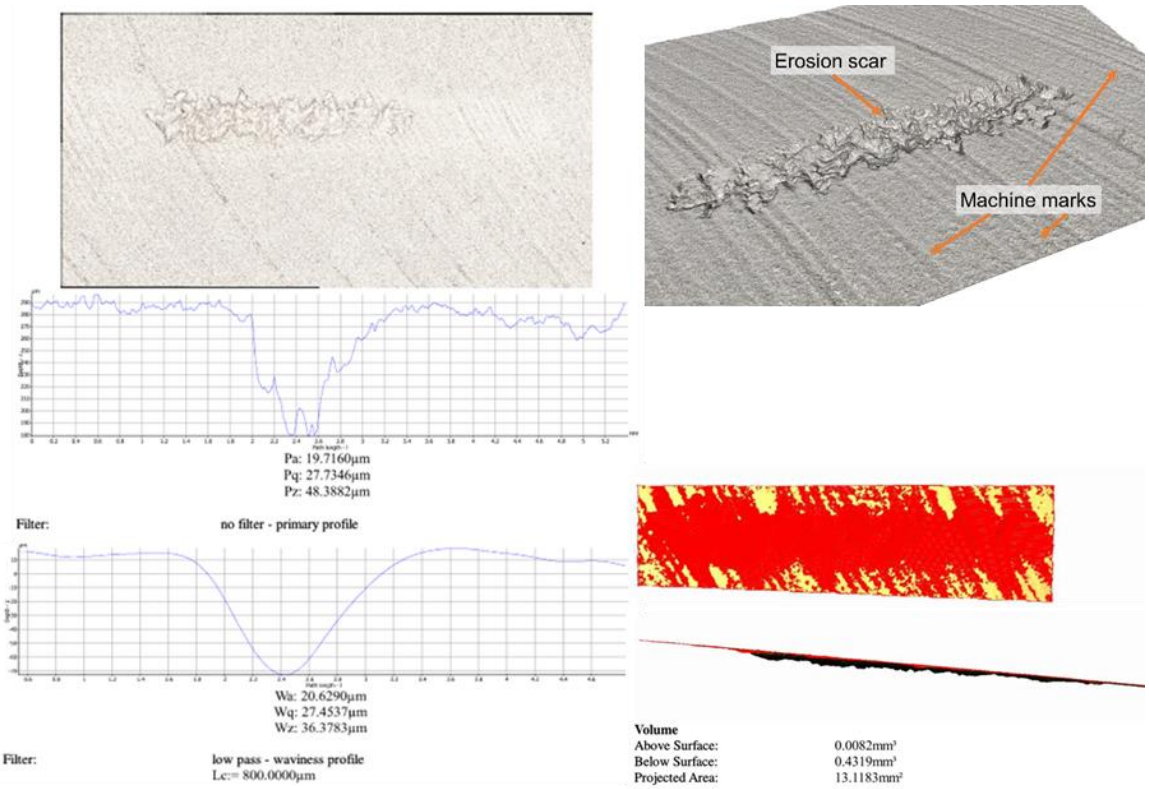

Figure 5-44 Aluminium reference sample: Primary and waviness profiles (left) – 3D image of Alicona scan (top right) and volume loss (bottom right)

The samples were sectioned and ground by hand on a grinding machine to a final 1200 grid paper and also polished with 3 µm and 1 µm diamond suspension. The specimens were etched using a solution with 4.76% Nitric acid, 47.62% Hydrochloric acid and 47.62% distilled water to reveal the grain boundaries and substructures of the microstructure. Typically 2% Nital solution would be used for etching, however, it was found during the analysis of the railway twin disc tests (6.1) that the clad material required a stronger etchant. Figure 5-45 is a though thickness image of the clad material stitched together from optical microscope images. A fine dilution zone stands out and almost parallel to the ground surface of the clad. The waviness of the dilution zone is acceptable (30 µm, see Figure 5-46) and much improved from traditional welding clads, which is an advantage of the laser clad process. The clad material is dense with no porosity, various large pores are visible which are mainly stains from the preparation of the sample. The grain size in the S275JR substrate is much smaller near the dilution zone. The fine grain indicates that this is the heat affected zone (HAZ) from the cladding process and it has a thickness of about 1 mm into the substrate, which is the same thickness as the clad layer. The large HAZ is attributed to the soft substrate and although its thickness is large in comparison to the clad layer, it does not mean that the tribological performance is negatively affected, the contrary the large HAZ may have allowed for a smoother hardness transition from the very soft substrate (150 HV) to the very hard clad layer (500 HV).

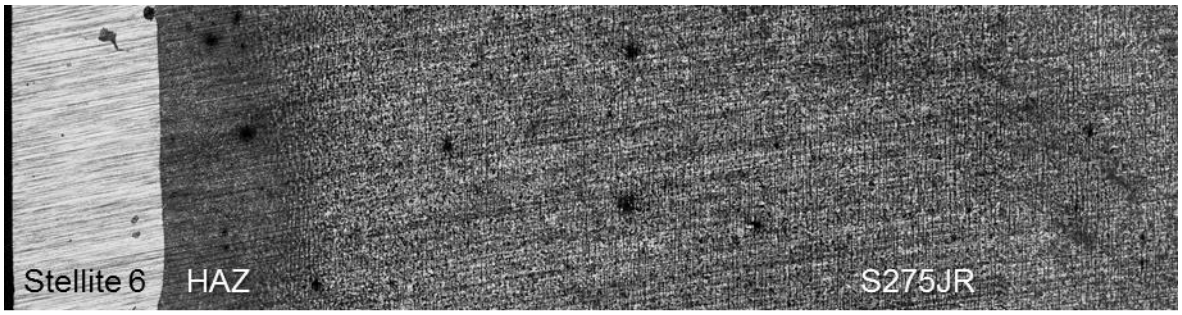

Figure 5-45 Optical microscope image of Stellite 6 clad on S275JR plate

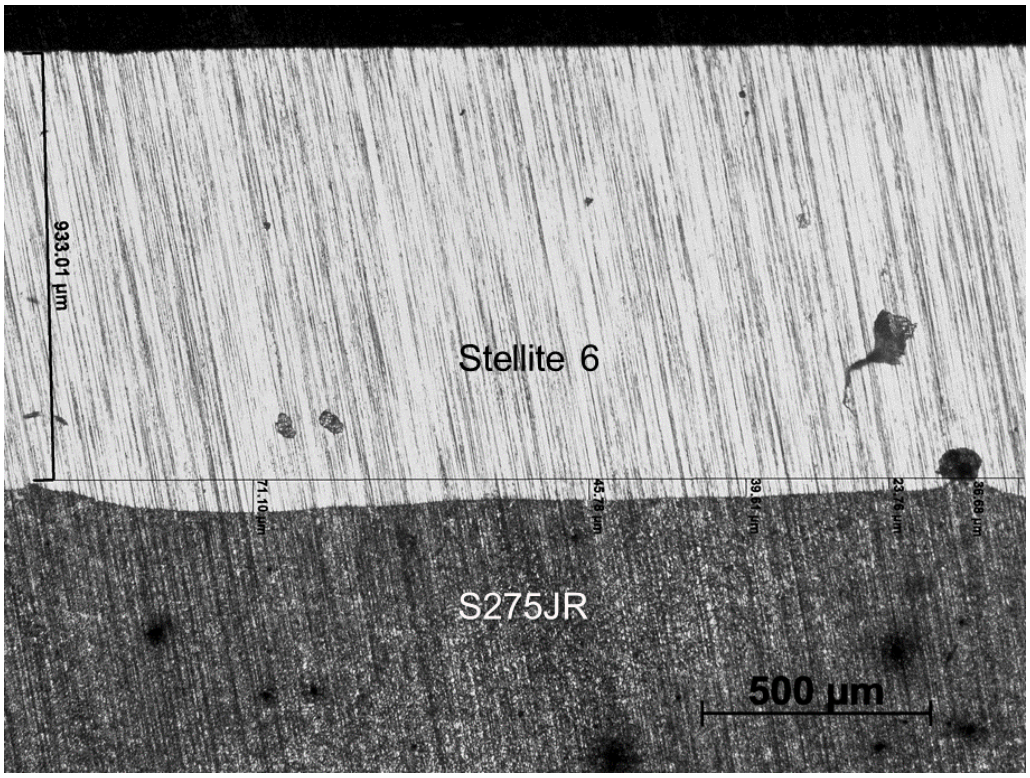

Figure 5-46 Optical microscope image of Stellite 6 clad on S275JR plate

Apart from the aluminium sample test, a prolonged test with the Stellite 6 clad was performed to set a benchmark for the comparison tests with other materials. Two target areas were tested, A and B as shown in Figure 5-47, where the test duration for area A was 4 hours and 8 hours for area B, at 160 Bar pressure.

Although the test sample in Figure 5-47 has been ground flat on a surface grinding machine, the top and bottom faces are not perfectly parallel, resulting in a slop of the roughness profile measurement in Figure 5-48. The dimples from scars A and B have been identified and indicated on the graph. The scars are better highlighted by the waviness profile in the same figure. After modifications to the rig and motor inverter, a maximum water pressure of 186 Bar was achieved and there was a significant difference in eroding power. It was decided to run the comparison tests at the higher pressure in order to reduce the test time.

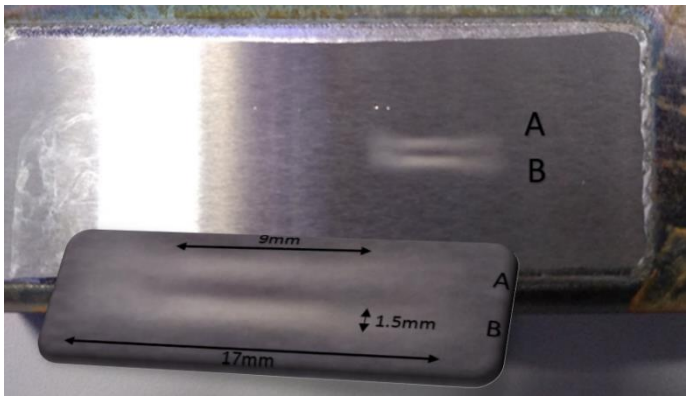

Figure 5-47 Image of Stellite 6 clad scars after 4 hours (A) and 8 hours (B) of testing at 160 Bar water pressure

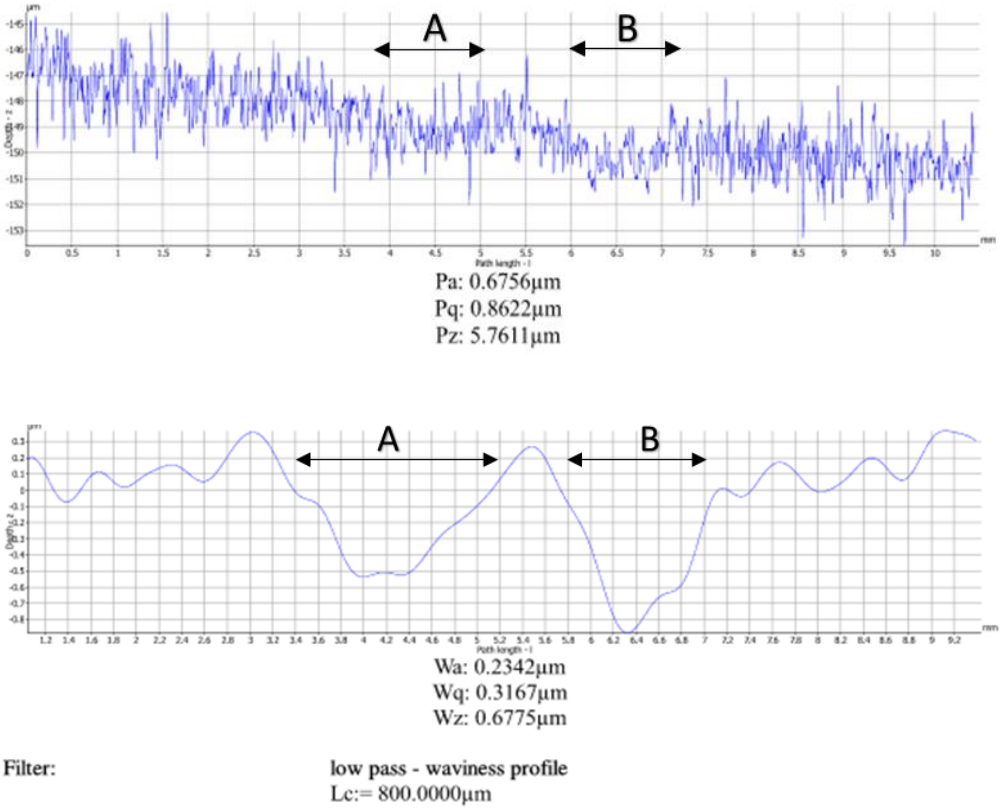

Figure 5-48 Primary roughness and waviness profile for tests A and B

5.6 Bending tests - Procedure

Fatigue crack growth tests on EA4T steel indicated an improvement in the fatigue life with the use of an Iron-based alloy clad material [160]. A three point bend test was chosen to generate cracks as a direct comparison of crack initiation properties of the coating materials. Furthermore, strain measurements were obtained with the use of Digital Image Correlation (DIC) software [203]. Thin chromium coatings typically contain microcracks caused by the electroplating process and due the

brittle nature of the material. Similarly the Technolase® coating also contained microcracks as a result of the extremely hard carbide particles that are fused in a comparably softer nickel-based alloy.

Preliminary tests on a three point bend test in the Camscan Series II Scanning Electron Microscope was performed with a chrome coated sample. Although an effort was made to produce thin test specimens to allow bending at lower force, the bending module reached the end of the load capacity at 4,8 kN. The Technolase® coating was 1 mm thick, which is five times thicker than the chrome plated coating of 0.2 mm, so it was decided to perform the remaining bending tests on a Universal Testing Machine (UTM) which has a higher loading capacity.

A UTM is typically used for flexural tests to obtain the modulus of elasticity in bending, flexural stress and strain. In this study the three point bend test was used to intensify the stress in a selected volume of the specimen in order to generate cracks and to identify the coating's resistance to crack initiation. In addition, strain was measured for direct comparison between the two specimens. The Tinius Olsen H25I S machine was used for the test, which is a bench mounted electromechanical machine capable of up to 25 kN loading force, either in tension or compression. A load cell was available for measuring the loading force. Figure 5-49 is an image of the testing equipment and corresponding schematic diagram of the three-pin arrangement.

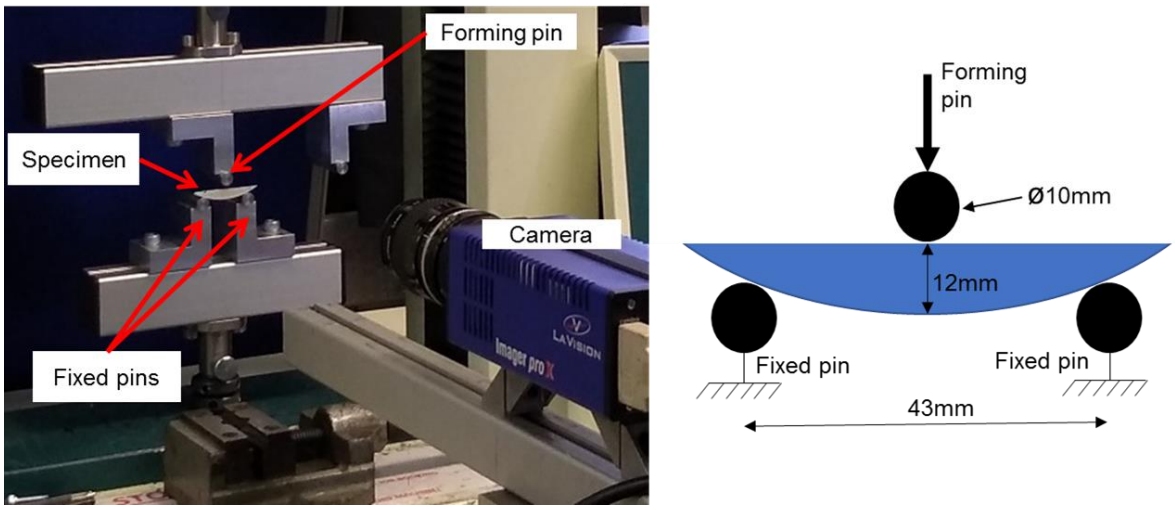

Figure 5-49 The Tinius Olsen H25IS UTM and LaVision camera used for the three point bend test (left) and schematic diagram (right)

Specimens were obtained from a roll pinion which was taken out of service due to cracking in various areas of the surface. Two sets of test specimen samples were produced from the same pinion. One set of specimens was taken from the chrome plated surface, while the second set of specimens was taken from an area of the pinion where two coating layers were deposited in two separate batches, see Figure 5-50. The laser cladding was produced by removing the chrome coating from the original pinion with a grinding machine, followed by pre-heating and application of the laser cladding using the Lasercarb® process. Smaller specimens from both sets were cut using Electrical Discharge Machining (EDM) to ensure accurate cutting of thin specimens with low heat input from the cutting process.

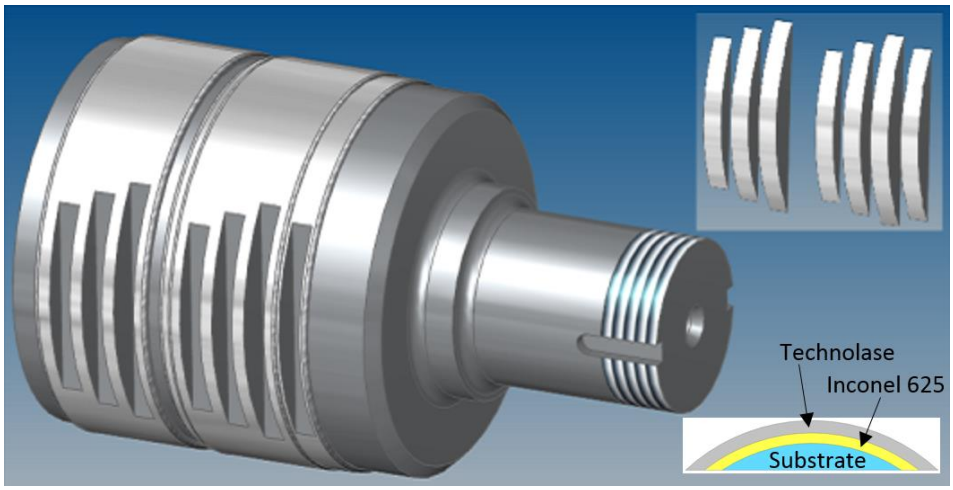

Figure 5-50 Diagram of various laser clad specimens taken from the clad pinion using EDM

The clad specimens were ground manually on a grinding machine to a final 1200 grid paper and polished with 3 μm and 1 μm diamond suspension. The specimens were etched using a solution with 4.76% Nitric acid, 47.62% Hydrochloric acid and 47.62% distilled water to reveal the grain boundaries and substructures of the microstructure that would enable a random surface pattern for the DIC identification in the SEM tests. For DIC identification during the UTM tests, matt acrylic white paint was applied on the specimens, while matt acrylic black paint was sprayed on top with an airbrush in order to create a speckle pattern. Figure 5-51 shows the detail of the speckle pattern for the macro specimen, which is 12 mm wide and for the micro specimen, which is 8 mm wide. All specimens have a thickness of 5 mm. Roughness measurements were obtained with the Alicona InfiniteFocusSL. Microhardness measurements were obtained with the Struers Durascan automated tester, using a Vickers indenter with 0.3 kg load. Nanoindentation tests were performed using the Hysitron Ti-Premier and with a Berkovich diamond indenter with an Elastic Modulus of 1140 GPa and Poisson's Ratio of 0.07. The equipment was calibrated with fused quartz and polycarbonate calibration samples prior to testing. A load of 8 mN was applied and held for 5 seconds while the load and displacement of the indenter was recorded. The reduced elastic modulus and hardness were calculated as a function of contact depth using the Oliver and Pharr methodology [194]. The Technolase® and Inconel 625 material characterisation results are presented in section 5.1.

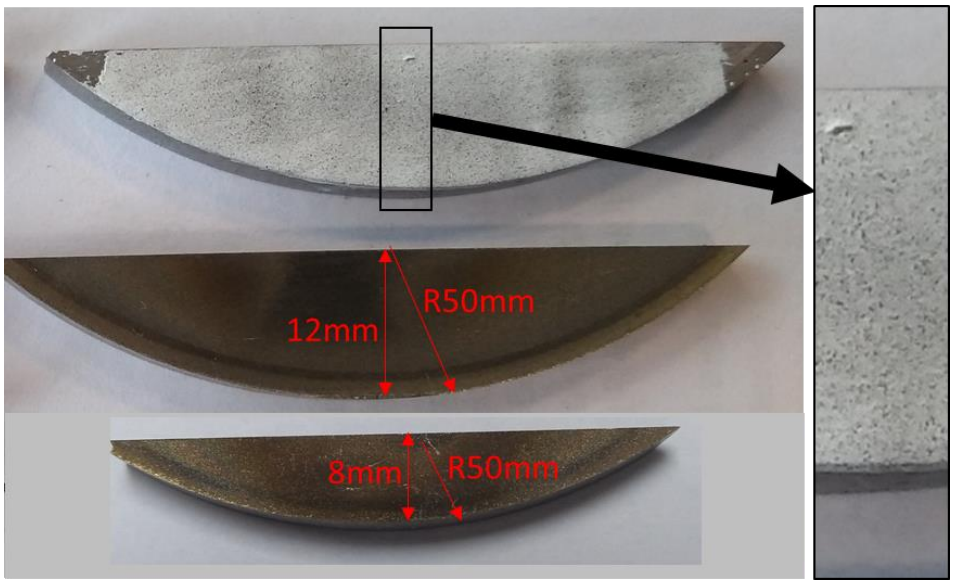

Figure 5-51 Laser clad test specimens of 5mm thickness, macro (12mm) and micro (8mm)

Micrographs of in-situ bend tests with specimens machined from pinions were obtained using the Camscan series 2 SEM. The bend test was performed using a Deben tensile and horizonal bend test module, with a capacity of 5 kN, see Figure 5-52. A sample inserted in the in-situ module having undergone preparation revealing the microstructure to be observed under load.

The loading was performed at a speed of 0.1 mm min^{-1} and the tooling geometry consisted of 5 mm diameter pins with the collinear support pins having a 37 mm spacing between them and in contact with the coated concave face. The flat face of the substrate was in contact with a centrally located 5 mm diameter forming pin, which was preloaded to 30 N to take up some of the slack in the module prior to being inserted in the SEM vacuum chamber. The specimen could be observed with up to 4.8 KN bending force. An interrupted bend test was performed allowing micrographs of the stationary specimen to be obtained.

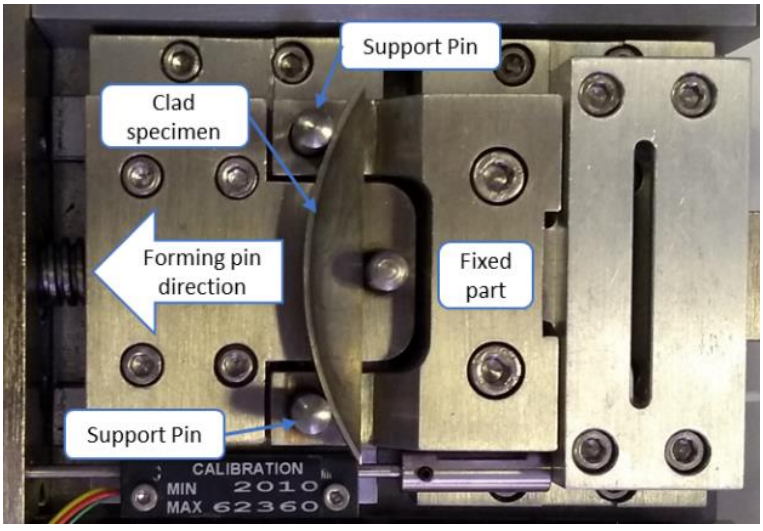

Figure 5-52 Specimen loaded onto the bending stage

Post-test DIC analysis of the micrographs to study the strain behaviour was not successful due to the lack of speckles in the intermediate layer microstructure which is essential for DIC, but also because the bending range was not sufficient to produce significant deformation and damage to the micro specimen. For this reason, repeat tests were performed on a Universal Testing Machine (UTM) for three point bending to a breaking point of the specimen by displacement control at a displacement rate of 0.04 mm s^{-1}. Two collinear pins of 10 mm diameter were in contact with the curved face of the specimens and at a distance of 43 mm between them. The forming pin was in contact with the flat face, aligned with the centreline of the specimen.

6 RESULTS ANALYSIS

6.1 Railway materials rolling/sliding

6.1.1 Railway materials twin disc - Results

The results are presented in terms of wear rate for the rail steel (Figure 6-1) and for the wheel steel (Figure 6-2). The line connecting the datapoints is for visualisation purposes only. Data are presented in terms of wear rate plotted against Tγ/A for the rail (Figure 6-3) and as system wear which includes the sum of wheel and rail steel wear (Figure 6-4).

In Figure 6-1 and Figure 6-2 the wear rates are plotted for the three slip ratios tested, split into three graphs. Additional data from tests on MSS laser clad rail performed under the same conditions [1, 200] are included in the figure for comparison with the R260 baseline and premium material data. The reference wear rates for 10% and 20% were only available for the overall test, for example wear rates for the 10% test were available as the mass loss divided by 10,000 cycles and for the 20% test as the mass loss divided by 1,000 cycles. An effort was made to interrupt the tests and to provide wear rates at interim stages. This is crucial for capturing the wear in period and identifying the steady state. For the 10% tests, measuring mass loss every 1,000 cycles was sufficient, as the steady state was identified around 3,000-4,000 cycles. It was not practical to capture wear in for the 20% tests, the test was interrupted only once at 500 cycles.

Regarding the final wear rate figures from the tests that are used for comparison in Figure 6-3 and Figure 6-4, the wear rate values at the last cycle datapoint for each test was chosen. This means that for the 1% slip tests the mass loss in the last 5,000 cycles was used. Variation of wear rate is rapid in the initial cycles under the 1% slip condition, so rate measured later will be closer to the steady state value applicable to the majority of rail life. The 10% and 20% wear rate is significantly higher than the 1% wear rate and occur at much shorter durations. In service, these will take effect on a single event or events taking place in a short period of time, as a matter of minutes, as opposed to equivalent 1% slip wear that may take place over hours or days. Therefore, it is justifiable not to identify the steady state for the rapid wearing slip conditions and to compare the steady state wear rate of the 1% test with the overall wear rate of the rapid wearing tests. Furthermore, previous tests from which the wear rates of R260 and MSS Clad were included here for comparison, only included wear rates for the overall mass loss and did not identified if this was the steady state.

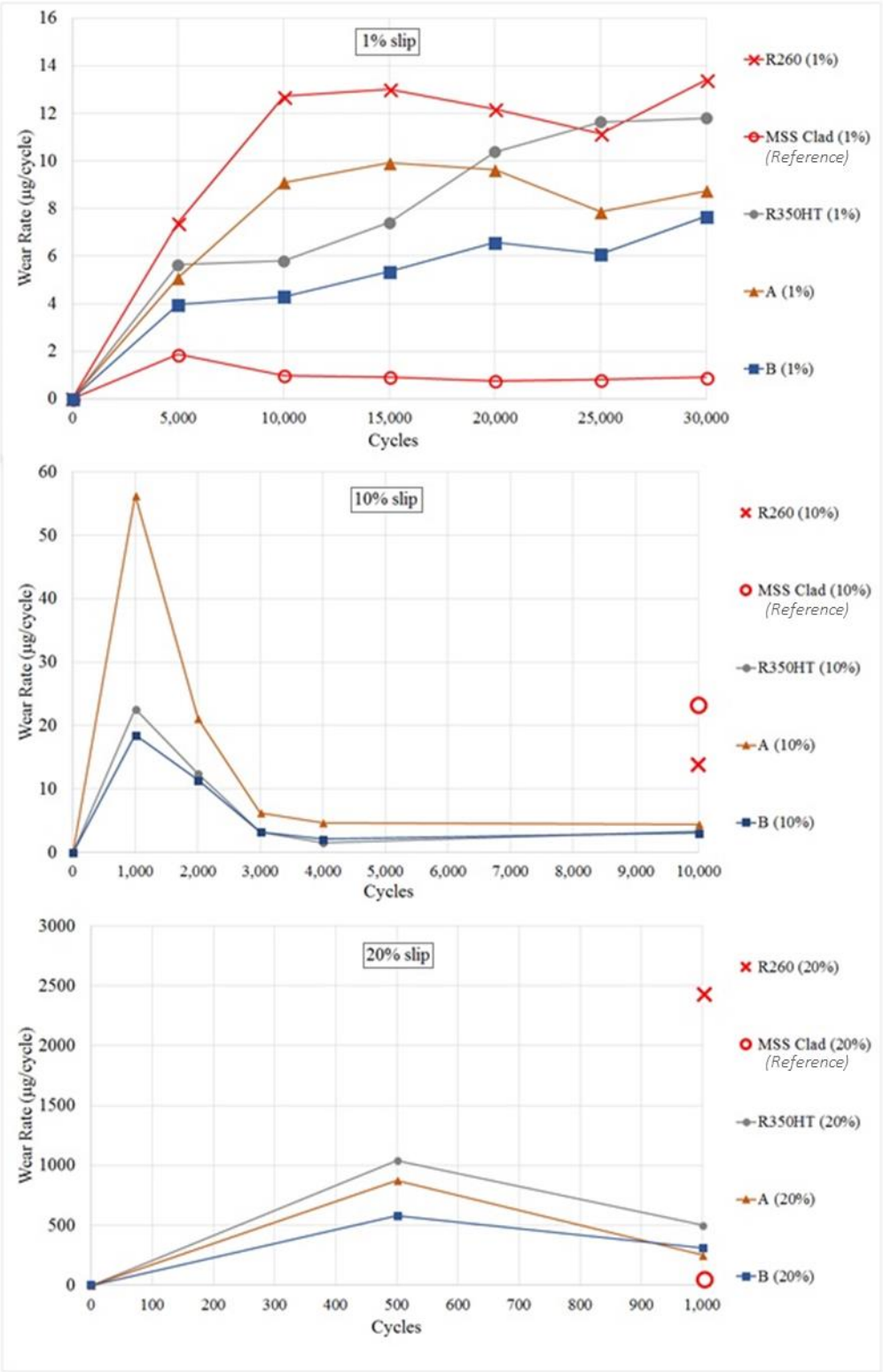

Figure 6-1 Rail wear rate per cycle at 1%, 10% and 20% with 1500MPa contact pressure and 400 rpm primary rotational speed.

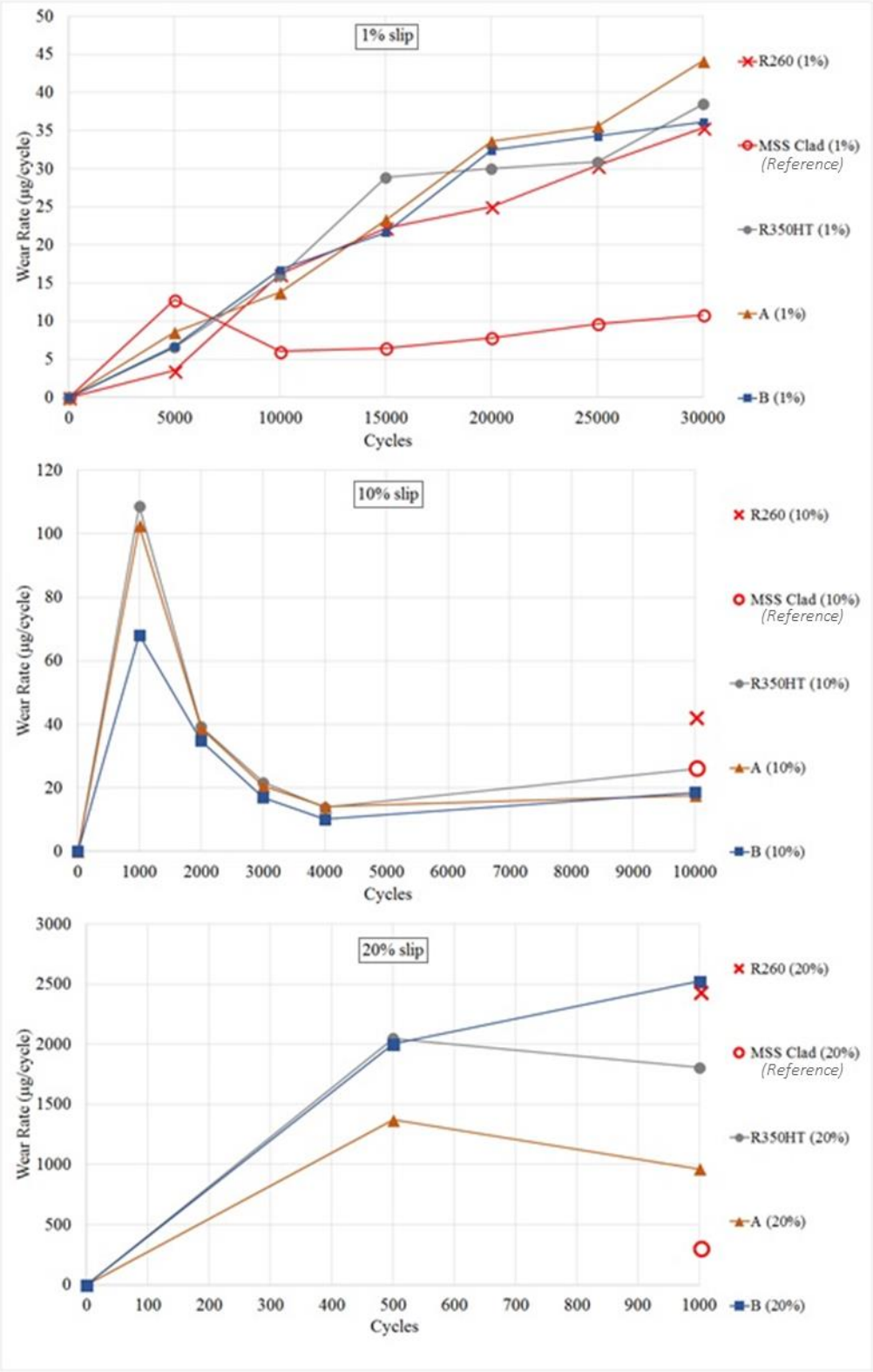

Figure 6-2 Wheel wear rate per cycle at 1%, 10% and 20% with 1500MPa contact pressure and 400 rpm primary rotational speed.

In Figure 6-3 all data is brought together using the full test duration mass loss to define wear. Material C showed poor wear resistance in comparison to the other materials at 1% slip and an extremely high wear in 10% and 20% slip tests. In addition, the material C rail disc became polygonised during testing, although the corresponding wheel disc remained cylindrical. This polygonisation of rail material C was observed in all slip conditions. Material C was developed to improve RCF resistance rather than improved wear resistance and it is difficult to say why the rail disc became polygonised. For this reason, the results for material C for 10% and 20% have been omitted from Figure 6-1 and Figure 6-2.

In Figure 6-3, the wear rate (µg/m/mm^2) is plotted against the contact energy over 1mm^2 area (Tγ/A). The data points are forming three distinct areas on the graph, which resemble the three wear regimes of "Type I-Mild", "Type II-Severe" and "Type III-Catastrophic" [20, 21, 196]. A Schematic of this typical relationship of pearlitic steel indicating a predicted path for the data points is illustrated in Figure 2-15. This path on the graph is verified in Figure 6-3 and highlighted with the exception of material C. Repeat tests were performed for all grades and at all conditions for validation of the results, with the exception of R260 at 20% and MSS Clad at 1%.

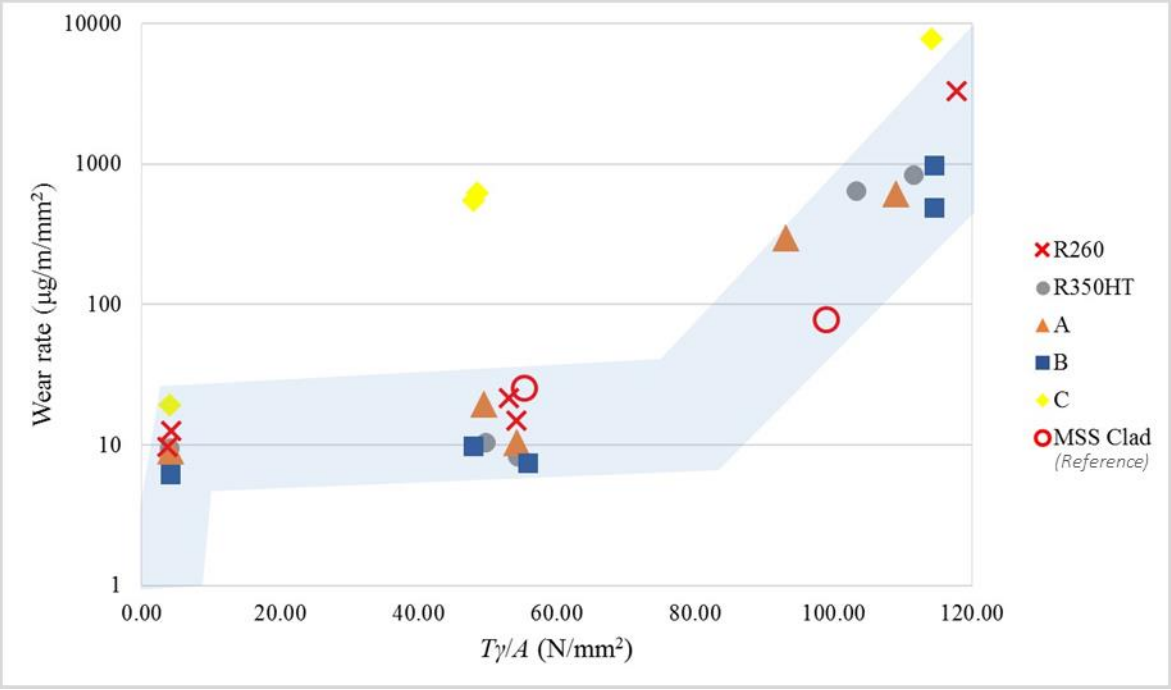

Figure 6-3 ***Rail wear rate vs Tγ/A.***

Figure 6-4 allows exploration of how much wear damage is attributed to the wheel and how much to the rail. The overall wear in µg for the wheel and rail is shown in for each slip condition, with the exception of material C. It can be seen that at low slip conditions (1%) the wear rate values are similar for all rail materials with the exception of the MSS material which is significantly lower. Similar performance is observed at 10% slip tests and more variation is observed at 20% slip tests between R260 and materials A, B and C. The system wear rate (rail and wheel wear rate) is indicated by the addition of the lower and upper parts of the graph bars. Although the MSS material is performing better at 1% and 20% slip tests in terms of system wear, during the 10% slip test the wheel is worn

significantly and as a result the system wear rate is raised to comparable levels to the other materials. Significant wheel wear for the R260 at 20% slip test has increased the system wear to much higher values than the other materials at the same slip conditions.

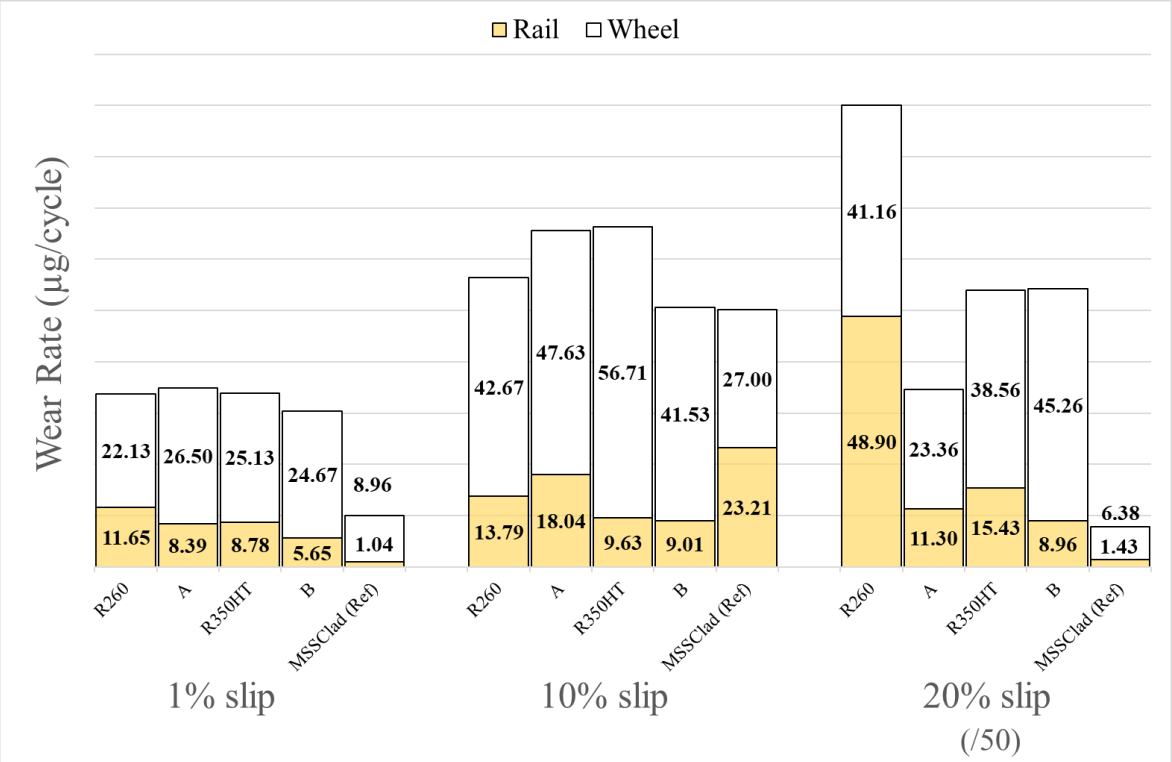

Figure 6-4 Cumulative System wear (20% is shown on a different scale).

Etched images from an optical microscope are shown in Figure 6-5 to Figure 6-9. In some images the hardness diamond indentation is still visible after etching. The grain deformation indicates the rolling direction, which is the direction of motion for a driving wheel, i.e. on these figures wheel motion would have been over the rail surface right to left, with traction applied left to right.

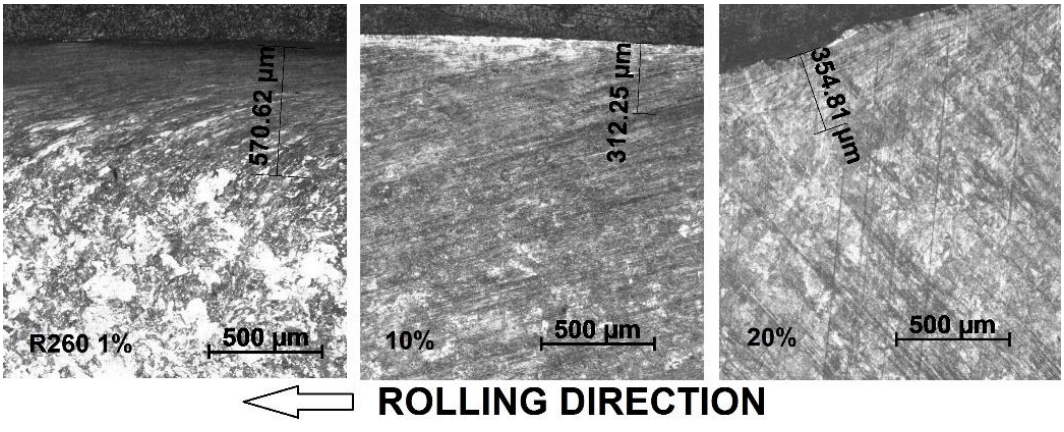

Figure 6-5 Optical microscope images of R260 (1%, 10%, 20% slip).

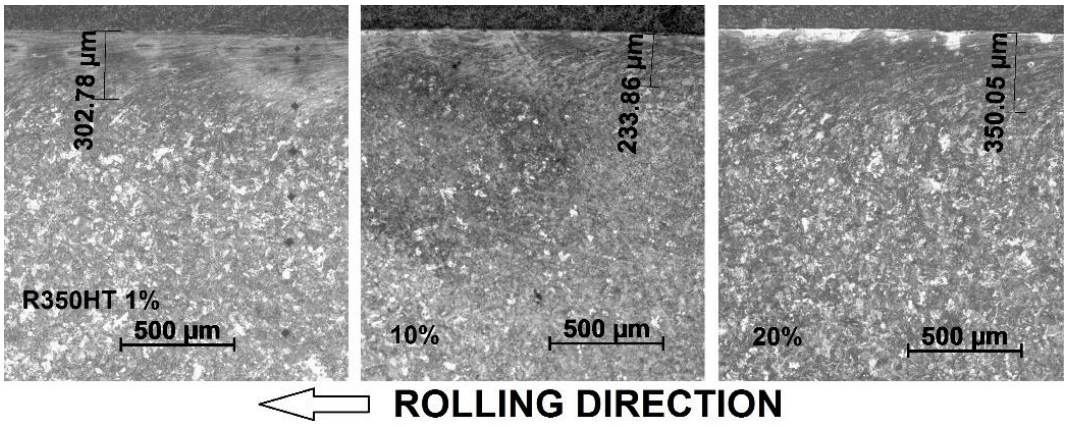

Figure 6-6 Optical microscope images of R350HT (1%, 10%, 20% slip).

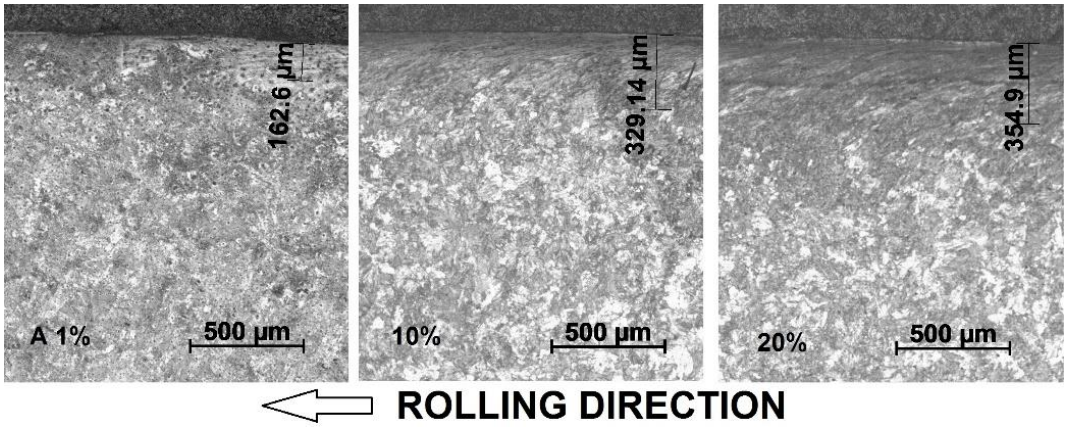

Figure 6-7 Optical microscope images of A (1%, 10%, 20% slip).

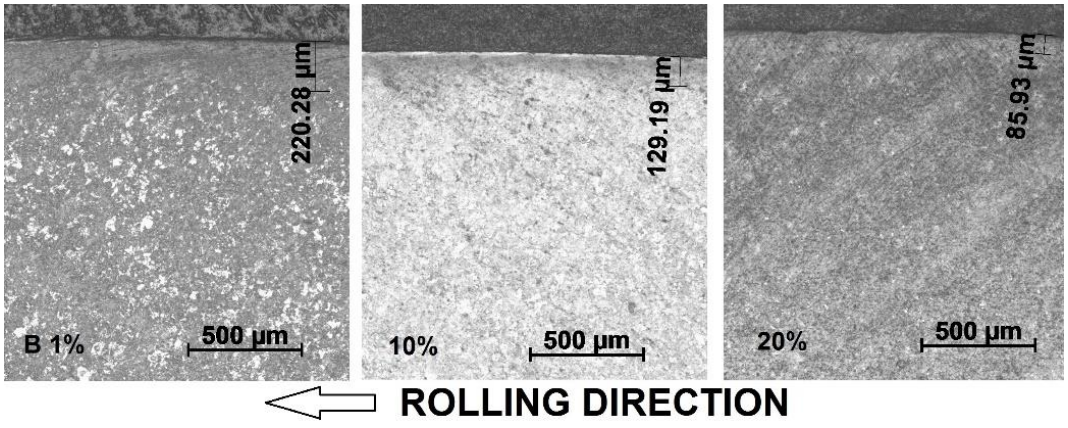

Figure 6-8 Optical microscope images of B (1%, 10%, 20% slip).

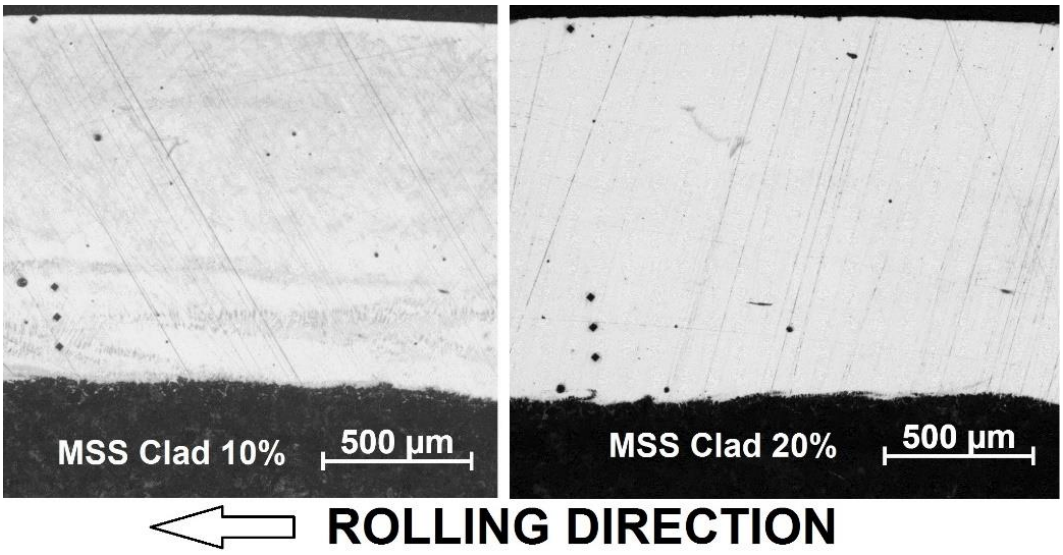

Figure 6-9 Optical microscope images of material R260 with MSS clad, from 10% and 20% slip etched samples - Very small plastic deformation. The clad coating is very hard and difficult to polish and some scratches remain on the surface.

Finally Figure 6-11 shows pairs of rail and wheel discs for the 20% slip test, while Figure 6-12 shows images of the etched samples taken from the 20% slip test of the R8 wheel material. The notation on the images indicates the rail discs material reference, R260, R350HT, A and B. There is a peculiar phenomenon of plastic deformation which differs in each material combination and rolling conditions. It is worth noting that although related through the ratchetting mechanism, plastic flow does not lead to wear until material reaches ductility exhaustion. In these high slip test for R350HT and R260 rail grades there was considerable plastic damage, but with grossly deformed material still retained within the disc. Figure 6-10 is an adaptation of Figure 2-18 which highlights in red the R260 friction values from the tests. At 20% slip a friction value of 0.59 was measured, it is likely that surface ratcheting took place and this might be possible explanation for the plastic deformation that can be seen in Figure 6-11.

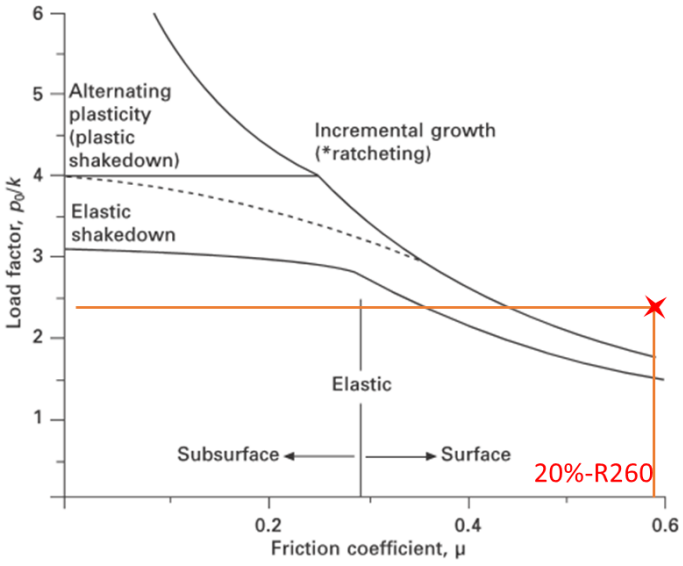

Figure 6-10 Shakedown map of friction and load-carrying capacity of contact

Figure 6-11 Image of wheel and rail discs after testing at 20% slip.

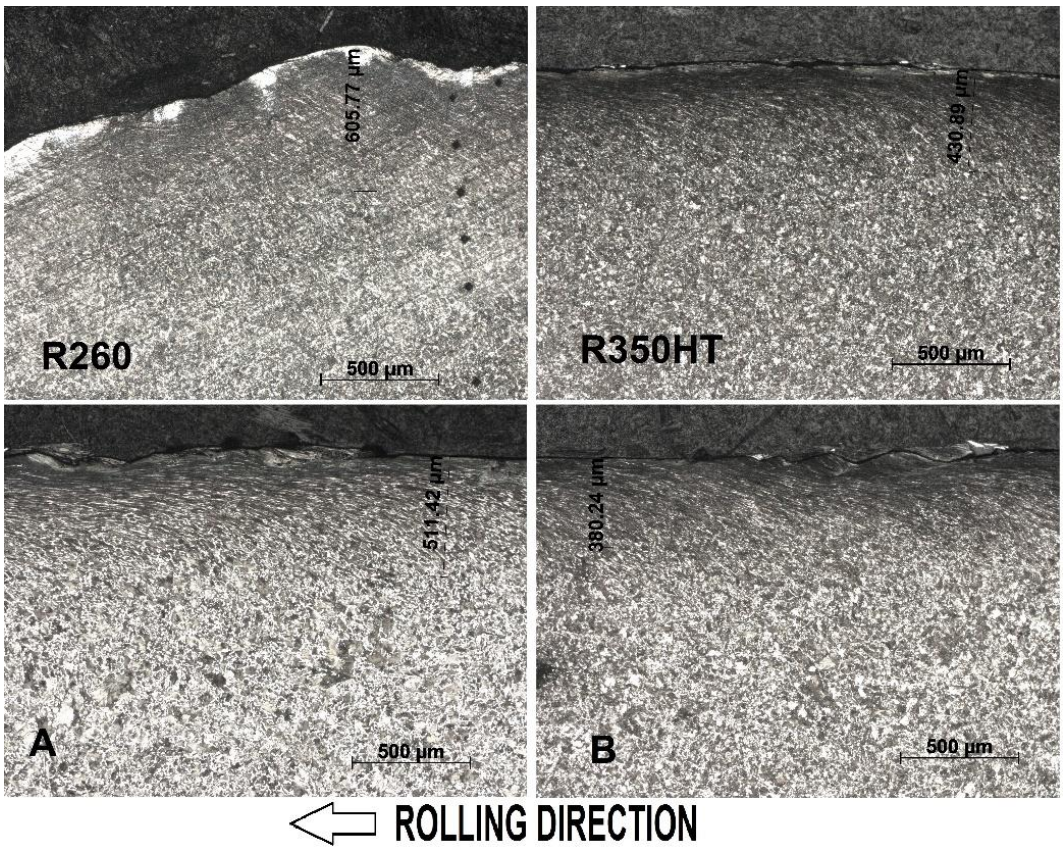

Figure 6-12 Optical microscope images of wheel material R8, rolled against R260, R350HT, A and B rail discs, taken from 20% slip etched samples.

For the material A test, the wheel exhibits short flat areas which did not form on the rail material. This is similar to the material B tests, where the rail exhibits minor out-of-roundness on the surface profile, while the wheel has remained round. This can be observed in Figure 6-12 between the edge profile of R350HT and the edge profile of material B. In magnification the plastic deformation near the surface of material B exhibits a wave pattern, as shown in Figure 6-13.

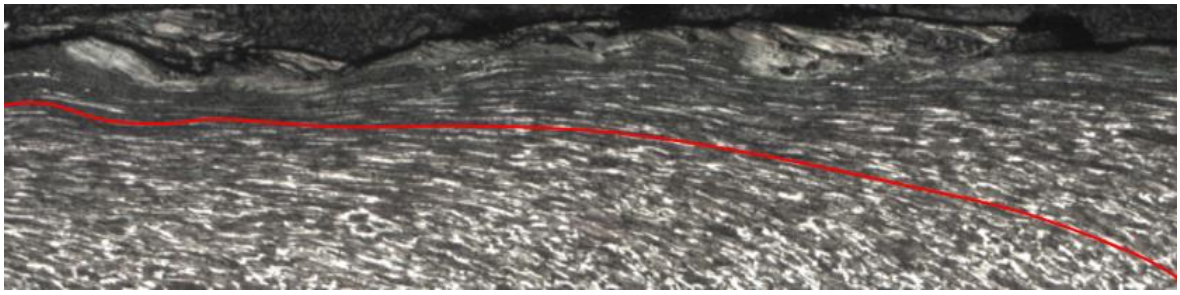

Figure 6-13 Image of wheel disc (Material B-tested at 20% slip) indicating the waviness of plastic deformation near the surface.

For the material R350HT test, the wear patterns on both the wheel and rail are similar for high (20%) and lower slip tests. The R260 test has shown another peculiar phenomenon where both the wheel and rail discs have formed a matching pattern between them that resembles a helical gear. This is visible in Figure 6-11, where the edge of the disc is sloping and where material has been removed as well as plastically deformed. This phenomenon could be induced by many things such as high temperatures in the contact zone and the plastic deformation attributed to the work hardening properties of R260, although the exact mechanism is unknown.

Hardness mapping of rail heads and disc samples was performed using a Struers Durascan micro hardness machine, as an additional verification step of the disc sample quality. Cylindrical off cuts of the SUROS discs were ground and polished. Railhead specimens of the premium materials were cut from unused rail with an Electrical Discharge Machine (EDM) which is a slow process that induces only very small localised heat and plasticity to the sample, which is easily removed by grinding, as opposed to other cutting methods. The cutting profile in the Electrical Discharge Machine produced 20 mm thick slices out of R260, R350HT, A, B, and C rail materials, which were cut from the railhead, excluding the web and foot. The cuts were obtained perpendicular to the running surface of the rail. The indentations were distributed across the surface of each sample at a macro level of 3 kgf load. Based on the code described by Brayshaw et al. [204] an interpolation method is used between the indentation datapoints and a surface plot is created. Outside the datapoint boundary (i.e. within 0.5-1 mm from the surface where reliable hardness indentation cannot be performed) the values are normalised to the average hardness value of the dataset to allow the sample boundary to be shown. The results are shown in Figure 6-14 to Figure 6-18.

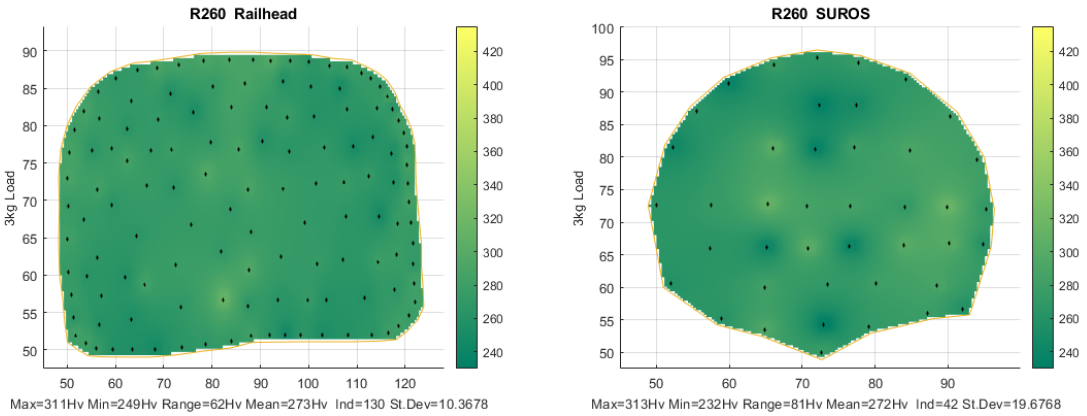

Figure 6-14 Hardness mapping on the surface of material R260 Rail and SUROS disc specimens

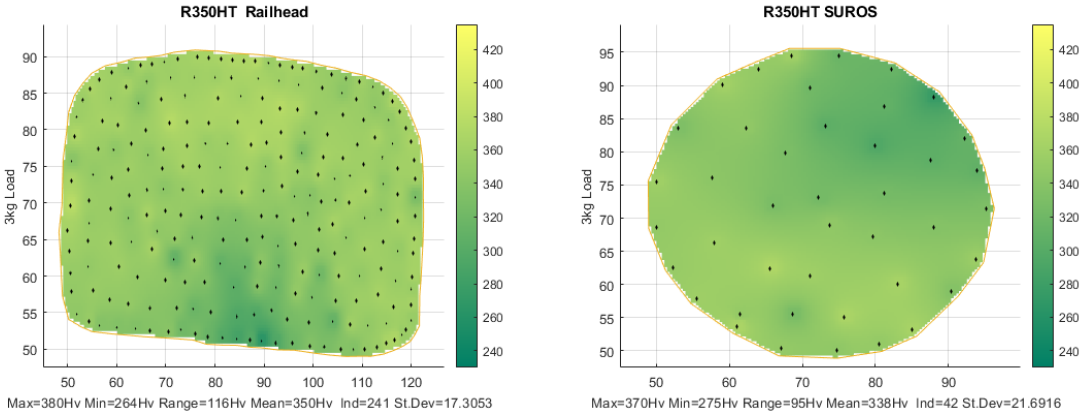

Figure 6-15 Hardness mapping on the surface of material R350HT Rail and SUROS disc specimens

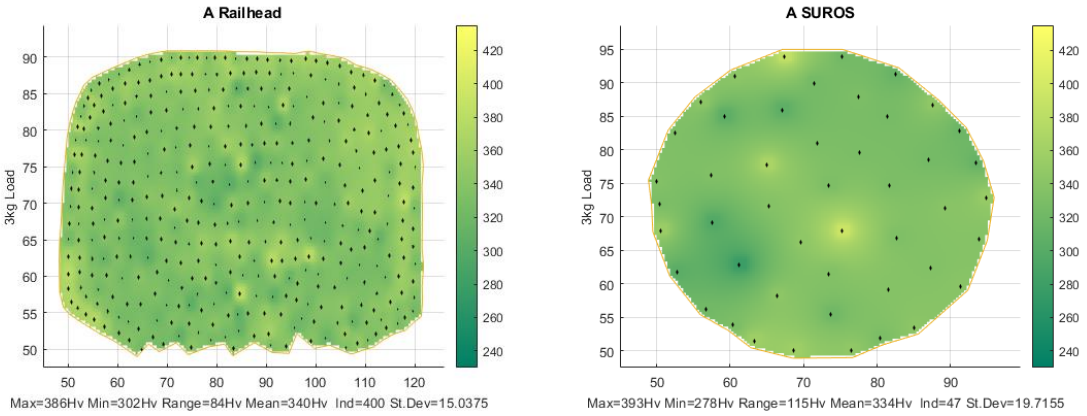

Figure 6-16 Hardness mapping on the surface of material A Rail and SUROS disc specimens

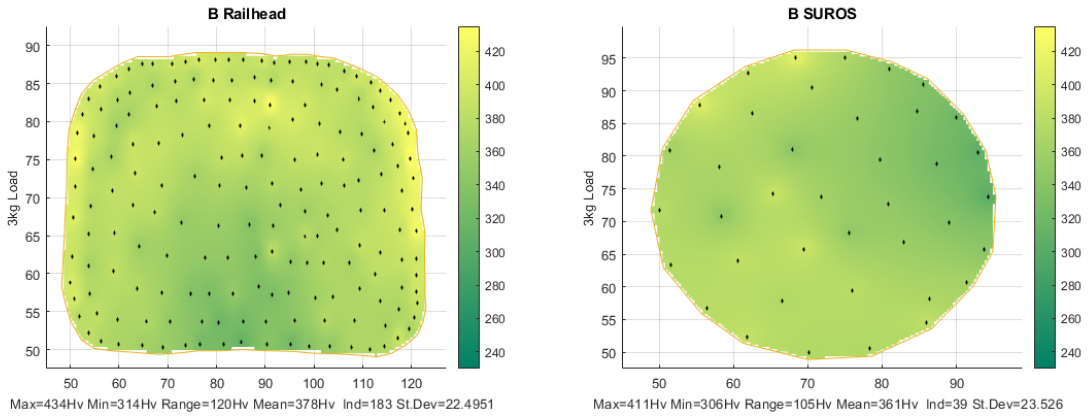

Figure 6-17 Hardness mapping on the surface of material B Rail and SUROS disc specimens

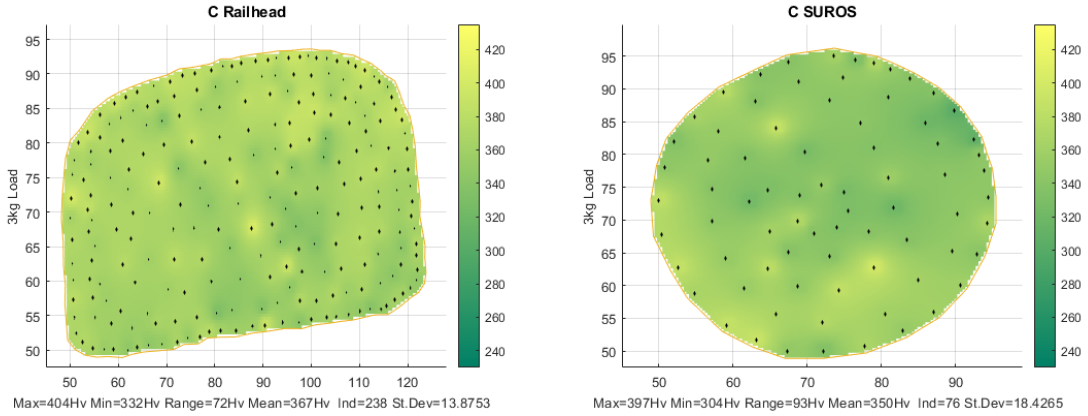

Figure 6-18 Hardness mapping on the surface of material C Rail and SUROS disc specimens

Figure 6-19 is a descriptive analysis of the hardness results and a comparison is made for the sample dataset between rail and SUROS disc materials, without generalisation on the hardness distribution of the full-length rails used in service. The median value and quartiles are indicated by the box marker, while the whiskers indicate the minimum and maximum values measured in each specimen. Cross markers indicate the mean hardness value of the indentation samples and the number of samples in each dataset is shown above the corresponding material on the graph. It is evident that the mean hardness between rail and SUROS disc material is very similar for the softer R260 material, despite the significantly smaller number of 42 samples for the SUROS discs (130 for the rail) and the wider range of hardness measured on the SUROS disc. The R260 mean value is 273 HV which is the equivalent designated material hardness for this rail grade of around 260 HB. With increasing hardness of the materials, it was observed that the difference in mean value was increasing as well, A SUROS disc was around 1.5% softer than A railhead, while the remaining SUROS disc materials were around 4% softer than their equivalent railhead materials. The number of indentation samples was roughly proportionate to the sample's surface, so more indentations were obtained for the railhead as opposed to the SUROS disc. Excluding R260, the ratio of indentation samples between railhead and SUROS disc varies from very high (454 to 47) to very low (238 to 76). In all cases the maximum and minimum SUROS disc hardness values are lower than the their equivalent railhead values, which yields lower mean and median values for the SUROS disc than the railhead.

For the R350HT material the mean value is the equivalent of 330 HB, which is lower than the designated material surface hardness of 350 HB. However, R350HT is a heat treated material, which shows a hardness distribution from the centre of the railhead outwards, where the centre is the softest part of the railhead. This is captured in Figure 6-15 where the centre of the railhead is softer (darker in colour), while the non-heat treated R260 rail (Figure 6-14) shows a more uniform distribution of hardness, with some isolated harder spots in the centre axis of the railhead. This is a natural result of the rail heat treatment process caused as the outer surface of the rail cools quicker via convection but the relatively insulated centre cools slower by conduction into the surrounding steel which is of similar temperature. The hardness range in Figure 6-14 is 62 HV, while in Figure 6-15 is 116 HV, almost double. This means that the isolated harder spots in R260 are not as significant as the hardness variation in R350HT. This is also evident by the whiskers in Figure 6-19, which show the range of hardness measured for R260 is smaller than the range of measurement in R350HT.

Materials A and C indicate a uniform distribution of sporadic harder areas, while material B exhibits a similar pattern to R350HT, which indicates a softer rail head centre and this is confirmed by the hardness range of 120 HV, centre to edge of railhead. The hardness range for materials A and C is 94 HV and 72 HV respectively, indicated by the whiskers in Figure 6-19.

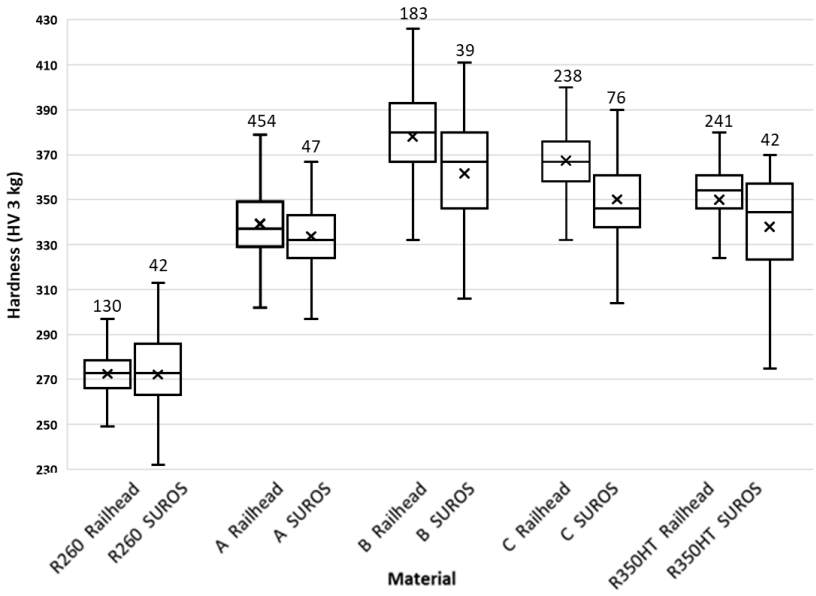

Figure 6-19 Hardness results for all materials (0.3 kg indentation load)

6.1.2 Railway materials twin disc – Discussion

The rail wear rate for all materials at 1% slip, increases until a steady state is reached before 30k cycles, see Figure 6-1, while for the laser clad material it decreases to a steady value. Blau [74] explains that the wearing behaviour during testing happens in stages, depending on the type of wear. Transitions from one stage to the next can be induced by external changes (Type 1) or they can occur naturally (Type 2), for example running-in, wear of coating and thermally-induced from the build-up of heat. An oxide layer on the surface of the specimens is thought to contribute to the initial running-in stage.

For rolling-sliding wheel-rail contacts the evolution of wear was studied in great detail by Kapoor et al. [205, 206], linking the variation of rate to the ratchetting and ductility exhaustion process. Since this is an accumulative and iterative material failure process as plastic strain builds up with each contact passage the wear rate is initially low. Depending on the surface traction level and sub-surface contact stress distribution strain accumulates at different rates at each depth below the surface. As very near surface material reaches its ductility exhaustion strain it drops away as wear debris and the layers below are revealed. These will have already accumulated some plastic strain and may therefore reach failure in fewer additional contact cycles than the original surface. If the contact stress distribution has generated significant sub-surface damage there can be a dramatic increase in cycle by cycle wear rate as these layers reach the surface, but a steady state is eventually reached when all material reaching the surface has been through a similar strain history. Stabilisation with wear rates in the order of 10 μg / cycle is evident in the 1% slip tests (similar to behaviour observed for normal grade steels [205, 206]), whereas the 10% slip tests show a very high initial wear peak (order of 20-50 μg / cycle) followed by stabilisation up to 10,000 cycles at around 4-5 μg / cycle. The peak and fall back in rate reflects the very near surface peak in sub-surface stress at the traction levels characteristic of high slip testing. It is possible that a longer duration test at high slip would reveal additional variation in wear rate as sub-surface pre-damaged material reaches the surface, however, such very high slip contact conditions are unlikely to persist as a steady state input for any real wheel-rail applications. A similar peak and fall back is present in 20% slip testing, although these tests are of even shorter duration, reflecting the catastrophic wear rates (order of 500-1000 μg / cycle) and again the improbability of these contact conditions existing as a long term steady state on the railway.

Figure 6-3 is a typical representation of wear rate against Tγ/A and most data points seem to follow the observations of Lewis et al. [21] as explained in the previous section and described by Figure 2-15. The wear rate is expected to increase with more traction in the interface and this is achieved with each increase of the slip ratio. Three groups can be observed, representing the 1%, 10% and 20% slip, each with a calculated Tγ/A value, with 1% at Tγ/A values below 10 N mm^{-2}, 10% at values in the region of 50 N mm^{-2} and 20% at values over 90 N mm^{-2}. The standard rail R260 showed the worst wear resistance at higher Tγ levels along with material C which was wearing significantly more in all slip cases and it is outside the expected wear zone, as highlighted in Figure 6-3. A result for R260 at 20% slip was omitted from this graph as the test was not comparable to the other data due to the large plastic deformation that cause the helical gear patterns as shown in Figure 14. Due to this conformal shape between the discs the friction coefficient in the system was increased to more than 0.5, resulting in high Tγ values outside of the scale of Figure 6-3 and subsequent very high wear under non rolling/sliding conditions.

Materials A and R350HT are designed for wear resistance and they have a similar performance at all slip conditions. There is a difference in system wear though which indicates that at 20% slip material R350HT is wearing the wheel more than material A. Material B is designed to be the most wear resistant grade and indeed it stands out as a lower wearing material in all cases. Even though the data points at 20% indicate higher wear, these are at very high Tγ/A indicating the harsh conditions. However, the system wear (Figure 6-4) for material B is worse than the other materials at

20% and this is due to the wheel wearing more at high creepage. Material C is mainly designed for RCF resistance and during these tests it showed poor wear resistance with high plastic deformation at all slip ratios and wear outside of the expected performance in comparison to the other rail materials. An R260 laser clad with MSS was tested to provide another point of reference of a non-commercial rail material. Although the laser clad material exhibits higher wear than the other rail materials at 10% slip, it is performing much better at 20% slip, with much lower wear than the other rail materials. In all cases for the laser clad material, the system wear is low because the wheel is wearing very little relative to other cases when the laser clad material is used. This observation highlights the importance of considering the wheel wear when comparing different rail materials and perhaps the selection of premium rail should be conducted as a system wear methodology.

The balance between rail wear and wheel wear varies for each material at 1% slip, and this can be seen in Figure 6-4. The overall system wear is more or less the same for all materials with the exception of material B which is slightly lower and the laser clad material which is significantly lower. This is an indication, that despite the various materials with various hardness levels, the system is behaving in such a way that it tends to wear the same amount for these conditions, either from the wheel or the rail. It is only for material B and for the laser clad material that the system wear is reduced. Figure 6-4 illustrates that in both of these cases the wheel is wearing significantly more than the rail, but still the overall system wear is lower than the other cases. It was observed that the wheel wore more than the rail in all the conditions tested, with the exception of R260 at 20% slip where the rail wore more than the wheel. The difference in wear rate between wheel and rail is small at low slip ratio, for example at 1% slip it is in the region of 15 µg / cycle. For the 20% slip the difference in wear rate between wheel and rail has increased and it is in the region of 1200 µg / cycle with the exception of R260 and MSS materials which is in the region of 300 µg / cycle.

For both the rails and the SUROS specimens it is the hardness near their running surfaces which is of interest since these are the areas which will be subject to shear and contact stresses. The hardness difference between the railheads and their corresponding laboratory SUROS discs can be seen in Figure 6-19. In each case the hardness range on the SUROS discs is higher than the railheads, except for R350HT and material B. In all cases the mean SUROS disc hardness is slightly lower than the corresponding railhead mean hardness. The mean hardness might not be as important for this comparison, as explained the hardness near the circumference of the sample can influence the test as it is closer to the contacting face. The hardness maps in Figure 6-14 to Figure 6-18 provide a visual representation of the hardness distribution for the SUROS discs compared to their corresponding rail heads. The discs were made from the centre of railheads and this is evident in R260 where the isolated harder spots of the centre railhead are found in the SUROS disc. For R350HT and material B, part of the softer centre of the railhead is found concentrated in almost a third of the circumference of the SUROS discs, with about 100 HV hardness difference with the rest of the circumference. For materials A and C, although the hardness difference on the circumference can vary by around 100 HV, it is not concentrated but intermitted. The variable hardness on the running face, along with the intrinsic properties of material C, might have been the cause of the polygonal deformation and extreme wear that resulted from the twin disc testing at all slip conditions.

6.2 Railway materials impact

6.2.1 Impact - Results

Impact tests were performed on four rail materials, the results are discussed in terms of test performance and tribological damage on the specimens. The potential energy was 21.7 J and therefore the estimated speed at impact was 5.56 m s-1 (see modelling section 4.2.3). The potential energy in the FEA was found to be the same, 5.4 J for a quarter model, see Figure 4-8. The measured speed from the speed sensor on the rig was 6.5 m s^{-1}. The drop time was calculated at 0.28 s while the measured drop time was 0.66 s. The speed and drop time measured were not very reliable, the system is based on a simple optical sensor and some lag in recording the event is expected. Similarly, the recorded impact load from the loadcell varied from 15 kN to 33 kN. As discussed in the modelling section 4.2.3, analytical calculation of the impact forces can be challenging due to the extremely short duration and ever changing amplitude of the force during that duration. The recorded sample rate was very low for capturing this type of event, a spike is shown in Figure 6-20 as opposed to a waveform, as predicted by the FEA (see Figure 4-16) which was calculated in small timesteps. It is likely that the loadcell is not measuring strain energy correctly as opposed to using strain gauges when measuring impact. Strain gauges calibrated for the impact application will measure strain directly from that component and translate into force based on the calibration, while the loadcell will measure strain on the internal component of the loadcell, which was calibrated for different conditions, for example static loading. Specific experiment and devices have been developed to deal with strain rate measurements higher than that of a typical hydraulic tensile test machine, 100 to 1,000 s^{-1}, one example is the Hopkinson pressure bar and for even higher rates the Taylor test, by projecting the test body onto a rigid target [207]. Substituting the force in Equation 4-10 with the minimum measured force of 15 kN would produce a contact stress of 141 GPa which would yield far more severe damage than that observed in the experimental results. In addition, the loadcell has been used previously in different experiments and it may have drifted from its original calibration. Another hypothesis is that the loadcell stiffness is out of phase with the effect of mass from the falling pin, in which case additional signal filtering could be applied in Labview using Fourier or frequency domain analysis, for filtering the force measurement at the correct frequency [208].

A lot of effort was made to re-commission the drop test rig, producing risk assessments and components for testing railway materials. Although it would be useful to capture realistic impact measurements, it was not the aim of this project to do so, therefore no further effort was made to achieve this, for example to apply signal filtering. Similarly, a load cell calibration was not performed, the recorded value for no load was over 1kN as shown in Figure 6-25. Instead, the direct loadcell readings were used as a comparison between the different materials and to enable detection of the pin deformation equilibrium state.

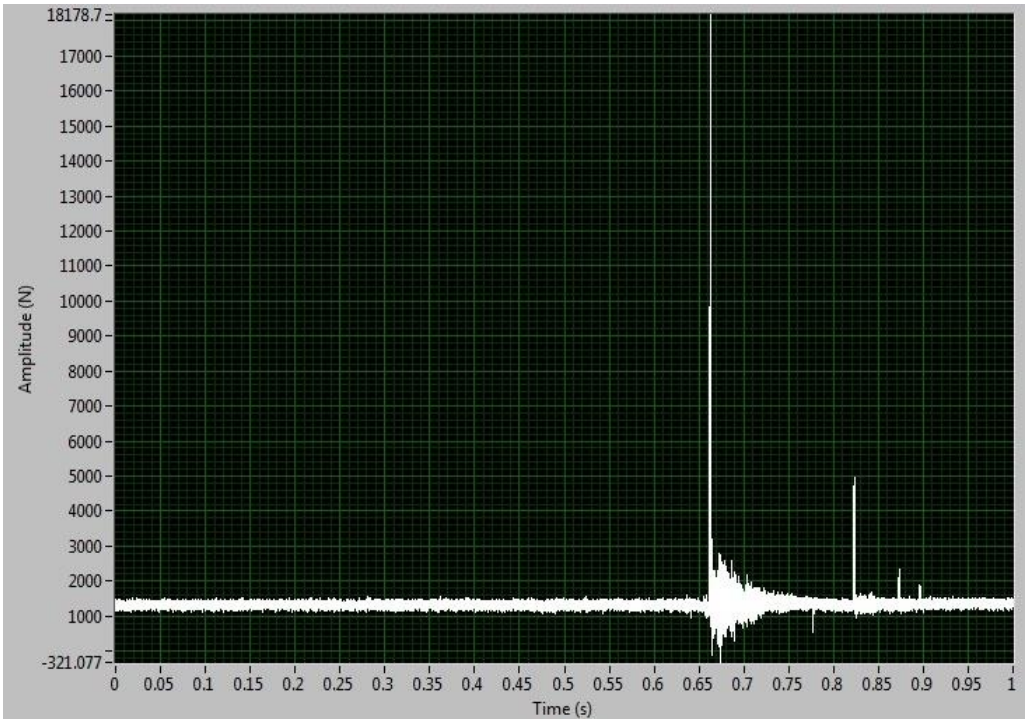

Figure 6-20 Loadcell measurement from the clad material impact test

With each impact, there was a rebound as explained earlier, which resulted in the pin impacting the sample multiple times. With each rebound the kinetic energy of the pin was transferred to the specimen, deforming it and raising its internal energy. The rebound, also known as restitution is recoverable elastic strain energy from the compression during impact. Restitution is repeated with less kinetic energy each time since kinetic energy is partially dissipated in the specimen, until no energy is left to lift the pin and frame mass, resulting in halting the pin. Dissipated energy from impact could be due to plastic deformation, elastic vibrations or rate-dependent processes such as viscoplasticity [192]. Figure 6-20 is the recorded force from a clad sample test, where the first impact was recorded at 18 kN and at 0.66 s. The second impact from rebound was recorded at around 5 kN and at 0.83 s. The third rebound impact was recorded just above 2 kN and fourth just below 2 kN at around 0.9 s. Further rebounding of the pin must have taken place prior to coming to a halt, however, this was not recorded due to a combination of very low values with high frequency. In fact, the noise from the datalogging system is significant, as it can be shown by the noise signal at just over 1 kN. This is present in all recordings and it could mean that the loadcell measurements were offset by around 1 kN, which would be important if the aim was to obtain absolute measurements.

Images of the impacted discs with corresponding primary roughness and selected volume profiles are shown in Figure 6-21 to Figure 6-24 for all materials tested. The primary roughness is an indication of the cavity depth, since the measurements in the Aicona were derived from the deepest point of the cavity, an example of how the primary roughness path was derived is shown in Figure 6-21. The graphs were combined together for a visual representation while the data from these measurements are shown in Figure 6-25, Figure 6-26 and Figure 6-31. The numbers next to each cavity indicate the order they were indented by the impact test. In some images the red arrows on the surface of the sample indicate where the rebound impact hit. The 3D images in colour are the

Alicona volume calculation from the measurements. Cross-sectional images showing the microstructure of the larger cavity of each material are shown in Figure 6-27 to Figure 6-30.

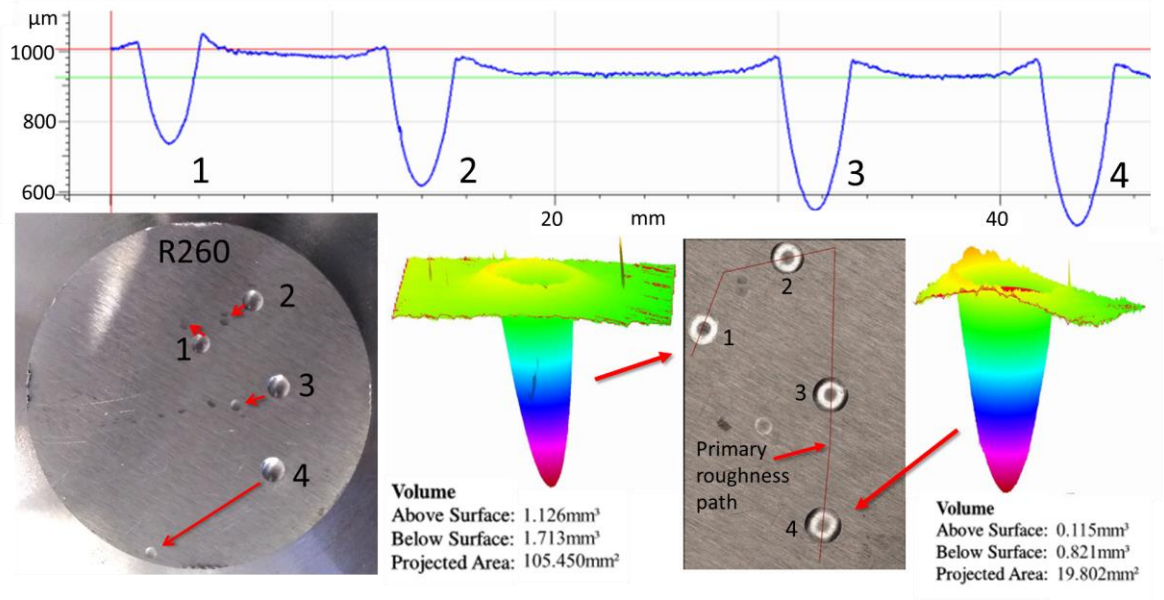

Figure 6-21 R260 test sample and volume surface scans

Rebound cavities, highlighted in Figure 6-21 by the red arrows on the sample (image on the bottom left), have not been measured. It can be seen from the images that they are significantly smaller than the first impact, which correlates with the recorded load pattern shown in Figure 6-20. With each consecutive impact, the pin is deforming plastically and becomes stiffer, resulting in the cavity depth and width to progressively increase. This is evident in the primary roughness profile in Figure 6-21, where the depth of the cavity is clearly increasing with each subsequent impact. Similarly, a raised surface around the cavity is increasing with each subsequent impact, this is more evident for the Manganese steel and it is discussed in the next section. Another effect that was observed was the reflectivity of the cavity surface. The R350HT cavity surface stood out from the rest as having a mirror finish. This is an interesting visual observation, however, it was not explored further in this study.

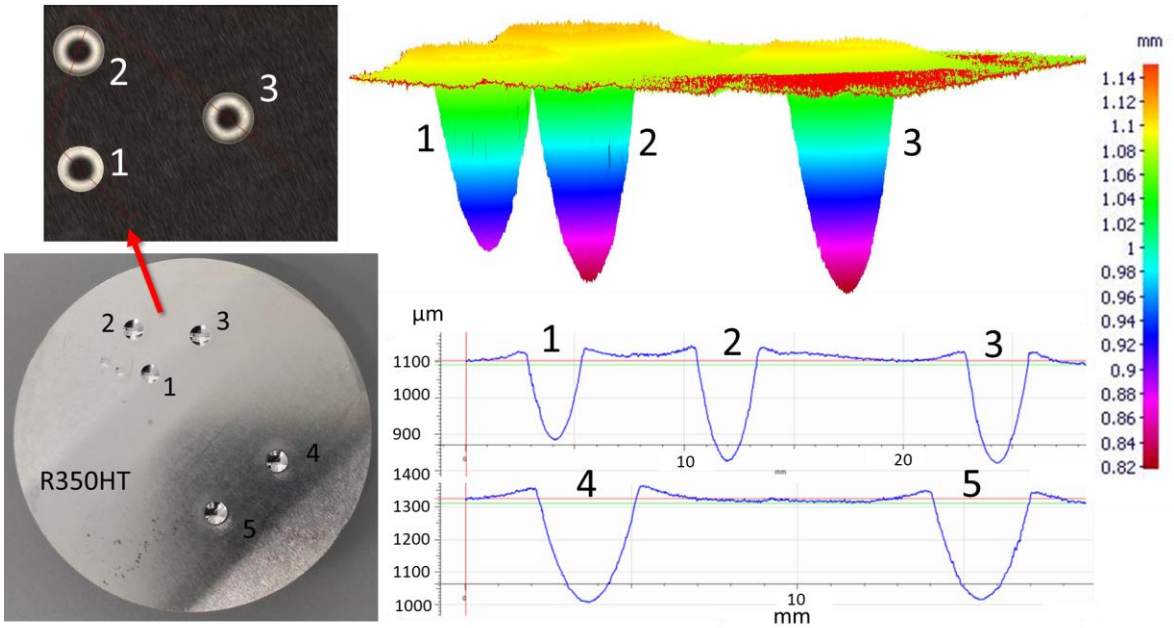

Figure 6-22 R350HT test sample and volume surface scans

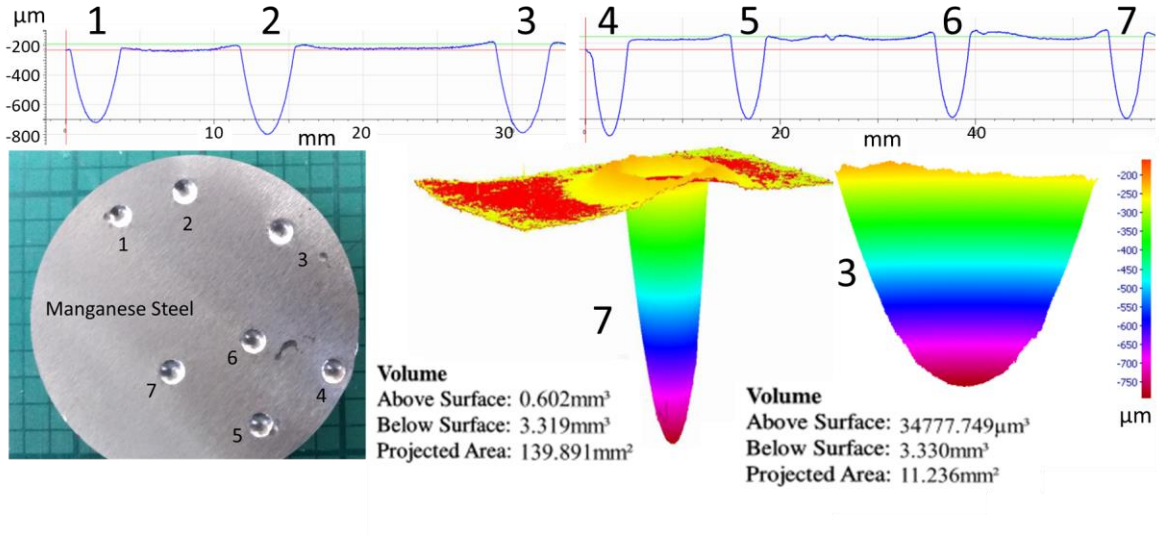

Figure 6-23 Manganese test sample and volume surface scans

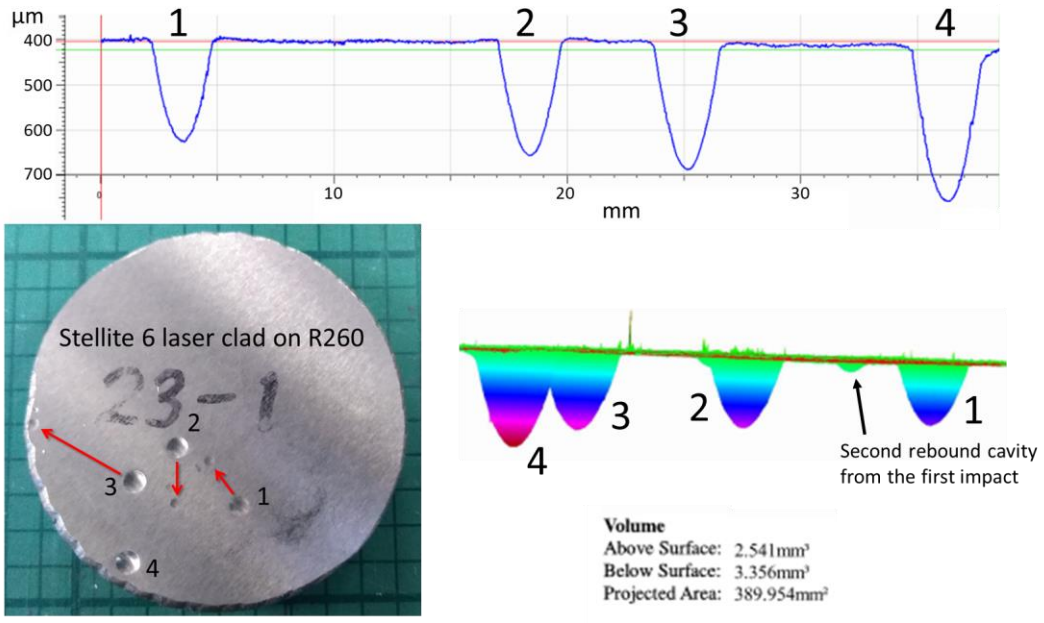

Figure 6-24 Stellite6 clad test sample and volume surface scans

The load force against repeat test with the same pin was plotted in Figure 6-25. Manganese sample data from repeats three and four are missing due to a datalogger issue. Despite this issue an increase in measured force is recorded with each subsequent impact. The force increases between impact three and four is smaller than between first and second impact. For example, R260 force increase is 4.5% (3rd & 4th) as opposed to 20% (1st & 2nd). The pin has a brass body which is significantly softer than the other materials and it is expected to continue to deform in unpredictable ways. Therefore, in terms of the pin deformation reaching an equilibrium state, the fourth impact for all materials was considered suitable for comparison.

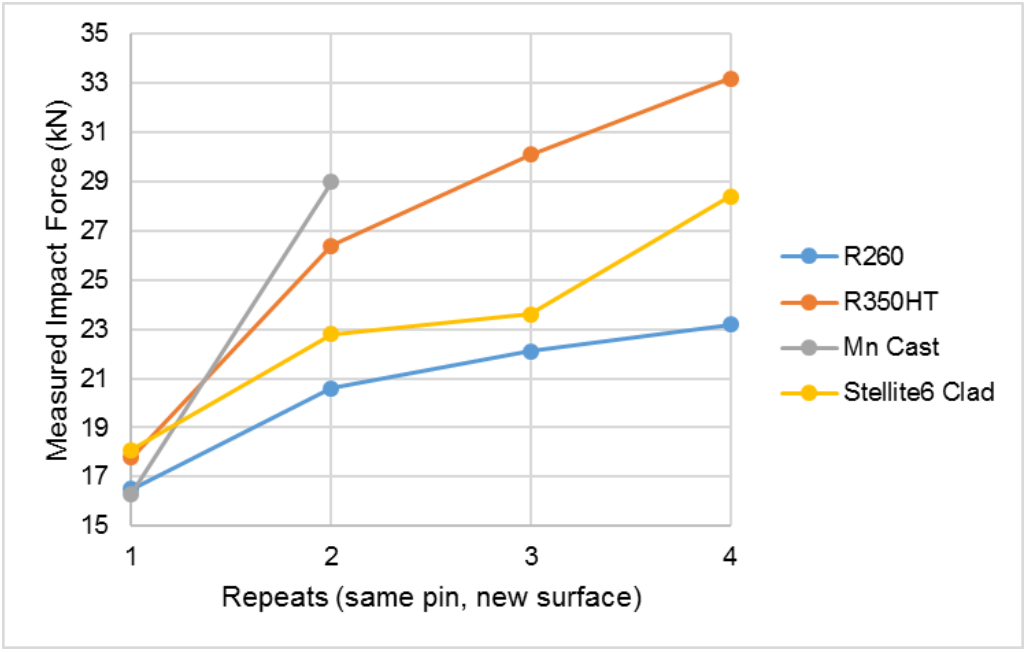

Figure 6-25 Load force as measured by the impact rig load cell. The line connecting the datapoints is for visualisation purposes only.

Volume deformation was calculated in Alicona by selecting a small area around each cavity. The selected area varied with each specimen, so the figures must not be compared directly, but to be used as an indication of the volume deformation trend. The Alicona software estimated the mean lateral position of the surface and from that position, the volume above and below this surface was calculated. Volume above the mean position is the raised surface, while below is the cavity. As shown in Figure 6-26 the cavity is much larger that the raised surface, for all materials. Although all samples had a raised surface, the diameter of the raised surface is as important as its height. The volume calculation below does not distinguish between the two and this was not explored further in this study.

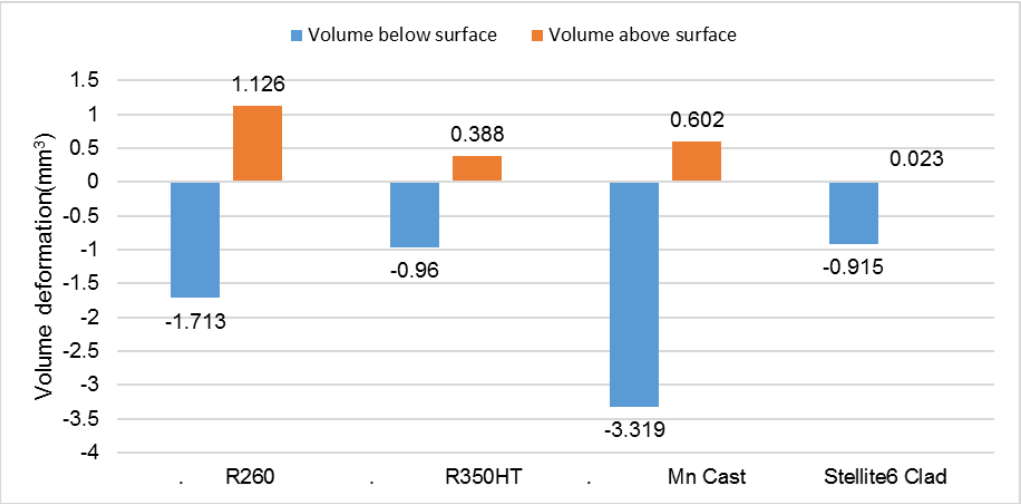

Figure 6-26 Volume deformation, measured with the Alicona

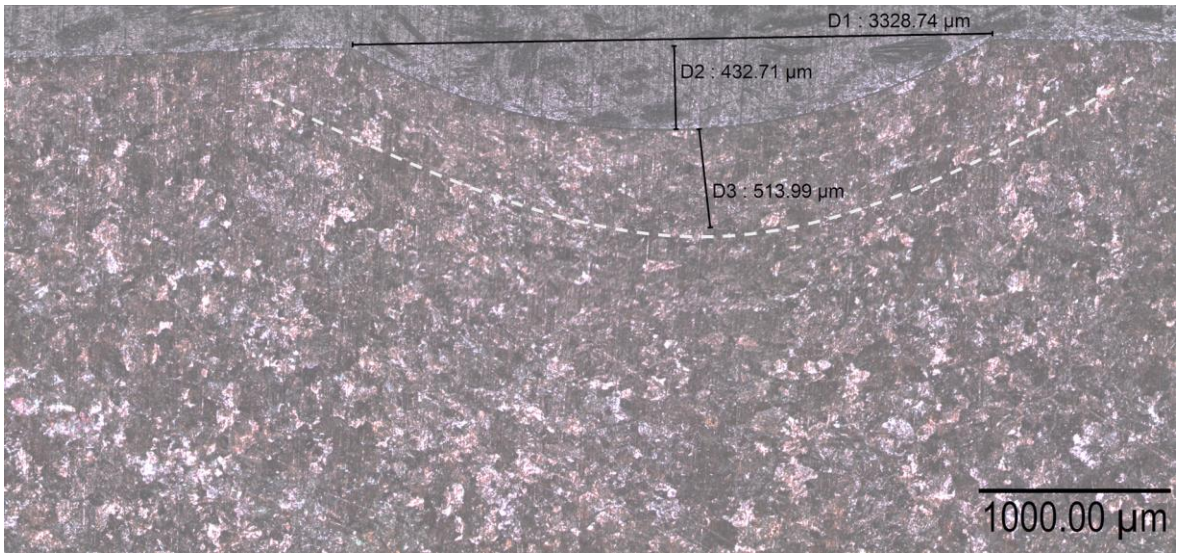

Figure 6-27 R260 impact damage 3.3mm wide, 0.43mm deep

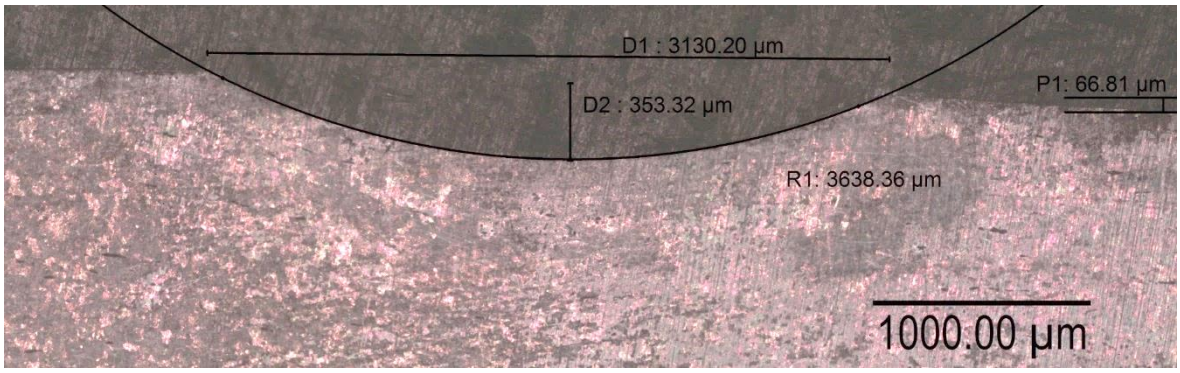

Figure 6-28 R350HT impact damage 3.1mm wide, 0.35mm deep with a "raised disc" area

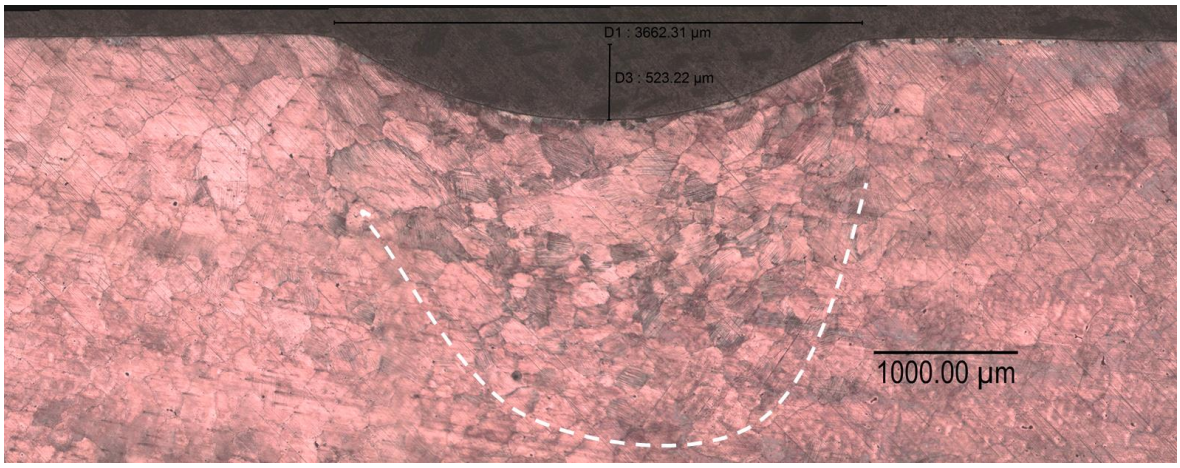

Figure 6-29 Manganese steel impact damage 3.7mm wide, 0.52mm deep

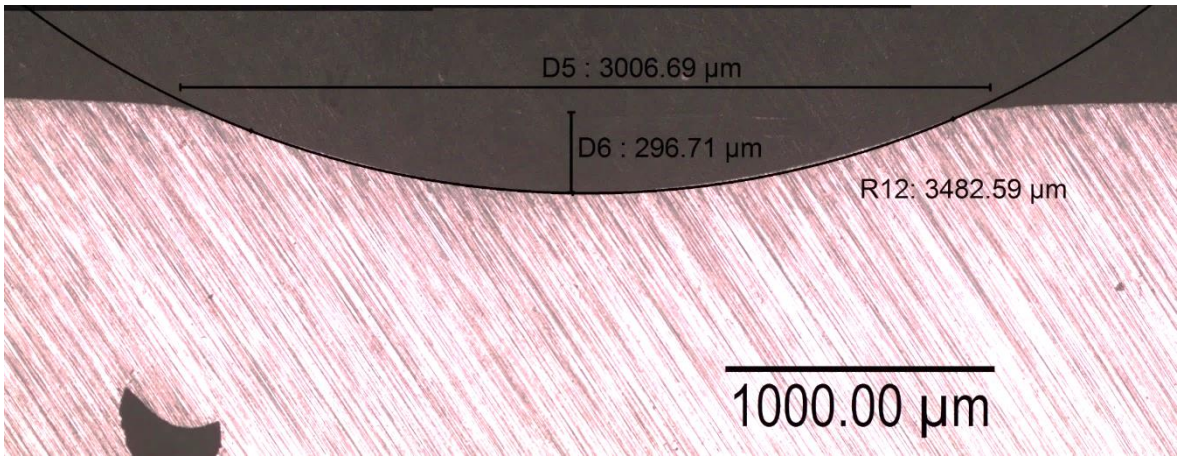

Figure 6-30 Stellite 6 clad impact damage 3mm wide, 0.3mm deep

Cavity depth and width for the fourth impact from each sample was measured using the Alicona scanned data and represented in Figure 6-31. The section micrograph images are not suitable for precision measurement of the width-depth, as the cutting plane may not be aligned with the centre point of the cavity. Multiple repeat tests would have yielded more measurements, allowing the results to be analysed statistically. However, there is a clear trend in the depth-width measurements that aligns with the hardness measurements, thus giving confidence in the results obtained here.

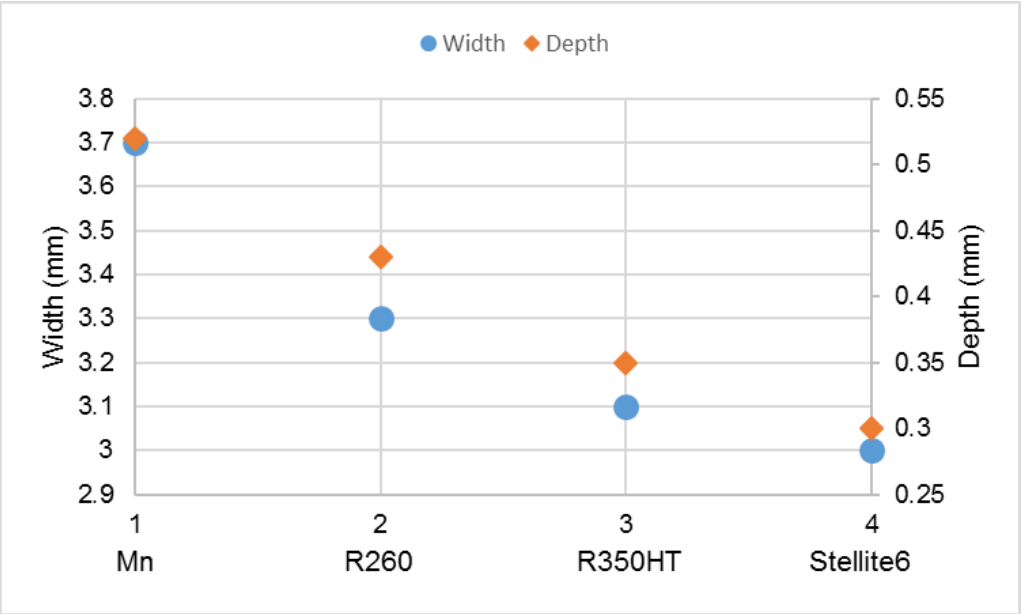

Figure 6-31 Comparison of impact damage width-depth of the various materials

6.2.2 Impact - Discussion

An effort was made to compare the damaging effects by small scale impact on various rail materials including a laser clad coated material. The measured impact force in Figure 6-25 showed that after impacting four times with the same pin, the pin reached acceptable deformation levels. This may not be a full equilibrium state, as this can differ for each rail material. Also, the measurements for the third and fourth impacts of the Manganese material have not been recorded due to a datalogger issue. The fourth impact was considered the point for comparison. The impact load and cavity depth increased with each impact from the same pin. This is especially clear in Figure 6-21 for the R260 material primary roughness measurements. Stellite 6 had the least deformation, followed by R350HT, then R260 and Manganese steel (see Figure 6-31). The variation in width-depth between the materials is in the region of 20-40% and that is sufficient evidence to conclude on the initial performance of each material. However, this is as far as the conclusions from this study can be extended, since work hardening and other effects have not been included. As explained in section 2.2.2, Manganese steel is preferred as a premium crossing nose material, due to its unique feature of rapid work hardening from yield strength (379 MPa) to ultimate tensile strength (965 MPa). Due to machining restrictions the Manganese steel samples were cut with a waterjet in areas away from the top surface of the crossing nose. The top surface of the crossing nose may have been explosion hardened [193] or work hardened in service by the rolling and impact forces caused by passing trains. Therefore, the comparison here is with unhardened Manganese steel and not with explosion or work hardened material.

On the other hand, Stellite 6, in as clad condition, has shown resistance to deformation in comparison to the other materials, without the need for heat treatment or work hardening. The result values for R260 material and its heat-treated version of R350HT lie between the values the Manganese and Stellite 6 materials, for cross-sectional width-depth measurement and the volume measurement

(Figure 6-26). Some of the cross-sectional microstructure images show deformation below the cavity, for example in the region of 0.5 mm in depth for the R260, as highlighted by the white dashed line in Figure 6-27. Deformation in R350HT is not very clear and the Stellite 6 deformation is not visible due to the etching process which was not sufficient to expose the microstructure. The manganese steel has larger grains that have undergone some deformation to a much higher depth below the cavity, around 2.5 mm as shown by the white dashed line in Figure 6-29. The deformation of the grain boundaries is not significant, meaning that the grain boundary shape has not elongated enough to follow the form of the cavity as clearly visible in the R260 material, however deformation bands seem to have increased inside the grains. This explains that the Manganese steel has not work hardened yet. To benefit from the work hardening properties, the material would have to be impacted multiple times so until larger deformations would appear. The severe deformation that comes with the work hardening of the Manganese steel can range from microns to millimetres. This is not desirable in rail, where the rail head profile is critical for safety and performance since this affects the wheel-rail contact. Employing clad materials like Stellite 6 may offer less initial deformation on crossing nose rail, thus eliminating the need for re-grinding or early replacement of the crossing nose.

In all cases, except for the clad material, the surface surrounding the cavity has been raised slightly due to displacement of the material from the impact. This is evident in all the primary roughness and volume graphs (Figure 6-21 to Figure 6-24). The R350HT material behaviour was different than the other materials when it comes to the raised surface. The risen profile is much wider and formed deformation circles around the cavities. It is not clear if all materials exhibit the same behaviour but only the R350HT is visible due to higher deformation. Also, it was noticeable that the cavity surface of the R350HT was more reflective than the other materials, meaning that the impact left a polished surface. An effort was made to photograph the deformation circles around the cavities by projected light at such angle that would highlight this feature, see Figure 6-32. The lack of flow of material around the cavities of the clad sample contributes to the conclusions of improved performance in comparison to the other materials.

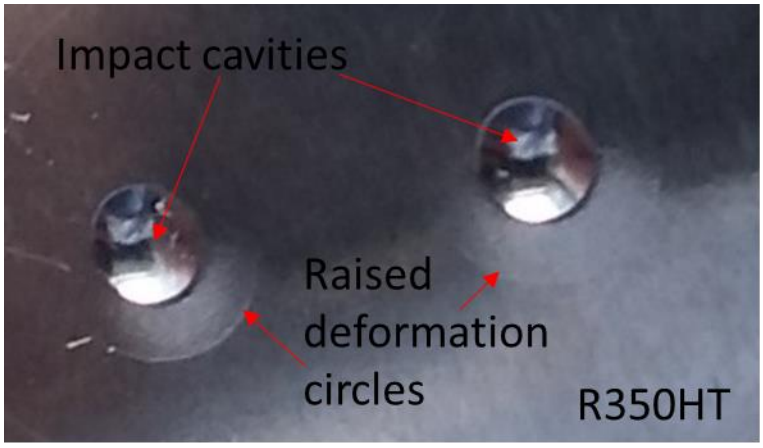

Figure 6-32 Distinctive rings formed around the impact area on R350Ht material

An effort to understand the modelling requirements for predicting impact damaged was discussed in section 4.2.3. Generic material properties for steel were used in a simulation of the impact test, where the simulation resultant cavity size was similar to the Manganese steel results. The raised deformation and strain deformation below the contact area with the pin was also predicted by the model, however, it was not analysed in detail and the material model was not adjusted to much the experimental results.

6.3 Textured rolling/sliding

6.3.1 Textured rolling/sliding – Results

The texture from the cladded ring was imprinted onto the softer rail disc, this can be observed by the dull surface of the 2.1 set of discs in Figure 6-33. Finally, 1.1 set of discs in Figure 6-33 shows the existing grooves blending with the texture transfer from the work roll material, where the texture from the ring has not been fully transferred to the disc.

Figure 6-33 Images of rings and discs from the first set of tests (200 cycles)

Roughness measurements were taken using the Alicona IFM SL G1, which performs mathematical filtering, thus allowing the user to filter out undesirable results. A cut off value determines the filter wavelength, for example a cut off value larger than the wavelength of the waviness on a surface will result in showing the waviness and not highlighting the asperities. On the other hand, a cut off value smaller than the wavelength of the surface waviness will exclude the waviness and highlight the asperities of the surface. A cut off value of Lc=800 μm was found to be appropriate for showing the texture and to exclude surface waviness. The measurements are listed in Table 6-2, with a nomenclature in Table 6-1. Mass loss measurements are listed in Table 6-3. Average roughness difference before and after the test has been calculated as a percentage and shown in Table 6-2. The aluminium strip transfer ratio measurements in Table 6-2 have lower values than the measurements taken from the rings, as the texture imprint cannot be transferred fully under these contact conditions. Optical microscope images of the transfer ratio test, from the aluminium strip are shown in Figure 6-34 to Figure 6-37.

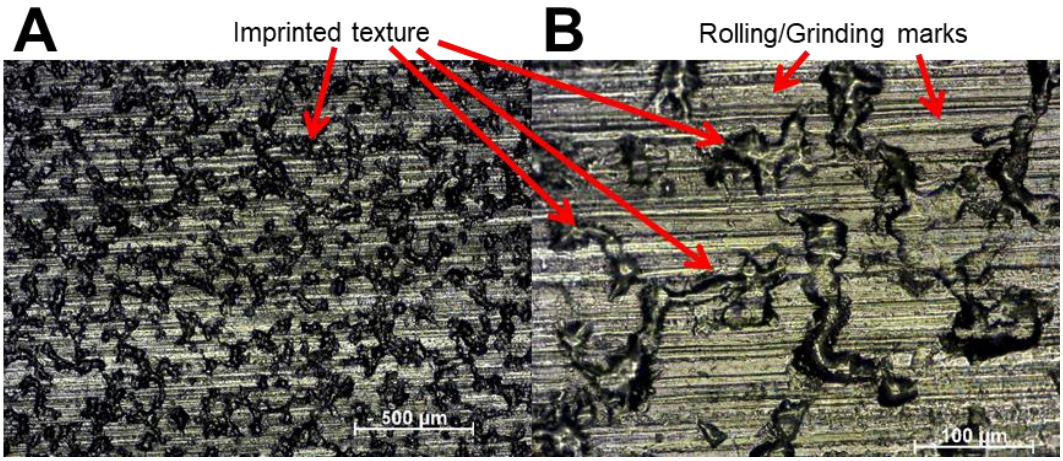

Figure 6-34 Surface of the aluminium strip optical image with an impression of the treated-unclad ring (no. 1.2) texture, prior to testing - B is a magnification of image A

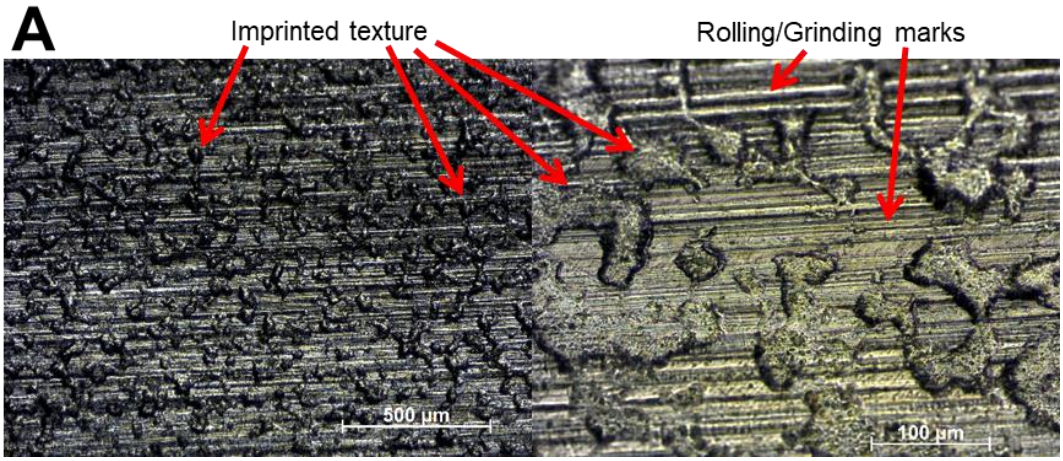

Figure 6-35 Surface of the aluminium strip optical image with an impression of the treated-unclad ring (no. 1.2) texture, after testing - B is a magnification of image A

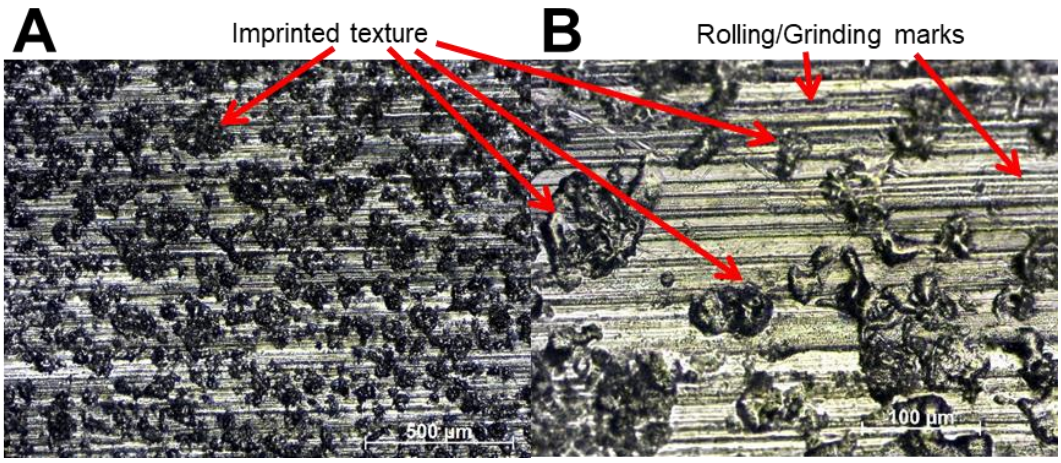

Figure 6-36 Surface of the aluminium strip optical image with an impression of the treated-clad ring (no. 2.2) texture, prior to testing - B is a magnification of image A

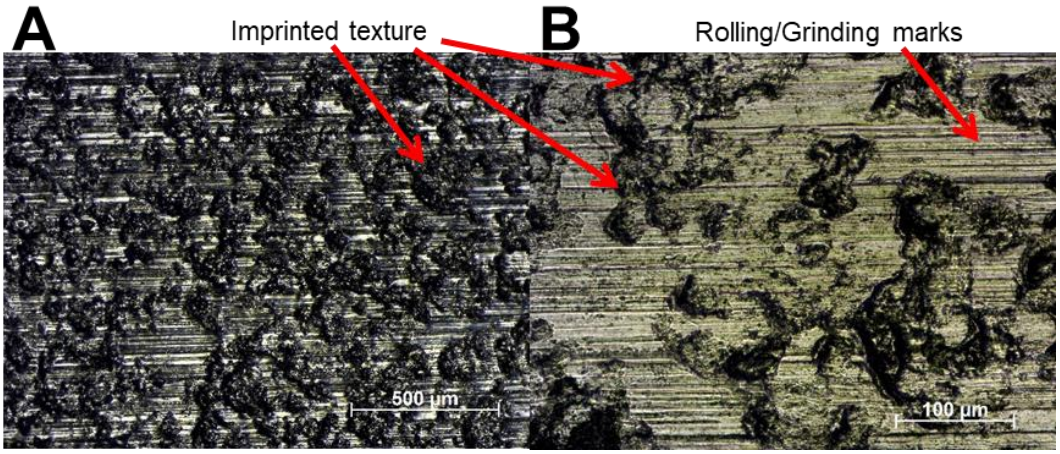

Figure 6-37 Surface of the aluminium strip optical image with an impression of the treated-clad ring (no. 2.2) texture, after testing - B is a magnification of image A

Some staining was observed on the clad ring impression sample, see Figure 6-38. This might be caused by oxidation or an interaction/chemical reaction with the lubricant or cleaning agent (acetone). The severe staining was present only when tested with the clad material, large stains were up to 5 mm wide and elongated to various lengths.

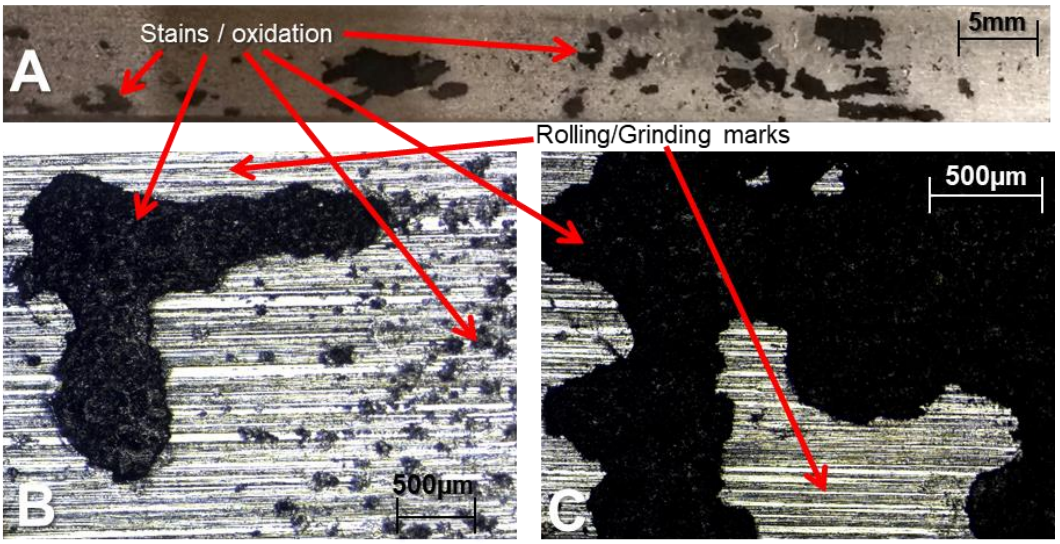

Figure 6-38 Surface of the aluminium strip optical image with an impression of the treated-clad ring (no. 2.2) texture, after testing - A is an image of the overall strip, B and C are closeup views of various areas on the strip

Table 6-1 Parameter nomenclature

Name	Unit	Description
Ra	µm	Average roughness of profile
Rq	µm	Root-Mean-Square roughness of profile
Rz	µm	Mean peak to valley height of roughness profile
Rsk	---	Skewness of roughness profile
Sa	µm	Average height of selected area
Sp	µm	Maximum peak height of selected area
Sv	µm	Maximum valley depth of selected area
Ssk	---	Skewness of selected area
Lc (λc)	µm	LambdaC: cut off wavelength

Table 6-3 Mass loss measurements for the ring and disc

Ring material and test duration	Ring and Disc no.	Sequence	R400HT		Textured Rings	
			Mass (g)	Loss (g)	Mass (g)	Loss (g)
Treated-Unclad 200 cycles (0.5mins)	1.1 S-R-35	Before	165.587		80.536	
		After	165.5859	0.0011	80.5333	0.0027
Treated-Unclad 1000 cycles (2.5 mins)	1.2 S-R-40	Before	165.4251		80.4417	
		After	165.4219	0.0032	80.4408	0.0009
Treated-Clad 200 cycles (0.5mins)	2.1 S-R-47	Before	165.5118		82.078	
		After	165.5103	0.0015	82.071	0.007
Treated-Clad 1000 cycles (2.5 mins)	2.2 S-R-51	Before	165.5663		81.8359	
		After	165.5333	0.033	81.8305	0.0054
Untreated-Unclad 200 cycles (0.5mins)	5.1 S-R-21	Before	165.5722		80.3054	
		After	165.5722	0.000	80.3053	0.0001
Treated-Clad 200 cycles (0.5mins)	4.1 S-R-20	Initial trial Before	165.7806		82.0255	
		Initial trial After	165.752	0.0286	82.0459	-0.0204

Table 6-2 Various roughness measurement at 0.8 cut off values – Ra % difference shown in bold

Ring material and test duration	Ring and Disc no.	Sequence	Ra % difference	Ring							
				Ra	Rq	Rz	Rsk	Sa	Sp	Sv	Ssk	Area
Treated-Unclad 200 cycles (0.5mins)	1.1 S-R-35	Before	**18.1%**	1.686	2.146	11.755	0.207	2.003	22.293	13.729	0.584	7 x 3.5 mm
		After		1.38	1.721	8.037	-0.119	1.922	48.839	13.912	0.442	8 x 8 mm
Treated-Unclad 1000 cycles (2.5 mins)	1.2 S-R-40	Before	**34.7%**	1.826	2.299	11.150	0.088	2.039	15.051	15.389	0.532	5 x 3 mm
		After		1.192	1.545	8.180	-0.331	1.632	20.138	14.742	0.575	8 x 8.5 mm
Treated-Clad 200 cycles (0.5mins)	2.1 S-R-47	Before	**-1.2%**	1.688	2.163	12.056	-0.392	2.249	42.356	118.029	-7.707	6 x 9 mm
		After		1.709	2.525	14.956	-3.4	2.097	60.655	117.122	-8.754	8.3 x 9.3 mm
Treated-Clad 1000 cycles (2.5 mins)	2.2 S-R-51	Before	**23.1%**	1.984	2.451	11.854	-0.552	------	------	------	------	------
		After		1.526	2.100	10.872	-1.126	1.967	11.579	111.231	-9.578	8 x 8 mm
Untreated-Unclad 200 cycles (0.5mins)	5.1 S-R-21	Before	**19.9%**	2.052	2.614	15.513	-0.105	2.138	31.564	19.131	0.564	8.5 X 7.5 mm
		After		1.643	2.05	9.85	0.081	1.747	41.392	13.685	1.012	8.2 x 8.6 mm

Ring material and test duration	Ring and Disc no.	Sequence	Ra % difference	Transfer ratio measurement from the aluminium strip							
				Ra	Rq	Rz	Rsk	Sa	Sp	Sv	Ssk	Area
Treated-Unclad 1000 cycles (2.5 mins)	1.2 S-R-40	Before	**12.9%**	1.066	1.399	7.003	-0.060	1.122	8.299	7.931	-0.177	3 x 3 mm
		After		0.928	1.182	5.917	0.154	1.110	36.503	6.701	1.142	3 x 3 mm
Treated-Clad 1000 cycles (2.5 mins)	2.2 S-R-51	Before	**-17.1%**	0.930	1.178	5.561	-0.038	1.068	7.609	9.232	0.053	3 x 3 mm
		After		1.089	1.390	6.832	-0.266	1.142	9.349	8.118	-0.128	3 x 3 mm

Two materials were compared in a short duration rolling/sliding wear test. The bulk hardness of the coating/surface varied from around 600 HV on the non-coated material to 2000 HV on the coated material. Due to this major hardness difference, it is difficult to conclude on their performance and texture durability without extensive testing on various materials, slip conditions and load combinations. For this reason, the test was simplified by using a material with a hardness of 400 HV, which is closer to the softer ring material, but not higher than either ring material. In the case of the untreated ring material (244 HV), the hardness of the opposing interface was higher than, which resulted in an instant loss of texture, therefore this test was not repeated. The duration and slip have an influence on the performance, so the second test duration was increased by five times, but the slip/load conditions were kept the same to make the results comparable.

The rise in Rz for the clad material may be due to the short duration of the test, where effects of wear in may not have taken place and the steady wear has not been achieved. The wear in of the clad layer takes place later than the unclad material, so the clad material may be more durable during the first few cycles of service as opposed to unclad material. Texture changes are attributed to material deformation due to softness, while for the harder materials the texture changes are mostly attributed to wear. This is indicated by the mass loss measurements from the tests. The results from the transfer ratio test, after the specimens were tested for 1,000 cycles, indicates that both the Ra and Sa are decreasing for the unclad ring while increasing for the clad ring.

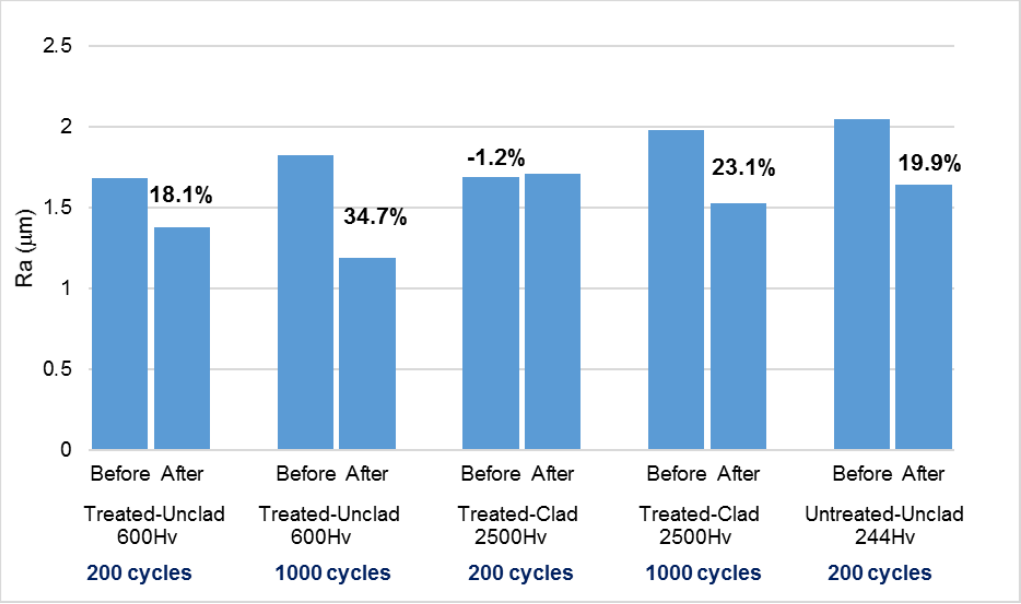

Figure 6-39 Average roughness of textured rings for the various tests

6.3.2 Textured rolling/sliding – Discussion

An alternative texturing technique to the well-established EDT is laser melting, which is a readily available technique. Potentially the texture could be formed during the laser cladding process, thus reducing the two-step process into one-step process [209]. The one-step process could prove beneficial in terms of time/cost when cladding industrial components such as work rolls, pinions, bridle rolls and other similar components that require a textured surface as part of their tribological design.

The combination of tests performed is described by the schematic in Figure 5-37. Twin disc tests were performed with R400HT material against textured work roll material in three conditions (unclad/untreated, unclad/treated, clad/treated). The twin disc tests were conducted in three parts, where the conditions for the first and last parts were 0% slip, at slow speed and for very short duration, enough to roll an aluminium strip through the discs in order to produce an impression of the texture. Between the impression phases the wear tests took place, where the test conditions were 1% slip and 400 rpm rotational speed. Two sets of wear tests took place, the first for 200 cycles and the second for 1,000 cycles. The unclad/untreated material was rejected after the first test since its original texture was not retained due to its surface having a very low hardness of 244 HV. Only two material conditions remained for comparison, clad and unclad, where in both the bulk material has been heat treated prior to cladding. The materials are shown in Figure 5-37 as 2 and 3 for 200 cycles and 4 and 5 for 1,000 cycles. The hardness values in Figure 5-37 refer to the bulk hardness as opposed to the surface hardness in order to identify if the sample was heat treated. Surface hardness for each sample is listed in Table 5-5.

The SUROS machine has been mainly used for testing railway materials and forged steel materials were tested using this machine for the first time. It was also the first time that the SUROS machine was used to take impression of texture on a third body by means of rolling. The wear test was very similar to the tests described in 6.1 for railway twin disc tests, where for 1% slip condition the test duration was 30,000 cycles. This duration has been shown to be sufficient for the railway materials to reach steady state with regards to wear rate. For the work roll material, especially when cladded, it is unknown what the wear rate steady state would be without extensive tests. Only a few samples were available as listed in Table 5-5, so it was decided to run tests at 200 and 1,000 cycles for a direct comparison. These tests do not fully characterise the behaviour of R400HT or the Technolase® clad material, they are a first approach in characterising the durability of texture on a clad coating. It is observed in Figure 6-40 that there is higher wear for the textured ring at 200 cycles and a higher wear for the R400HT disc at 1,000 cycles. This is observed for both clad and unclad materials. This indicates that the initial wear is probably damage at the asperities level and mostly on the textured surface. This is logical since the textured surface has essentially a smaller contact area (due to the texture asperities) than the opposing surface which is smoother. After some initial wear in of the asperities, the wear reverses and the softer surface (R400HT) is wearing significantly more than the textured rings. The clad ring also caused more wear to the opposing surface in comparison to the unclad ring.

The true evaluation of the texture durability is seen by the transfer ratio of the texture impressions on aluminium samples in Figure 6-41 for average roughness values (Ra), and in Figure 6-42 for average height values (Sa). Two cut off values were used for filtering the results, 0.8 mm and 2.5 mm and both are presented here for comparison. The results from these values are fairly similar and this gives confidence that the waviness measurements are not shown here but only the texture roughness.

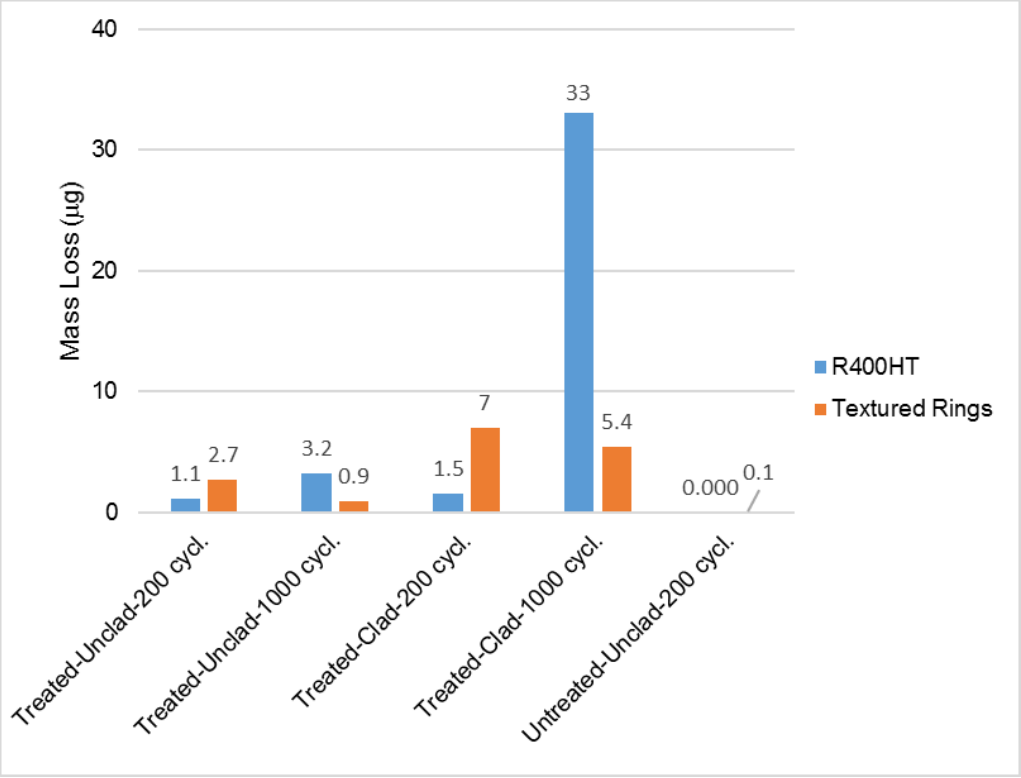

Figure 6-40 Mass loss measurements for the various tests

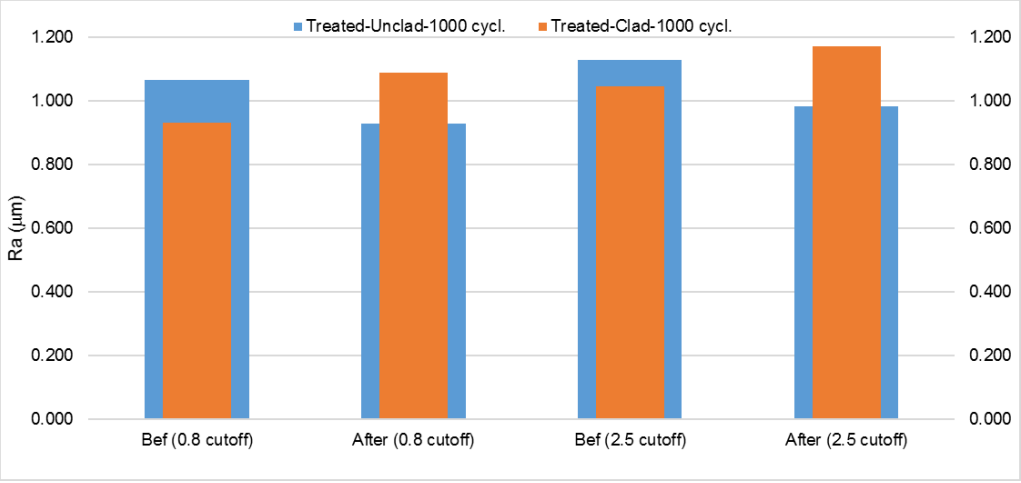

Figure 6-41 Transfer average roughness on aluminium strip

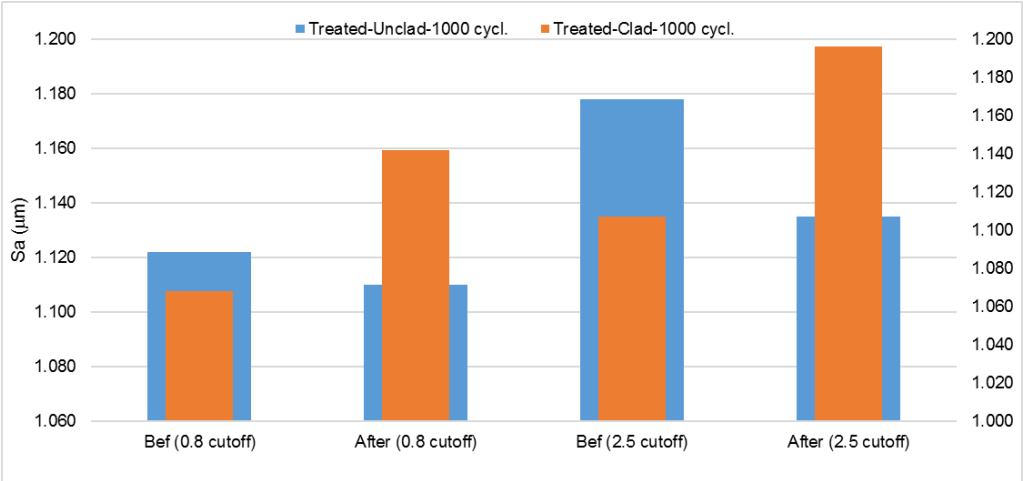

Figure 6-42 Transfer average height on aluminium strip (3x3mm area)

The overall conclusion is that the roughness is being reduced for the unclad material, while it is increasing for the clad material. This may happen because the unclad material is wearing as normal, thus slowly losing its texture from wearing of the asperities. For the clad material the surface wear is much slower and the increase in surface roughness may be attributed in multiple mechanisms such as removal of WC particles from the surface of the Technolase® or other much smaller fragments. Another observation in Figure 6-38 is staining on the aluminium impression samples. This might be caused by oxidation or by the heated lubricant. This may be key to why the roughness is increasing slightly.

The data in this study may not be sufficient to produce conclusive results and statistical variation by testing a large number of samples is needed in such tests. The laser clad sample has sustained its texture and it has not failed in terms of delamination or mechanical bond with the substrate. Additionally, the harder laser clad texture ring has made an impression of the texture to the opposite disc, which did not occur with the unclad textured ring. This is optimistic that laser clad rolls would perform better in rolling harder products, for example steel or high strength aluminium such as 7000 series alloys. The effect of testing a clad disc against another clad disc has not been investigated in this study and it would be crucial in service as work rolls will interact with each other at times, not just in contact through the rolled product. The results are positive enough to encourage further research in cladding of work roll materials that require texturing. The major potential benefit to industry is increasing yield, by reducing the frequency of grinding and texturing of work rolls.

6.4 Erosion

6.4.1 Erosion – Results

Results from testing each material at 185 Bar are shown below in individual sections:

- 6.4.1.1 S275JR test for 1, 3, 10 and 30 minutes
- 6.4.1.2 Hardox 500 test for 30 and 90 minutes
- 6.4.1.3 Stellite 6 clad test for 90 minutes and 420 minutes

6.4.1.1 S275JR test

The erosive scarring on the softer specimen was clearly visible early on the test, therefore tests in different parts of the specimen were conducted for 1, 3, 10 and 30 minutes duration and later scanned with the Alicona (Figure 6-43). Light surface damage occurs outside the cavity damage. It is obvious that the soft S275JR plate has insignificant wear resistance, at least to the parameters of this test and the material volume loss in the cavity was around 2.7 mm^3 after 30 minutes testing (Figure 6-44).

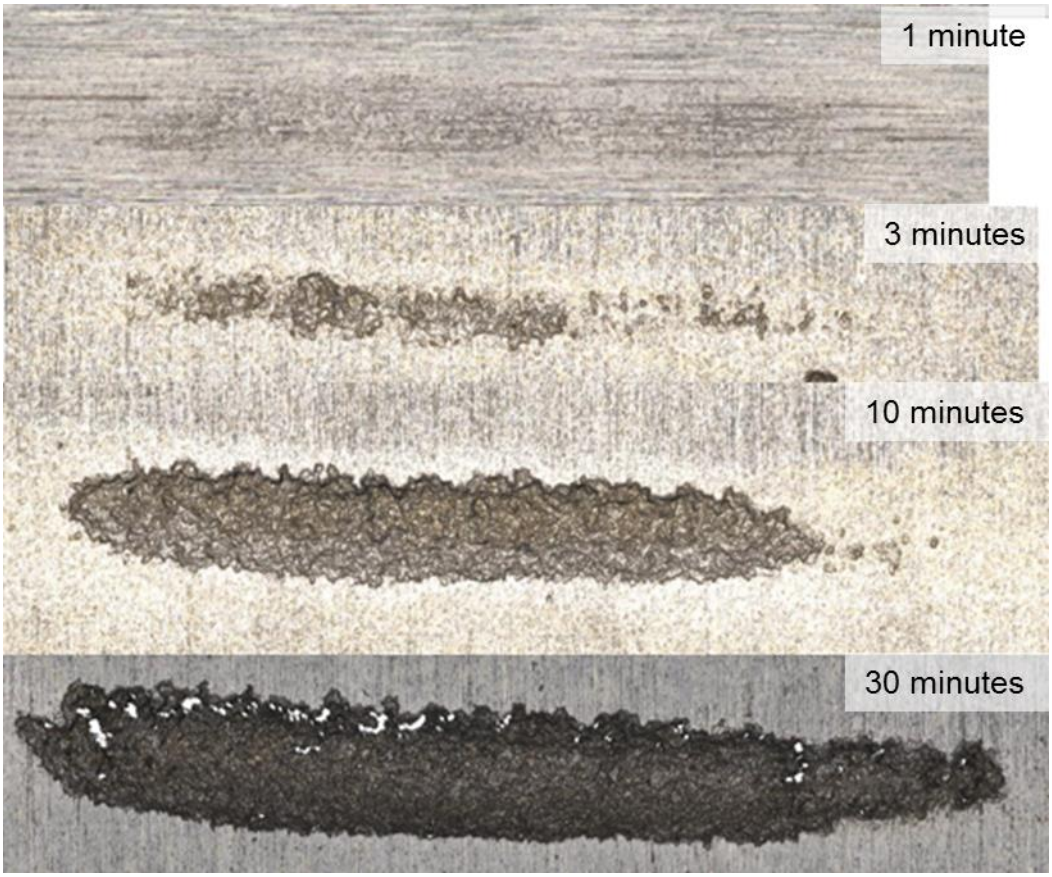

Figure 6-43 Erosion scars for 1, 3, 10 and 30 minutes testing (images taken with the Alicona IFM SL)

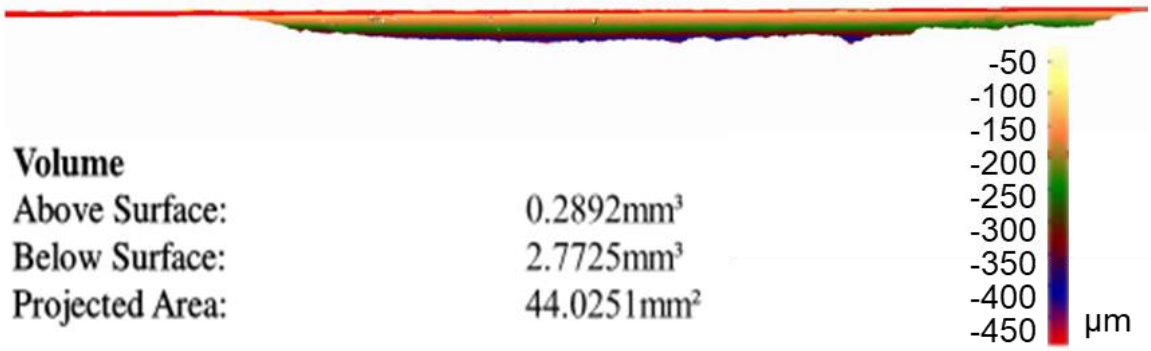

Figure 6-44 Volume loss of S275JR specimen after 30 minutes testing at 185 Bar water pressure

The roughness profile in Figure 6-45 is a good representation of the erosive cavity profile, whereby it is made of three rough faces as illustrated by the red lines, a fairly flat face on the bottom with two angular faces either side joining the bottom face and the specimens surface. The two faces have different angles to the bottom face, and this is evidence of the spray direction, which is illustrated by the blue arrow. The face on the right, which is somehow parallel to the spray direction seems to erode more than the face to the left, which is perpendicular to the spray direction.

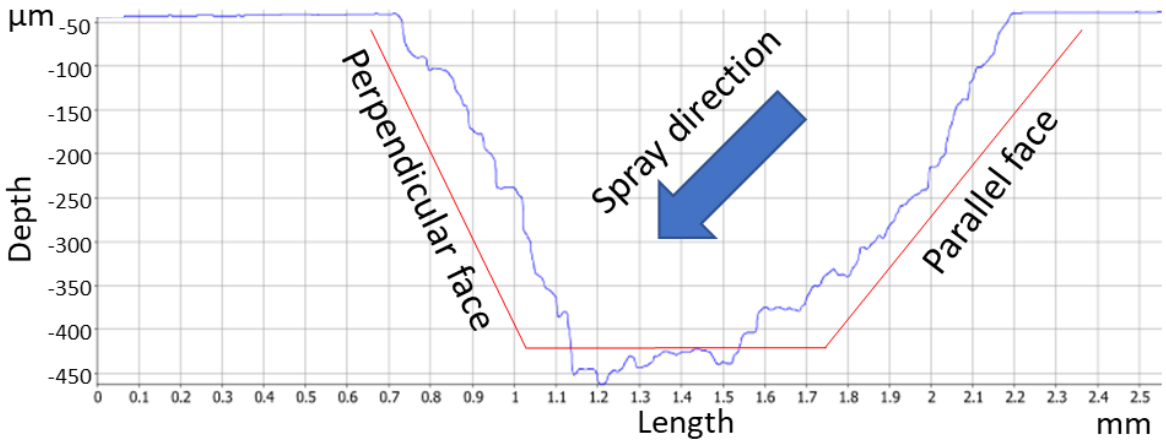

Figure 6-45 Primary roughness profile of S275JR specimen after 30 minutes testing at 185 Bar water pressure

The specimen was sectioned and lightly polished in order to allow for hardness measurements. A closer view of the parallel face in Figure 6-46 shows multiple cracks to appear on the surface of the cavity, where “craters” of 20-120 µm appear to branch out into much smaller cracks. Hardness measurements with the Struers Durascan were conducted using 300 g load and also 10 g load, where the latter allowed measuring hardness near the damaged area.

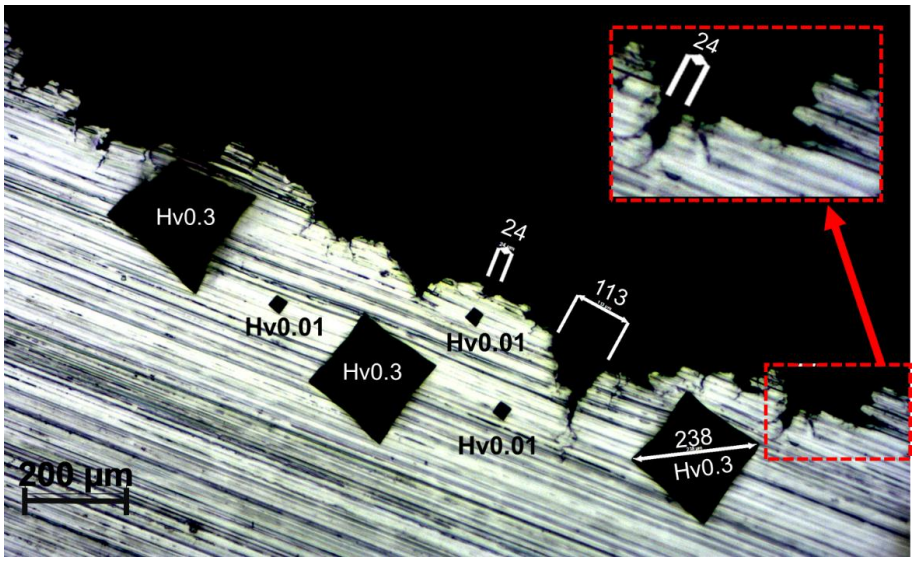

Figure 6-46 Optical microscope view of the S275JR damage in the erosion scar – HV 0.3 kg and HV 0.01 kg diamond indents are visible

The 300 g load measurements were chosen as suitable to represent the hardness around the cavity since hardness measured too close to the damaged area may have not been comparable to the rest of the material due to the multiple cracks in the region. The results are plotted in Figure 6-47 as a contour map. The areas near the parallel and bottom faces of the cavity have a lower hardness than the opposite face or the rest of the specimen. This may be an indication that more material is removed from the parallel face due to a softening mechanism, as opposed to the perpendicular face.

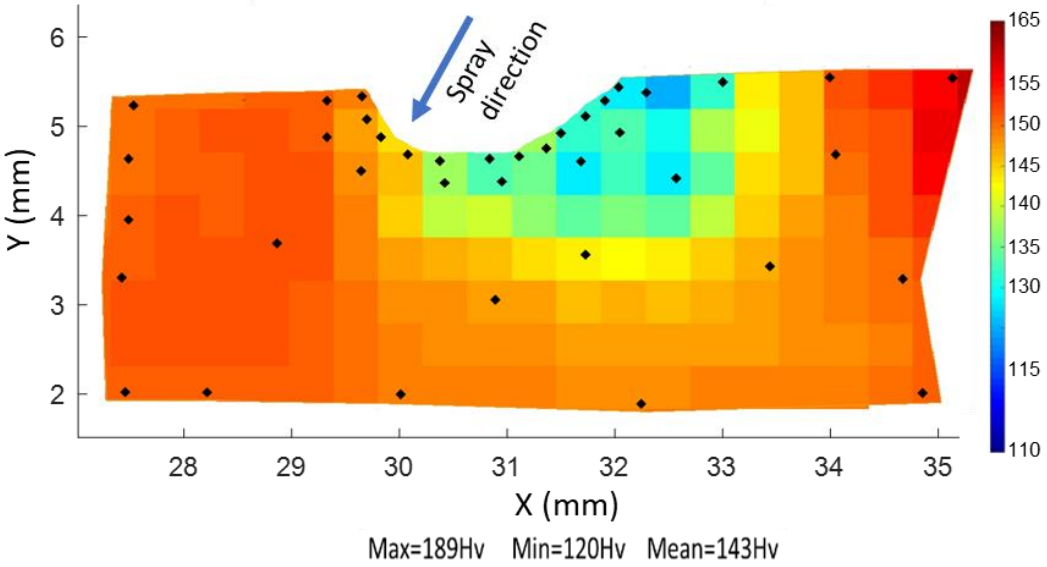

Figure 6-47 Hardness mapping around the S275JR scar (30 minute erosion test) – black markers show the indentation positions for HV 0.3 kg

As discussed in section 2.3.2, erosion resistance is affected by the hardness but also the toughness and ductility of the material. During erosion local stress fields induce plasticity beneath the surface and the softening mechanism found here is unknown. It might be attributed to the multiple cracks initiated which branch out. It could also be due to the way the droplets rebound away from the parallel

face in a normal trajectory and the reaction forces are absorbed by the parallel face. This might lead to softening of the material to a higher depth in the parallel face than the perpendicular face. The assumption is that impacting pressure is high enough to induce softening as opposed to compressive stresses from impact. This mechanism can affect any of the faces throughout the test with everchanging behaviour according to rebound angle and dynamic softening/damage of the material.

6.4.1.2 Hardox 500 test

Hardox 500 tests were conducted for longer, 30 and 90 minutes. The 3D images in Figure 6-48 were obtained with the Alicona from the longer test specimen. In the centre it is obvious that material loss has formed a cavity, while the surface roughness was increased by the spray and denotes the spray shape. The volume loss was significantly lower than the S275JR tests at 0.19 mm^3 and the waviness profile on the bottom right of Figure 6-48 shows the parallel and perpendicular faces, while the top right images on the same figure illustrates the cavity profile in three dimensions as scanned from the surface.

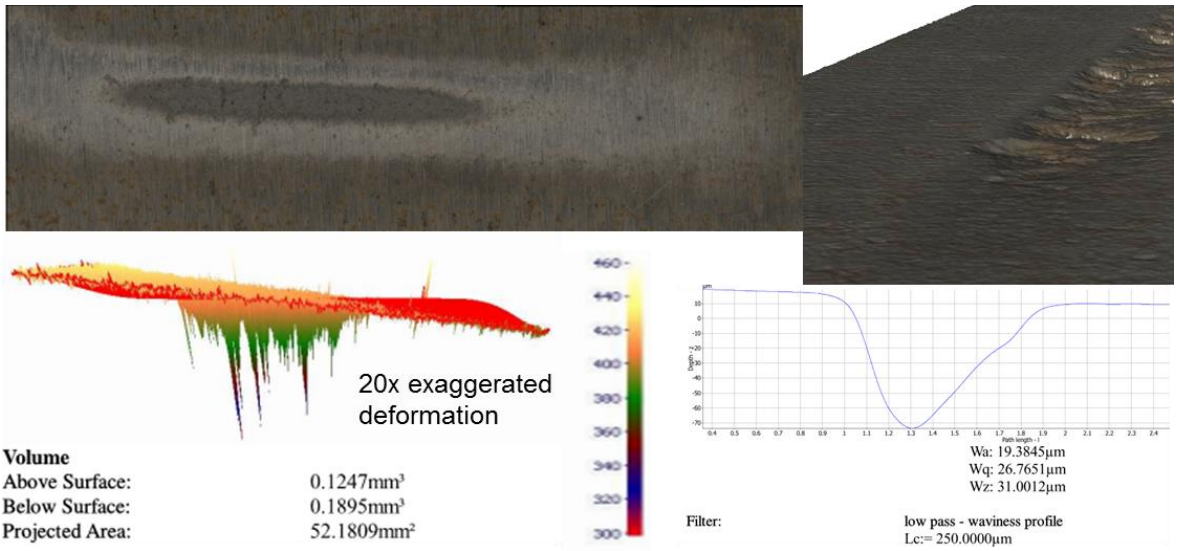

Figure 6-48 Hardox 500 specimen after testing for 90 minutes at 185 Bar water pressure. Volume measurement (bottom left) and waviness profile measured in the centre of the scar (bottom right)

6.4.1.3 Stellite 6 clad test

For the clad tests it was not obvious that the specimen was eroding, therefore the test was stopped after 1.5 hours to analyse the damage. The roughness was altered significantly, having higher roughness values in the spray impact area. It was difficult to reposition the specimen to the exact position so the test was restarted to a position close to the original scar. The second test was stopped after 4 hours for surface analysis and re-positioned back for another test that lasted 3 hours, bringing the total test duration to 7 hours. Special markers were places on the specimen mount to ensure that re-positioning of the specimen was as accurate as possible.

Waviness profiles in Figure 6-49 show the difference between the two tests. The parallel face that was identified in previous tests is on the right for both tests, while the perpendicular face is on the left side. There is no real cavity generated by this test, rather a scar that blends in with the surrounding roughness and this comment is justified by the extremely low volume loss of 0.03 mm³.

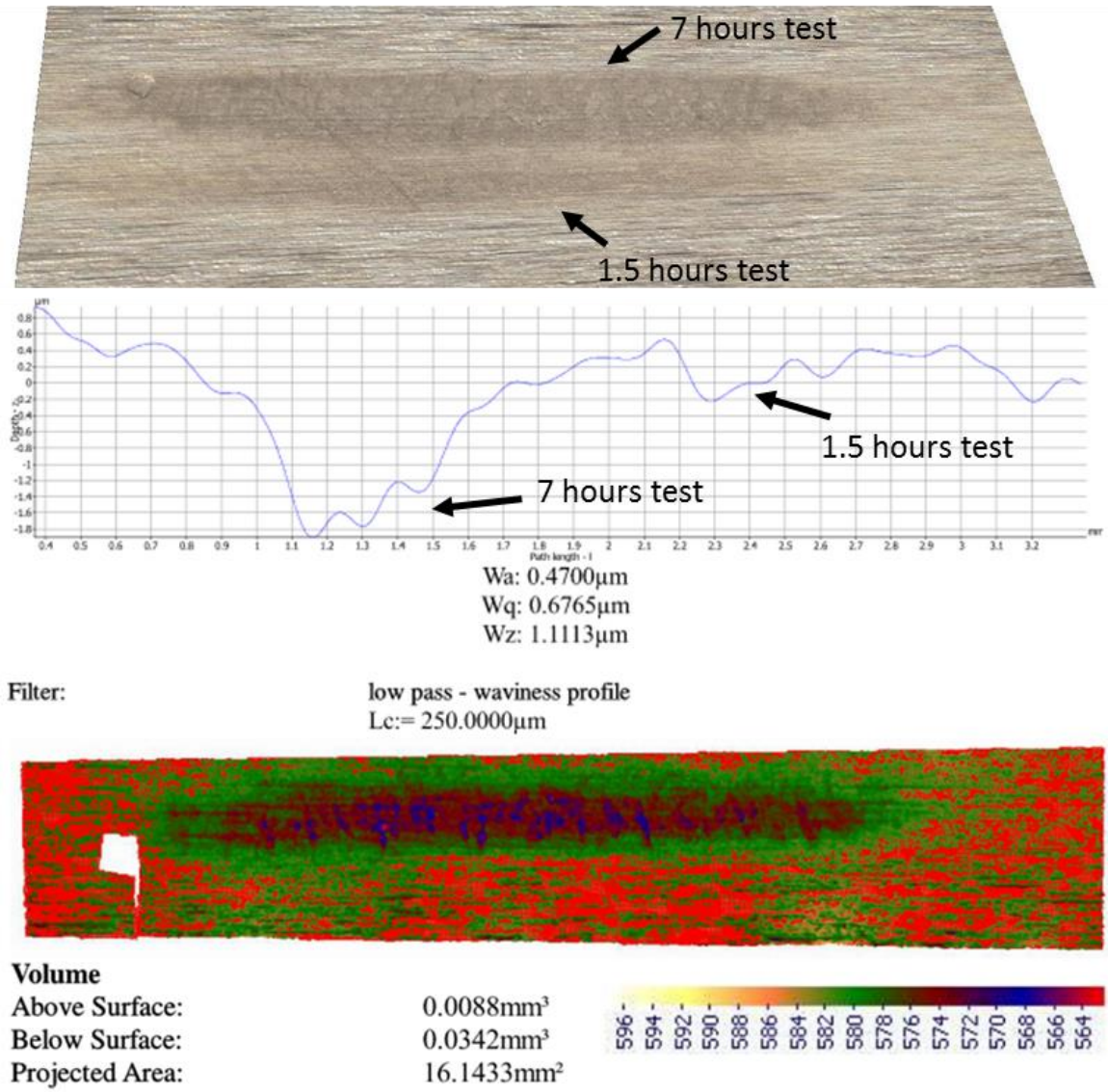

Figure 6-49 Stellite 6 specimen after testing for 1.5 and 7 hours at 185 Bar water pressure. Volume measurement plot is for the 7 hours test (bottom)

6.4.1.4 Erosion test results summary

Three materials were tested under high pressure water jet for variable lengths of time. The water pressure near the nozzle was measured with a pressure transducer and found to be around 185 Bar. The volume wear was calculated with a confocal method, using the Alicona InfiniteFocusSL. The volume wear results, including an aluminium reference sample, are listed in Table 6-4 and compared graphically in Figure 6-50. All the volume wear data are presented in a logarithmic time scale in Figure 6-51.

Table 6-4 Volume wear

Material	Duration (min)	Volume Wear (mm^3)
Aluminium	0.1	0.4237
S275JR	1	0.0114
S275JR	3	0.0485
S275JR	10	0.5975
S275JR	30	2.4833
Hardox500	30	0.0648
Hardox500	90 (1.5 hrs)	0.4075
Clad	90 (1.5hrs)	0.001
Clad	240 (4hrs)	0.0014
Clad	420 (7hrs)	0.0254

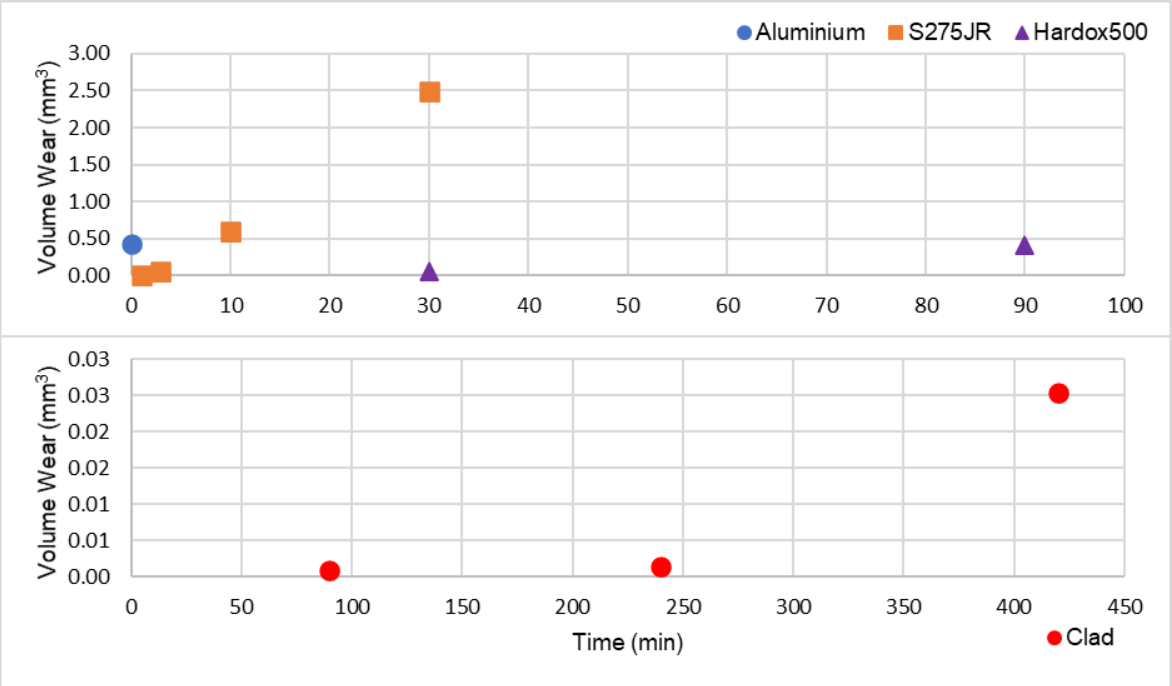

Figure 6-50 Volume wear in mm^3

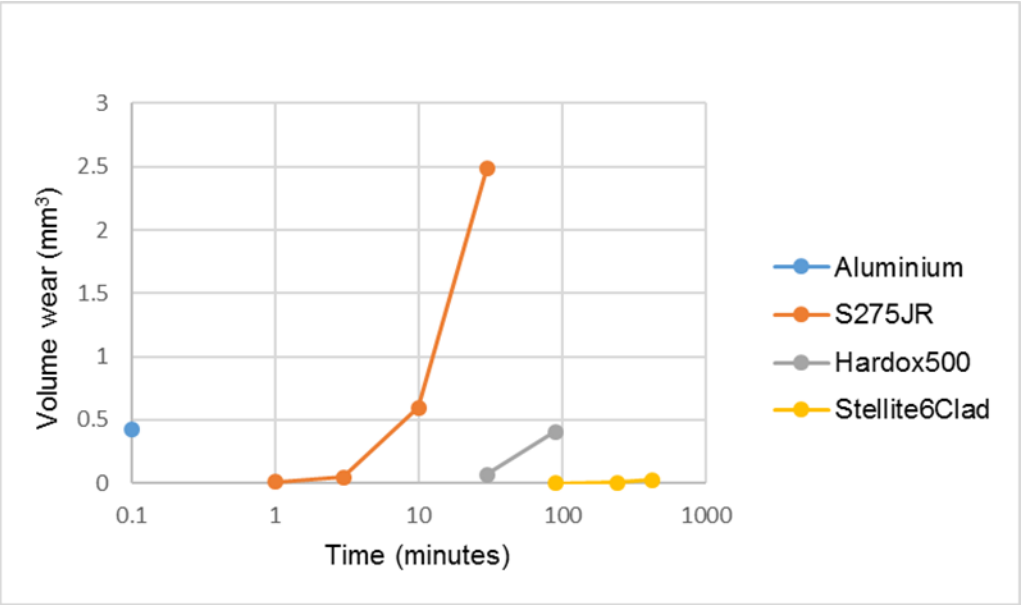

Figure 6-51 Volume wear. The line connecting the datapoints is for visualisation purposes only.

Wear rates have been calculated based on the duration of the test and shown in Figure 6-52. Finally, the peak (Rz), mean root square (Rq) and mean (Ra) roughness values are plotted together for each material in Figure 6-53.

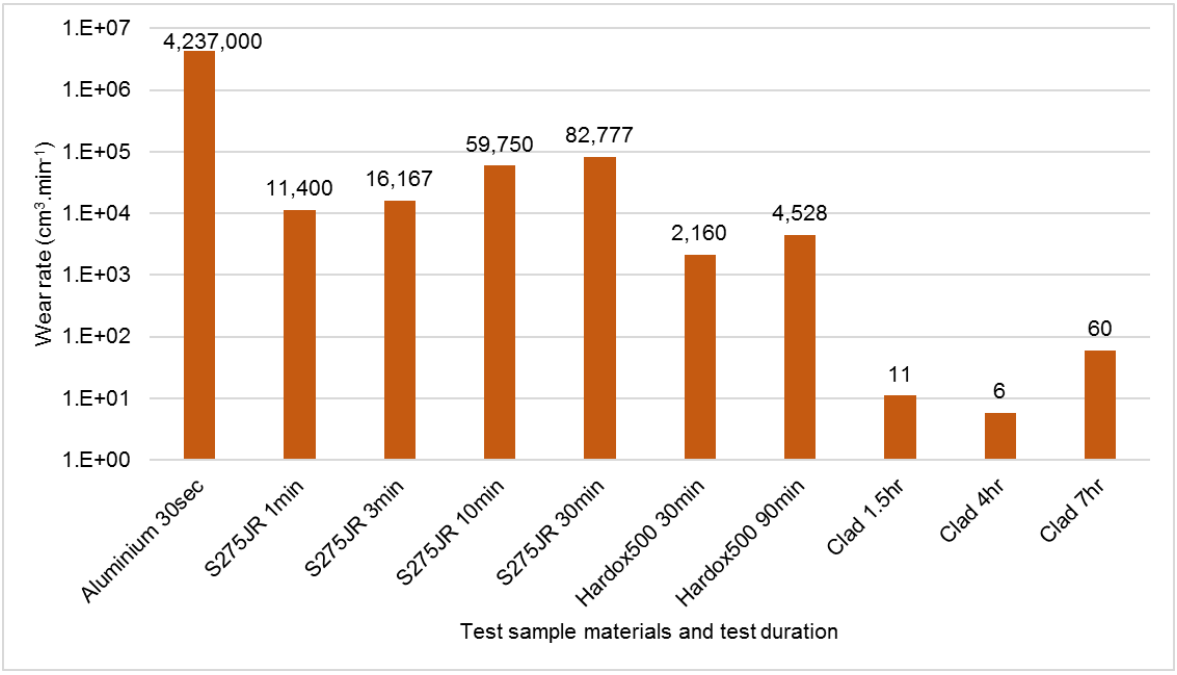

Figure 6-52 Wear rate in $cm^3.min^{-1}$

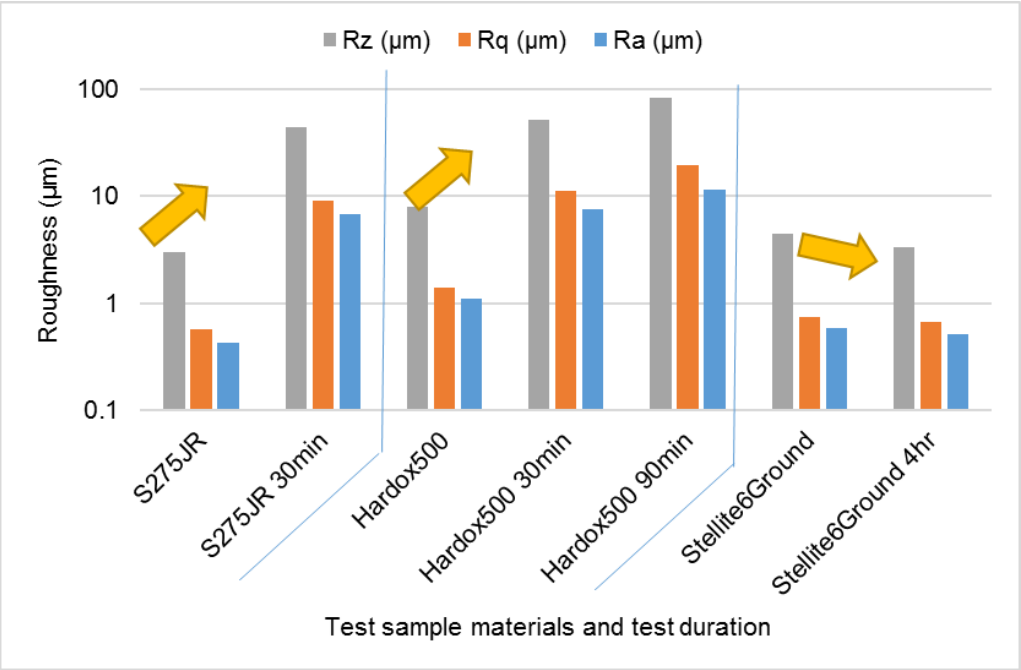

Figure 6-53 Roughness comparison (185Bar test)

6.4.2 Erosion – Discussion

Engel introduced the concept of “zero wear” phase, describing an initial number of cycles during percussive impact, where no wear damage is taking place until the depth of the wear scar has reached half the original surface roughness height [210]. This is evident in the erosion tests where the wear scar in the clad material was not significantly large to measure, even after prolonged testing. However, the clad scar could be distinguished visually from the rest of the surface and this was the same for the area surrounding the erosion cavities in all other samples. This is attributed to roughness changes from the spray impact area. A descaling nozzle was used and typically the impact pressure of these nozzles is not uniform through the impact area, but higher in the centre. This is reflected in these tests, for example the higher roughness is an imprint of the spray impact area while the cavity generated indicates where in the spray pattern the pressure was higher.

In S275JR material the erosion scar was developed further into a “cavity” and this sample was analysed further with a hardness testing through the thickness of the sample. In all cases it was identified that the cavity has a parallel face, a perpendicular face, and a bottom face. Sometimes the bottom face stands out or it can blend with one or both other faces. Once the cavity has progressed to a substantial size, the spray is not impacting the surface of the specimen or the bottom face, but the perpendicular face directly, while a steeper angle is introduced in this way for the parallel face. The steeper angle is most likely caused by more material removal. Hardness measurements indicate that the parallel face is softer than the rest of the material. However, without further tests it is difficult to conclude on this observation. One hypothesis is that the material is damaged more by the higher loading. The rebound of the spray is normal to the parallel face, therefore the reaction force of the rebound is absorbed by the parallel face, resulting in higher wear than the opposite face. Multiple

cracks have appeared, and further investigation could reveal if the softening mechanism is related to the cavity cracks or whether it is a subsurface phenomenon, since lower hardness values were measured well below the cavity surface. Three wear phases of zero-wear, asperity level wear and particle removal are described in Figure 6-54.

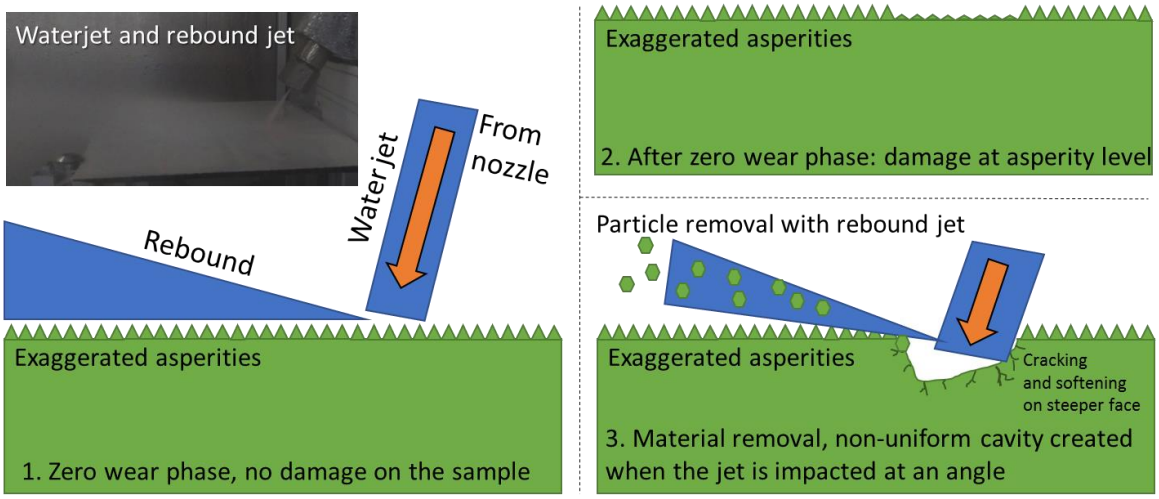

Figure 6-54 Three wear phases with waterjet angular impact

The hypothesis of parallel and perpendicular faces could be investigated further by testing multiple samples whereby the duration of the test would be incremental between tests and each sample sectioned and analysed in order to capture in detail a step-by-step formation of the cavity. Repeated tests for different impact angles would indicate whether the two faces identified in this research are dependent on spray angle and if the softening of the material measured for S275JR is consistent and how it is related to cracking and spray conditions.

The performance of the Stellite 6 clad is superior to the other materials, especially Hardox 500, which is a material often chosen for its erosive resistance properties. Volume wear graphs in Figure 6-50 and Figure 6-51 show the difference in erosion resistance by comparison of the volume loss. This property is shown better in Figure 6-51 where both axis are in logarithmic scale and this justifies how the Stellite 6 performance is superior to the other materials. Roughness measurements in Figure 6-53 show an increase in roughness for S275JR and Hardox 500 while a slight decrease is surface roughness in the scar area for the clad material. Material is not removed, but only superficial changes are taking place on the surface asperities. This might explain why a deep cavity has not been generated in the clad layer as with the other materials, however, the underline mechanism for this is not proven in this research.

An effort was made to obtain Stellite 6 clad on S275JR plate by the plasma transferred arc method (PTA), to be compared with the laser clad coating on the same erosion test. PTA is a hardfacing technique that could probably generate clad coatings of similar quality to Stellite 6. Unfortunately, it was not possible to obtain PTA clad material on time.

6.5 Bending tests

6.5.1 Bending tests - Results

Cracks appeared in the curved face in all samples because this face experienced tension during the test. Cracks in all specimens that propagated into the substrate were off centre of the bending axis and this might be attributed to an imbalance in the positioning of the specimen, see Figure 6-55 of a preliminary test of a clad specimen.

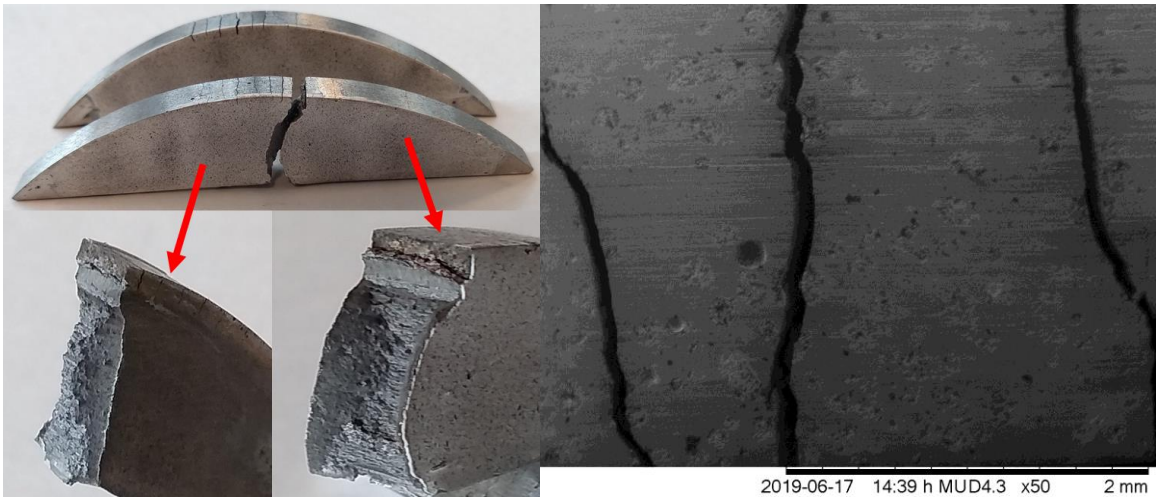

Figure 6-55 Total fracture (left) and SEM image of the surface cracks (right)

Although multiple cracks may have been initiated, the stress was concentrated to one of the cracks, which has propagated through to the substrates, as shown in Figure 6-56. For the laser clad samples, the energy has been distributed to multiple cracks and none have penetrated through to the intermediate layer. Clad 2, shown in Figure 6-56 was driven further to a breaking point. The weakest crack that propagated was off centre from the bending axis.

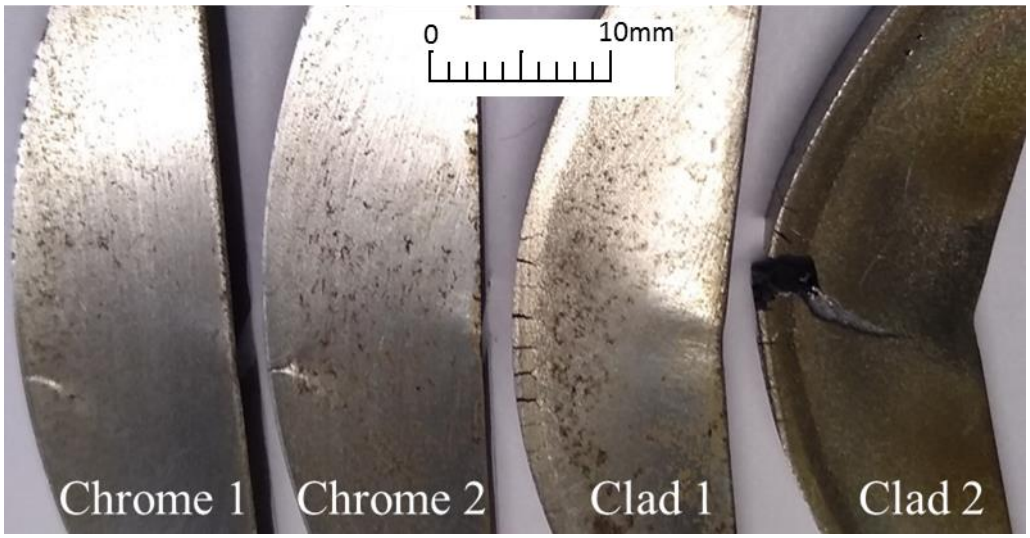

Figure 6-56 Samples from UTM 3-point bend test

An effort was made to drive to test ratchetting effects by loading and partially unloading the specimen in steps, using force control. Unfortunately, the force control did not work as intended due to the closed loop control sampling rate being out of sync with the feedback received from the loadcell, thus oscillations where produced that amplified during testing before stabilising at a higher load, as shown by Clad 3 in Figure 6-57. The oscillation measurement was omitted and replaced by a dashed line. The curve inclination of Clad 3 varies in comparison to the inclination of Clad 1 and 2. The breaking point is also higher and this might be attributed to the ratcheting mechanism. The chrome samples have a higher breaking point and a steeper inclination, indicating that they are stiffer than the clad specimens. The smooth curve change of Clad 1 and 2, around 15 kN load, indicated that the material has started yielding due to the multiple cracks that appeared. Clad 1 has not fully fractured, while Clad 2 has fully fractured at 18 kN.

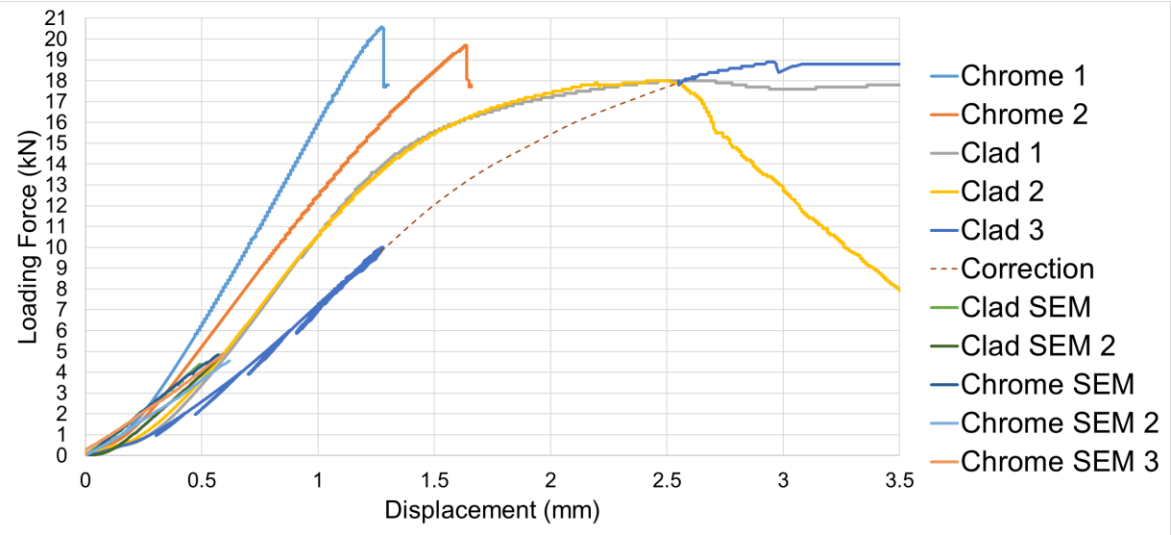

Figure 6-57 Loading Force vs Displacement for UTM testing

Clad and Chrome specimens tested in the SEM are also included in Figure 6-57. Early UTM displacement measurements can be seen separately in Figure 6-58. The initial deformation is not linear and the inclination varies until the equipment has settled. Another reason for the early unsettlement might be the initiation of micro-cracking which affected the stiffness of the specimen, linear behaviour does not start until 0.25 mm displacement in Figure 6-58. This is a “pop-in” effect, as described as described in [211]. The pop in effect was also audible during testing, with a high pitch metallic creaking sound occurring multiple times throughout the test. SEM test results are shown separately in Figure 6-59. The force/displacement curves are linear and no significant difference can be observed between the specimens tested.

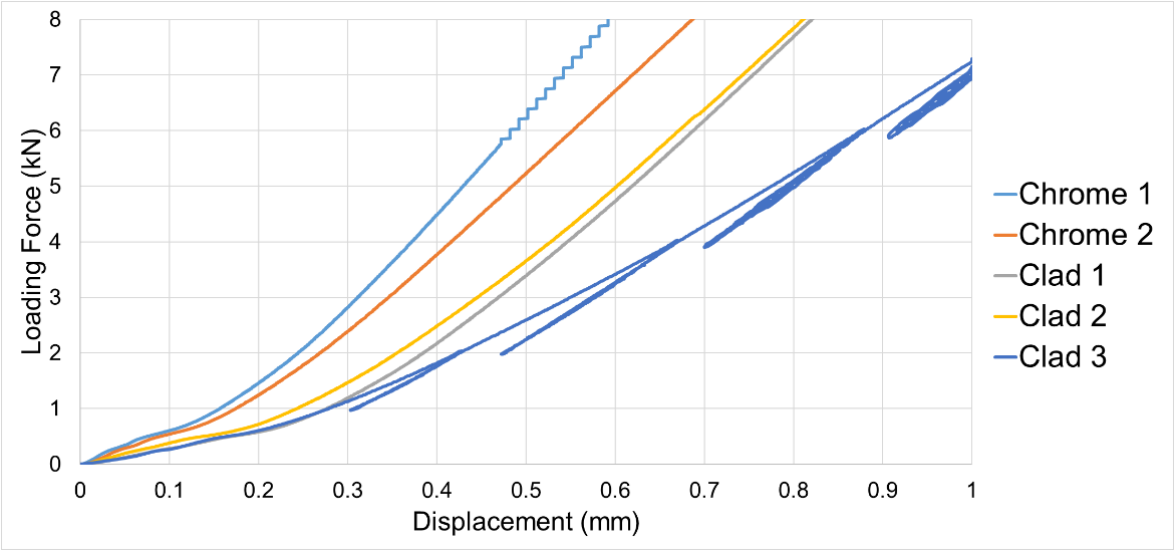

Figure 6-58 Loading Force vs Displacement early loading plot (UTM tests)

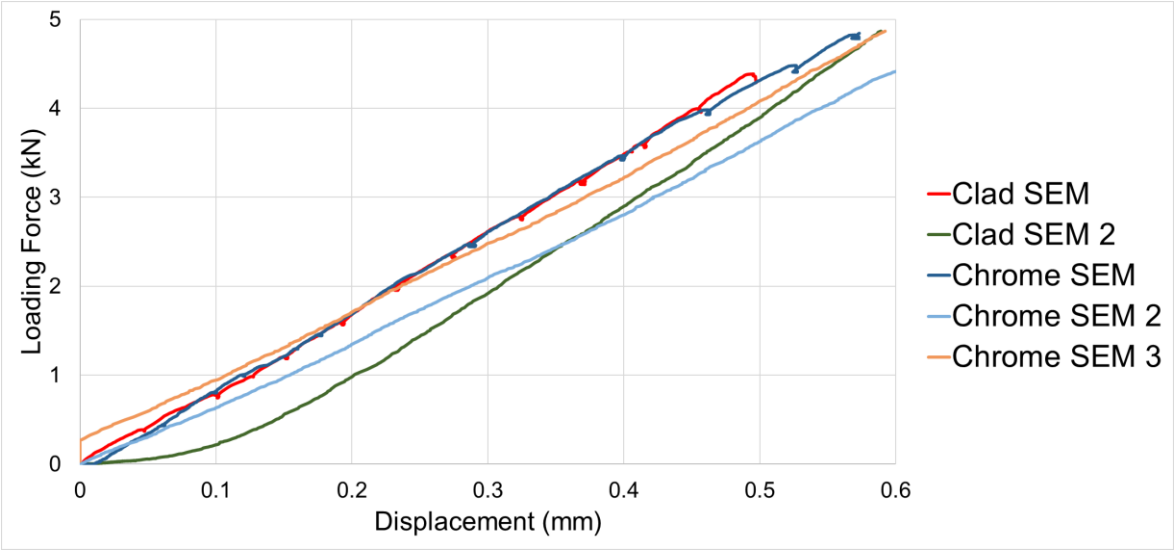

Figure 6-59 Loading Force vs Displacement (SEM tests)

Sequenced images from the SEM and the UTM have been analysed using Digital Image Correlation (DIC) software [203]. It was challenging to obtain DIC images based on the etched microstructure, especially in the intermediate layer where the microstructure pattern was not as dense as in the other regions, therefore only results from UTM specimens that had a speckle pattern of black paint are shown here. The shear strain analysis of the clad specimen highlighted the behaviour of the intermediate layer. Strain analysis in Figure 6-60 was calculated from images obtained by loading the clad specimen from rest up to 18 kN. High strain appears as expected and concentrated around a few cracks that opened up during loading. Above these cracks, a narrow shear strain band appears, which correlates with the location of the intermediate clad layer. Figure 6-61 results from the speckle patter on the chrome UTM sample only indicated significant shearing value after the crack has appeared in the coating. The software analysis picked up shearing bands from the edge of the crack at 45^{o} towards the substrate and 90^{o} to each other. These bands indicate that the crack may follow

either direction and this is evident by the first two images in Figure 6-56 where the crack propagates into the substrate and changes direction by 45º.

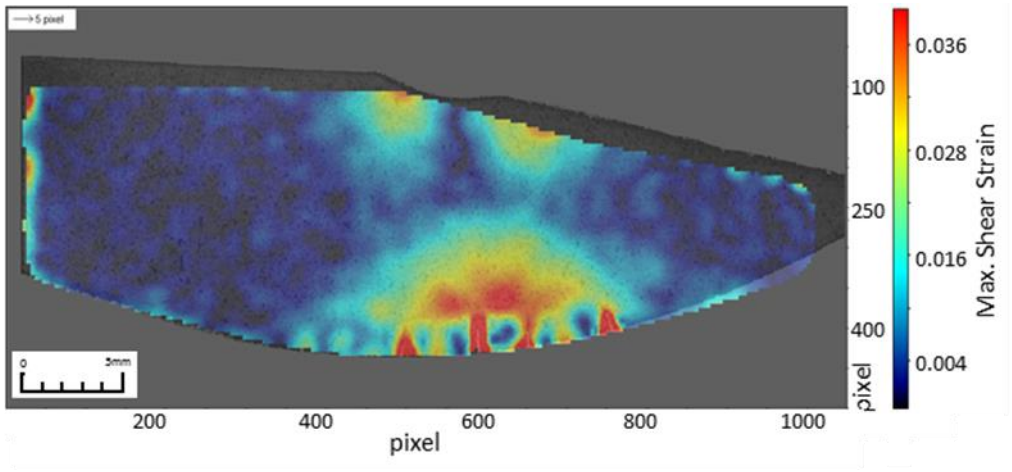

Figure 6-60 Maximum shear strain of clad specimen, loaded up to 18 kN (tested on a UTM)

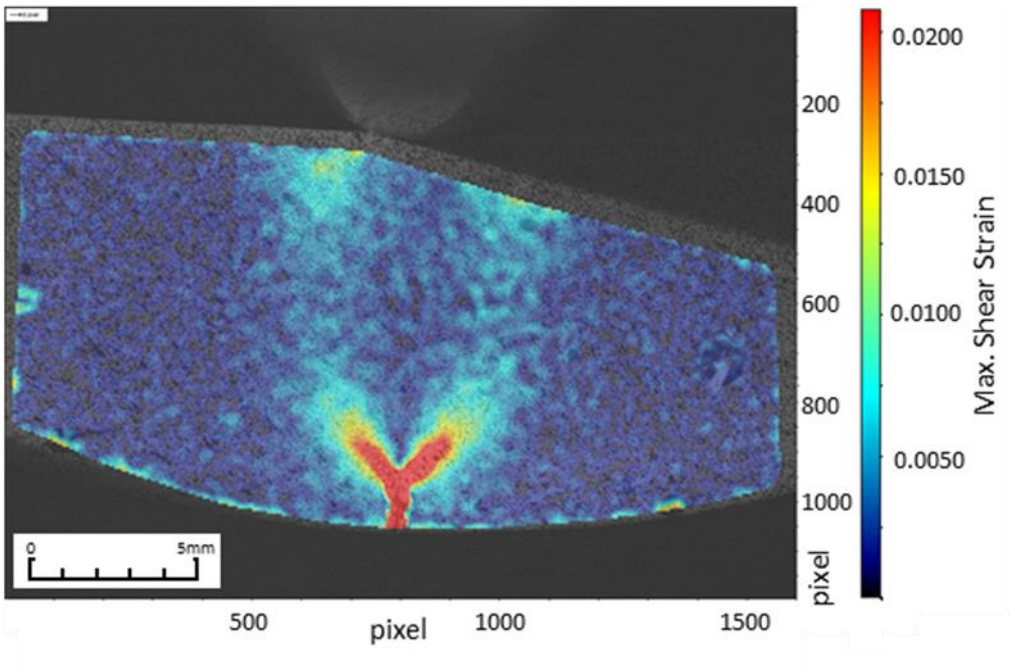

Figure 6-61 Maximum shear strain of chrome specimen, loaded up to 20 kN (tested on a UTM)

Maximum shear strain values at 18 kN force are higher in the clad specimen in comparison to values at 20 kN force for the chrome specimen. Strain near the edges of the boundary may not be realistic. The DIC was restricted to a particular area in the specimen in order to exclude unwanted features such as shadows, for example in the top right section of the specimen. An interesting observation here is that the maximum shear strain away from the cracks is still concentrated around the intermediated layer and around the individual cracks, distributing the strain energy in a wider area by acting as a pivoting mechanism. This allows for a delay in crack propagation to the substrate. A less ductile intermediate layer or the lack of it may have resulted in behaviour similar to the chrome specimen in Figure 6-61, whereby the strain energy is concentrated to a small region and crack propagation takes place earlier with respect to displacement.

Micro-cracks were present in both the clad and chrome samples. In both coatings, cracks appeared in multiple locations, more dominant in either side of the bending axis as indicated in Figure 6-62. Cracks in the Technolase® coating have an origin from flaws in the microstructure and grow in multiple direction. This is evident in Figure 6-63. Due to the bending forces, the cracks were encourage to grow towards the substrate and it is clear that no cracks have propagated into the intermediate layer.

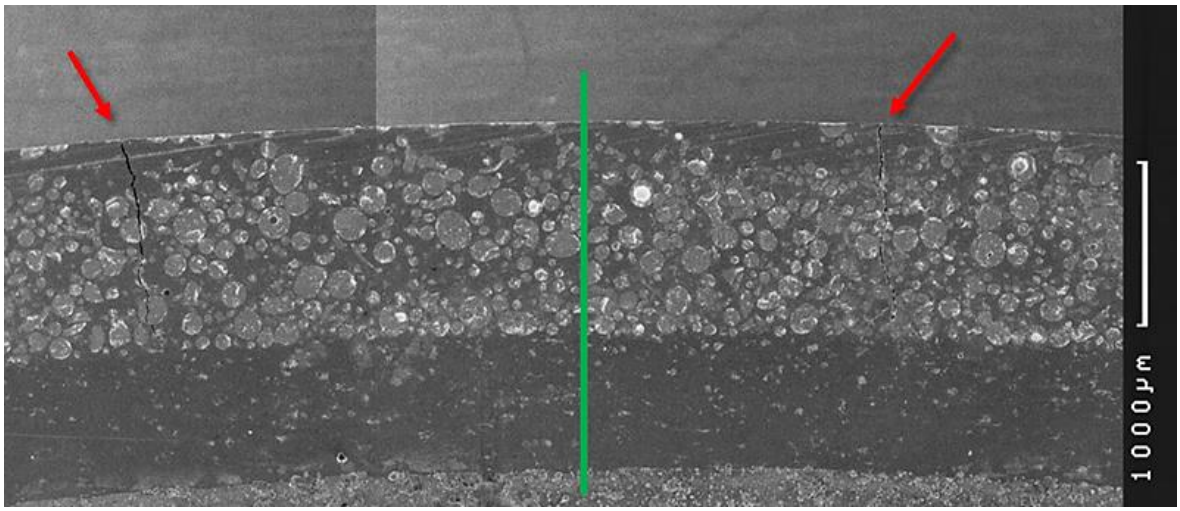

Figure 6-62 Bending axis (green line) and cracks at either end (red arrows) for SEM clad specimen

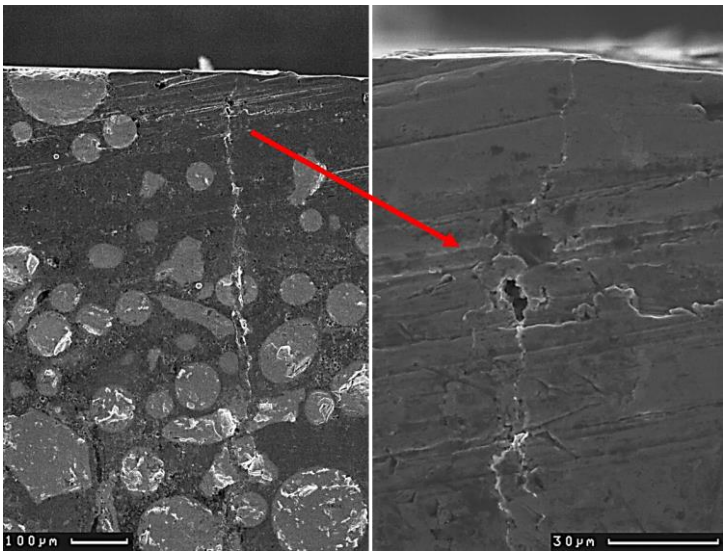

Figure 6-63 Possible microstructure flaw or porosity that may have contributed to cracking

Figure 6-64 is a good example showing the root of a crack in the Technolase® coating leading to a WC particle, which branched out into multiple cracks out of the WC particle. The bottom right image of Figure 6-64 shows one crack being directed to another WC particle and other cracks being directed towards the Inconel 625 layer and to stop at the dilution zone. Figure 6-65 highlights the mechanism that enables this behaviour. When the specimen is loaded, the crack opens up by pivoting around the softer intermediate layer and because the intermediate layer is more ductile, it stretches to accommodate the bending forces and prevents the crack from propagating, as opposed to behaving in a brittle manner.

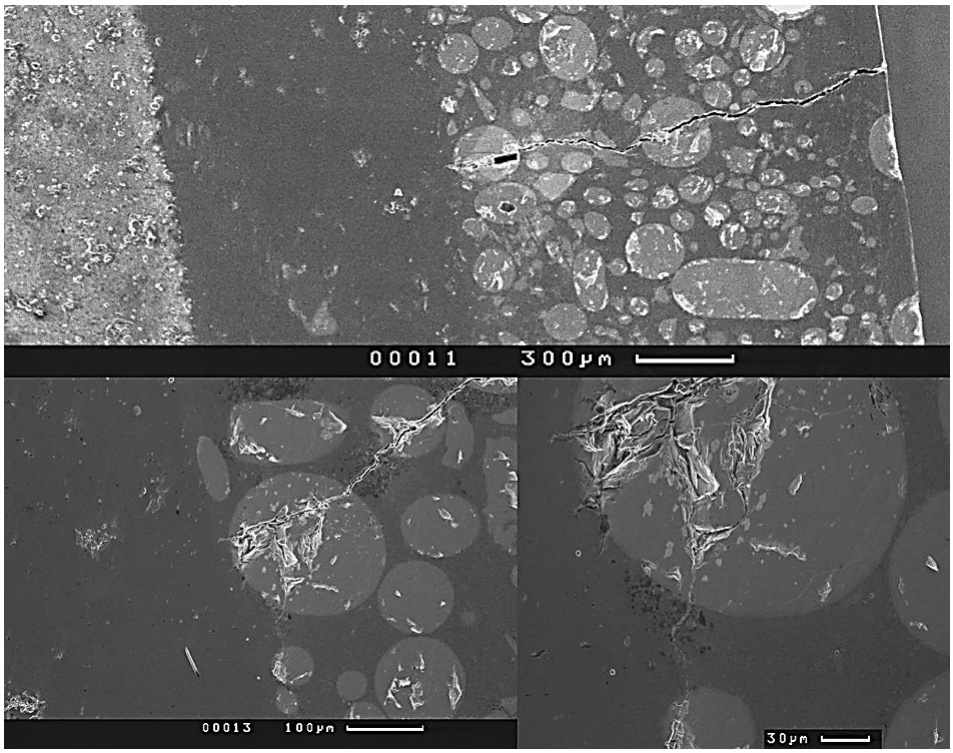

Figure 6-64 Magnification on the crack end, indicating how cracks stop at the softer intermediate layer

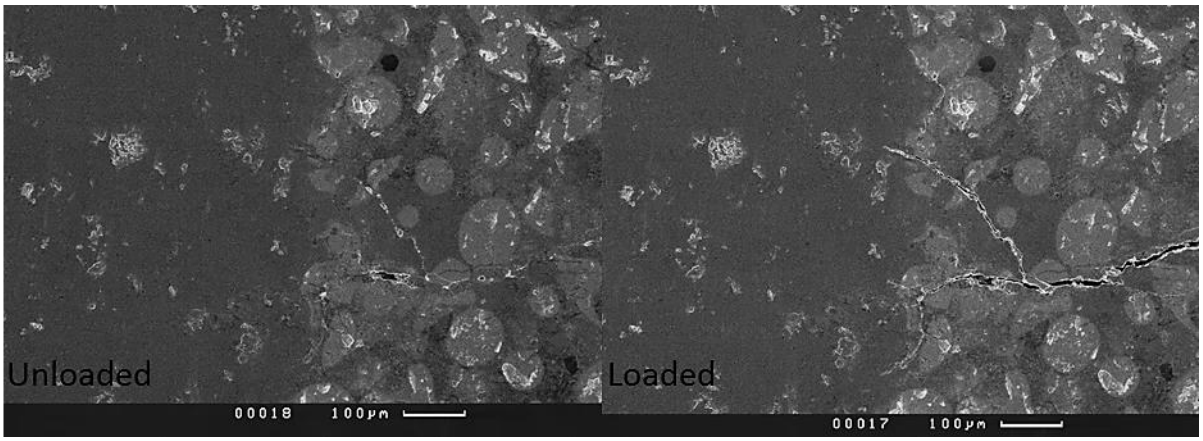

Figure 6-65 Crack image with and without bending load.

The opposite occurred in the chrome layer, where intermitted cracks exist through the thickness of the coating and the bending load has either extended the cracks through the full thickness of the coating (Figure 6-66) or generating smaller cracks which branched out to join other existing cracks (Figure 6-67).

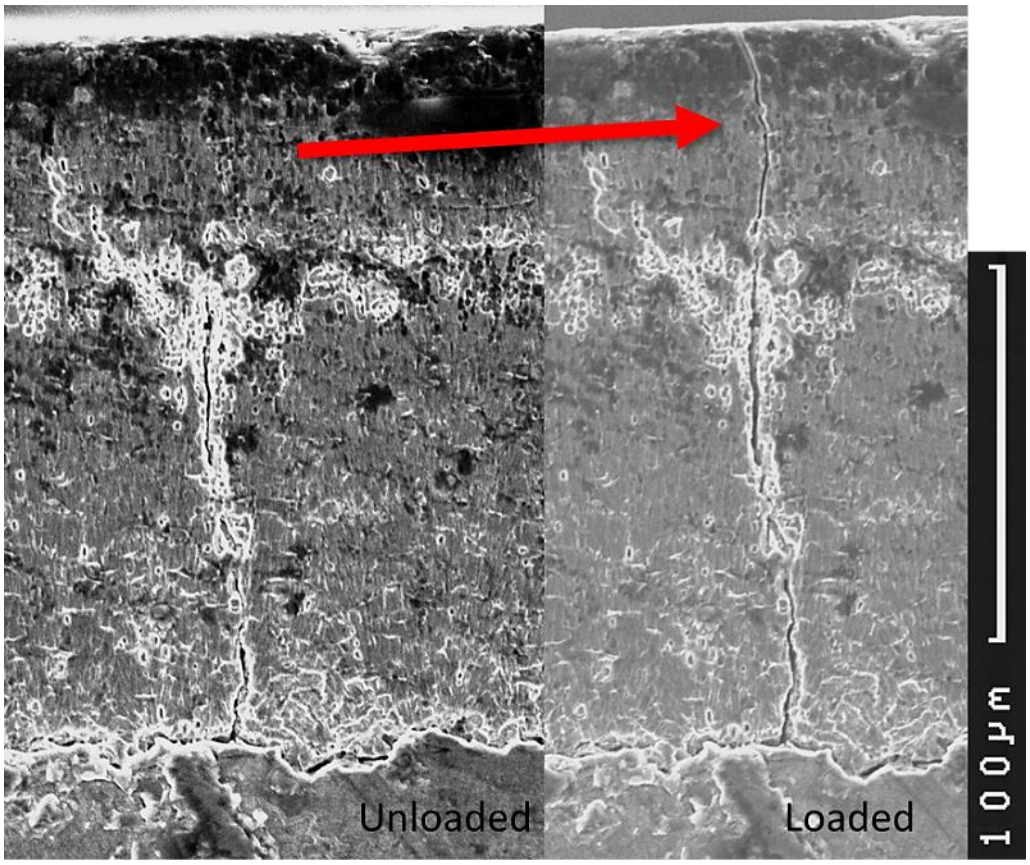

Figure 6-66 Cracks appearing on chrome sample after testing in the SEM

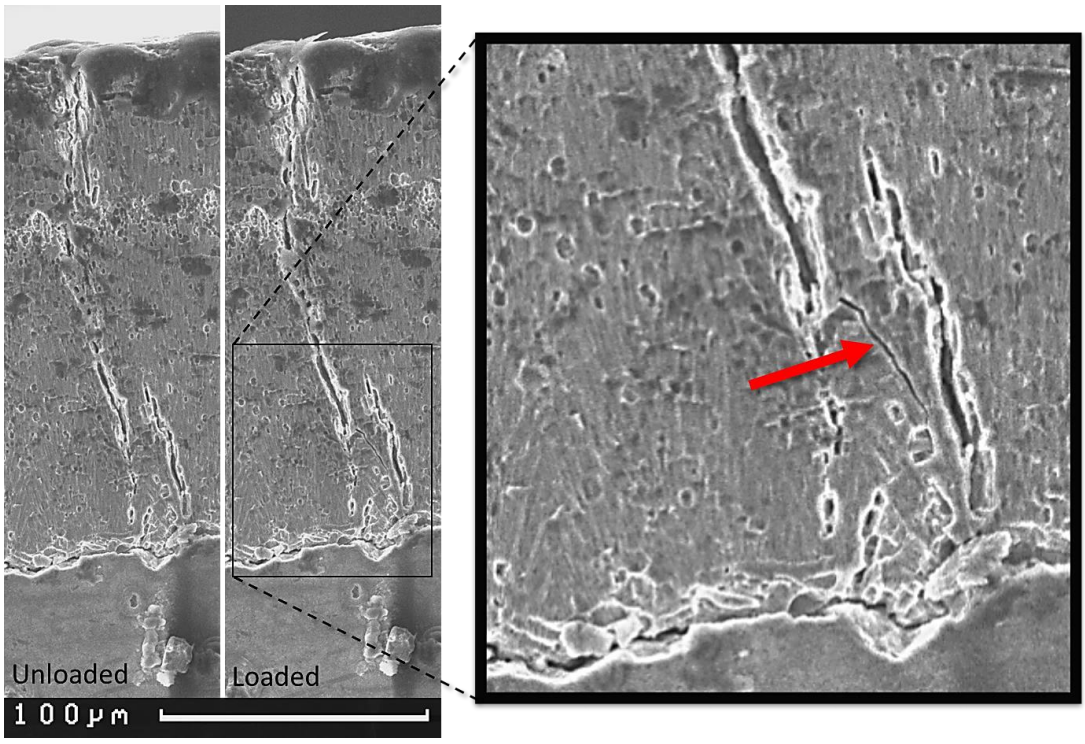

Figure 6-67 Cracks appearing on chrome sample after testing in the SEM

6.5.2 Bending tests – Discussion

The composite properties of the Technolase® coating consist of Sphérotène®, spherical cast Tungsten Carbide particles, within a nickel based alloy matrix layer. The second layer of Inconel 625 has a marginally softer hardness than the steel substrate which has hardness of 325 HV 0.3 kg. The hardness varies through the thickness of the two coatings and when under deformation the softer matrix material is expected to deform to resist the bending strain due to its ductility. The areas of interest are at the dilution regions between layers. High hardness is found in both of these regions at around 450 HV. This combined with some softening around the dilution region suggests possible heat affected zones or changes in chemical composition in this area. However, the thickness of the dilution zone is very small in comparison to the clad layer, which is one of the advantages of the laser cladding process as opposed to other hardfacing methods.

While the chrome plated specimens exhibited higher stiffness and load than the Technolase® coated specimens the failure had very limited plasticity prior to failure due to the lack of ductility in the single layer of chrome plating. Whereas the composite structure used in the Technolase® promoted plasticity in the Inconel 625 prior to failure, this allowed for greater deformation.

Both Technolase® and chrome electroplating had minor cracks within them. The cracks appeared after cutting the specimens with the EDM, which has released residual stresses that were formed from the coating processes. During bending, these cracks propagated in both coatings, but the Technolase® coating cracks did not propagate into the Inconel 625. While the cracks did not propagate into the Inconel they continued to grow in the Technolase®. During the test, the strain energy resulted in several cracks, distributing the localised strain in the Inconel. The Technolase® bend tests had a greater displacement and undergo significantly more plasticity. In the chrome coating, the bending stress was concentrated into a small region due to the lack of ductility and the failure resulted in one major crack that propagated into the substrate. Principal stresses were visualised with the use of FEA in section 4.2.4.

While the bending test is a useful means of promoting a failure in the coatings, in service the failure will occur as a material is drawn across the surface and a load is applied to deform it. If friction is applied the delamination observed in the chrome electroplated layer might result in spallation and the loss of this layer. Whereas the superior dilution between layers with the Lasercarb® process resists delamination and so the coating may have an extended lifetime.

Generally, the chrome plating finish roughness is about 0.1-0.2 μm Ra. A surface roughness of up to 0.6 μm Ra would be acceptable for parts of the pinion surface that are in direct contact with bearing components. This is to ensure a smooth surface, free from large asperities that may contribute to material pick-up during mounting and dismounting of the tapered sleeve. The resultant roughness was found to be 1.6 μm Ra in the direction parallel to the pinion's axis and 0.9 μm Ra in the circumferential direction. The roughness and pitting on the surface is probably caused by the grinding process, with the removal of WC spherical particles near the outer clad surface. Such surface roughness values are not acceptable for direct contact with the bearings. However, clad work roll

material from a parallel study (see Figure 5-11) has shown an improvement in the surface roughness with values of 0.62 μm Ra in the axial direction and 0.88 μm Ra in the circumferential direction. The improvement is attributed to the use of a ceramic grinding disc as opposed to a diamond grinding disc, during the surface preparation after cladding. The circumferential roughness of the clad work roll is higher than 0.6 μm Ra, however, the diameter of the sample was 45 mm as opposed to the pinion diameter of 100 mm and this may have affected the roughness in the circumferential direction. Therefore, it is expected that the clad pinion roughness could improve with the use of ceramic grinding disc, in both the axial and circumferential directions.

There is a need to replace the chrome electroplating process due to the carcinogenic chemicals required in manufacturing. The Technolase® coating applied by the Lasercarb® process has been found to operate as designed with the hard outer coating suitable for load bearing without significant deformation and without delamination when tested under extreme bending conditions. The localisation of strain in the Inconel 625 was reduced which had sufficient ductility to limit crack propagation allowing in some bend tests more than twice the displacement without failure. The improved deformation characteristics and dilution between layers can increase the lifespan of coatings as the cracking of the outer coating is less prone to result in delamination and failure. Further tests should include wear performance and to consider the bearing interface under the same conditions as when in service. The performance of the clad layer in this study signifies that the laser clad coating could be an alternative to the chrome electroplating coating. Improvements in surface roughness should be considered prior to an industrial trial, perhaps with improvements in the grinding process or the use of alternative surface modifications methods such as laser surface remelting.

This page was intentionally left blank

7 DISCUSSION

A gap in the use of laser cladding for high load bearing applications was identified through the literature review. The interfaces chosen for this research are highly loaded or operate with high friction in the contact of the interfaces. The term extreme is used to describe such interfaces. Five extreme interfaces with laser clad coatings were investigated for tribological performance under extreme conditions, erosion, impact, bending to obtain stiffness and to investigate crack propagation and two rolling/sliding interfaces, one of which is regarding texture evolution.

The choice of clad materials was paramount for evaluating the coating durability under extreme conditions. All clad materials were produced from powder, which is the most common and established method in industry and research. Coatings with significantly higher hardness than the substrate and properties that benefit the contact conditions were chosen, as well as multilayer coatings that combine such properties on a lamellar structure. A two-layer lamellar coating of Inconel 625 and a nickel-based material with WC particles called Technolase®, were investigated under bending and texture rolling-sliding tests. Stellite 6 clad material was tested in erosion and impact tests, while Martensitic Stainless Steel (MSS) was tested under rolling-sliding for extreme slip conditions for rail. The tests and materials are summarised in Table 2-3.

Typical material analysis techniques found in laser clad research literature were used in this study, such as micro and nano hardness measurements through the thickness of the coating. Other techniques were the use of micrographs for analysis of the dilution zone, crack investigation, quality of the clad in terms of porosity and grain deformation near the contact surface. Chemical composition was obtained through optical emission spectroscopy. All clad coatings were manufactured by an external supplier, using their knowledge and expertise aiming to achieve non-porous coatings, with low dilution zone and microstructure as defined by the material grade. A lot of the objectives of research literature reviewed here were to investigate the effects of various parameters on the laser clad process and/or the materials and their composition. The objective in this research was to investigate laser clad materials under their corresponding in-service interface and the parameters used to produce the clad coatings were not investigated further. This means that the Stellite 6, MSS and two-layer (WC/Inconel 625) coatings used in the tests are in the form/grade available commercially and could be replicated for use in industrial applications without specific adjustments in the laser clad process and clad materials.

Some aspects of the tests were not found in other research and were unique to this thesis, for example twin disc testing of clad material under high slip (20%) conditions. The twin disc test represents the interface found in the field, as opposed to testing the materials using standard tribological methods, such as pin-on-disc tribometers. A novel approach for testing erosion was also adopted. A fan jet spray pattern and impact pressure similar to those found in industrial descalers were used. Conventional fluid erosion tests use column fluid jets with low flow rates, which allow for calculating flows and fluid impact pressure since the jet geometry is known with a constant pressure on the impact area. The descaler jet is designed to remove scale from steel plates, thus an extreme

condition for testing, however it had a challenging interface since the impact pressure is not constant over the impacting area. The use of Digital Image Correlation (DIC) has been used previously for testing laser clad materials during tensile testing and during the cladding process. A new approach was taken in this research to test with the use of DIC under a three-point bend test of a two-layer clad coating. This unique test allowed an insight into the behaviour of the coatings when stressed to conditions outside the operating range of the component. Tensile test specimens are designed with a specific geometry in mind, typically based on known standards, they do not necessarily represent the interface found in service. The importance of the test performed here was that the geometry of the clad coating used was the same as the in-service interface. Although this geometry, unlike tensile test specimen geometry, makes it impossible to obtain absolute values of stress, it allowed evaluation of the clad performance and the ability of the two-layer coating to stop crack propagation to the substrate. The geometry of the curved specimen, taken from an industrial spindle, made it difficult to calculate the stress distribution, however, the use of DIC, UTM load and displacement measurements, together with FEA simulations enabled the investigation of the performance under these conditions. The impact test was a new test in terms of the rig design. While the other rigs were used under standard testing conditions and the erosion rig was purposely designed for this study, an existing impact rig for composite materials was modified for use with steel specimens as required by this study. The rig modifications resulted in producing comparable results that were sufficient for the thesis, however, further work is required for obtaining good quality results. For example, the lack of repeatability and identification of a steady state in the drop pin material deformation was not sufficient to produce results for defining material models for simulations. The approach of comparing a single impact from various materials was unique to this study, especially for laser clad materials.

The results from each test were discussed in detail in chapter 6, a summary of that discussion is presented here for each of the five tests:

Twin disc tests concluded in Tγ/A values that characterise the performance of the premium railway materials and MSS laser clad material proposed for use in cladding rails. Three slip conditions yielded Tγ/A values in the region of 10 N mm^{-2} (1%), 50 N mm^{-2} (10%) and over 90 N mm^{-2} (20%). The MSS clad material exhibited low wear at high and low slip, while at medium slip conditions the unclad materials exhibited higher wear resistance. When accounting for the system wear (wheel and rail wear together), the MSS clad excelled in all slip conditions as it was causing less wearing on the wheel material.

Impact tests produced comparable results for R260, R3500HT and Manganese steel, materials used in switches and crossings. Laser clad Stellite 6 was proposed as an alternative material that showed the least deformation under the same test conditions, for width and depth of the cavity that resulted from the impact but also for the bulging of the surface surrounding the cavity.

Textured on clad material tests showed that after an accelerated wear test, the texture was transferred successfully to aluminium samples by rolling. The clad material roughness has increased after the wear test, as opposed to the unclad material surface roughness which had decreased as

expected. This is due to the morphology of the chosen clad material and this behaviour may benefit some applications while it may not be desirable for others.

Excellent erosion resistance was identified for Stellite 6 from high pressure erosion tests. A new rig was built for this purpose which operated at extreme test conditions. Extreme erosion was benchmarked on an aluminium sample which showed significant wear on the surface in just 30 seconds. The range of the test duration for each steel test material varied significantly, with S275JR rolled plate to show signs of significant wear only a few minutes into the test, the specialised rolled plate Hardox 500 after testing for 1.5 hours and the Stellite 6 clad after a staggering 7 hours, whereby the wear was much lower than the counterpart materials. In-situ wear measurements such as laser scanning [212], could prove beneficial in identifying stages of wear and to distinguish wear on materials with similar performance.

Strength and crack behaviour of a two-layer steel composite clad was tested under bending in the SEM and UTM, which resulted in interesting conclusions. Although the chrome plated alternative exhibited higher stiffness during the test, local strain resulted in the propagation of a major crack, while the two-layer coating being more ductile distributed strain widely in the Technolase®, resulting in multiple cracks that were arrested by the intermediate layer of Inconel 625.

Through the literature research it was found that there was a gap in testing high loading interfaces and with geometries and conditions similar to the interfaces found in the field. The tests in this study were designed to bridge that gap by testing on true in-service geometry and at extreme conditions. Other trends identified through literature were the use of hybrid laser claddings using assistive technologies and a combination of machining with inspection systems. Such technologies have not been investigated in this study, the clad on the samples was manufactured and ground or textured using standalone equipment, without being guided by intelligent sensors, rather by operator expertise. The common theme found in literature is that a lot of research is focused on controlling the various parameters of the cladding process, aiming at achieving desirable and consistent coatings. This will extend the electromechanical capability of laser clad systems beyond the basic guiding of the laser head with traditional CNC, using automated systems with continuous feedback loops from various sensors such as thermocouples and video processing from cameras.

Such automated capabilities will increase the alloying possibilities for the coatings. More customisation will be possible, for example building lamellar structures in a single process or producing coatings with varying grades through the thickness or in selected regions on the coated surfaces. For example, the two-layer coating used here could be produced in a single process with the nickel based material and WC additives alone, in a single layer that has a varying grade representative of the two materials used in this study. This can be done by controlling the powder feed mix ratio and clad process parameters, which can only be done with the addition of sensors and intelligent systems.

Industrial applications were identified such as feed rollers for casters used in the steel industry and coatings for hydraulic cylinder rods, which indicate a superior performance of laser clad over hardfacing techniques. In parallel to these references, tests performed here for bending and erosion

indicate that laser cladding can produce coatings that could be competitive for existing hardfacing solutions on components. Hardfacing can be easily applied with simplistic equipment and at low cost, as opposed to complicated laser cladding equipment which results in higher process costs. Niche industrial applications that warrant the additional cost could benefit from replacing current hardfacing coatings with laser clad coatings, in favour of extending the durability of the coatings.

Finally, as mentioned in this section, the interface geometry was not always represented in the various research found in literature. The focus in the wider research for materials is to characterise materials regarding their mechanical properties, as means of using this information in modelling and in the decision making for the application of materials in research. A common method for obtaining mechanical properties is with tensile testing of material specimens. This is valid for homogeneous materials, however it is questionable whether tensile testing on composite specimens of clad and substrate materials [156] can be used to obtain the true mechanical properties of the clad material, for example to be used in modelling. A step closer to obtaining accurate mechanical properties would be to isolate the laser clad coating from the substrate and to test at an appropriate scale, for example by performing tensile testing in the SEM, since the coating sample will be very thin and small samples can be obtained in comparison to traditional bench mount UTM specimens. Such tests were not found in the literature. In other cases the shear stress and its relationship to yield strength was obtained by shear punch stress [213]. More work however is needed in this area, as machining processes required to isolate the clad material may interfere with residual stresses and the metallurgical state of the coating. For this reason, the nanoindentation method was used in this study to obtain the reduced elastic modulus directly from the as-clad specimen. Also, the tests were performed with the interface geometry and contact conditions found in the field to obtain direct performance results. The rolling/sliding geometry was not exactly the same as the one found in the field, since it would be impractical to perform tests on full size rail wheels or work rolls for the steel industry tests. All other aspects of the contact were included, such as the contact pressure and contact patch area.

8 CONCLUSIONS

8.1 General conclusion and recommendations

The aim of the thesis was to investigate whether laser clad coatings were suitable for high load bearing applications and if the selected applications had increased the surface durability in comparison to alternative coatings. Novel test methods were tried in this study to represent extreme damage, for example for extreme erosion. Extreme damage was also tried on existing test methods, such as the twin disc test for rail materials, where slip conditions up to 20% were tested for the first time on laser clad materials. Texture evolution was tested on twin disc as well, however it is the first time that laser clad materials were tested for texture evolution in this way. A new combination of a two-layer laser clad materials was also proposed and tested in a unique way of recording and understanding crack arrest that results from the proposed material combination, under a three point bend test and the use of digital image correlation. A new novel method for obtaining impact damage information from a single impact was tested, which although successful for comparison between materials, with further improvement it is promising for obtaining individual material impact damage properties for use in modelling.

Generally, the chosen clad materials exhibited an increase in durability for the extreme test conditions of load bearing applications. The MSS clad showed wear resistance at low slip, but most importantly at high slip and with reduced wear effects on the wheel material, so the recommendation from these trials is that the use of MSS cladding on rails should take place in areas of the rail network where high slip wear dominates. For cladding switches and crossings, Stellite 6 showed significant improvement over standard rail and unhardened Manganese steel casting. The results showed that cladding of crossing nose directly could reduce material deformation from impact, therefore reducing the need for reprofiling. It could further reduce the frequency of crossing nose replacement due to sever wear and deformation. Other materials available by laser cladding may be suitable for use in railways. However, the results from this study indicate that the chosen material withstood the test conditions and could be suitable for trials in the field, under similar conditions.

Stellite 6 also showed superior erosion resistance under high pressure erosion, outperforming materials such as Hardox, known for their hard wearing and erosion resistant properties. It is unknown as to whether Stellite 6 produced in other forms such as plasma transferred arc (PTA) would yield the same wear resistance and it would be of interest to identify if the manufacturing process with laser cladding and subsequent microstructure was the underline factor that contributed to this performance.

The two-layer composite steel clad of softer Inconel 625 and harder Technolase® showed to be a promising combination, where an outer layer of significantly higher bulk hardness than the substrate provides protection and durability. The intermediate softer alloy provides ductility between the substrate and brittle coating, acting as a barrier for crack propagation. It also acts as a disposable layer that can be removed when necessary to allow re-cladding with a new coating, thus extending

the life of the component. The Technolase® proved to be suitable for retaining texture, it was evident from the texture tests that the Technolase® coating maintained the texture after testing. In some cases, roughness values were slightly increased, which could be beneficial on tribological interfaces that require to maintain their roughness above a certain level. Initial high roughness on the surface resulting from the WC particles was also an issue for the spindle case study as this component required lower roughness values than the as clad roughness. A careful grinding regime may be a temporary solution for this issue and further work is needed to provide a solution that produces a smooth surface from the cladding process, for example re-melting the surface, as opposed to relying on additional processes. In applications where a rough texture is an essential part of the interface, the Technolase® may be an ideal candidate. Inherent microcracks on the surface from the laser clad process were present but were not of concern during the rolling-sliding tests. The cracks were encouraged to grow under extreme bending tests, where the Inconel 625 successfully stopped the propagation to the substrate. In all cases the clad thickness was in the region of 1-2 mm, much higher than protective coatings from traditional techniques, which was sufficient for the chosen interfaces and conditions.

Various experimental and modelling limitations were identified and discussed throughout the thesis. Modelling was restricted to Hertzian contact calculations for setting up the rolling/sliding tests, while FEA were used to estimate the stress state of materials under the impact and the three-point bend tests. The proposed approach of characterising the material behaviour from the tests in order to calibrate the FEA model was not entirely successful. The results are promising, however a lot of work is needed to improve the tests to achieve this. For the bending tests, it is a case of testing a lot of samples in order to produce sufficient statistical analysis to produce appropriate stiffness to be used in the FEA model. The model has to be modified further, to ensure that the boundary conditions between the clad layers and substrate are represented correctly, for example a bonded or otherwise contact. The material properties through the clad layers are not always homogeneous, as this was shown by the hardness tests and this should be reflected in the FEA modelling somehow, along with the presence of hard WC particles. The impact modelling produced satisfactory results, more good quality experimental measurements are needed to improve the modelling for standalone material predictions.

The impact test rig was a good first approach to test the concept of impact and for material comparison. A new rig would be recommended for obtaining accurate material properties to be used in modelling. The pin material used (AISI 52100 bearing steel ball) was suitable, however this was encased in a brass fitting. A fitting of the same material would enable most of the impacting energy to be absorbed by the specimen under test, thus eliminating the need of initial impacts to achieve an equilibrium state. A pendulum arm with rigid components would be more suitable than the rig used in these tests and could potentially allow for multiple impacts on the same spot, thus obtaining strain deformation from repeated loading and extend the data available for modelling to that similar of non-linear kinematic hardening data, which would be useful for modelling repeated wheel impact on crossing nose, as described in 4.2.3. For single impact tests, a catchment mechanism is recommended to catch the pin after the first impact and to avoid further impact one the specimen.

The use of strain gauges on the pin arrangement is also recommended, as opposed to the use of a readily available loadcell. The strain gauge would provide correct strain energy information, which can be translated into impact force and energy. A high frequency response datalogger must be used in order to capture the event during impact. Strain measurements on the pin arrangement and the specimen can be used to evaluate the FEA model.

Twin disc tests at high slip conditions were restricted in terms of obtaining accurate wear rates at discrete time intervals. This is due to the short test time (1,000 cycles total) in comparison to the 1% slip tests, where the mass loss was measured every 5,000 cycles (30,000 cycle overall test). An improvement would be the use of direct disc profile measurement on the twin disc, such as a 2D profile laser scanner, which would result in a continuous measurement of the disc profile, allowing for volume loss during testing, which can then be converted into mass loss. This would also enable tests of 100% slip, which would represent full slide from braking or wheel spin on a static train. The same or similar sensor could be used to improve the erosion rig and to obtain direct measurements (by pausing the water jet) without the need to unload the specimen intermittently for measuring mass loss or volume loss with the Alicona.

The texture tests were performed successfully, however the method of obtaining the transfer ratio on aluminium strip and the method of applying a lubricant for the transfer ratio sampling could be improved. Testing a wider range of contact conditions and obtaining a lot more measurements could yield more conclusive results for evaluating the use of texture with clad materials on applications not considered so far in this study.

Notes on the future of cladding: process improvements, for example, the potential of cladding at higher speeds was demonstrated by a combination of Plasma-Transferred-Arc (PTA) welding and a laser beam, where the laser beam was used to stabilise the plasma arc [214]; the use of nano materials, lamellar structures and new grades resulting from the laser cladding process could provide solutions for expanding the working envelop of interfaces and enable operation at different conditions. For example, colder/hotter temperature, higher loads, faster speeds, harsher environments.

Laser cladding is an expensive process with high initial investment costs. Although it has been widely used in industries such as oil and gas, the transition to other industries is still slow. The production of wear properties and material models could convey confidence in the use of laser cladding in industry. Case studies and small scale tests such as the ones in this thesis could contribute to the decision making for adopting laser cladding in new applications, especially as a replacement of chrome plating. Such applications could benefit wear plates found in various forms in the steel industry, forming tools and dies, printing rolls, automotive brakes discs and other engine components including drive shafts and gears. Furthermore, high value components in aerospace such as landing gears which experience high loads and of which reliability is crucial for the safety of travellers may benefit from a similar approach to replacing the current coatings with laser clad materials. Heavy machinery and equipment that comes in contact with fluids and particles, as well as seismic isolators in buildings which experience extreme conditions and heavy loads. Extreme conditions can also be found at sea, for example cavitation wear caused on impellers and propellers. There is a large, growing industry

for the supply of sea equipment, from oil and gas platform, vessels, wind and tidal power equipment, all of which are affected by the environment and experience high loads from exposure to the elements, whether the equipment is above or below the sea level.

8.2 Publications arising from this work

Journal papers:

- Review of laser cladding tribology for high load applications (under review with Taylor and Francis Tribology journal)
- P. Christoforou, D. I. Fletcher, and R. Lewis, "Benchmarking of premium rail material wear," *Wear,* p. 202990, 2019
- R. Lewis, P. Christoforou, W. J. Wang, A. Beagles, M. Burstow, and S. R. Lewis, "Investigation of the influence of rail hardness on the wear of rail and wheel materials under dry conditions (ICRI wear mapping project)," *Wear,* vol. 430-431, pp. 383-392, 2019
- J. F. Santa *et al.*, "Twin disc assessment of wear regime transitions and rolling contact fatigue in R400HT – E8 pairs," *Wear,* vol. 432-433, 2019
- M. Watson *et al.*, "An analysis of the quality of experimental design and reliability of results in tribology research," *Wear,* vol. 426, pp. 1712-1718, 2019

11th International Conference on Contact Mechanics and Wear of Rail/Wheel Systems-CM2018, Delft, the Netherlands, September 24–28, 2018:

- Benchmarking of premium rail material wear
- Investigation of the influence of rail hardness on the wear of rail and wheel materials under dry conditions, Co-author (ICRI wear mapping project)
- Evaluation of rolling contact fatigue or rail materials in twin disc tests, Co-author
- Twin disc assessment of wear regime transitions in R400HT-E8 pairs, Co-author

This page was intentionally left blank

9 REFERENCES

[1] S. R. Lewis *et al.*, "Improving rail wear and RCF performance using laser cladding," *Wear,* Article; Proceedings Paper vol. 366, pp. 268-278, Nov 2016, doi: 10.1016/j.wear.2016.05.011.

[2] K. Hilgenberg and K. Steinhoff, "Texturing of skin-pass rolls by pulsed laser dispersing," *Journal of Materials Processing Technology,* vol. 225, pp. 84-92, Nov 2015, doi: 10.1016/j.jmatprotec.2015.05.027.

[3] R. Singh, D. Kumar, S. K. Mishra, and S. K. Tiwari, "Laser cladding of Stellite 6 on stainless steel to enhance solid particle erosion and cavitation resistance," *Surface & Coatings Technology,* 2014, doi: 10.1016/j.surfcoat.2014.04.008.

[4] "UK rail industry financial information 2018-19." Accessed: 2020. [Online]. Available: https://orr.gov.uk/__data/assets/pdf_file/0019/42562/uk-rail-industry-financial-information-2018-19.pdf

[5] E. R. Agency, "Railway Safety Performance in the European Union," 2016. [Online]. Available: https://erail.era.europa.eu/documents/SPR.pdf

[6] "HSE's annual report on railway safety 2003-04." [Online]. Available: http://orr.gov.uk/__data/assets/pdf_file/0016/1663/railsafety0304.pdf

[7] S. P. Timoshenko, *History of strength of materials, with a brief account of the history of theory of elasticity and theory of structures*. London: McGraw-Hill, 1953.

[8] S. Y. Yarema and L. Tóth, "Formation of the science of fatigue of metals. Part 1. 1825–1870," *Materials science.,* vol. 42, no. 5, pp. 673-680, 2006, doi: 10.1007/s11003-006-0132-3.

[9] E. E. Magel, "Rolling contact fatigue: a comprehensive review," U.S. Department of Transportation. Federal Railroad Administration, 2011.

[10] *RIS-2766-RST Rail Industry Standard for Wheelsets*, RSSB, 2017.

[11] C. Casanueva, P. A. Jonsson, S. Stichel, and Asme, "USE OF ARCHARD'S WEAR LAW FOR THE CALCULATION OF UNIFORM WHEEL WEAR OF HIGH TONNAGE FREIGHT VEHICLES," *Proceeding of the Asme Joint Rail Conference, 2013,* Proceedings Paper p. 6, 2013, Art no. Unsp t02a013.

[12] E. Magel, J. Kalousek, and R. Caldwell, "A numerical simulation of wheel wear," *Wear,* Article; Proceedings Paper vol. 258, no. 7-8, pp. 1245-1254, Mar 2005, doi: 10.1016/j.wear.2004.03.033.

[13] U. Olofsson, and R. Lewis, *Wheel-rail interface handbook*. Oxford: Woodhead Publishing, 2009.

[14] G. W. Stachowiak, *Engineering tribology*, Fourth edition. Oxford: Elsevier/Butterworth-Heinemann, 2014.

[15] M. Godet, "The third- body approach - A mechanical view of wear," *Wear,* vol. 100, pp. 437-452, 1984.

[16] S. Descartes, C. Desrayaud, E. Niccolini, and Y. Berthier, "Presence and role of the third body in a wheel-rail contact," *Wear,* Article; Proceedings Paper vol. 258, no. 7-8, pp. 1081-1090, Mar 2005, doi: 10.1016/j.wear.2004.03.068.

[17] R. W. K. Honeycombe, *Steels: microstructure and properties*. London: Edward Arnold, 1981.

[18] K. L. Johnson, *Contact Mechanics*. Cambridge University Press, 1985.

[19] T. M. Beagley, "SEVERE WEAR OF ROLLING-SLIDING CONTACTS," *Wear,* Article vol. 36, no. 3, pp. 317-335, 1976, doi: 10.1016/0043-1648(76)90110-1.

[20] P. J. Bolton and P. Clayton, "Rolling sliding wear damage in rail and tyre steels," *Wear,* Article vol. 93, no.2, pp.145-165, 1984, doi: 10.1016/0043-1648(84)90066-8.

[21] R. Lewis *et al.*, "Mapping railway wheel material wear mechanisms and transitions," *Proceedings of the Institution of Mechanical Engineers, Part F: Journal of Rail and Rapid Transit,* vol. 224, no. 3, pp. 125-137, 2010, doi: 10.1243/09544097JRRT328.

[22] E. J. M. Hiensch *et al.*, "Prevention of RCF damage in curved track through development of the INFRA-STAR two-material rail," *Fatigue & Fracture of Engineering Materials & Structures,* vol. 26, no. 10, pp. 1007-1017, 2003, doi: 10.1046/j.1460-2695.2003.00663.x.

[23] M. Hiensch *et al.*, "Two- material rail development: field test results regarding rolling contact fatigue and squeal noise behaviour," *Wear,* vol. 258, no. 7, pp. 964-972, 2005, doi: 10.1016/j.wear.2004.03.067.

[24] S. L. Grassie, "Rolling contact fatigue on the British railway system: treatment," *Wear,* vol. 258, no. 7, pp. 1310-1318, 2005, doi: 10.1016/j.wear.2004.03.065.

[25] R. Nilsson and U. Olofsson, "Surface cracks and wear of rail: A full-scale test on a commuter train track," *Proceedings of the Institution of Mechanical Engineers.,* vol. 216, no. 4, pp. 249-264, 2002, doi: 10.1243/095440902321029208.

[26] K. L. Johnson, "The Strength of Surfaces in Rolling Contact," 1989, doi: 10.1243/PIME_PROC_1989_203_100_02.

[27] J. E. Garnham, R. G. Ding, and C. L. Davis, "Ductile inclusions in rail, subject to compressive rolling-sliding contact," *Wear,* vol. 269, no. 11, pp. 733-746, 2010, doi: 10.1016/j.wear.2010.07.010.

[28] R. Lewis and R. S. Dwyer-Joyce, "Wear mechanisms and transitions in railway wheel steels," *Proc. Inst. Mech. Eng. Part J.-J. Eng. Tribol.,* Article vol. 218, no. J6, pp. 467-478, Dec 2004, doi: 10.1243/1350650042794815.

[29] S. Wise, "British railway research - the first hundred years," York University of Railway Studies and Transport History, 2000.

[30] P. J. Bolton and P. Clayton, "Rolling-sliding wear damage in rail and tyre steels," *Wear,* vol. 93, no. 2, pp. 145-165, 1984, doi: 10.1016/0043-1648(84)90066-8.

[31] R. Lewis, R. S. Dwyer-Joyce, and E. A. Gallardo-Hernandez, "Temperature in a twin-disc wheel/rail contact simulation," *Tribology international,* vol. 39, no. 12, pp. 1653-1663, 2006, doi: 10.1016/j.triboint.2006.01.028.

[32] E. K. Magel, J. Sroba, "Chasing the Magic Wear Rate," in *CCP: 104 PROCEEDINGS OF THE SECOND INTERNATIONAL CONFERENCE ON RAILWAY TECHNOLOGY: RESEARCH, DEVELOPMENT AND MAINTENANCE*, 2014, doi: http://doi.org/10.4203/ccp.104.116.

[33] T. Jendel, "Prediction of wheel profile wear-comparisons with field measurements," *Wear,* vol. 253, no. 1-2, pp. 89-99, 2002, doi: 10.1016/S0043-1648(02)00087-X.

[34] A. Kapoor, "Wear by plastic ratchetting," *Wear,* vol. 212, no. 1, pp. 119-130, 1997, doi: 10.1016/S0043-1648(97)00083-5.

[35] M.Burstow, "Whole Life Rail Model Application and Development for RSSB: Development of an RCF Damage Parameter," Rail Safety & Standards Board, Derby, AEATR-ES-2003-832, 2003, issue 1.

[36] M. Hiensch and M. Steenbergen, "Rolling Contact Fatigue on premium rail grades: Damage function development from field data," *Wear,* vol. 394-395, pp. 187-194, 2018, doi: 10.1016/j.wear.2017.10.018.

[37] R. Pippan and R. Stock, "Rail grade dependent damage behaviour – Characteristics and damage formation hypothesis," *Wear,* vol. 314, no. 1-2, pp. 44-50, 2014, doi: 10.1016/j.wear.2013.11.029.

[38] R. Pippan and R. Stock, "RCF and wear in theory and practice-The influence of rail grade on wear and RCF," *Wear,* vol. 271, no. 1-2, pp. 125-133, 2011, doi: 10.1016/j.wear.2010.10.015.

[39] H.K. Jun, S.J. Kwon, D.H. Lee, and J.W. Seo, "Rolling contact fatigue and wear of two different rail steels under rolling-sliding contact," *International journal of fatigue,* vol. 83, pp. 184-194, 2016, doi: 10.1016/j.ijfatigue.2015.10.012.

[40] "Operational failure modes of Switches and Crossings," in "Public deliverable D 1.3.1," CAPACITY4RAIL, 2015.

[41] NetworkRail. "Reliable and resilient switches." https://www.networkrail.co.uk/wp-content/uploads/2017/03/Challenge-Statement-SC-Reliable-and-resilient-switches.pdf (accessed 24 April, 2017).

[42] NetworkRail. An Introduction to Switches & Crossings - Network Rail engineering education. Available: https://youtu.be/ZuR5QTlfOzk.

[43] Y. N. Dastur and W. C. Leslie, "Mechanism of work hardening in Hadfield manganese steel," *Metallurgical Transactions A,* vol. 12, no. 5, pp. 749-759, 1981/05/01 1981, doi: 10.1007/BF02648339.

[44] A. Johansson *et al.*, "Simulation of wheel-rail contact and damage in switches & crossings," *Wear,* vol.271,no.1, pp.472-481,2011, doi: 10.1016/j.wear.2010.10.014.

[45] A. Brooker, J. Gonder, L. Wang, E. Wood, and L. Ramroth, "FASTSim: A Model to Estimate Vehicle Efficiency, Cost and Performance," 2015.

[46] DEsolver. "GENSYS." http://www.gensys.se/ (accessed June, 2019).

[47] W. Daves, F. D. Fischer, H. Ossberger, and M. Wiest, "Deformation and damage of a crossing nose due to wheel passages," *Wear,* vol. 265, no. 9-10, pp. 1431-1438, 2008, doi: 10.1016/j.wear.2008.01.033.

[48] M. Wiest, W. Daves, and F. D. Fischer, "Four Different Numerical Approaches of Calculating Strains and Stresses During Impact in Wheel-Rail Rolling Contact," no.42010, pp.327-328,2005,doi:10.1115/WTC2005-63624.

[49] J. C. O. Nielsen and E. Kassa, "Dynamic interaction between train and railway turnout: full-scale field test and validation of simulation models," *Vehicle system dynamics,* vol. 46, no.1, pp. 521-534, 2008, doi: 10.1080/00423110801993144.

[50] J. C. O. Nielsen and E. Kassa, "Dynamic train–turnout interaction in an extended frequency range using a detailed model of track dynamics," *Journal of sound and vibration,* vol. 320, no. 4-5, pp. 893-914, 2009, doi: 10.1016/j.jsv.2008.08.028.

[51] A. Nunez, Z. Li, and R. Dollevoet, "Evaluating Degradation at Railway Crossings Using Axle Box Acceleration Measurements," *Sensors.,* vol. 17, no. 10, p. 2236, 2017, doi: 10.3390/s17102236.

[52] R. Skrypnyk, M. Ekh, J. C. O. Nielsen, and B. A. Pålsson, "Prediction of plastic deformation and wear in railway crossings - Comparing the performance of two rail steel grades," *Wear,* vol. 428-429, pp. 302-314, 2019, doi: 10.1016/j.wear.2019.03.019.

[53] F. C. Robles Hernández, A. O. Okonkwo, V. Kadekar, T. Metz, and N. Badi, "Laser cladding: The alternative for field thermite welds life extension," *Materials & Design,* vol. 111, pp. 165-173, 2016, doi: 10.1016/j.matdes.2016.08.061.

[54] M. Bergmann *et al.*, "A novel model-based approach for the prediction of wear in cold rolling," *Wear,* vol.376, pp.1245-1259, 2017, doi: 10.1016/j.wear.2016.12.056.

[55] "Electric discharging method for texturing the work roll," *Transactions of the Iron and Steel Institute of Japan,* vol. 26, no. 8, pp. 759-759, 1986.

[56] O. Pawelski, W. Rasp, W. Zwick, H. J. Nettelbeck, and K. Steinhoff, "The influence of different work-roll texturing systems on the development of surface-structure in the temper rolling process of steel sheet used in the automotive industry," *Journal of Materials Processing Technology,* vol. 45, no. 1-4, pp. 215-222, Sep 1994.

[57] J. Simao, D. K. Aspinwall, M. L. H. Wise, and M. F. Elmenshawy, "Mill roll texturing using EDT," *Journal of Materials Processing Technology,* Article; Proceedings Paper vol. 45, no. 1-4, pp. 207-214, Sep 1994, doi: 10.1016/0924-0136(94)90342-5.

[58] J. Crahay *et al.*, *Substitution of chrome plating for the rolls of skin- pass mill (CRFREEROLLS) final report*. Luxembourg: Publications Office, 2016.

[59] R. e. a. Bröcking. "Development of Electrical Discharge Coating (EDC) as Chrome-Free Alternative for Increasing Campaign Length of Temper Mill Work Rolls." https://pdfs.semanticscholar.org/6039/5431b49bca99fe8eb22f78f89ae823b828cc.pdf (accessed June, 2019).

[60] M. F. Frolish and J. H. Beynon, "Design criteria for rolling contact fatigue resistance in back-up rolls," *Ironmaking & Steelmaking,* Article vol. 31, no. 4, pp. 300-304, Aug 2004, doi: 10.1179/030192304225018181.

[61] S. Kaltwalzen. *The basics about cold rolls, a professional's handbook*, 3 ed., 2014.

[62] M. F. Frolish, D. I. Fletcher, and J. H. Beynon, "A quantitative model for predicting the morphology of surface initiated rolling contact fatigue cracks in back-up roll steels," *Fatigue & Fracture of Engineering Materials & Structures,* Article vol. 25, no. 11, pp. 1073-1086, Nov 2002, doi: 10.1046/j.1460-2695.2002.00601.x.

[63] D.-G. f. R. a. Innovation, "Innovative high temperature and mechanical descaling (HIDES)," 2013. [Online]. Available: https://publications.europa.eu/en/publication-detail/-/publication/24628475-9c4a-4110-8321-f3c5f01a5b3e

[64] "Lechler Descaling." https://www.lechler.com/de-en/applications/descaling/ (accessed June, 2019).

[65] L. Bendig, M. Raudensky, and J. Horsky, "Descaling with high pressure nozzles," presented at the ILASS-Europe, Zurich, 2001.

[66] J. I. Bech, C. B. Hasager, and C. Bak, "Extending the life of wind turbine blade leading edges by reducing the tip speed during extreme precipitation events," *Wind Energy Science,* vol. 3, no. 2, pp. 729-748, 2018, doi: 10.5194/wes-3-729-2018.

[67] M. H. Keegan, D. H. Nash, and M. M. Stack, "On erosion issues associated with the leading edge of wind turbine blades," *Journal of Physics D*, vol. 46, ed, 2013, p. 383001.

[68] M. A. S. Shohag, E. C. Hammel, D. O. Olawale, and O. I. Okoli, "Damage mitigation techniques in wind turbine blades: A review," *Wind Engineering,* vol. 41, no. 3, pp. 185-210, 2017, doi: 10.1177/0309524X17706862.

[69] İ. Özen and H. Gedikli, "Solid Particle Erosion on Shield Surface of a Helicopter Rotor Blade Using Computational Fluid Dynamics," *Journal of Aerospace Engineering,* vol. 32, no. 1, 2019, doi: 10.1061/(ASCE)AS.1943-5525.0000962.

[70] D. P. Davies and S. L. Jenkins, "Mechanical and metallurgical characterisation of electroformed nickel for helicopter erosion shield applications," *Materials Science & Engineering A,* vol. 607, pp. 341-350, 2014, doi: 10.1016/j.msea.2014.03.122.

[71] M. Pepi, R. Squillacioti, L. Pfledderer, and A. Phelps, "Solid Particle Erosion Testing of Helicopter Rotor Blade Materials," *Journal of Failure Analysis and Prevention,* vol. 12, no. 1, pp. 96-108, 2012, doi: 10.1007/s11668-011-9531-3.

[72] F. P. Burton and J. H. Brunton, "The deformation of solids by liquid impact at supersonic speeds," *Proceedings of the Royal Society of London. Series A. Mathematical and Physical Sciences,* 10.1098/rspa.1961.0172 vol. 263, no. 1315, p. 433, 1961.

[73] V. Arya, B. S. Mann, and V. Arya, "HVOF coating and surface treatment for enhancing droplet erosion resistance of steam turbine blades," *Wear,* vol. 254, no. 7-8, pp. 652-667, 2003, doi: 10.1016/S0043-1648(03)00253-9.

[74] P. J. Blau, "How common is the steady- state? The implications of wear transitions for materials selection and design," *Wear,* vol. 332-333, pp. 1120-1128, 2015, doi: 10.1016/j.wear.2014.11.018.

[75] M. Brandt, S. Sun, N. Alam, P. Bendeich, and A. Bishop, "Laser cladding repair of turbine blades in power plants: from research to commercialisation," *International Heat Treatment and Surface Engineering,* vol. 3, no. 3, pp. 105-114, 2009/09/01 2009, doi: 10.1179/174951409X12542264513843.

[76] J. Zhao, A. Ma, X. Ji, J. Jiang, and Y. Bao, "Slurry Erosion Behavior of AlxCoCrFeNiTi0.5 High-Entropy Alloy Coatings Fabricated by Laser Cladding," *Metals,* vol. 8, no. 2, p. 126, 2018, doi: 10.3390/met8020126.

[77] Primetals, "Primetals Technologies ships highest capacity roll unit for Chinese wire rod mill," [press release], 2019.

[78] M. Schlesinger, M. Paunovic, and M. Paunovic, *Modern electroplating*, 5th ed. Hoboken, N.J.: Wiley, 2010.

[79] J. Davis, *Surface engineering of carbon and alloy steels*. pp. 701-740, 1994.

[80] M. Nascimento and H. Voorwald, "The significance of and determination by image analysis of microcrack density in hard chromium plating," *Plating and Surface Finishing,* vol. 3, pp. 36-42, 2008.

[81] A. Brenner, P. Burkhead, and C. Jennings, "Physical Properties of Electrodeposited Chromium," *Journal of Research of the National Bureau of Standards,* vol. 40, no. 1, pp. 31-59, 1948.

[82] V. V. Diaz, J. C. Dutra, and A. S. C. M. D'Oliveira, "Hardfacing by plasma transfer arc process," *Welding International,* vol. 26, no. 2, pp. 87-95, 2012, doi: 10.1080/09507116.2010.527486.

[83] Y. Pang, M. Yu, and P. Zhang, "Effects of WC Particle Types on the Microstructures and Properties of WC-Reinforced Ni60 Composite Coatings Produced by Laser Cladding," *Metals.,* vol. 9, no. 5, p. 583, 2019, doi: 10.3390/met9050583.

[84] D. Deschuyteneer, F. Petit, M. Gonon, and F. Cambier, "Processing and characterization of laser clad NiCrBSi/ WC composite coatings - Influence of microstructure on hardness and wear," *Surface & Coatings Technology,* vol. 283, pp. 162-171, 2015, doi: 10.1016/j.surfcoat.2015.10.055.

[85] J. M. Amado, M. J. Tobar, J. C. Alvarez, J. Lamas, and A. Yáñez, "Laser cladding of tungsten carbides (Spherotene®) hardfacing alloys for the mining and mineral industry," *Applied Surface Science,* vol. 255, no. 10, pp. 5553-5556, 2009, doi: 10.1016/j.apsusc.2008.07.198.

[86] WorldSteelAssociation. "How many types of steel are there?" https://www.worldsteel.org/about-steel/steel-facts.html (accessed 2019).

[87] R. M. Barnsby and T. A. Harris, "Life ratings for ball and roller bearings," *Proceedings of the Institution of Mechanical Engineers.,* vol. 215, no. J6, pp. 577-595, 2001, doi: 10.1243/1350650011543817.

[88] J. Hardell, B. Prakash, and D. W. Gebretsadik, "Tribological performance of tin-based overlay plated engine bearing materials," *Tribology international,* vol. 92, pp. 281-289, 2015, doi: 10.1016/j.triboint.2015.06.014.

[89] W. Bensalah, N. Loukil, M. D. P. Wery, and H. F. Ayedi, "Assessment of automotive coatings used on different metallic substrates," *International Journal of Corrosion,* vol. 2014, Article ID 838054, p. 12, 2014, doi: 10.1155/2014/838054.

[90] S. Deshpande, A. Kulkarni, S. Sampath, and H. Herman, "Application of image analysis for characterization of porosity in thermal spray coatings and correlation with small angle neutron scattering," *Surface & Coatings Technology,* vol. 187, no. 1, pp. 6-16, 2004, doi: 10.1016/j.surfcoat.2004.01.032.

[91] SulzerMetco. "An Introduction to Thermal Spray - Sulzer Metco 2013." https://www.upc.edu/sct/en/documents_equipament/d_324_id-804-2.pdf (accessed 2019).

[92] T. T. Wohlers, *Wohlers report 2014 : 3D printing and additive manufacturing state of the industry annual worldwide progress report*. Fort Collins, Colo.: Wohlers Associates, 2015.

[93] T. H. Maiman, "Stimulated optical radiation in ruby," *Nature,* Article vol. 187, no. 4736, pp. 493-494, 1960, doi: 10.1038/187493a0.

[94] "Our Story - 3D Systems" https://uk.3dsystems.com/our-story (accessed 2019).

[95] A. K. Ehsan Toyserkani, Stephen F. Corbin, *Laser Cladding*, 1st edition (12 Aug. 2004) CRC Press, Taylor and Francis Group, p. 280, 2017.

[96] L. Dubourg and J. Archambeault, "Technological and scientific landscape of laser cladding process in 2007," *Surface & Coatings Technology,* vol. 202, no. 24, pp. 5863-5869, 2008, doi: 10.1016/j.surfcoat.2008.06.122.

[97] S. Kaierle, A. Barroi, C. Noelke, J. Hermsdorf, L. Overmeyer, and H. Haferkamp, "Review on Laser Deposition Welding: From Micro to Macro," *Physics Procedia,* vol. 39, pp. 336-345, 2012, doi: 10.1016/j.phpro.2012.10.046.

[98] L. Pawlowski, "Thick laser coatings: A review," *J Therm Spray Tech,* vol. 8, no. 2, pp. 279-295, 1999, doi: 10.1361/105996399770350502.

[99] F. Weng, C. Chen, and H. Yu, "Research status of laser cladding on titanium and its alloys: A review," *Materials & Design,* vol. 58, pp. 412-425, Jun 2014, doi: 10.1016/j.matdes.2014.01.077.

[100] S. Liu *et al.*, "Friction surface cladding: An exploratory study of a new solid state cladding process," *Journal of Materials Processing Tech.,* vol. 229, pp. 769-784, 2016, doi: 10.1016/j.jmatprotec.2015.10.029.

[101] J. W. Sears, "Direct laser powder deposition - State of the Art," *ASTM/TMS Materials Week, Cincinnati,* 1999.

[102] R. Vilar, "Laser cladding," *J. Laser Appl.,* vol. 11, no. 2, pp. 64-79, 1999, doi: 10.2351/1.521888.

[103] T. Torims, G. Pikurs, A. Ratkus, A. Logins, J. Vilcans, and S. Sklariks, "Development of Technological Equipment to Laboratory Test In-Situ Laser Cladding for Marine Engine Crankshaft Renovation," *25th Daaam International Symposium on Intelligent Manufacturing and Automation, 2014,* vol. 100, pp. 559-568, 2015 2015, doi: 10.1016/j.proeng.2015.01.405.

[104] N. Hutasoit, W. Yan, R. Cottam, M. Brandt, and A. Blicblau, "Evaluation of Microstructure and Mechanical Properties at the Interface Region of Laser- Clad Stellite 6 on Steel Using Nanoindentation," *Metallogr. Microstruct. Anal.,* vol. 2, no. 5, pp. 328-336, 2013, doi: 10.1007/s13632-013-0093-5.

[105] G. Chryssolouris, S. Zannis, K. Tsirbas, and C. Lalas, "An experimental investigation of laser cladding," *Cirp Annals-Manufacturing Technology,* vol. 51, no. 1, pp. 145-148, 2002, doi: 10.1016/s0007-8506(07)61486-3.

[106] D. Bartkowski, A. Młynarczak, A. Piasecki, B. Dudziak, M. Gościański, and A. Bartkowska, "Microstructure, microhardness and corrosion resistance of Stellite- 6 coatings reinforced with WC particles using laser cladding," *Optics and Laser Technology,* vol. 68, pp. 191-201, 2015, doi: 10.1016/j.optlastec.2014.12.005.

[107] W. Ya, B. Pathiraj, and S. J. Liu, "2D modelling of clad geometry and resulting thermal cycles during laser cladding," *J. Mater. Process. Technol.,* vol. 230, pp. 217-232, Apr 2016, doi: 10.1016/j.jmatprotec.2015.11.012.

[108] E. Toyserkani, A. Khajepour, and S. Corbin, "3-D finite element modeling of laser cladding by powder injection: effects of laser pulse shaping on the process," *Optics and Lasers in Engineering,* vol. 41, no. 6, pp. 849-867, Jun 2004, doi: 10.1016/s0143-8166(03)00063-0.

[109] M. Hao and Y. Sun, "A FEM model for simulating temperature field in coaxial laser cladding of TI6AL4V alloy using an inverse modeling approach," *International Journal of Heat and Mass Transfer,* vol. 64, pp. 352-360, Sep 2013, doi: 10.1016/j.ijheatmasstransfer.2013.04.050.

[110] P. Farahmand and R. Kovacevic, "An experimental-numerical investigation of heat distribution and stress field in single- and multi-track laser cladding by a high-power direct diode laser," *Optics and Laser Technology,* vol. 63, pp. 154-168, Nov 2014, doi: 10.1016/j.optlastec.2014.04.016.

[111] F. K. Mirzade *et al.*, "Kinetic approach in numerical modeling of melting and crystallization at laser cladding with powder injection," *Physica B: Physics of Condensed Matter,* vol. 423, pp. 69-76, 2013, doi: 10.1016/j.physb.2013.04.053.

[112] J. Ahlstrohm, B. Karlsson, and S. Niederhauser, "Modelling of laser cladding of medium carbon steel - a first approach," *Journal De Physique Iv,* vol. 120, pp. 405-412, Dec 2004, doi: 10.1051/jp4:2004120046.

[113] H. Qi, J. Mazumder, and H. Ki, "Numerical simulation of heat transfer and fluid flow in coaxial laser cladding process for direct metal deposition," *J. Appl. Phys.,* vol. 100, no. 2, 2006, doi: 10.1063/1.2209807.

[114] E. Toyserkani, A. Khajepour, and S. Corbin, "Application of experimental-based modeling to laser cladding," *J. Laser Appl.,* vol. 14, no. 3, pp. 165-173, Aug 2002, doi: 10.2351/1.1494079.

[115] M. Bamberger, W. D. Kaplan, B. Medres, and L. Shepeleva, "Calculation of process parameters for laser alloying and cladding," *J. Laser Appl.,* vol. 10, no. 1, pp. 29-33, Feb 1998.

[116] M. Zeinali and A. Khajepour, "Development of an adaptive fuzzy logic-based inverse dynamic model for laser cladding process," *Engineering Applications of Artificial Intelligence,* vol. 23, no. 8, pp. 1408-1419, Dec 2010, doi: 10.1016/j.engappai.2009.11.006.

[117] F. Luo, J.-h. Yao, X.-x. Hu, and G.-z. Chai, "Effect of Laser Power on the Cladding Temperature Field and the Heat Affected Zone," *Journal of Iron and Steel Research International,* vol. 18, no. 1, pp. 73-78, Jan 2011, doi: 10.1016/s1006-706x(11)60014-9.

[118] C. Zeng, W. Tian, W.-H. Liao, and L. Hua, "Study of laser cladding thermal damage: A quantified microhardness method," *Surface & Coatings Technology,* vol. 236, pp. 309-314, 2013, doi: 10.1016/j.surfcoat.2013.10.005.

[119] J. T. Hofman, D. F. de Lange, B. Pathiraj, and J. Meijer, "FEM modeling and experimental verification for dilution control in laser cladding," *Journal of Materials Processing Tech.,* vol. 211, no. 2, pp. 187-196, 2011, doi: 10.1016/j.jmatprotec.2010.09.007.

[120] I. Tabernero, A. Lamikiz, S. Martínez, E. Ukar, and L. N. L. D. Lacalle, "Geometric Modelling of Added Layers by Coaxial Laser Cladding," *Physics Procedia,* vol. 39, pp. 913-920, 2012, doi: 10.1016/j.phpro.2012.10.116.

[121] W. C. Tseng and J. N. Aoh, "Simulation study on laser cladding on preplaced powder layer with a tailored laser heat source," *Optics and Laser Technology,* vol. 48, pp. 141-152, 2013, doi: 10.1016/j.optlastec.2012.09.014.

[122] V. Ocelik, M. Eekma, I. Hemmati, and J. T. M. De Hosson, "Elimination of Start/Stop defects in laser cladding," *Surface & Coatings Technology,* vol. 206, no. 8-9, pp. 2403-2409, 2012, doi: 10.1016/j.surfcoat.2011.10.040.

[123] J. T. Hofman, B. Pathiraj, J. van Dijk, D. E. de Lange, and J. Meijer, "A camera based feedback control strategy for the laser cladding process," *J. Mater. Process. Technol.,* vol. 212, no. 11, pp. 2455-2462, Nov 2012, doi: 10.1016/j.jmatprotec.2012.06.027.

[124] I. Smurov, M. Doubenskaia, and A. Zaitsev, "Complex Analysis of Laser Cladding based on Comprehensive Optical Diagnostics and Numerical Simulation," *Physics Procedia,* vol. 39, pp. 743-752, 2012, doi: 10.1016/j.phpro.2012.10.096.

[125] I. Smurov, M. Doubenskaia, and A. Zaitsev, "Comprehensive analysis of laser cladding by means of optical diagnostics and numerical simulation," *Surface & Coatings Technology,* vol. 220, pp. 112-121, Apr 15 2013, doi: 10.1016/j.surfcoat.2012.10.053.

[126] A. Calleja, I. Tabernero, A. Fernández, A. Celaya, A. Lamikiz, and L. N. López de Lacalle, "Improvement of strategies and parameters for multi- axis laser cladding operations," *Optics and Lasers in Engineering,* vol. 56, pp. 113-120, 2014, doi: 10.1016/j.optlaseng.2013.12.017.

[127] F. Meriaudeau, F. Truchetete, C. Dumont, E. Renier, and P. Bolland, "Acquisition and image processing system able to optimize laser cladding process," vol. 2, pp. 1628-1631, 1996.

[128] F. Wang, H. Mao, D. Zhang, X. Zhao, and Y. Shen, "Online study of cracks during laser cladding process based on acoustic emission technique and finite element analysis," *Applied Surface Science,* vol. 255, no. 5, pp. 3267-3275, 2008, doi: 10.1016/j.apsusc.2008.09.039.

[129] B. N. R. Munjuluri, S. Agarwal, and F. W. Liou, "Process modeling, monitoring and control of laser metal forming," 2001.

[130] F. Klocke, C. Brecher, M. Wegener, D. Heinen, B. Fischer, and D. Do-Khac, "Scanner- based Laser Cladding," *Physics Procedia,* vol. 39, pp. 346-353, 2012, doi: 10.1016/j.phpro.2012.10.047.

[131] F. Bruckner, S. Nowotny, and C. Leyens, "Innovations in laser cladding and direct metal deposition," in *Conference on High Power Laser Materials Processing - Lasers, Beam Delivery, Diagnostics, and Applications*, San Francisco, CA, Jan 24-26 2012, vol. 8239, BELLINGHAM: Spie-Int Soc Optical Engineering, in Proceedings of SPIE, 2012, doi: 10.1117/12.906706.

[132] S. R. Lewis *et al.*, "Improving rail wear and RCF performance using laser cladding," pp. 268-278. ISSN 0043-1648, 2016.

[133] A. Gebhardt, *Generative Fertigungsverfahren: rapid prototyping-rapid tooling-rapid manufacturing,* Carl Hanser Verlag GmbH & Co. KG 2007.

[134] E. Diaz, J. M. Amado, J. Montero, M. J. Tobar, and A. Yanez, "Comparative study of Co-based alloys in repairing low Cr-Mo steel components by laser cladding," *Laser Assisted Net Shape Engineering 7 (Lane 2012),* vol. 39, pp. 368-375, 2012 2012, doi: 10.1016/j.phpro.2012.10.050.

[135] J. Zhang, Y. Hu, X.-J. Tan, L. Guo, and Q.-M. Zhang, "Microstructure and high temperature tribological behavior of laser cladding Ni60A alloys coatings on 45 steel substrate," *Transactions of Nonferrous Metals Society of China,* vol. 25, no. 5, pp. 1525-1532, 2015, doi: 10.1016/S1003-6326(15)63754-2.

[136] A. Oliveira, P. Da Silva, and R. Vilar, "Microstructural features of consecutive layers of Stellite 6 deposited by laser cladding," *Surface & Coatings Technology,* vol. 153, no. 2, pp. 203-209, 2002, doi: 10.1016/S0257-8972(01)01687-5.

[137] J. L. de Mol van Otterloo and J. T. M. De Hosson, "Microstructure and abrasive wear of cobalt- based laser coatings," *Scripta Materialia,* vol. 36, no. 2, pp. 239-245, 1997, doi: 10.1016/S1359-6462(96)00346-6.

[138] C. Leyens, Brückner, F., Nowotny, S., "Lastest Development Work on Induction Assisted Laser Cladding Processes," presented at the Laser Additive Manufacturing LAM 2012 Workshop 2012.

[139] M. Rütering, "Optimizing components and surfaces with diode laser - generating, cladding and hardening of products," Laserline GmbH.

[140] F. Wang, H. Mao, D. Zhang, and X. Zhao, "The crack control during laser cladding by adding the stainless steel net in the coating," *Applied Surface Science,* vol. 255, no. 21, pp. 8846-8854, 2009, doi: 10.1016/j.apsusc.2009.06.066.

[141] B. Valsecchi, B. Previtali, E. Gariboldi, and A. Liu, "Characterisation of the Thermal Damage in a Martensitic Steel Substrate Consequent to Laser Cladding Process," *11th International Conference on the Mechanical Behavior of Materials (Icm11),* vol. 10, 2011, doi: 10.1016/j.proeng.2011.04.474.

[142] H. Köhler, R. Rajput, P. Khazan, and J. R. Kornmeier, "On the Influence of Laser Cladding and Post- processing Strategies on Residual Stresses in Steel Specimens," *Physics Procedia,* vol. 56, pp. 250-261, 2014, doi: 10.1016/j.phpro.2014.08.169.

[143] U. de Oliveira, V. Ocelík, and J. T. M. De Hosson, "Residual stress analysis in Co-based laser clad layers by laboratory X-rays and synchrotron diffraction techniques," *Surface & Coatings Technology,* vol. 201, no. 3, pp. 533-542, 2006, doi: 10.1016/j.surfcoat.2005.12.011.

[144] H. Köhler, K. Partes, J. R. Kornmeier, and F. Vollertsen, "Residual Stresses in Steel Specimens Induced by Laser Cladding and their Effect on Fatigue Strength," *Physics Procedia,* vol. 39, pp. 354-361, 2012, doi: 10.1016/j.phpro.2012.10.048.

[145] J. Y. Chen, K. Conlon, L. Xue, and R. Rogge, "Experimental study of residual stresses in laser clad AISI P20 tool steel on pre- hardened wrought P20 substrate," *Materials Science & Engineering A,* vol. 527, no. 27, pp. 7265-7273, 2010, doi: 10.1016/j.msea.2010.07.098.

[146] A. L. Schawlow and C. H. Townes, "Infrared and optical masers," *Physical Review,* vol. 112, no. 6, pp. 1940-1949, 1958, doi: 10.1103/PhysRev.112.1940.

[147] N. AMRC, "Nuclear AMRC News, Issue 16," The University of Sheffield, 2014.

[148] "Case Study: Reclaim." http://www.the-mtc.org/our-case-studies/reclaim (accessed 2019).

[149] D. Wang, Q. Hu, Y. Zheng, Y. Xie, and X. Zeng, "Study on deposition rate and laser energy efficiency of Laser- Induction Hybrid Cladding," *Optics and Laser Technology,* vol. 77, pp. 16-22, 2016, doi: 10.1016/j.optlastec.2015.08.019.

[150] F. Luo *et al.*, "Performance comparison of Stellite 6® deposited on steel using supersonic laser deposition and laser cladding," *Surface & Coatings Technology,* vol. 212, pp. 119-127, 2012, doi: 10.1016/j.surfcoat.2012.09.031.

[151] G. Telasang, et al., "Effect of laser parameters on microstructure and hardness of laser clad and tempered AISI H13 tool steel," *Surface & Coatings Technology,* vol. 258, pp. 1108-1118, Nov 15 2014, doi: 10.1016/j.surfcoat.2014.07.023.

[152] G. Hammersley, L. A. Hackel, and F. Harris, "Surface prestressing to improve fatigue strength of components by laser shot peening," *Optics and Lasers in Engineering,* vol.34, no.4-6, pp.327-337, 2000, doi:10.1016/S0143-8166(00)00083-X.

[153] W. Zhao, G. Zha, M. Xi, and S. Gao, "Effects of Synchronous Rolling on Microstructure, Hardness, and Wear Resistance of Laser Multilayer Cladding," *Journal of Materials Engineering and Performance,* vol. 27, no. 4, pp. 1746-1752, 2018, doi: 10.1007/s11665-018-3286-x.

[154] P. Beaty, B. Temple, M. B. Marshall, and R. Lewis, "Experimental modelling of lipping in insulated rail joints and investigation of rail head material improvements," *Proc. Inst. Mech. Eng. Part F-J. Rail Rapid Transit,* Article vol. 230, no. 4, pp. 1375-1387, May 2016, doi: 10.1177/0954409715600740.

[155] S. Niederhauser and B. Karlsson, "Fatigue behaviour of Co–Cr laser cladded steel plates for railway applications," *Wear,* vol. 258, no. 7, pp. 1156-1164, 2005, doi: 10.1016/j.wear.2004.03.026.

[156] S. Niederhauser and B. Karlsson, "Mechanical properties of laser cladded steel," *Materials Science and Technology,* vol. 19, no. 11, pp. 1611-1616, Nov 2003, doi: 10.1179/026708303225008103.

[157] T. Roy *et al.*, "Effect of deposition material and heat treatment on wear and rolling contact fatigue of laser cladded rails," *Wear,* vol. 412-413, pp. 69-81, 2018, doi: 10.1016/j.wear.2018.07.001.

[158] Q. Lai *et al.*, "Influences of depositing materials, processing parameters and heating conditions on material characteristics of laser-cladded hypereutectoid rails," *Journal of Materials Processing Tech.,* vol. 263, pp. 1-20, 2019, doi: 10.1016/j.jmatprotec.2018.07.035.

[159] Q. Lai *et al.*, "Investigation of a novel functionally graded material for the repair of premium hypereutectoid rails using laser cladding technology," *Composites Part B,* vol. 130, pp. 174-191, 2017, doi: 10.1016/j.compositesb.2017.07.089.

[160] W. Chen, H. Chen, C. Li, X. Wang, and Q. Cai, "Microstructure and fatigue crack growth of EA4T steel in laser cladding remanufacturing," *Engineering Failure Analysis,* vol. 79, pp. 120-129, 2017, doi: 10.1016/j.engfailanal.2017.03.005.

[161] S. Ayrault, A. Chateauminois, J. P. Soulier, D. Tréheux, and A. B. Vannes, "Deposition of a ceramic coating on a thermoplastic polymer by atmospheric plasma and laser cladding," *Surface and Coatings Technology,* vol. 79, no. 1-3, pp. 119-130, 1996.

[162] Z. Xiaoyan, T. Zengyi, Z. Beidi, Z. Erhua, and C. Kun, "Investigation of laser cladding ceramic-metal composite coatings: processing modes and mechanisms," *Surface & Coatings Technology,* vol.79, no.1, pp.209-217, 1996, doi:10.1016/0257-8972(95)02431-X.

[163] M. Ellis, D. C. Xiao, C. Lee, W. M. Steen, K. G. Watkins, and W. P. Brown, "Processing aspects of laser cladding an aluminium alloy onto steel," *Journal of Materials Processing Tech.,* vol.52, no.1, pp.55-67, 1995, doi:10.1016/0924-0136(94)01443-5.

[164] A. Riveiro *et al.*, "Optimization of Laser Cladding for Al Coating Production," *Physics Procedia,* vol. 41, pp. 327-334, 2013, doi: 10.1016/j.phpro.2013.03.085.

[165] A. Emamian, M. Alimardani, and A. Khajepour, "Correlation between temperature distribution and in situ formed microstructure of Fe-TiC deposited on carbon steel using laser cladding," *Applied Surface Science,* vol. 258, no. 22, pp. 9025-9031, 2012, doi: 10.1016/j.apsusc.2012.05.143.

[166] P. Wen, Z. Cai, Z. Feng, and G. Wang, "Microstructure and mechanical properties of hot wire laser clad layers for repairing precipitation hardening martensitic stainless steel," *Optics and Laser Technology,* vol. 75, pp. 207-213, 2015, doi: 10.1016/j.optlastec.2015.07.014.

[167] Z. K. Fu, H. H. Ding, W. J. Wang, Q. Y. Liu, J. Guo, and M. H. Zhu, "Investigation on microstructure and wear characteristic of laser cladding Fe- based alloy on wheel/ rail materials," *Wear,* vol. 330-331, pp. 592-599, 2015, doi: 10.1016/j.wear.2015.02.053.

[168] Q. Wu, W. Li, N. Zhong, W. Gang, and W. Haishan, "Microstructure and wear behavior of laser cladding VC– Cr7C3 ceramic coating on steel substrate," *Materials and Design,* vol. 49, pp. 10-18, 2013, doi: 10.1016/j.matdes.2013.01.067.

[169] J. Yang, J. Huang, D. Fan, and S. Chen, "Microstructure and wear properties of Fe–6wt.%Cr–0.55wt.%C–Xwt.%Nb laser cladding coating and the mechanism analysis," *Materials & Design,*vol.88,pp.1031-1041,2015, doi: 10.1016/j.matdes.2015.09.108.

[170] X. Duan *et al.*, "Reinforcement mechanism and wear resistance of Al2O3/ Fe- Cr- Mo steel composite coating produced by laser cladding," *Surface & Coatings Technology,* vol. 291, pp. 230-238, 2016, doi: 10.1016/j.surfcoat.2016.02.045.

[171] J. Jiang, Y. Zhou, M. Kang, and J. Wang, "Optimization of Process Parameters, Microstructure, and Properties of Laser Cladding Fe- Based Alloy on 42CrMo Steel Roller," *Materials,* vol. 11, no. 10, 2018, doi: 10.3390/ma11102061.

[172] "Eatonite Anti-Corrosion Laser Cladding Hydraulic Cylinders." http://www.eaton.com/Eaton/ProductsServices/Hydraulics/PlatingTechnology/eatonite-laser-cladding/index.htm (accessed 2019).

[173] K. Sobiyi and E. Akinlabi, "Microstructure and Wear Properties of Laser-Cladded cBN/Ti 3 Al on Pure Titanium," *The Arabian Journal for Science and Engineering. Section B, Engineering,* vol. 42, no. 11, pp. 4597-4604, 2017, doi: 10.1007/s13369-017-2585-0.

[174] M. Wolff, M. Böhm, and D. Helm, "Material behavior of steel - Modeling of complex phenomena and thermodynamic consistency," *International Journal of Plasticity,* vol. 24, no. 5, pp. 746-774, 2008, doi: 10.1016/j.ijplas.2007.07.005.

[175] R. I. Borja, *Plasticity: Modeling and Computation*, 1st ed. Berlin, Heidelberg, 2013.

[176] F. Dunne, *Introduction to computational plasticity [electronic resource]*. Oxford University Press, 2005.

[177] I. M. Hutchings, "Leonardo da Vinci's studies of friction," *Wear,* vol. 360, pp. 51-66, 2016, doi: 10.1016/j.wear.2016.04.019.

[178] K. C. Ludema and H. C. Meng, "Wear models and predictive equations: their form and content," *Wear,* vol. 181, pp. 443-457, 1995, doi: 10.1016/0043-1648(95)90158-2.

[179] J. F. Archard, "Friction between metal surfaces," *Wear,* vol. 113, no. 1, pp. 3-16, 1986, doi: 10.1016/0043-1648(86)90052-9.

[180] M. O. Robbins and S. Cheng, "Defining Contact at the Atomic Scale," *Tribology letters.,* vol. 39, no. 3, pp. 329-348, 2010, doi: 10.1007/s11249-010-9682-5.

[181] J. F. Archard and W. Hirst, "THE WEAR OF METALS UNDER UNLUBRICATED CONDITIONS," *Proceedings of the Royal Society of London Series a-Mathematical and Physical Sciences,* Article vol. 236, no. 1206, pp. 397-&, 1956, doi: 10.1098/rspa.1956.0144.

[182] M. Elyyan. "Better Particle Erosion Fluid Dynamics Modeling in ANSYS Fluent 18." https://www.ansys.com/en-gb/blog/erosion-fluid-dynamics-modeling (accessed 2019).

[183] I. Finnie, "Erosion of surfaces by solid particles," *Wear,* vol. 3, no. 2, pp. 87-103, 1960, doi: 10.1016/0043-1648(60)90055-7.

[184] Y. I. Oka and T. Yoshida, "Practical estimation of erosion damage caused by solid particle impact: Part 2: Mechanical properties of materials directly associated with erosion damage," *Wear,* vol. 259, no. 1-6, pp. 102-109, 2005, doi: 10.1016/j.wear.2005.01.040.

[185] B. S. McLaury, S. A. Shirazi, J. R. Shadley, and E. F. Rybicki, "Modeling erosion in chokes," in *Proceeding of ASME Fluids Eng. Summer Meeting*, California, 1996.

[186] J. Higgins, "Drop Test Simulation Made Easy With ANSYS Simulation," 2008, https://support.ansys.com/staticassets/ANSYS/Conference/Confidence/Boston/Downloads/drop-test-simulation-made-easy-with-ansys-simulation.pdf.

[187] L. Crocker, "Good Practice Guide to the application of finite element analysis to erosion modelling," *Good Practice Guide No.146*, NPL Management Limited, 2017.

[188] W. Goldsmith, *Impact : the theory and physical behaviour of colliding solids*. London: Edward Arnold, 1960.

[189] R. Lewis, A. Yoxall, L. A. Canty, and E. R. Romo, "Development of engineering design tools to help reduce apple bruising," *Journal of Food Engineering,* vol. 83, no. 3, pp. 356-365, 2007.

[190] W. Golsdmith and S. A. Finnegan, "Penetration and perforation processes in metal targets at and above ballistic velocities," *International Journal of Mechanical Sciences,* vol. 13, no. 10, pp. 843-866, 1971, doi: 10.1016/0020-7403(71)90111-1.

[191] M. Pletz, W. Daves, W. Yao, and H. Ossberger, "Rolling contact fatigue of three crossing nose materials - Multiscale FE approach," *Wear,* vol. 314, no. 1-2, pp. 69-77, 2014, doi: 10.1016/j.wear.2013.11.013.

[192] W. J. Stronge, *Impact mechanics*, First paperback edition. ed. Cambridge, United Kingdom: Cambridge University Press, 2004.

[193] F. C. Zhang *et al.*, "Explosion hardening of Hadfield steel crossing," *Materials Science and Technology,* vol.26, no.2, pp.223-229, 2010, doi: 10.1179/174328408X363263.

[194] W. C. Oliver and G. M. Pharr, "An improved technique for determining hardness and elastic modulus using load and displacement sensing indentation experiments," *Journal of Materials Research,* Article vol. 7, no. 6, pp. 1564-1583, 1992, doi: 10.1557/jmr.1992.1564.

[195] M. F. Ashby and S. C. Lim, "Wear mechanism maps," *Scripta Metallurgica et Materiala,* vol. 24, no. 5, pp. 805-810, 1990, doi: 10.1016/0956-716X(90)90116-X.

[196] R. Lewis and U. Olofsson, "Mapping rail wear regimes and transitions," *Wear,* vol. 257, no. 7-8, pp. 721-729, 2004, doi: 10.1016/j.wear.2004.03.019.

[197] J. F. Archard, "Contact and Rubbing of Flat Surfaces," *Journal of Applied Physics,* vol. 24, no. 8, pp. 981-988, 1953, doi: 10.1063/1.1721448.

[198] S. Lewis and D. I. Fletcher, "Creep curve measurement to support wear and adhesion modelling, using a continuously variable creep twin disc machine," *Wear,* vol. 298, pp. 57-65, 2013, doi: 10.1016/j.wear.2012.11.065.

[199] D. I. Fletcher and J. H. Beynon, "Development of a machine for closely controlled rolling contact fatigue and wear testing," *Journal of Testing and Evaluation,* Article vol. 28, no. 4, pp. 267-275, Jul 2000.

[200] R. Lewis *et al.*, "Towards a Standard Approach for Wear Testing of Wheel and Rail Materials," *Proceedings of the Institution of Mechanical Engineers, Part F: Journal of Rail and Rapid Transit,* vol. 231, no. 7, pp. 760-774, 2017.

[201] M. Watson *et al.*, "An analysis of the quality of experimental design and reliability of results in tribology research," *Wear,* vol. 426, pp. 1712-1718, 2019, doi: 10.1016/j.wear.2018.12.028.

[202] T. Slatter, R. Lewis, and A. H. Jones, "The influence of induction hardening on the impact wear resistance of compacted graphite iron (CGI)," *Wear,* vol. 270, no. 3, pp. 302-311, 2011, doi: 10.1016/j.wear.2010.11.003.

[203] LaVision. "DaVis - Software Solution for Intelligent Imaging." https://www.lavision.de/en/products/davis-software/ (accessed June, 2019).

[204] W. J. Brayshaw, M. J. Roy, T. Sun, V. Akrivos, and A. H. Sherry, "Iterative mesh-based hardness mapping," *Science and Technology of Welding and Joining,* Article vol. 22, no. 5, pp. 404-411, 2017, doi: 10.1080/13621718.2016.1251713.

[205] W. R. Tyfour, J. H. Beynon, and A. Kapoor, "The steady state wear behaviour of pearlitic rail steel under dry rolling-sliding contact conditions," *Wear,* vol. 180, no. 1, pp. 79-89, 1995, doi: 10.1016/0043-1648(94)06533-0.

[206] F. J. Franklin, I. Widiyarta, and A. Kapoor, "Computer simulation of wear and rolling contact fatigue," *Wear,* vol. 251, no. 1, pp. 949-955, 2001, doi: 10.1016/S0043-1648(01)00732-3.

[207] P. Bailly, *Materials and structures under shock and impact*. London: Hoboken, WILEY, 2014.

[208] Novatech. "Dynamic Force Measurement With Loadcells." https://www.novatechloadcells.co.uk/eng/e006.htm (accessed 2019).

[209] A. Grueninger *et al.*, "Surface texturing by laser cladding," *Journal of Laser Applications,* vol. 23, no. 2, p. 6, 2011, doi: 10.2351/1.3573371.

[210] P. A. Engel, "Percussive impact wear: A study of repetitively impacting solid components in engineering," *Tribology International,* vol. 11, no. 3, pp. 169-176, 1978, doi: 10.1016/0301-679X(78)90002-6.

[211] C. Chang, D. Verdi, M. Angel Garrido, and J. Ruiz-Hervias, "Micro-scale mechanical characterization of Inconel cermet coatings deposited by laser cladding," *Boletin De La Sociedad Espanola De Ceramica Y Vidrio,* vol. 55, no. 4, pp. 136-142, 2016, doi: 10.1016/j.bsecv.2016.01.001.

[212] M. Gee, L. Orkney, T. Fry, and J. Nunn, "In situ remote hot erosion scar measurement," *Wear,* vol. 380-381, pp. 217-227, 2017, doi: 10.1016/j.wear.2017.02.038.

[213] Q. Lai *et al.*, "Effects of preheating and carbon dilution on material characteristics of laser-cladded hypereutectoid rail steels," *Materials Science & Engineering A,* vol. 712, pp. 548-563, 2018, doi: 10.1016/j.msea.2017.12.003.

[214] C. Brunner-Schwer, T. Petrat, B. Graf, and M. Rethmeier, "Highspeed-plasma-laser-cladding of thin wear resistance coatings: A process approach as a hybrid metal deposition technology," *Vacuum,* vol. 166, pp. 123-126, 2019, doi: 10.1016/j.vacuum.2019.05.003.

[215] *GMRT2466 Railway Wheelsets*, RSSB, 2017.

10 APPENDIX

Table 10-1 GB wheel tread profile wear limits (from RSSB GMRT2466) [215]

Tread profile	Flange width (mm) (measured at 13 mm above wheel datum D_0)		Flange height details (mm)	
	As new, maximum	Minimum (worn)	As new	Maximum (worn)
P1	28	24	30	36.5
P5	31.5	27	29	33
P6	28.5	24	30	36.5
P8	28.5	24	30	36.5
RD9	26	24	30	36.5
P9 (see Note)	25 (21.5)	21 (18)	30	36.5
P10	31	27	28	33
P11	28	24	30	34
P12	28.5	24	30	36.5
P10/RD9	25.5	24	28	33

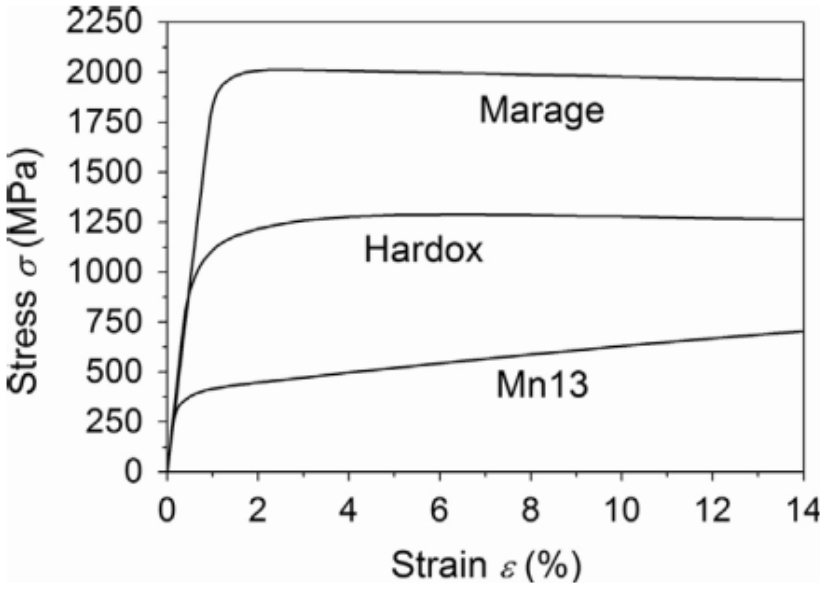

Figure 10-1 Tensile stress-strain curves for three materials by Pletz et al. [191]

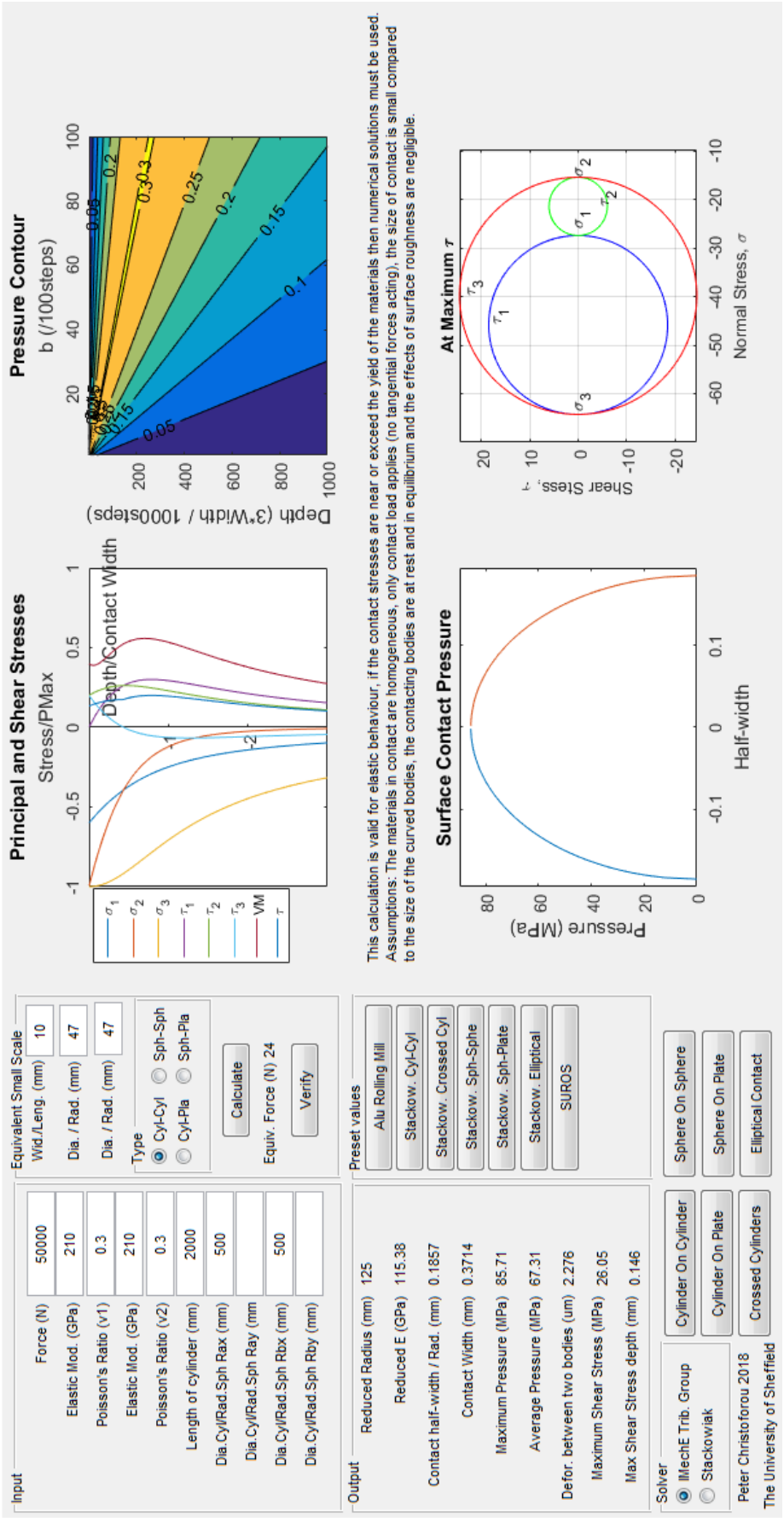

Figure 10-2 Example of Hertzian contact calculator GUI that was produced with Matlab

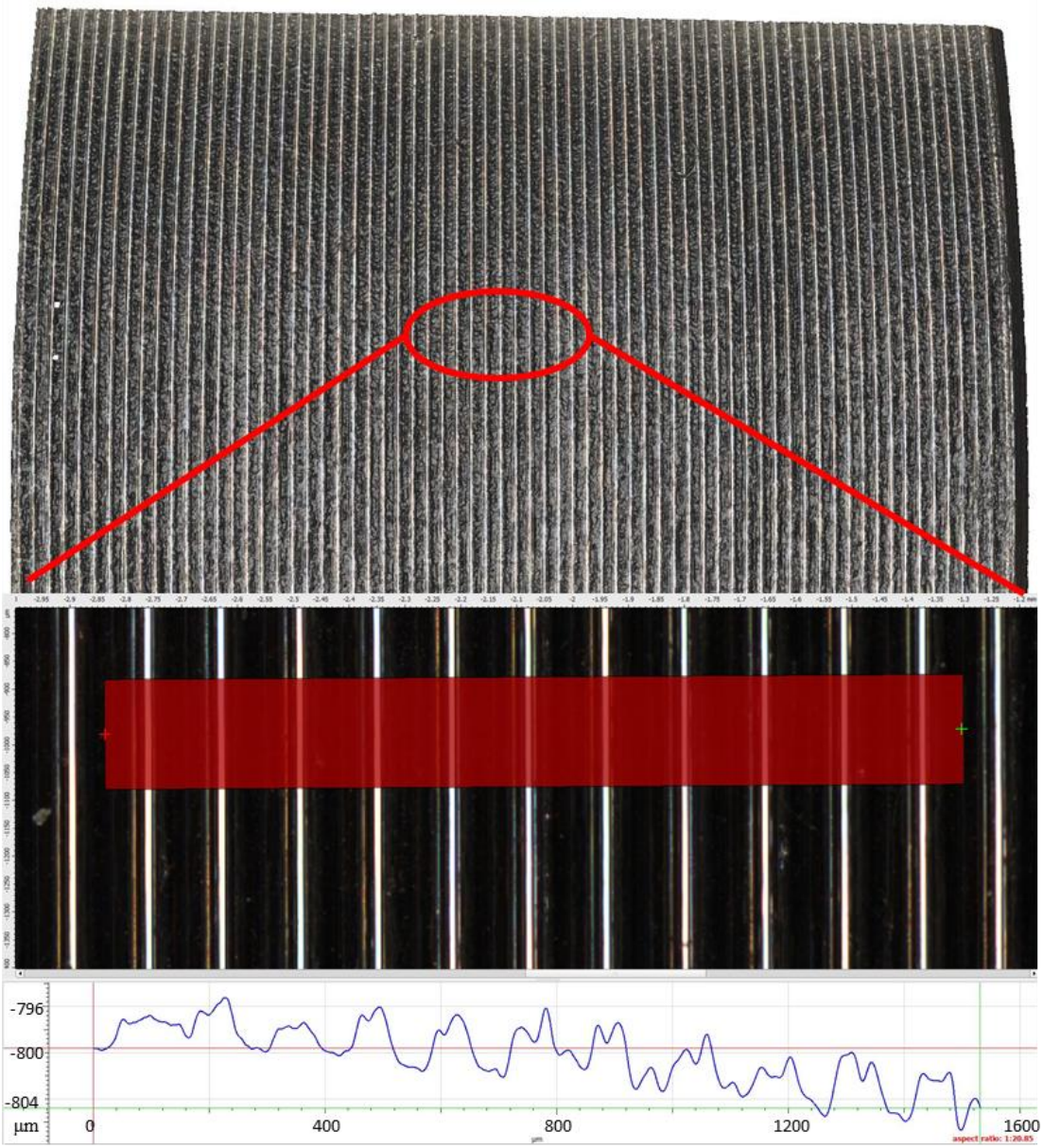

Figure 10-3 Surface of the R400HT SUROS disc (texture test) and profile measurement (bottom)

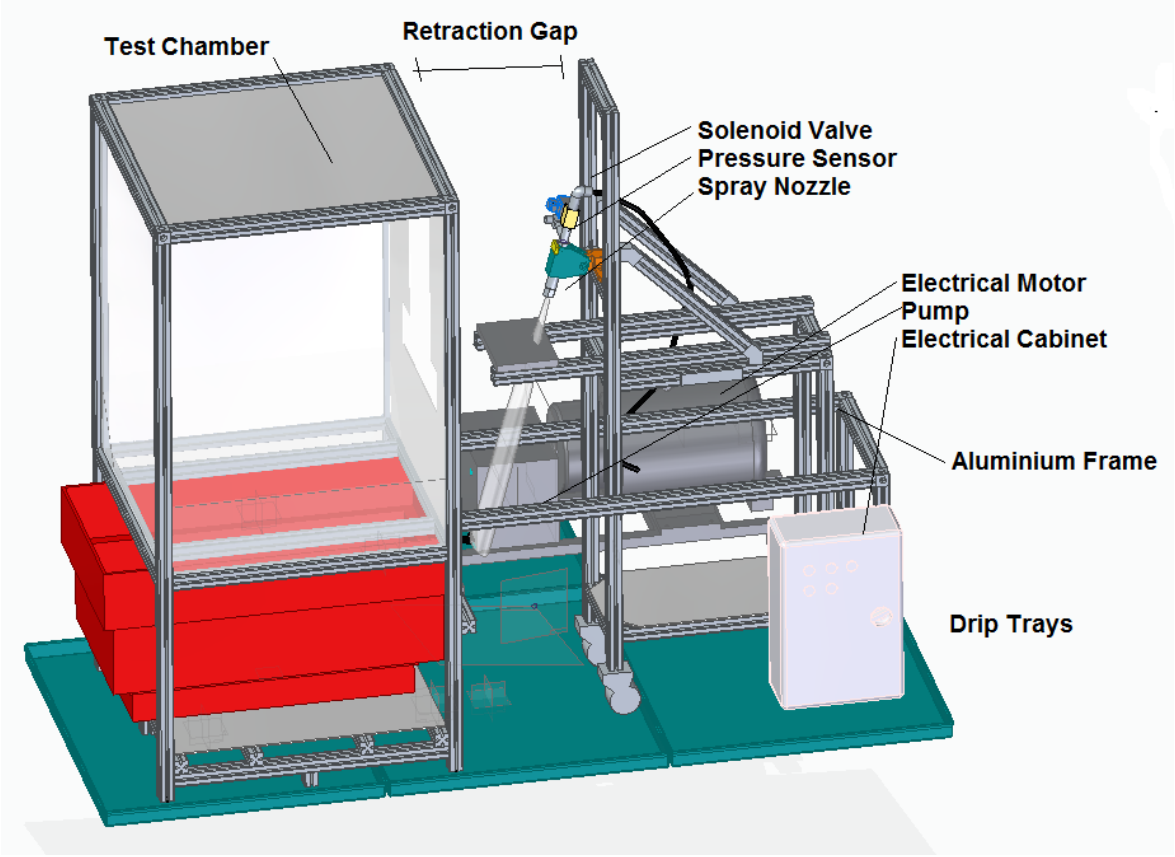

Figure 10-4 3D model of the test erosion rig used for ordering components and assembly

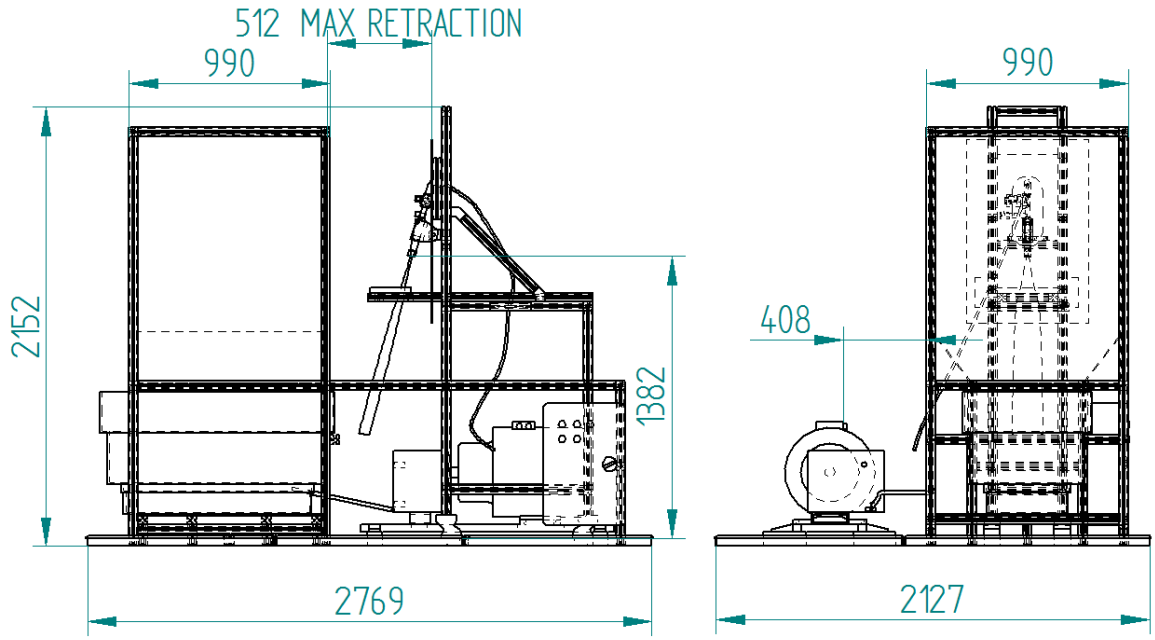

Figure 10-5 General dimensions of the erosion rig

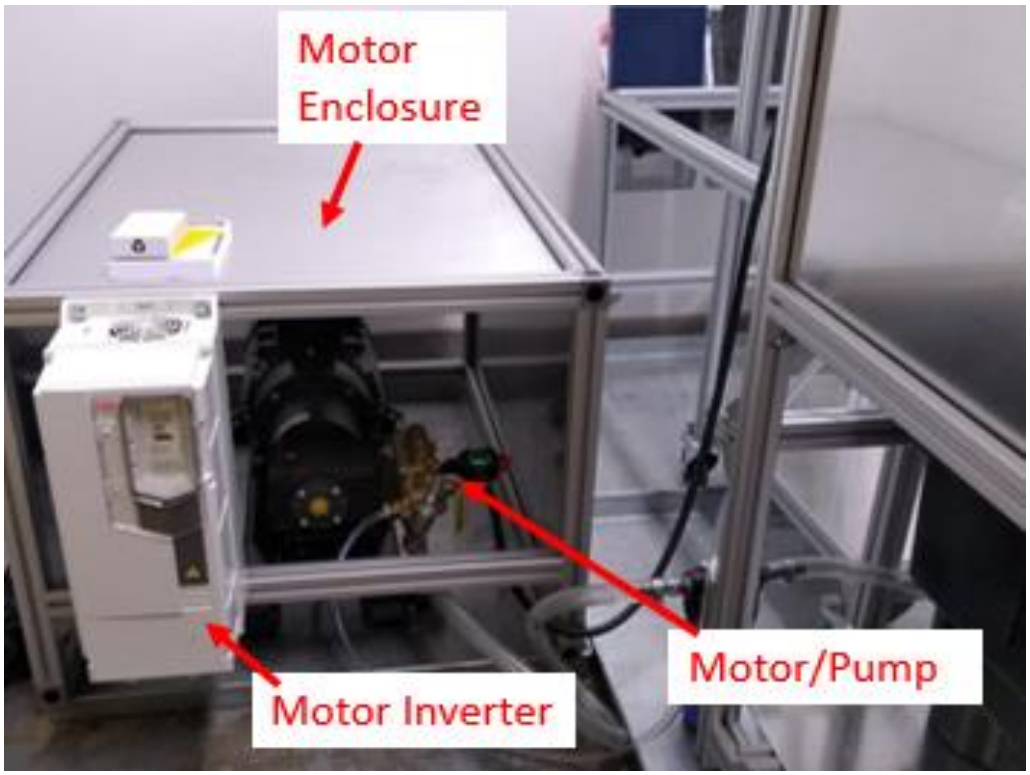

Figure 10-6 Motor inverter and motor pump in a protective casing next to the erosion rig